Optimization of the Geometry of Axisymmetric Point-absorber Wave Energy Converters

by

Emma Edwards

Submitted to the Department of Mechanical Engineering
in partial fulfillment of the requirements for the degree of

Doctor of Philosophy in Mechanical Engineering

at the

MASSACHUSETTS INSTITUTE OF TECHNOLOGY

September 2020

Author .....
Department of Mechanical Engineering
August 14, 2020

Certified by .....
Dick K. P. Yue
Philip J. Solondz Professor of Engineering; Professor of Mechanical & Ocean Engineering
Thesis Supervisor

Accepted by .....
Nicolas Hadjiconstantinou
Chairman, Department Committee on Graduate Theses

Optimization of the Geometry of Axisymmetric Point-absorber Wave Energy Converters

by

Emma Edwards

Submitted to the Department of Mechanical Engineering
on August 14, 2020, in partial fulfillment of the
requirements for the degree of
Doctor of Philosophy in Mechanical Engineering

Abstract

Wave energy represents an abundant source of renewable energy, but as yet the potential is not fully utilized. Aiming to exploit this vast potential, many theoretical, experimental and pilot-scale studies have been conducted on wave energy converters (WECs), however as yet there has been no convergence on the optimal shape of a WEC. Furthermore, there is no agreed-upon definition of what it means for a WEC to be 'optimal' and no established framework to find optimal shapes. This thesis establishes a novel, scientifically rigorous framework to find practically realistic optimal shapes of WECs. Through a general, efficient and efficacious procedure, we systematically investigate groups of shapes to reveal powerful new results for the optimal shapes of axisymmetric WECs. Finally, we analyze these results to develop insights and gain physical intuition about the best WEC shapes.

Although the hydrodynamics of WECs under operating conditions can generally be considered linear, the dependence of the hydrodynamics and power extraction of the geometry can be highly nonlinear. In this thesis, we assume linear hydrodynamics but allow the geometry to be very general and consider a wide range of possible geometries. We optimize a single-body deep-water 3D axisymmetric point absorber WEC, with linear power take-off mechanisms, assuming a monochromatic unidirectional incoming wave with given wavenumber k. We consider two separate problems: a WEC moving and extracting energy in the heave mode only, as well as the complete 3D problem of an axisymmetric WEC moving and extracting energy in heave, surge and pitch.

This thesis develops a robust computational approach for finding the optimal WEC shape underpinned by a strong theoretical grounding. We describe general geometries using piecewise parametric polynomial basis functions and develop a multi-objective optimization to minimize WEC surface area and volume, while ensuring constant, maximum power for all shapes. We show that constraints are necessary to ensure feasible body motion, weight distribution and stability. We present a novel theorem to find roots of the heave resonance equation, which adds to our understanding of the problem and significantly speeds up the optimization process by effectively decreasing the degree of freedom of the optimization.

Our systematic investigation encompasses a broad range of shapes, starting with truncated cylinders and then generalizing to significantly more complex shapes. We show that shapes that protrude outwards below the waterline generally perform better, due to their high heave damping coefficient, which enables smaller volumes while still adhering to the motion constraint. Furthermore, in general the maximum radius occurs closer to the waterline than the maximum draft. Compared to the heave-only problem, the optimal shapes from the heave-surge-pitch problem are generally wider and less protruding outwards, resulting in a larger volume and surface area. The trends that we observe in the optimal shapes are consistent across all the groups of shapes, implying these may be features of a general optimum. Optimizing the geometry can significantly decrease the material used to produce the same, maximum power: for example, the optimal shapes have up to 72 % less surface are and 93 % less volume than the optimized cylinders.
The methodology developed, along with the results found, in this thesis will help to inform future WEC development. Through the discovery of WEC shapes which extract maximum power and require minimum material use, whilst ensuring the WEC shapes are practically feasible, this thesis is a step forward in our understanding of WECs and ultimately contributes towards wave energy becoming a viable source of renewable energy in future.

Thesis Supervisor: Dick K. P. Yue
Title: Philip J. Solondz Professor of Engineering; Professor of Mechanical & Ocean Engineering

Acknowledgments

Firstly, I would like to thank Professor Yue for supporting me throughout my PhD. You have taught me so much, not only about hydrodynamics, but also about what makes good research: to step back and observe the whole process, but equally to be extremely rigorous at every step.

I would also like to thank my committee members: Dr. Liu, Professor Akylas, and Professor Triantafyllou. Thank you for much for your guidance and advice throughout the last few years.

Additionally, I would like to thank everyone from the VFRL group during my time at MIT. Especially during the last few months during quarantine/ lockdown, our (virtual) coffee meetings have been something to look forward to! I would like to particularly thank Grgur Tokić for all of your help throughout my entire PhD process. You have been there to talk to about everything from classes to theory to presentation help. I sincerely appreciate your eagerness to help. I learned so much from you and look forward to continuing collaboration in the future on wave energy!

I also want to give a large acknowledgement to the MIT cycling team and all of my friends from the team. I had never raced my bike before coming to MIT, but during my time here I became so involved in bike racing, and none of that would have been possible without the MIT cycling team. Also, it allowed me to meet some of my best friends at MIT. Thank you for all of the long rides, the town lines, the great hotel breakfasts from roadside motels for 2 months straight each spring, the leadouts and the coffee (cake) rides. The MIT cycling team is truly a special group, and I will miss you all very much.

And to my family: mom, dad, Sarah and Grif, thank you so much for being by my side since the start. Thank you for always believing in me and encouraging me to pursue subjects that not many women pursue. Without this support, I never would have made it to where I am today. Thank you for inspiring me, and thank you for always being there when I need you.

And finally, to Eddie. I'm not sure even how to express my gratitude to you for all of

your support throughout my PhD. Thank you for moving to Boston to be with me. Thank you for absolutely always believing in me. Thank you for hours and hours of talking about my research. Thank you for making up a song about my thesis. Your support never waivered and I am so grateful for you. And now to our next chapter!

Contents

1 Introduction **35**

1.1 Wave energy potential and state of the art of wave energy converters 35

1.2 Problem statement and thesis objectives 39

1.3 Thesis outline 40

2 Hydrodynamic theory for an axisymmetric floating wave energy converter **43**

2.1 Assumptions and problem setup 43

2.2 Theory 45

2.2.1 Derivation of the equation of motion of a floating body in waves 45

2.2.2 Equation of motion of a floating WEC 52

2.2.3 Extractable power 56

2.2.4 Maximum power 60

2.2.5 Matching equation of motion with optimal motion 68

2.2.6 Far-field analysis 69

2.3 Summary 75

3 Optimization Framework **77**

3.1 Main concepts involved for optimizing a WEC 77

3.2 Optimization framework 79

3.2.1 Multi-objective optimizations and Pareto Fronts 79

3.2.2 Constraints in our problem 81

3.2.3 Optimization statement summary 92

3.3 Other frameworks considered 95
3.3.1 Maximizing power, minimizing volume or surface area 95
3.3.2 Given volume, maximize power and minimize surface area . . 95
3.3.3 Minimizing motion and volume or surface area 96
3.4 Summary 96

4 Approach to obtain constrained optimized shapes 99
4.1 Geometric description of shapes 100
4.1.1 Chebyshev polynomial basis functions 100
4.1.2 Parametric description of the body geometry 101
4.1.3 Introducing classes of shapes 107
4.1.4 Examples of classes of shapes 109
4.1.5 Groups of shapes 113
4.2 Theorem for finding roots of heave resonance equation 119
4.2.1 Theorem 119
4.2.2 Proof 120
4.2.3 Discussion of theorem and its use 121
4.2.4 Computational notes 122
4.3 General observations and conclusions for any given class of shapes . . 123
4.3.1 The set of all shapes in a class that solve the heave resonance equation 124
4.3.2 Heave motion constraint 128
4.3.3 Heave steepness constraint 131
4.3.4 Resulting shape of the heave population curve and Pareto Front 132
4.3.5 Resulting shape of the heave-surge-pitch population curve and Pareto Front 135
4.3.6 Summary 136
4.4 Forming heave and heave-surge-pitch populations and Pareto Fronts for groups of shapes 137
4.5 Multi-objective evolutionary algorithm 141

4.5.1 Flow chart and explanation . . . 141
4.6 Summary . . . 144

5 Optimizing the dimensions of a cylinder 147
5.1 Detailed example of approach . . . 148
5.1.1 Finding roots of the heave resonance equation . . . 149
5.1.2 Heave constraints and where they affect the population . . . 152
5.1.3 Surge pitch constraints and where they affect the population . 155
5.2 Heave-only optimization . . . 161
5.2.1 Populations . . . 162
5.2.2 Pareto Fronts . . . 164
5.3 Heave-surge-pitch optimization . . . 170
5.3.1 Populations . . . 171
5.3.2 Pareto Fronts . . . 172
5.4 Summary . . . 180

6 Optimization of a broad range of general geometries 185
6.1 Introduction . . . 185
6.2 Flat-bottomed . . . 189
6.2.1 Heave-only . . . 189
6.2.2 Heave-surge-pitch . . . 192
6.3 One-kink shapes . . . 195
6.3.1 Heave-only . . . 195
6.3.2 Heave-surge-pitch . . . 198
6.4 Compound cylinder . . . 202
6.4.1 Heave-only . . . 202
6.4.2 Heave-surge-pitch . . . 205
6.5 No-kink-2nd-order . . . 209
6.5.1 Heave-only . . . 209
6.5.2 Heave-surge-pitch . . . 213
6.6 Overall . . . 216

6.6.1 Heave . . . 216
6.6.2 Heave-surge-pitch . . . 219
6.7 Discussion of general trends and physical insights . . . 223
6.8 Showing the benefit of optimization . . . 232
6.9 Discussing the overall optimal shape . . . 236
6.10 Summary . . . 238

7 Conclusions **241**
7.1 Thesis contributions . . . 241
7.2 Future work . . . 247

A Stability constraint **251**

B Verifications for theorem **255**
B.1 Verification of added mass approximation . . . 256
B.2 Verification of finding roots . . . 260

C Sensitivity study for multi-objective evolutionary algorithm **265**
C.1 Heave . . . 266
C.1.1 Initial population size . . . 266
C.1.2 Mutation probability . . . 268
C.2 Heave surge pitch . . . 268
C.2.1 Initial population size . . . 268
C.2.2 Mutation probability . . . 269

D Wall-sided results **271**
D.1 Heave-only . . . 271
D.1.1 $\alpha = 3, \epsilon = 0.1$ . . . 272
D.1.2 $\alpha = 3, \epsilon = 0.2$ . . . 273
D.1.3 $\alpha = 1, \epsilon = 0.1$ . . . 273
D.1.4 $\alpha = 1, \epsilon = 0.2$ . . . 274
D.2 Heave-surge-pitch . . . 275

D.2.1 $\alpha = 3, \epsilon = 0.1$ 276
D.2.2 $\alpha = 3, \epsilon = 0.2$ 277
D.2.3 $\alpha = 1, \epsilon = 0.1$ 278
D.2.4 $\alpha = 1, \epsilon = 0.2$ 278

List of Figures

2-1 WEC restricted to motion and energy extraction in the heave mode only (ξ_3), with power take-off (PTO) modeled as a linear damper with damping coefficient β_3 44

2-2 WEC moving and extracting energy in heave (ξ_3), surge (ξ_1) and pitch (ξ_5), with power take-off (PTO) modeled as linear dampers with damping coefficients $\beta_1, \beta_3, \beta_{15}$ and β_5 45

2-3 Description of motions for floating body S_B 46

3-1 Example of plotting a **population**. f_1 and f_2 are the two objective functions, where the objectives are both minimization. 80

3-2 The **Pareto Front** of the population shown in figure 3-1, shown in blue. 81

3-3 Formation of the population for the heave-only problem, given α and ϵ 84

3-4 How stricter motion and steepness constraints affect the heave population and Pareto Front 85

3-5 The formation of the set of shapes that adhere to the five constraints for WECs moving and extracting energy in surge and pitch, $\mathbb{P}_{15}$ . . . 90

3-6 Finding $\mathbb{PF}_{135}$, the **heave-surge-pitch Pareto Front**: The intersection of the heave population, $\mathbb{P}_3$, and the set of shapes that adhere to the surge-pitch constraints, $\mathbb{P}_{15}$, is the **heave-surge-pitch population**. The heave-surge-pitch Pareto Front is a subset of the population 91

4-1 Example of the 2D cross-section, in the $r - z$ plane, of a 3D axisymmetric shape 102

4-2 Example of a 'one-kink' shape (i.e. a shape with a slope discontinuity) 102

4-3 Showing boundary values for a shape described by continuous parametric functions 103

4-4 Showing boundary values for a shape with one slope discontinuity. Each piecewise continuous segment is described by unique parametric equations. 104

4-5 Example of a class of shapes: cylinders 109

4-6 Example of class of shapes: $\overline{r_1} = 2, \overline{z_1} = -1$ 110

4-7 Example of class of shapes: $\overline{r_1} = 1, \overline{z_1} = -2$ 111

4-8 Example of class of shape: $\overline{a_2} = -0.25$ 112

4-9 Example of class of shape: $\overline{b_2} = 0.25$ 112

4-10 'Flat-bottomed' group of shapes: linear piecewise segments with one slope discontinuity at (r_1, z_1). $\overline{z_1} = \frac{z_1}{H} = -1$, so that the segment from the centerline to the slope discontinuity is horizontal. $\overline{r_1} = \frac{r_1}{R} > 1$ represents a 'protruding outwards' shape 114

4-11 'Flat-sided' group of shapes: piecewise linear segments with one slope discontinuity at (r_1, z_1). $\overline{r_1} = \frac{r_1}{R} = 1$, so that the segment from the waterline to the slope discontinuity is vertical. $\overline{z_1} = \frac{z_1}{H} < -1$ represents a 'dipping down' shape 115

4-12 'One-kink' group of shapes: piecewise linear segments with one slope discontinuity at (r_1, z_1). $\overline{z_1} = \frac{z_1}{H} < -1$ represents a 'dipping down' shape, and $\overline{r_1} = \frac{r_1}{R} > 1$ represents a 'protruding outward' shape . . . 116

4-13 Compound cylinder group of shapes: shapes consisting of one cylinder on top of another. $\overline{r_2} = \frac{r_2}{R}$ is the ratio of the radius of the bottom cylinder to the radius of the top cylinder. Therefore, $\overline{r_2} > 1$ represents a larger bottom cylinder. $\overline{z_2} = \frac{z_2}{H}$ is the ratio of the draft of the top cylinder to the total draft. 117

4-14 'No-kinks-2nd-order' group of shapes: one second-order continuous segment with no slope discontinuities. The parametric equations ahve coefficients of the second-order polynomial basis function a_2 and b_2 (in the r and z directions, respectively). $\overline{a_2} = \frac{a_2}{R} < -0.1$ signifies a 'protruding outward' shape and $\overline{b_2} = \frac{b_2}{H} > 0.1$ signifies a 'dipping down' shape 118

4-15 Example of $\mathcal{S}(\mathbb{R}_3^{\overline{\mathscr{B}_E}})$, the curve of the set of all shapes in class $\mathscr{C}^{\overline{\mathscr{B}_E}}$ that solve the heave resonance equation in the $kl_V - kl_S$ space 126

4-16 Some general characteristics observed for the set of all shapes of a given class that solve the heave resonance equation, plotted in the $kl_V - kl_S$ space: for $kl_V = kl_S = 0$, the shape is deep and narrow. Progressing along the curve, $\overline{R}$ increases and $\overline{H}$ decreases, until the bottom left where the shape is wide and shallow (like a disk) 127

4-17 Examples of $\mathcal{S}(\mathbb{R}_3^{\overline{\mathscr{B}_E}})$ for different $\overline{\mathscr{B}_E}$ 128

4-18 The effect of the heave motion constraint: as α decreases (so that the constraint becomes more restrictive), more of the left branch of $\mathcal{S}(\mathbb{R}_3^{\overline{\mathscr{B}_E}})$ will be eliminated. 131

4-19 The effect of the heave steepness constraint on $\mathcal{S}(\mathbb{R}_3^{\overline{\mathscr{B}_E}})$. The heave steepness constraint eliminates shapes where $kH < \epsilon\frac{|\xi_3|}{A}$, so as ϵ increases (so that the constraint becomes more restrictive), more from the ends of both branches will be eliminated. 132

4-20 Different options for the shape of $\mathbb{P}_3$, the final heave population curves, for a given class of shapes. The shapes of curves for the population will be referred to as $\mathbb{P}_A$, $\mathbb{P}_B$, and $\mathbb{P}_C$ 133

4-21 Corresponding Pareto Fronts for the options for the shape of the final heave population curve, shown in figure 4-20. The shapes of curves for the Pareto Front will be referred to as $\mathbb{PF}_A$, $\mathbb{PF}_B$, and $\mathbb{PF}_C$ 134

4-22 Examples of a population from a group of shapes consisting of three classes: $\overline{\mathscr{B}_E}^1$, $\overline{\mathscr{B}_E}^2$ and $\overline{\mathscr{B}_E}^3$ 138

4-23 Resulting Pareto Front for the population shown in figure 4-22 139

4-24 Flow chart of optimization process (not algorithm) 141

4-25 Flow chart of optimization algorithm 142

5-1 Illustrating how roots of the heave resonance equation are found by using the added mass approximation and theorem presented in the previous chapter 151

5-2 $\mathbb{R}_3^{cyl}$, the set of cylinders that solve the heave resonance equation. The left plot shows $\mathcal{S}(\mathbb{R}_3^{cyl})$, the curve of $\mathbb{R}_3^{cyl}$ in the $kl_V - kl_S$ space, where the colors, from purple to red, correspond to increasing kl_S. The right plot shows the shape, in the $r - z$ plane of some of the cylinders in the set, with colors corresponding to the left plot. Shapes at the lower left branch of $\mathcal{S}(\mathbb{R}_3^{cyl})$ correspond to deep, narrow cylinders. Along the curve, $\overline{R}$ increases and $\overline{H}$ decreases, so the shapes at the lower right branch correspond to wide, shallow cylinders. 152

5-3 Illustration of the effect of the heave motion constraint on $\mathcal{S}(\mathbb{R}_3^{cyl})$. The purple shapes are eliminated when $\alpha = 3$. The red and purple shapes are eliminated when $\alpha = 2$. The green, red, and purple shapes are eliminated when $\alpha = 1$. 153

5-4 Illustration of the effect of the heave steepness constraint on $\mathcal{S}(\mathbb{R}_3^{cyl})$. The yellow shapes are eliminated when $\epsilon = 0.1$, and the pink and yellow shapes are eliminated when $\epsilon = 0.2$. 155

5-5 Illustration of the effect of the surge motion constraint on $\mathcal{S}(\mathbb{R}_3^{cyl})$. The purple shapes are eliminated when $\alpha = 3$, the red and purple shapes are eliminated when $\alpha = 2$, and the green, red and purple shapes are eliminated when $\alpha = 1$. 156

5-6 Illustration of the effect of the pitch motion constraint on $\mathcal{S}(\mathbb{R}_3^{cyl})$ . . 158

5-7 Illustration of the effect of the pitch steepness constraint on $\mathcal{S}(\mathbb{R}_3^{cyl})$. The yellow shapes are eliminated if $\epsilon = 0.1$. If $\epsilon = 0.2$, the yellow and pink shapes are eliminated. 159

5-8 Illustration of the effect of the pitch moment of inertia constraint on $\mathcal{S}(\mathbb{R}_3^{cyl})$. The pink shapes will be eliminated due to this constraint. . . 160

5-9 Illustration of the effect of the center of gravity constraint on $\mathcal{S}(\mathbb{R}_3^{cyl})$. The light blue shapes will be eliminated due to this constraint. 161

5-10 Heave-only populations of cylinders for different constraint values. Row 1 is the population for $\alpha = 3, \epsilon = 0.1$, row 2 is for $\alpha = 3, \epsilon = 0.2$, row 3 is for $\alpha = 1, \epsilon = 0.1$ and row 4 is for $\alpha = 1, \epsilon = 0.2$. In each row, the left figure shows a scatter plot of the population in the $kl_V - kl_S$ space, and the right figure shows the corresponding shapes of the cylinders in 2D $r - z$ space. The colors range from smaller kl_S (purple) to larger kl_S (red). 163

5-11 $\mathbb{PF}_{3,3,0.1}$, the Pareto Front for the heave-only case of cylinders with an α constraint value of 3 and ϵ constraint value of 0.1 164

5-12 Pareto Front for the heave-only case of cylinders with a α constraint value of 3 and ϵ constraint value of 0.2 166

5-13 Pareto Front for the heave-only case of cylinders with a α constraint value of 1 and ϵ constraint value of 0.1 167

5-14 Pareto Front for the heave-only case of cylinders with a α constraint value of 1 and ϵ constraint value of 0.2 168

5-15 Heave-surge-pitch populations of cylinders for different constraint values. Row 1 is the population for $\alpha = 3, \epsilon = 0.1$, row 2 is for $\alpha = 3, \epsilon = 0.2$, row 3 is for $\alpha = 1, \epsilon = 0.1$ and row 4 is for $\alpha = 1, \epsilon = 0.2$. In each row, the left figure shows a scatter plot of the population in the $kl_V - kl_S$ space, and the right figure shows the corresponding shapes of the cylinders. The colors correspond to the same colors in figure 5-10.172

5-16 Pareto Front for the heave-surge-pitch case of cylinders with a α constraint value of 3 and ϵ constraint value of 0.1 173

5-17 Pareto Front for the heave-surge-pitch case of cylinders with a α constraint value of 3 and ϵ constraint value of 0.2 175

5-18 Pareto Front for the heave-surge-pitch case of cylinders with a α constraint value of 1 and ϵ constraint value of 0.1 177

5-19 Pareto Front for the heave-surge-pitch case of cylinders with a α constraint value of 1 and ϵ constraint value of 0.2 178

6-1 Pareto Front (left) and corresponding shapes in the $r-z$ plane (right), resulting from the multi-objective evolutionary algorithm for 'flat-bottomed' shapes for the heave-only problem, with motion constraint $\alpha = 3$ and steepness constraint $\epsilon = 0.1$ 189

6-2 Pareto Front (left) and corresponding shapes in the $r-z$ plane (right), resulting from the multi-objective evolutionary algorithm for 'flat-bottomed' shapes for the heave-only problem, with motion constraint $\alpha = 3$ and steepness constraint $\epsilon = 0.2$ 190

6-3 Pareto Front (left) and corresponding shapes in the $r-z$ plane (right), resulting from the multi-objective evolutionary algorithm for 'flat-bottomed' shapes for the heave-only problem, with motion constraint $\alpha = 1$ and steepness constraint $\epsilon = 0.1$ 190

6-4 Pareto Front (left) and corresponding shapes in the $r-z$ plane (right), resulting from the multi-objective evolutionary algorithm for 'flat-bottomed' shapes for the heave-only problem, with motion constraint $\alpha = 1$ and steepness constraint $\epsilon = 0.2$ 191

6-5 Pareto Front (left) and corresponding shapes in the $r-z$ plane (right), resulting from the multi-objective evolutionary algorithm for 'flat-bottomed' shapes for the heave-surge-pitch problem, with motion constraint $\alpha = 3$ and steepness constraint $\epsilon = 0.1$ 192

6-6 Pareto Front (left) and corresponding shapes in the $r-z$ plane (right), resulting from the multi-objective evolutionary algorithm for 'flat-bottomed' shapes for the heave-surge-pitch problem, with motion constraint $\alpha = 3$ and steepness constraint $\epsilon = 0.2$ 193

6-7 Pareto Front (left) and corresponding shapes in the $r-z$ plane (right), resulting from the multi-objective evolutionary algorithm for 'flat-bottomed' shapes for the heave-surge-pitch problem, with motion constraint $\alpha = 1$ and steepness constraint $\epsilon = 0.1$ 193

6-8 Pareto Front (left) and corresponding shapes in the $r-z$ plane (right), resulting from the multi-objective evolutionary algorithm for 'flat-bottomed' shapes for the heave-surge-pitch problem, with motion constraint $\alpha = 1$ and steepness constraint $\epsilon = 0.2$ 194

6-9 Pareto Front (left) and corresponding shapes in the $r-z$ plane (right), resulting from the multi-objective evolutionary algorithm for 'one-kink' shapes for the heave-only problem, with motion constraint $\alpha = 3$ and steepness constraint $\epsilon = 0.1$ 195

6-10 Pareto Front (left) and corresponding shapes in the $r-z$ plane (right), resulting from the multi-objective evolutionary algorithm for 'one-kink' shapes for the heave-only problem, with motion constraint $\alpha = 3$ and steepness constraint $\epsilon = 0.2$ 196

6-11 Pareto Front (left) and corresponding shapes in the $r-z$ plane (right), resulting from the multi-objective evolutionary algorithm for 'one-kink' shapes for the heave-only problem, with motion constraint $\alpha = 1$ and steepness constraint $\epsilon = 0.1$ 196

6-12 Pareto Front (left) and corresponding shapes in the $r-z$ plane (right), resulting from the multi-objective evolutionary algorithm for 'one-kink' shapes for the heave-only problem, with motion constraint $\alpha = 1$ and steepness constraint $\epsilon = 0.2$ 197

6-13 Pareto Front (left) and corresponding shapes in the $r-z$ plane (right), resulting from the multi-objective evolutionary algorithm for 'one-kink' shapes for the heave-surge-pitch problem, with motion constraint $\alpha = 3$ and steepness constraint $\epsilon = 0.1$ 199

6-14 Pareto Front (left) and corresponding shapes in the $r-z$ plane (right), resulting from the multi-objective evolutionary algorithm for 'one-kink' shapes for the heave-surge-pitch problem, with motion constraint $\alpha = 3$ and steepness constraint $\epsilon = 0.2$ 199

6-15 Pareto Front (left) and corresponding shapes in the $r-z$ plane (right), resulting from the multi-objective evolutionary algorithm for 'one-kink' shapes for the heave-surge-pitch problem, with motion constraint $\alpha = 1$ and steepness constraint $\epsilon = 0.1$ 200

6-16 Pareto Front (left) and corresponding shapes in the $r-z$ plane (right), resulting from the multi-objective evolutionary algorithm for 'one-kink' shapes for the heave-surge-pitch problem, with motion constraint $\alpha = 1$ and steepness constraint $\epsilon = 0.2$ 201

6-17 Pareto Front (left) and corresponding shapes in the $r-z$ plane (right), resulting from the multi-objective evolutionary algorithm for 'compound-cylinder' shapes for the heave-only problem, with motion constraint $\alpha = 3$ and steepness constraint $\epsilon = 0.1$ 202

6-18 Pareto Front (left) and corresponding shapes in the $r-z$ plane (right), resulting from the multi-objective evolutionary algorithm for 'compound-cylinder' shapes for the heave-only problem, with motion constraint $\alpha = 3$ and steepness constraint $\epsilon = 0.2$ 203

6-19 Pareto Front (left) and corresponding shapes in the $r-z$ plane (right), resulting from the multi-objective evolutionary algorithm for 'compound-cylinder' shapes for the heave-only problem, with motion constraint $\alpha = 1$ and steepness constraint $\epsilon = 0.1$ 203

6-20 Pareto Front (left) and corresponding shapes in the $r-z$ plane (right), resulting from the multi-objective evolutionary algorithm for 'compound-cylinder' shapes for the heave-only problem, with motion constraint $\alpha = 1$ and steepness constraint $\epsilon = 0.2$ 204

6-21 Pareto Front (left) and corresponding shapes in the $r-z$ plane (right), resulting from the multi-objective evolutionary algorithm for 'compound-cylinder' shapes for the heave-surge-pitch problem, with motion constraint $\alpha = 3$ and steepness constraint $\epsilon = 0.1$ 205

6-22 Pareto Front (left) and corresponding shapes in the $r-z$ plane (right), resulting from the multi-objective evolutionary algorithm for 'compound-cylinder' shapes for the heave-surge-pitch problem, with motion constraint $\alpha = 3$ and steepness constraint $\epsilon = 0.2$ 206

6-23 Pareto Front (left) and corresponding shapes in the $r-z$ plane (right), resulting from the multi-objective evolutionary algorithm for 'compound-cylinder' shapes for the heave-surge-pitch problem, with motion constraint $\alpha = 1$ and steepness constraint $\epsilon = 0.1$ 207

6-24 Pareto Front (left) and corresponding shapes in the $r-z$ plane (right), resulting from the multi-objective evolutionary algorithm for 'compound-cylinder' shapes for the heave-surge-pitch problem, with motion constraint $\alpha = 1$ and steepness constraint $\epsilon = 0.2$ 208

6-25 Pareto Front (left) and corresponding shapes in the $r-z$ plane (right), resulting from the multi-objective evolutionary algorithm for 'no-kink-2nd-order' shapes for the heave-only problem, with motion constraint $\alpha = 3$ and steepness constraint $\epsilon = 0.1$ 210

6-26 Pareto Front (left) and corresponding shapes in the $r-z$ plane (right), resulting from the multi-objective evolutionary algorithm for 'no-kink-2nd-order' shapes for the heave-only problem, with motion constraint $\alpha = 3$ and steepness constraint $\epsilon = 0.2$ 210

6-27 Pareto Front (left) and corresponding shapes in the $r-z$ plane (right), resulting from the multi-objective evolutionary algorithm for 'no-kink-2nd-order' shapes for the heave-only problem, with motion constraint $\alpha = 1$ and steepness constraint $\epsilon = 0.1$ 211

6-28 Pareto Front (left) and corresponding shapes in the $r-z$ plane (right), resulting from the multi-objective evolutionary algorithm for 'no-kink-2nd-order' shapes for the heave-only problem, with motion constraint $\alpha = 1$ and steepness constraint $\epsilon = 0.2$ 212

6-29 Pareto Front (left) and corresponding shapes in the $r-z$ plane (right), resulting from the multi-objective evolutionary algorithm for 'no-kink-2nd-order' shapes for the heave-surge-pitch problem, with motion constraint $\alpha = 3$ and steepness constraint $\epsilon = 0.1$ 213

6-30 Pareto Front (left) and corresponding shapes in the $r-z$ plane (right), resulting from the multi-objective evolutionary algorithm for 'no-kink-2nd-order' shapes for the heave-surge-pitch problem, with motion constraint $\alpha = 3$ and steepness constraint $\epsilon = 0.2$ 214

6-31 Pareto Front (left) and corresponding shapes in the $r-z$ plane (right), resulting from the multi-objective evolutionary algorithm for 'no-kink-2nd-order' shapes for the heave-surge-pitch problem, with motion constraint $\alpha = 1$ and steepness constraint $\epsilon = 0.1$ 214

6-32 Pareto Front (left) and corresponding shapes in the $r-z$ plane (right), resulting from the multi-objective evolutionary algorithm for 'no-kink-2nd-order' shapes for the heave-surge-pitch problem, with motion constraint $\alpha = 1$ and steepness constraint $\epsilon = 0.2$ 215

6-33 The overall Pareto Front (left) and corresponding shapes in the $r-z$ plane (right), after combining the Pareto Fronts from all 6 groups in this chapter, for the heave-only problem with motion constraint $\alpha = 3$ and steepness constraint $\epsilon = 0.1$ 216

6-34 The overall Pareto Front (left) and corresponding shapes in the $r-z$ plane (right), after combining the Pareto Fronts from all 6 groups in this chapter, for the heave-only problem with motion constraint $\alpha = 3$ and steepness constraint $\epsilon = 0.2$ 217

6-35 The overall Pareto Front (left) and corresponding shapes in the $r-z$ plane (right), after combining the Pareto Fronts from all 6 groups in this chapter, for the heave-only problem with motion constraint $\alpha = 1$ and steepness constraint $\epsilon = 0.1$ 218

6-36 The overall Pareto Front (left) and corresponding shapes in the $r-z$ plane (right), after combining the Pareto Fronts from all 6 groups in this chapter, for the heave-only problem with motion constraint $\alpha = 1$ and steepness constraint $\epsilon = 0.2$ 218

6-37 The overall Pareto Front (left) and corresponding shapes in the $r-z$ plane (right), after combining the Pareto Fronts from all 6 groups in this chapter, for the heave-surge-pitch problem with motion constraint $\alpha = 3$ and steepness constraint $\epsilon = 0.1$ 220

6-38 The overall Pareto Front (left) and corresponding shapes in the $r-z$ plane (right), after combining the Pareto Fronts from all 6 groups in this chapter, for the heave-surge-pitch problem with motion constraint $\alpha = 3$ and steepness constraint $\epsilon = 0.2$ 220

6-39 The overall Pareto Front (left) and corresponding shapes in the $r-z$ plane (right), after combining the Pareto Fronts from all 6 groups in this chapter, for the heave-surge-pitch problem with motion constraint $\alpha = 1$ and steepness constraint $\epsilon = 0.1$ 221

6-40 The overall Pareto Front (left) and corresponding shapes in the $r-z$ plane (right), after combining the Pareto Fronts from all 6 groups in this chapter, for the heave-surge-pitch problem with motion constraint $\alpha = 1$ and steepness constraint $\epsilon = 0.2$ 222

6-41 Demonstrating populations for 'flat-bottomed' shapes with different $\overline{r_1} = \frac{r_1}{R}$ values, which shows that the shapes that protrude outward more are better since they have smaller minimum kl_V and kl_S values 224

6-42 Showing how heave added mass (A_{33}) and heave damping (B_{33}) increase with increasing $\overline{r_1}$, keeping r_{max}, $\overline{z_1}$ and kH constant 225

6-43 Showing how heave added mass (A_{33}) decreases and damping (B_{33}) increases with increasing $\overline{z_1}$, keeping R, $\overline{r_1}$ and kH constant 227

6-44 Demonstrating protruding downwards shapes, and showing how heave added mass (A_{33}) increases and heave damping (B_{33}) decreases with decreasing $\overline{z_1}$, keeping R, $\overline{r_1}$ and kH constant 231

6-45 Comparing the optimal shapes from the overall Pareto Fronts to the optimal cylinders, for the heave-only problem 234

6-46 Comparing the optimal shapes from the overall Pareto Fronts to the optimal cylinders, for the heave-surge-pitch problem 234

6-47 Comparing one of the optimal shapes with the cylinder with radius equal to the maximum r dimension and draft equal to the maximum z dimension. The green shape extract more than 9 times the red cylinder.235

6-48 The response (in blue) of the optimal shape (shown in figure 6-47 in green), compared to a typical ocean spectrum - the Bretschneider spectrum (in purple) 237

A-1 A small angle $\delta\phi$ of pitch displacement to a body. 251

B-1 Cylinder added mass approximation verification 257

B-2 One-kink shape added mass approximation verification 258

B-3 Compound cylinder added mass approximation verification 259

B-4 No-kink 2nd-order shape added mass approximation verification . . . 260

B-5 Cylinder finding roots verification 261

B-6 One-kink shape finding roots verification 262

B-7 Compound cylinder finding roots verification 263

B-8 No-kinks 2nd-order shape finding roots verification 264

C-1 Sensitivity study for initial population size for the heave problem. The first plot shows the average number of generations needed for the minimum kl_V and kl_S values in the optimization to get within 5% of the actual minimum kl_V and kl_S values, the second plot shows the maximum number of generations, the third plot shows the total number of runs (popsize + number of generations) and the fourth plot shows the maximum total number of runs 267

C-2 Sensitivity study for mutation probability for the heave problem. The first plot shows the average number of generations needed for the minimum kl_V and kl_S values in the optimization to get within 5% of the actual minimum kl_V and kl_S values, the second plot shows the maximum number of generations 268

C-3 Sensitivity study for initial population size for the heave-surge-pitch problem. The first plot shows the average number of generations needed for the minimum kl_V and kl_S values in the optimization to get within 5% of the actual minimum kl_V and kl_S values, the second plot shows the maximum number of generations, the third plot shows the total number of runs (popsize + number of generations) and the fourth plot shows the maximum total number of runs 269

C-4 Sensitivity study for mutation probability for the heave-surge-pitch problem. The first plot shows the average number of generations needed for the minimum kl_V and kl_S values in the optimization to get within 5% of the actual minimum kl_V and kl_S values, the second plot shows the maximum number of generations 270

D-1 Pareto Front (left) and corresponding shapes in the $r-z$ plane (right), resulting from the multi-objective evolutionary algorithm for 'flat-sided' shapes for the heave-only problem, with motion constraint $\alpha = 3$ and steepness constraint $\epsilon = 0.1$ 272

D-2 Pareto Front (left) and corresponding shapes in the $r-z$ plane (right), resulting from the multi-objective evolutionary algorithm for 'flat-sided' shapes for the heave-only problem, with motion constraint $\alpha = 3$ and steepness constraint $\epsilon = 0.2$ 273
D-3 Pareto Front (left) and corresponding shapes in the $r-z$ plane (right), resulting from the multi-objective evolutionary algorithm for 'flat-sided' shapes for the heave-only problem, with motion constraint $\alpha = 1$ and steepness constraint $\epsilon = 0.1$ 273
D-4 Pareto Front (left) and corresponding shapes in the $r-z$ plane (right), resulting from the multi-objective evolutionary algorithm for 'flat-sided' shapes for the heave-only problem, with motion constraint $\alpha = 1$ and steepness constraint $\epsilon = 0.2$ 274
D-5 Pareto Front (left) and corresponding shapes in the $r-z$ plane (right), resulting from the multi-objective evolutionary algorithm for 'flat-sided' shapes for the heave-surge-pitch problem, with motion constraint $\alpha = 3$ and steepness constraint $\epsilon = 0.1$ 276
D-6 Pareto Front (left) and corresponding shapes in the $r-z$ plane (right), resulting from the multi-objective evolutionary algorithm for 'flat-sided' shapes for the heave-surge-pitch problem, with motion constraint $\alpha = 3$ and steepness constraint $\epsilon = 0.2$ 277
D-7 Pareto Front (left) and corresponding shapes in the $r-z$ plane (right), resulting from the multi-objective evolutionary algorithm for 'flat-sided' shapes for the heave-surge-pitch problem, with motion constraint $\alpha = 1$ and steepness constraint $\epsilon = 0.1$ 278
D-8 Pareto Front (left) and corresponding shapes in the $r-z$ plane (right), resulting from the multi-objective evolutionary algorithm for 'flat-sided' shapes for the heave-surge-pitch problem, with motion constraint $\alpha = 1$ and steepness constraint $\epsilon = 0.2$ 278

List of Tables

5.1 Dimensions and body motion of the cylinder represented by a purple dot in figure 5-11 165

5.2 Dimensions and body motion of the cylinders in the orange-red cluster in figure 5-11 165

5.3 Dimensions and body motion of the cylinder represented in figure 5-12 166

5.4 Dimensions and body motion of the cylinder represented by a teal dot in figure 5-13 167

5.5 Dimensions and body motion of the cylinders on the ends of the green-yellow-orange-red cluster in figure 5-13. The first row shows the values for the lightest green cylinder, and the second row shows the values for the darkest red cylinder. 168

5.6 Dimensions and body motion of three of the cylinders in figure 5-14. The first row shows the values for the lone teal dot. The second row shows the values for the cylinder on the upper left of the green-yellow-orange cluster: the lightest green one. The third row shows the values for the cylinder on the lower right of the cluster: the darkest orange one. 169

5.7 Characteristics of the heave-surge-pitch Pareto Front for $\alpha = 3, \epsilon = 0.1$, called $\mathbb{PF}_{135,3,0.1}$. Columns 1, 2, 3, and 4 are the same as for the heave-only case: they show kl_S, kl_V, kR and kH. Columns 5, 6 and 7 show the body motion for the three modes: surge, heave and pitch, respectively. Column 8 shows the nondimensional surge spring coefficient. Column 9 shows the nondimensional center of gravity. Column 10 shows the nondimensional radius of gyration for pitch 174

5.8 Characteristics of the heave-surge-pitch Pareto Front for $\alpha = 3, \epsilon = 0.2$, called $\mathbb{PF}_{135,3,0.2}$, shown in figure 5-17. 176

5.9 Characteristics of the heave-surge-pitch Pareto Front for $\alpha = 1, \epsilon = 0.1$, called $\mathbb{PF}_{135,1,0.1}$, shown in figure 5-18. 177

5.10 Characteristics of the heave-surge-pitch Pareto Front for $\alpha = 1, \epsilon = 0.2$, called $\mathbb{PF}_{135,1,0.2}$, shown in figure 5-19. 178

5.11 The percent increase in minimum kl_V and minimum kl_S values from the heave-only case to the heave-surge-pitch case, for each constraint regime 179

6.1 Dimensions and characteristics of the 'flat-bottomed' shapes on the Pareto Front for the heave-only problem, with motion constraint $\alpha = 3$ and steepness constraint $\epsilon = 0.1$ (shown in figure 6-1) 189

6.2 Dimensions and characteristics of the 'flat-bottomed' shapes on the Pareto Front for the heave-only problem, with motion constraint $\alpha = 3$ and steepness constraint $\epsilon = 0.2$ (shown in figure 6-2) 190

6.3 Dimensions and characteristics of the 'flat-bottomed' shapes on the Pareto Front for the heave-only problem, with motion constraint $\alpha = 1$ and steepness constraint $\epsilon = 0.1$ (shown in figure 6-3) 191

6.4 Dimensions and characteristics of the 'flat-bottomed' shapes on the Pareto Front for the heave-only problem, with motion constraint $\alpha = 1$ and steepness constraint $\epsilon = 0.2$ (shown in figure 6-4) 191

6.5 Dimensions and characteristics of the 'flat-bottomed' shapes on the Pareto Front for the heave-surge-pitch problem, with motion constraint $\alpha = 3$ and steepness constraint $\epsilon = 0.1$ (shown in figure 6-5) 192

6.6 Dimensions and characteristics of the 'flat-bottomed' shapes on the Pareto Front for the heave-surge-pitch problem, with motion constraint $\alpha = 3$ and steepness constraint $\epsilon = 0.2$ (shown in figure 6-6) 193

6.7 Dimensions and characteristics of the 'flat-bottomed' shapes on the Pareto Front for the heave-surge-pitch problem, with motion constraint $\alpha = 1$ and steepness constraint $\epsilon = 0.1$ (shown in figure 6-7) 194

6.8 Dimensions and characteristics of the 'flat-bottomed' shapes on the Pareto Front for the heave-surge-pitch problem, with motion constraint $\alpha = 1$ and steepness constraint $\epsilon = 0.2$ (shown in figure 6-8) 194

6.9 Dimensions and characteristics of the 'one-kink' shapes on the Pareto Front for the heave-only problem, with motion constraint $\alpha = 3$ and steepness constraint $\epsilon = 0.1$ (shown in figure 6-9) 195

6.10 Dimensions and characteristics of the 'one-kink' shapes on the Pareto Front for the heave-only problem, with motion constraint $\alpha = 3$ and steepness constraint $\epsilon = 0.2$ (shown in figure 6-10) 196

6.11 Dimensions and characteristics of the 'one-kink' shapes on the Pareto Front for the heave-only problem, with motion constraint $\alpha = 1$ and steepness constraint $\epsilon = 0.1$ (shown in figure 6-11) 197

6.12 Dimensions and characteristics of the 'one-kink' shapes on the Pareto Front for the heave-only problem, with motion constraint $\alpha = 1$ and steepness constraint $\epsilon = 0.2$ (shown in figure 6-12) 197

6.13 Dimensions and characteristics of the 'one-kink' shapes on the Pareto Front for the heave-surge-pitch problem, with motion constraint $\alpha = 3$ and steepness constraint $\epsilon = 0.1$ (shown in figure 6-13) 199

6.14 Dimensions and characteristics of the 'one-kink' shapes on the Pareto Front for the heave-surge-pitch problem, with motion constraint $\alpha = 3$ and steepness constraint $\epsilon = 0.2$ (shown in figure 6-14) 200

6.15 Dimensions and characteristics of the 'one-kink' shapes on the Pareto Front for the heave-surge-pitch problem, with motion constraint $\alpha = 1$ and steepness constraint $\epsilon = 0.1$ (shown in figure 6-15) 200

6.16 Dimensions and characteristics of the 'one-kink' shapes on the Pareto Front for the heave-surge-pitch problem, with motion constraint $\alpha = 1$ and steepness constraint $\epsilon = 0.2$ (shown in figure 6-16) 201

6.17 Dimensions and characteristics of the 'compound-cylinder' shapes on the Pareto Front for the heave-only problem, with motion constraint $\alpha = 3$ and steepness constraint $\epsilon = 0.1$ (shown in figure 6-17) 202
6.18 Dimensions and characteristics of the 'compound-cylinder' shapes on the Pareto Front for the heave-only problem, with motion constraint $\alpha = 3$ and steepness constraint $\epsilon = 0.2$ (shown in figure 6-18) 203
6.19 Dimensions and characteristics of the 'compound-cylinder' shapes on the Pareto Front for the heave-only problem, with motion constraint $\alpha = 1$ and steepness constraint $\epsilon = 0.1$ (shown in figure 6-19) 203
6.20 Dimensions and characteristics of the 'compound-cylinder' shapes on the Pareto Front for the heave-only problem, with motion constraint $\alpha = 1$ and steepness constraint $\epsilon = 0.2$ (shown in figure 6-20) 204
6.21 Dimensions and characteristics of the 'compound-cylinder' shapes on the Pareto Front for the heave-surge-pitch problem, with motion constraint $\alpha = 3$ and steepness constraint $\epsilon = 0.1$ (shown in figure 6-21) . 206
6.22 Dimensions and characteristics of the 'compound-cylinder' shapes on the Pareto Front for the heave-surge-pitch problem, with motion constraint $\alpha = 3$ and steepness constraint $\epsilon = 0.2$ (shown in figure 6-22) . 207
6.23 Dimensions and characteristics of the 'compound-cylinder' shapes on the Pareto Front for the heave-surge-pitch problem, with motion constraint $\alpha = 1$ and steepness constraint $\epsilon = 0.1$ (shown in figure 6-23) . 208
6.24 Dimensions and characteristics of the 'compound-cylinder' shapes on the Pareto Front for the heave-surge-pitch problem, with motion constraint $\alpha = 1$ and steepness constraint $\epsilon = 0.2$ (shown in figure 6-24) . 208
6.25 Dimensions and characteristics of the 'no-kinks-2nd-order' shapes on the Pareto Front for the heave-only problem, with motion constraint $\alpha = 3$ and steepness constraint $\epsilon = 0.1$ (shown in figure 6-25) 210
6.26 Dimensions and characteristics of the 'no-kinks-2nd-order' shapes on the Pareto Front for the heave-only problem, with motion constraint $\alpha = 3$ and steepness constraint $\epsilon = 0.2$ (shown in figure 6-26) 211

6.27 Dimensions and characteristics of the 'no-kinks-2nd-order' shapes on the Pareto Front for the heave-only problem, with motion constraint $\alpha = 1$ and steepness constraint $\epsilon = 0.1$ (shown in figure 6-27) 211

6.28 Dimensions and characteristics of the 'no-kinks-2nd-order' shapes on the Pareto Front for the heave-only problem, with motion constraint $\alpha = 1$ and steepness constraint $\epsilon = 0.2$ (shown in figure 6-28) 212

6.29 Dimensions and characteristics of the 'no-kinks-2nd-order' shapes on the Pareto Front for the heave-surge-pitch problem, with motion constraint $\alpha = 3$ and steepness constraint $\epsilon = 0.1$ (shown in figure 6-29) . 213

6.30 Dimensions and characteristics of the 'no-kinks-2nd-order' shapes on the Pareto Front for the heave-surge-pitch problem, with motion constraint $\alpha = 3$ and steepness constraint $\epsilon = 0.2$ (shown in figure 6-30) . 214

6.31 Dimensions and characteristics of the 'no-kinks-2nd-order' shapes on the Pareto Front for the heave-surge-pitch problem, with motion constraint $\alpha = 1$ and steepness constraint $\epsilon = 0.1$ (shown in figure 6-31) . 215

6.32 Dimensions and characteristics of the 'no-kinks-2nd-order' shapes on the Pareto Front for the heave-surge-pitch problem, with motion constraint $\alpha = 1$ and steepness constraint $\epsilon = 0.2$ (shown in figure 6-32) . 215

6.33 Dimensions and characteristics of the shapes on the *overall* Pareto Front for the heave-only problem, with motion constraint $\alpha = 3$ and steepness constraint $\epsilon = 0.1$ (shown in figure 6-33) 217

6.34 Dimensions and characteristics of the shapes on the *overall* Pareto Front for the heave-only problem, with motion constraint $\alpha = 3$ and steepness constraint $\epsilon = 0.2$ (shown in figure 6-34) 217

6.35 Dimensions and characteristics of the shapes on the *overall* Pareto Front for the heave-only problem, with motion constraint $\alpha = 1$ and steepness constraint $\epsilon = 0.1$ (shown in figure 6-35) 218

6.36 Dimensions and characteristics of the shapes on the *overall* Pareto Front for the heave-only problem, with motion constraint $\alpha = 1$ and steepness constraint $\epsilon = 0.1$ (shown in figure 6-35) 219

6.37 Dimensions and characteristics of the shapes on the *overall* Pareto Front for the heave-surge-pitch problem, with motion constraint $\alpha = 3$ and steepness constraint $\epsilon = 0.1$ (shown in figure 6-37) 220

6.38 Dimensions and characteristics of the shapes on the *overall* Pareto Front for the heave-surge-pitch problem, with motion constraint $\alpha = 3$ and steepness constraint $\epsilon = 0.2$ (shown in figure 6-38) 221

6.39 Dimensions and characteristics of the shapes on the *overall* Pareto Front for the heave-surge-pitch problem, with motion constraint $\alpha = 1$ and steepness constraint $\epsilon = 0.1$ (shown in figure 6-39) 221

6.40 Dimensions and characteristics of the shapes on the *overall* Pareto Front for the heave-surge-pitch problem, with motion constraint $\alpha = 1$ and steepness constraint $\epsilon = 0.2$ (shown in figure 6-39) 222

6.41 Percentage decrease of surface area for the optimal heave-only shapes, compared to the optimal cylinders 232

6.42 Percentage decrease of volume for the optimal heave-only shapes, compared to the optimal cylinders 232

6.43 Percentage decrease of surface area for the optimal heave-surge-pitch shapes, compared to the optimal cylinders 233

6.44 Percentage decrease of volume for the optimal heave-surge-pitch shapes, compared to the optimal cylinders 233

D.1 Dimensions and characteristics of the 'flat-sided' shapes on the Pareto Front for the heave-only problem, with motion constraint $\alpha = 3$ and steepness constraint $\epsilon = 0.1$ (shown in figure D-1) 272

D.2 Dimensions and characteristics of the 'flat-sided' shapes on the Pareto Front for the heave-only problem, with motion constraint $\alpha = 3$ and steepness constraint $\epsilon = 0.2$ (shown in figure D-2) 273

D.3 Dimensions and characteristics of the 'flat-sided' shapes on the Pareto Front for the heave-only problem, with motion constraint $\alpha = 1$ and steepness constraint $\epsilon = 0.1$ (shown in figure D-3) 274

D.4 Dimensions and characteristics of the 'flat-sided' shapes on the Pareto Front for the heave-only problem, with motion constraint $\alpha = 1$ and steepness constraint $\epsilon = 0.2$ (shown in figure D-4) 275
D.5 Dimensions and characteristics of the 'flat-sided' shapes on the Pareto Front for the heave-surge-pitch problem, with motion constraint $\alpha = 3$ and steepness constraint $\epsilon = 0.1$ (shown in figure D-5) 276
D.6 Dimensions and characteristics of the 'flat-sided' shapes on the Pareto Front for the heave-surge-pitch problem, with motion constraint $\alpha = 3$ and steepness constraint $\epsilon = 0.2$ (shown in figure D-6) 277
D.7 Dimensions and characteristics of the 'flat-sided' shapes on the Pareto Front for the heave-surge-pitch problem, with motion constraint $\alpha = 1$ and steepness constraint $\epsilon = 0.2$ (shown in figure D-8) 278
D.8 Dimensions and characteristics of the 'flat-sided' shapes on the Pareto Front for the heave-surge-pitch problem, with motion constraint $\alpha = 1$ and steepness constraint $\epsilon = 0.1$ (shown in figure D-5) 279

Chapter 1

Introduction

1.1 Wave energy potential and state of the art of wave energy converters

Wave energy represents an abundant source of renewable energy. Gunn and Stock-Williams (2012) estimate a global resource of 2 TW. A predictable, relatively consistent and energy-dense form of renewable energy, wave energy could help add diversity to the renewable energy sources needed to tackle the global climate crisis we are currently experiencing.

To demonstrate the immense potential of wave energy converters (WECs), consider the available energy per unit crest-length in an incident wave:

$$P_I = \frac{1}{2}\rho g A^2 V_g \tag{1.1.1}$$

where ρ is density of the water, g is gravitational constant, A is amplitude of the incident wave, and V_g is the group velocity of the incident wave. For a 10-second wave with an amplitude of 1 meter, there is approximately 40 kW/m of energy available, and for a 10-second wave with an amplitude of 5 meters, there is approximately 1000 kW/m of energy available.

Research on wave energy first widely gained traction in the 1960's and 1970's with the global energy crisis, but much like the profile of the wave, interest has gone through peaks and troughs throughout the years subsequent. The technology is still relatively in its infancy, with only a handful of wave energy converter designs having completed any real-sea testing (Al Shami et al., 2019), and as yet it is not economically competitive with other renewable energy resources, such as wind or solar energy (Chang et al., 2018). For wave energy technology to become economically viable, Chang et al. (2018) estimate that the capital expenditure and operating expenditure must be reduced by 45 % and power production must be increased by 200 %. Clearly, there needs to be a significant, not just incremental, improvement for wave energy to become a viable source of renewable energy.

Babarit et al. (2012) argue that performance metrics, instead of CAPEX or OPEX, should be used when technologies are still nascent, and suggested using surface area as a performance metric for cost, since mass could be made up mostly of water and/or concrete, which would be cheap. Dallman et al. (2018) reviewed the finalists for the 2016 US Department of Energy 'Wave Energy Prize,' and found that surface area is closest to estimating full cost estimates, rather than volume or PTO force. Uihlein and Magagna (2016) state that challenges for the technology are reliability, robustness, cost and deployment. Therefore, although surface area may be a good approximation of the cost of the device, to decrease deployment and maintenance cost, volume should also be considered, since a larger volume will require larger containers, ships, etc. to move and deploy. Furthermore, currently wave energy converters are only considered in very energetic locations, which corresponds to sea states with very large wave periods. WECs would consequently be large, and these sea states produce very high waves and large forces on the body. Therefore, if WECs can be made smaller and more efficient, and thus viable in less extreme sea states, it would dramatically increase their survivability and decrease operational costs. Again, this suggests that very significant improvements to the efficiency of the technology are needed, not just incremental improvements.

There have been a number of reviews of wave energy converters (Lehmann et al., 2016; Drew et al., 2009; Falnes, 2007; Ringwood et al., 2014; Al Shami et al., 2019; Falcão, 2010), which illustrate a plethora of different concepts for wave energy extraction. In fact, there have been over 1000 different wave energy converter designs (Drew et al., 2016). WECs can be generally classified into four main groups. There are 'overtopping' devices, where waves fill a reservoir above the waterline, and then, taking advantage of the potential energy, the water passes through a turbine at the waterline. There are 'attenuators,' which are multiple segments connected to one another lying perpendicular to the incident wave, where the relative motion between the segments is exploited for capturing energy. There are 'oscillating water columns,' consisting of a fixed structure with a turbine above the waterline, and the waves push air through the turbine (Martins-Rivas and Mei, 2009, Evans and Porter, 1997). However, the most common type of wave energy converter is a 'point absorber,' which is a floating body whose characteristic dimension is much smaller than the incoming wavelength and has a power take-off (PTO) device attached.

In 2016, the US Department of Energy sponsored the 'Wave Energy Prize,' a public prize challenge to design a 'game-changing' WEC to improve efficiency, and the range of designs, shapes, and technologies in the finalists was vast. Babarit (2015) compared the performance of a number of different WECs to form a 'database,' which showed the incredibly wide range of both performance and design. All of these studies and WEC concepts highlight a large knowledge gap in the field: the lack of convergence to an optimal shape.

While there is no convergence on the optimal shape of a WEC, there have been a number of studies that optimize the dimensions of a *specific* geometric design (Durren, 2012; Gomes et al., 2012; Rosenberg and Mundon, 2016; Shadman et al., 2018; Xu et al., 2018). There have also been studies that have looked at very simple geometries (such as a cylinder, hemisphere, cone) and optimized the dimensions of these shapes. For example, Hager et al. (2012) compared 2D shapes experimentally, Ricci et al. (2006) compared a hemisphere and a cylinder with a few different radius to draft ra-

tios, Saptono Warpindyasmoro and Gunaldi (2018) and Wen et al. (2018) optimized wave energy converters for a specific location, and Zhang et al. (2016) considered cylinders, hemispheres, paraboloids, and cones. Alamian et al. (2019) optimized a few shapes of pitch point absorbers for a particular location. Other studies, such as Andres et al (2014), examined how to change geometry of WEC (they considered only cylindrical WECs) based on different location and wave climate. Gilloteau and Ringwood (2010) studied the interplay between phyiscal geometry (again, they only considered cylinders) and control strategy. Esmaeilzadeh and Alam (2019) and Kelly and Alam (2019) optimize a submerged planar pressure differential for different spreads of incoming waves. Kurniawan and Moan (2012, 2013) considered a 'library' of shapes, including lines, circles and elliptical sections. McCabe (2009, 2010, 2013) optimized bi-cubic b-splines for non-axisymmetric WECs extracting energy in surge and/or pitch.

There is also a wide range of optimization functions in these studies, showing different definitions of what makes an 'optimal' WEC. For example, Goggins and Finnegan (2014) maximize a performance indicator they call the 'significant velocity,' which is similar to significant wave height but for the device motion. Kurnaiwan and Moan (2013) perform a multi-objective optimization, minimizing surface area and maximizing the integral of power over a given spectrum. McCabe (2013) considered three optimization functions, given a spectrum: overall power, power per characteristic length, and power per volume.

From these studies, we can see a second gap in the knowledge of wave energy: there is no agreed-upon definition of 'optimal' in wave energy, and there is no established framework or systematic study to find general optimal shapes of a WEC.

From all of these studies, we can conclude that for wave energy to become a viable and competitive source of renewable energy, there must be significant improvements to WECs to increase extracted power and decrease cost. Additionally, there is a need to determine a robust, clear definition of what it means for a WEC to be 'optimal,'

and to perform an optimization of general geometries to seek convergence on the optimal shape(s) of a wave energy converter.

1.2 Problem statement and thesis objectives

Optimizing geometry could provide the significant improvement needed in WECs to extract more power for less cost. In this thesis, we optimize WECs for normal operating conditions, rather than looking at extreme conditions. Therefore, we assume that wave motions are sufficiently small to linearize. Newman (1977) states that "for most practical purposes the linear results... are extremely accurate." Although the problem is linearized, the dependence of the hydrodynamic parameters, and consequently everything determined by these parameters, on the body geometry can be highly nonlinear. We assume that the bodies are large relative to the wave amplitude, so flow separation is unimportant. Therefore, assuming linear potential theory, we optimize a single-body deep-water 3D axisymmetric point absorber WEC, with linear power take-off (PTO) mechanisms, assuming a monochromatic unidirectional incoming wave with given wavenumber k. We consider two separate problems: a WEC moving and extracting energy in the heave mode only, as well as the complete 3D problem of an axisymmetric WEC moving and extracting energy in heave, surge and pitch.

We chose to optimize axisymmetric shapes since in the ocean wave direction is highly variable (Drew et al., 2009). Power take-off mechanisms are usually direct-drive linear generators (Al Shami et al., 2018), hence why we model it as a linear damper. While controls are sometimes used in WECs, there are known issues (Babarit, 2015; Cretel et al., 2011), and we choose not to introduce more parameters to our optimization than is necessary.

Therefore, the main objectives of this thesis are to

1. Establish a robust framework defining optimality of wave energy converters

2. Find the optimal shapes of an axisymmetric WEC

3. Develop physical insights about what makes an optimal WEC

1.3 Thesis outline

In chapter 2, we present the hydrodynamic theory for an axisymmetric floating wave energy converter. We show the derivation of the equation of motion of a standard floating body in waves, and then illustrate how this equation is altered to express the equation of motion for a floating WEC. We then show the expressions for extractable power, for heave-only extraction and a general multi-degree-of-freedom power extraction. We determine the maximum extractable power, and under what conditions this maximum occurs. We look at how to practically achieve this maximum power by matching the equation of motions with the expressions for maximum power. We then use far-field theory to find limits for capture width, which is the ratio of extractable power to incident power. We show the derivations for the known limits for heave and surge-pitch motions, and also present a derivation, which we believe to be novel, of the division of the capture width in the surge, pitch and surge-pitch coupled modes, when the WEC moves in surge and pitch.

In chapter 3, we present our novel, scientifically rigorous optimization framework to find practically realistic optimal shapes of WECs. We start by broadly summarizing the main concepts involved for optimizing a WEC, which are to maximize power, while ensuring that the shapes are practically feasible, and to minimize cost, which we do by using amount of material as a proxy for cost. We introduce the concept of a multi-objective optimization and a Pareto Front. Then, we describe our optimization framework in detail, including the constraints put on the problem to form the populations as well as the objective functions to find the set of optimal solutions. We also outline other frameworks we considered, before settling on the current one, to demonstrate some of the nuances of the problem and give motivation for our current framework.

In chapter 4, we present the general, efficient and efficacious procedure we developed to solve the optimization problem. We present our description of general geometries using piecewise parametric polynomial basis functions and how we use the coefficients of these functions as the parameters in the optimization. In this way, we can represent a vast range of geometries with relatively few parameters. Then, we present a novel theorem to find roots of the heave resonance equation. This theorem adds to our understanding of the problem, but also significantly decreases the computation time for the optimization: it is 100x more efficient than brute-force tests. We then present general observations and conclusions for any given class of shapes, which adds to our understanding of what populations and Pareto Fronts will look like and how the constraints affect them. We then discuss how populations are formed for groups of shapes. And finally, we present the flow chart and details of our multi-objective evolutionary algorithm.

In chapter 5, we present the optimal dimensions of a vertical truncated cylinder. We use the cylinder as an example to show the framework and procedure on a shape that is easily described and visualized. However, since in ocean engineering the cylinder is the easiest shape to build, and the most commonly built shape, the results for the optimal cylinders are an important result intrinsically. We present the results for different constraint regimes, to show how the constraints affect the optimal cylinders' performance and dimensions.

In chapter 6, we present the rest of the results for optimized shapes. We show our systematic investigation to find optimal shapes over a broad range of shapes. We discuss the dimensions of the shapes and compare performance among the groups as well as across groups, and look at how constraints affect the shapes and performance. We discuss general trends we saw, and the physical insights these trends give us by looking at how and why these shapes performed better than others.

In chapter 7, we summarize the main contributions of this thesis, and we discuss future work to be done on this topic.

Chapter 2

Hydrodynamic theory for an axisymmetric floating wave energy converter

2.1 Assumptions and problem setup

Consider a three-dimensional axisymmetric floating wave energy converter (WEC) in deep water. Linear potential flow is assumed with a single monochromatic unit-amplitude incoming wave with wavenumber k. For the first of two distinct problems, the WEC is restricted to motion in heave (ξ_3) only, and there is a single power take-off mechanism, which is modeled as a linear damper with damping coefficient β_3. For the second problem, the WEC is allowed to move in surge (ξ_1), heave, and pitch (ξ_5), and there are 4 power take-off mechanisms, modeled as four linear dampers: one in the surge mode with coefficient β_1, one in the heave mode with coefficient β_3, one in the pitch mode with coefficient β_5, and one in the surge-pitch coupled mode with coefficient β_{15}. Mooring line restoring force is modeled as a spring in surge with spring coefficient k_1. The vertical center of gravity is located at z-coordinate z_G, and the pitch moment of inertia is I_{55}. The first (heave-only) problem is shown in figure 2-1, whereas the second (heave-surge-pitch) is shown in figure 2-2.

In the following section, first the equations of motion for a general 6 degree-of-freedom floating body in waves is derived, and then extended to find the equations of motion for the floating wave energy converters described above. Equations for extractable power are presented, and equations for maximal power are derived. Specifically, we present the derivation of the important result that maximal power for an axisymmetric WEC does not depend on size or shape. Finally, far-field analysis is done to prove expressions for maximum extractble power. More details of these equations of motion and derivations for maximal power can be found in Newman (2018), Mei et al. (2005) and Falnes and Kurniawan (2020).

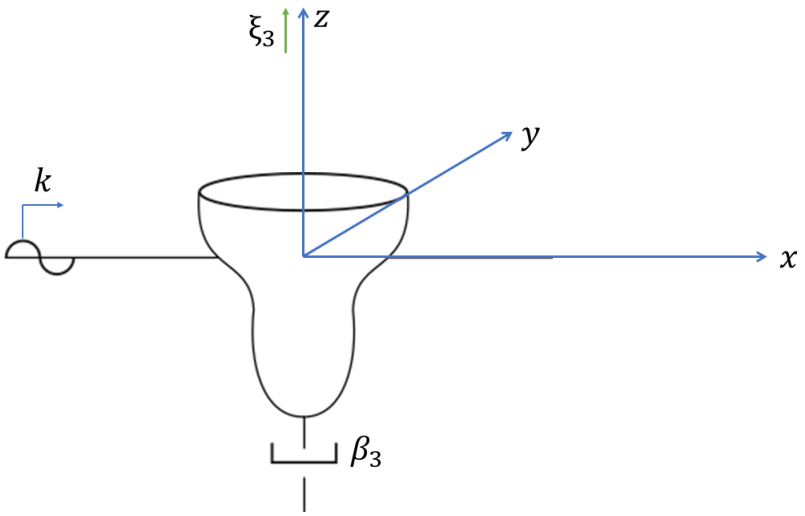

Figure 2-1: WEC restricted to motion and energy extraction in the heave mode only (ξ_3), with power take-off (PTO) modeled as a linear damper with damping coefficient β_3

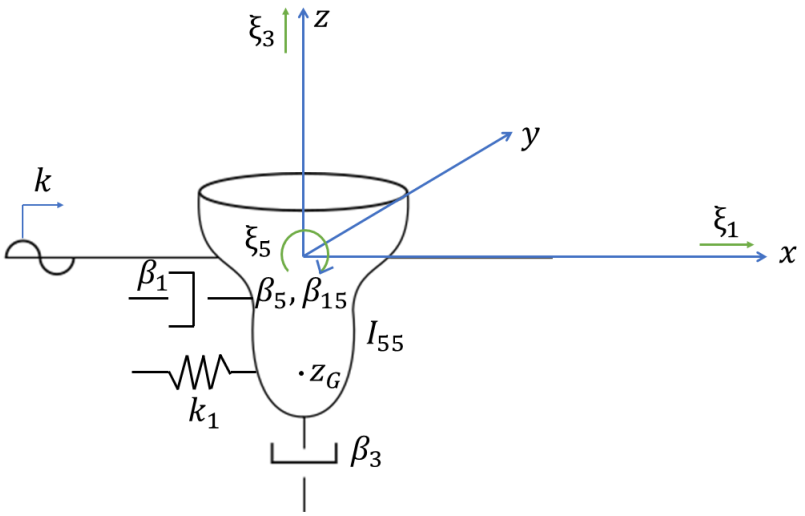

Figure 2-2: WEC moving and extracting energy in heave (ξ_3), surge (ξ_1) and pitch (ξ_5), with power take-off (PTO) modeled as linear dampers with damping coefficients $\beta_1, \beta_3, \beta_{15}$ and β_5

2.2 Theory

2.2.1 Derivation of the equation of motion of a floating body in waves

Newman (2018) derives the expression for the equation of motion of a freely floating body in waves. This derivation is summarized in this section.

Consider a plane progressive wave, with amplitude A and frequency ω, incident on a freely floating body in deep water, which can move in 6 degrees of freedom: surge (1), sway (2), heave (3), roll (4), pitch (5), and yaw (6), as shown in figure 2-3.

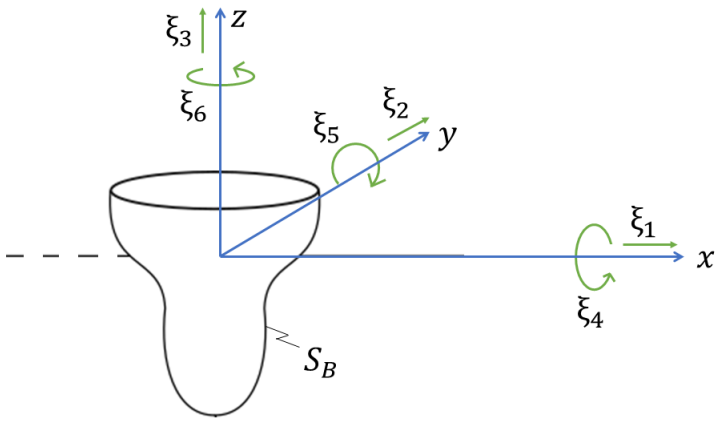

Figure 2-3: Description of motions for floating body S_B

Potential flow is assumed, so the flow is assumed to be incompressible and irrotational, and the fluid is assumed to be inviscid. With these assumptions, we can express the velocity field $\overline{v}$ in the fluid with a potential Φ, where

$$\overline{v} = \nabla\Phi \tag{2.2.1}$$

The deep-water dispersion relation is used to relate frequency to g, the gravitational acceleration constant and k, the wavenumber ($k = \frac{2\pi}{\lambda}$, where λ is wavelength).

$$\omega^2 = gk \tag{2.2.2}$$

Wave steepness is assumed to be small ($kA << 1$), so linear theory can be used to decompose the velocity potential into two parts: the potential due to a rigid body fixed in place, and the potential due to the same body forced to oscillate in the absence of waves:

$$\Phi = \Phi_D + \Phi_R \tag{2.2.3}$$

where Φ_D is the potential due to the incident wave and the resulting interactions with the body, and Φ_R is the potential due to the body oscillating in the absence of waves.

The potential can be expressed in the complex amplitude notation,

$$\Phi(x,y,z,t) = Re\left\{\phi(x,y,z)e^{i\omega t}\right\} \tag{2.2.4}$$

Accordingly, equation 2.2.3 can be expressed as:

$$\Phi(x,y,z,t) = Re\left\{\left(\sum_{j=1}^{6}\xi_j\phi_j\left(x,y,z\right) + A\phi_A\left(x,y,z\right)\right)e^{i\omega t}\right\} \tag{2.2.5}$$

where ϕ_j is the velocity potential of the body oscillating in the jth mode with unit velocity in the absence of waves. The boundary conditions for the six ϕ_j values are found by setting the normal derivative of each ϕ_j equal to the normal component of body velocity:

$$\frac{\partial\phi_j}{\partial n} = i\omega n_j, j = 1,2,3 \tag{2.2.6}$$

$$\frac{\partial\phi_j}{\partial n} = i\omega\left(\overline{r}\times\overline{n}\right)_{j-3}, j = 4,5,6 \tag{2.2.7}$$

Here, $\overline{n}$ is the unit normal vector on the body surface (into the body), and $\overline{r}$ is the position vector. In equation 2.2.5, ξ_j is the complex amplitude of body motion in the jth mode, and $\phi_A = \phi_D/A$ is the potential due to the incident wave and resulting disturbances to the incident wave due to the body, assuming the body is stationary. ϕ_A can be decomposed further into two parts: the incident wave, ϕ_I, and the resulting *scattering* potential, ϕ_7:

$$\phi_A = \phi_0 + \phi_7 \tag{2.2.8}$$

The *diffraction* (ϕ_A) problem must obey the body boundary condition: since the body is assumed to be stationary, the normal velocity of the diffraction potential at the boundary must be 0:

$$\frac{\partial\phi_A}{\partial n} = 0, \text{ on } S_B \tag{2.2.9}$$

Or,

$$\frac{\partial \phi_7}{\partial n} = -\frac{\partial \phi_0}{\partial n}, \text{ on } S_B \tag{2.2.10}$$

Note that each potential is governed by the Laplace equation:

$$\nabla^2 \phi_j = 0, \text{ for } j = 0, ..., 7 \tag{2.2.11}$$

And also each potential must satisfy the free surface linearized kinematic-dynamic boundary condition:

$$-\omega^2 \phi_j + g\frac{\partial \phi_j}{\partial z} = 0, \text{ for } j = 0, ..., 7, \text{on } z = 0 \tag{2.2.12}$$

As well as bottom boundary condition:

$$\phi_j \to 0 \text{ as } z \to -\infty \text{ for } j = 0, ..., 7 \tag{2.2.13}$$

And finally, the potentials (except ϕ_0) must satisfy the radiation condition, which states that waves must be outgoing at infinity to satisfy conservation of energy:

$$\phi \propto \frac{1}{\sqrt{R}} e^{-ikR} \text{ for } j = 1, ..., 7 \tag{2.2.14}$$

where $R = \sqrt{x^2 + y^2}$.

Pressure on the surface of the body can be found using the linearized Bernoulli equation:

$$p = -\rho \left(\frac{\partial \Phi}{\partial t} + gz \right) \tag{2.2.15}$$

Putting equation 2.2.5 into this equation, it becomes

$$p = -\rho Re \left\{ \left(\sum_{j=1}^{6} \xi_j \phi_j + A\left(\phi_0 + \phi_7\right) \right) i\omega e^{i\omega t} \right\} - \rho g z \tag{2.2.16}$$

Integrating the pressure over the wetted surface area of the body, S_B, we get the forces and moments on the body:

$$\overline{F} = \begin{cases} \iint_{S_B} p\overline{n}\ dS & i = 1,2,3 \\ \iint_{S_B} p\left(\overline{n} \times \overline{r}\right)\ dS & i = 4,5,6 \end{cases} \tag{2.2.17}$$

where $\overline{F}$ is the length-6 vector of forces (1,2,3) and moments (4,5,6) on the body. The equation for forces can be broken into three parts:

$$\overline{F} = \overline{F_1} + \overline{F_2} + \overline{F_3} \tag{2.2.18}$$

where $\overline{F_1}$ are the forces due the hydrostatic pressure, $\overline{F_2}$ are the forces due to radiation, and $\overline{F_3}$ are the exciting forces, due to the diffraction problem. Putting equation 2.2.16 into 2.2.17 and decomposing into the three equations, we get

$$\overline{F_1} = \begin{cases} -\rho g \iint_{S_B} \overline{n} z\ dS & i = 1,2,3 \\ -\rho g \iint_{S_B} \left(\overline{n} \times \overline{r}\right) z\ dS & i = 4,5,6 \end{cases} \tag{2.2.19}$$

$$\overline{F_2} = \begin{cases} -\rho Re\left\{\sum_{j=1}^{6} i\omega\xi_j e^{i\omega t} \iint_{S_B} \overline{n}\phi_j\ dS\right\} & i = 1,2,3 \\ -\rho Re\left\{\sum_{j=1}^{6} i\omega\xi_j e^{i\omega t} \iint_{S_B} \left(\overline{n} \times \overline{r}\right)\phi_j\ dS\right\} & i = 4,5,6 \end{cases} \tag{2.2.20}$$

$$\overline{F_3} = \begin{cases} -\rho Re\left\{i\omega A e^{i\omega t} \iint_{S_B} \overline{n}\left(\phi_0 + \phi_7\right)\ dS\right\} & i = 1,2,3 \\ -\rho Re\left\{i\omega A e^{i\omega t} \iint_{S_B} \left(\overline{n} \times \overline{r}\right)\left(\phi_0 + \phi_7\right)\ dS\right\} & i = 4,5,6 \end{cases} \tag{2.2.21}$$

It is convenient to add forces due to the weight of the body to the forces due to hydrostatic pressure ($\overline{F_1}$) to get the total static forces and moments, $\overline{F_{\tilde{1}}}$. For a freely floating body, this is shown in Newman (2018) to be

$$F_{\tilde{1},i} = -\sum_{j=1}^{6} C_{ij}\xi_j \tag{2.2.22}$$

where $[C] = C_{ij}$ is the matrix with 0 everywhere except

$$C_{33} = \rho g S \tag{2.2.23}$$

$$C_{44} = \rho g S_{22} + \rho g \forall z_B - m g z_G \tag{2.2.24}$$

$$C_{45} = -g(\rho \forall x_B - m x_G) \tag{2.2.25}$$

$$C_{65} = -g\left(\rho \forall z_B - m z_G\right) \tag{2.2.26}$$

$$C_{55} = \rho g S_{11} + \rho g \forall z_B - m g z_G \tag{2.2.27}$$

where $\overline{x}_B$ and $\overline{x}_G$ are the position vectors of the centers of gravity and buoyancy, respectively, S is the waterplane area, $\forall$ is displaced volume, and

$$S_{ij} = \iint_{S_0} x_i x_j dS \tag{2.2.28}$$

where S_0 is the static position of S_B.

$\overline{F_2}$ are the forces and moments due to radiation, and they can be written as

$$F_{2,i} = Re\left\{\sum_{j=1}^{6} \xi_j e^{i\omega t} f_{ij}\right\} \tag{2.2.29}$$

where

$$f_{ij} = -\rho \iint_{S_B} \frac{\partial \phi_i}{\partial n} \phi_j \, dS \tag{2.2.30}$$

f_{ij} is the force in direction i due to unit-amplitude motion in the j direction. We can express this force in terms of the component in phase with velocity and the component in phase with acceleration, which we call damping and added mass, respectively:

$$f_{ij} = \omega^2 A_{ij} - i\omega B_{ij} \tag{2.2.31}$$

A_{ij} is called the added mass coefficient, and B_{ij} is called the damping coefficient. $F_{2,i}$

can therefore be expressed as

$$F_{2,i} = Re\left\{\sum_{j=1}^{6} \xi_j \left(\omega^2 A_{ij} - i\omega B_{ij}\right)\right\} \tag{2.2.32}$$

Finally, $\overline{F_3}$ are the exciting forces and moments and can be expressed as

$$F_{3,i} = Re\left\{AX_i e^{i\omega t}\right\} \tag{2.2.33}$$

where, after applying boundary conditions defined by equations 2.2.6 and 2.2.7 to $\overline{F_3}$ in equation 2.2.21.

$$X_i = -\rho i\omega \iint_{S_B} (\phi_0 + \phi_7) \frac{\partial \phi_i}{\partial n}\, dS \tag{2.2.34}$$

Adding equations 2.2.22, 2.2.29 and 2.2.33, an expression for the sum of the forces acting on the body is

$$F_i = \sum_{j=1}^{6} \xi_j \left(-C_{ij} + f_{ij}\right) + AX_i \text{ for } i = 1, 2, ..., 6 \tag{2.2.35}$$

To form the equation of motion, we set this sum equal to the inertial force:

$$-\omega^2 \sum_{j=1}^{6} M_{ij}\xi_j = \sum_{j=1}^{6} \xi_j \left(-c_{ij} + f_{ij}\right) + AX_i \text{ for } i = 1, 2, ..., 6 \tag{2.2.36}$$

where M_{ij} is the matrix

$$M_{ij} = \begin{bmatrix} m & 0 & 0 & 0 & -mz_G & 0 \\ 0 & m & 0 & 0 & 0 & 0 \\ 0 & 0 & m & mz_G & 0 & 0 \\ 0 & 0 & mz_G & I_{44} & I_{45} & I_{46} \\ -mz_G & 0 & 0 & I_{54} & I_{55} & I_{56} \\ 0 & 0 & 0 & I_{64} & I_{65} & I_{66} \end{bmatrix} \tag{2.2.37}$$

where m is the body mass and I_{ij} is the moment of inertia. Rearranging equation

2.2.36, and inserting equation 2.2.31 for f_{ij}, we get the general 6 degree-of-freedom equation of motion

$$\sum_{j=1}^{6} \xi_j \left[-\omega^2 \left(M_{ij} + A_{ij} \right) + i\omega B_{ij} + C_{ij} \right] = AX_i \tag{2.2.38}$$

2.2.2 Equation of motion of a floating WEC

The equation of motion of a general body freely floating in waves derived in the previous section will be used to derive the more specific equations of motion for our two problems defined at the beginning of this chapter and summarized in figures 2-2 and 2-2. We will show that the heave and surge-pitch equations of motion are uncoupled, so it is sufficient to derive the three (heave-surge-pitch) degree of freedom equation of motion and then separate it into the separate problems afterwards. Notice that equation 2.2.38 looks similar to a typical spring-mass-damper system, with the mass term in this case including the standard inertia term as well as added mass, the damping term from damping due to radiation, and the restoring term due to the forces of buoyancy and gravity. To derive the equation of motion for a WEC, the following additional forces must be accounted for:

1. Power take-off forces, which are modeled as linear dampers, there will be one in the surge mode with damping coefficient β_1, one in the heave mode with coefficient β_3, one in the pitch mode with coefficient β_5, and one in the surge-pitch coupled mode with coefficient β_{15}.

2. Mooring forces, which are modeled as a spring in surge with spring coefficient k_1.

Accounting for the these forces, and assuming a unit-amplitude ($A = 1$) incident wave, the equation of motion for the WEC is thus

$$\sum_{j=1,3,5} M_{ij} \ddot{\Xi}_j = \mathbb{X}_i + \sum_{j=1,3,5} \left[-A_{ij} \ddot{\Xi}_j - \left(B_{ij} + \beta_{ij} \right) \dot{\Xi}_j - \left(C_{ij} + K_{ij} \right) \Xi_j \right] \tag{2.2.39}$$

where β_{ij} is the PTO damping matrix:

$$\beta_{ij} = \begin{bmatrix} \beta_1 & 0 & \beta_{15} \\ 0 & \beta_3 & 0 \\ \beta_{15} & 0 & \beta_5 \end{bmatrix} \tag{2.2.40}$$

and K_{ij} has the term $K_{11} = k_1$, the surge spring coefficient, and 0 elsewhere. Ξ_j is the harmonic body motion in mode j, and $\mathbb{X}_j$ is the harmonic exciting force in mode j. We can write

$$\Xi_j = Re\left\{\xi_j e^{-i\omega t}\right\} \tag{2.2.41}$$

$$\dot{\Xi}_j = Re\left\{-i\omega\xi_j e^{-i\omega t}\right\} \tag{2.2.42}$$

$$\ddot{\Xi}_j = Re\left\{-\omega^2\xi_j e^{-i\omega t}\right\} \tag{2.2.43}$$

$$\mathbb{X}_i = Re\left\{X_i e^{i\omega t}\right\} \tag{2.2.44}$$

Putting these expressions into equation 2.2.39, the time-harmonic term cancels, simplifying the equation of motion to

$$-\omega^2 \sum_{j=1,3,5} M_{ij}\xi_j = X_i + \sum_{j=1,3,5} \left[\omega^2 A_{ij} + i\left(B_{ij} + \beta_{ij}\right) - \left(C_{ij} + K_{ij}\right)\right]\xi_j \tag{2.2.45}$$

Rearranging, this becomes

$$\sum_{j=1,3,5} \left[-\omega^2\left(M_{ij} + A_{ij}\right) - i\left(B_{ij} + \beta_{ij}\right) - \left(C_{ij} + K_{ij}\right)\right]\xi_j = X_i \tag{2.2.46}$$

In matrix notation,

$$\left(-\omega^2\left([M] + [A]\right) - i\omega\left([B] + [\beta]\right) + \left([C] + [K]\right)\right)\overline{\xi} = \overline{X} \tag{2.2.47}$$

where $[M]$ is the mass matrix , $[A]$ is the added mass matrix, $[B]$ is the radiation

damping matrix, $[\beta]$ is the PTO damping matrix, $[C]$ is the restoring coefficient matrix and [K] is the spring restoring force. For our 3-mode system, the body motion vector $\overline{\xi}$ is

$$\overline{\xi} = \begin{bmatrix} \xi_1 \\ \xi_3 \\ \xi_5 \end{bmatrix} \tag{2.2.48}$$

and the exciting force vector $\overline{X}$ is

$$\overline{X} = \begin{bmatrix} X_1 \\ X_3 \\ X_5 \end{bmatrix} \tag{2.2.49}$$

For an axisymmetric body, mass matrix plus added mass matrix is

$$[M] + [A] = \begin{bmatrix} m & 0 & -mz_G \\ 0 & m & 0 \\ -mz_G & 0 & I_{55} \end{bmatrix} + \begin{bmatrix} A_{11} & 0 & A_{15} \\ 0 & A_{33} & 0 \\ A_{15} & 0 & A_{55} \end{bmatrix} \tag{2.2.50}$$

The total (radiation and PTO) damping matrix is

$$[B] = \begin{bmatrix} B_{11} + \beta_1 & 0 & B_{15} + \beta_{15} \\ 0 & B_{33} + \beta_3 & 0 \\ B_{15} + \beta_{15} & 0 & B_{55} + \beta_5 \end{bmatrix} \tag{2.2.51}$$

And the total restoring matrix is

$$[C] = \begin{bmatrix} k_1 & 0 & 0 \\ 0 & C_{33} & 0 \\ 0 & 0 & C_{55} \end{bmatrix} \tag{2.2.52}$$

where

$$C_{33} = \rho g S \tag{2.2.53}$$

where S is waterplane area, and

$$C_{55} = \rho g S_{11} + \rho g \forall z_B - m g z_G \tag{2.2.54}$$

Since the WEC is assumed to be axisymmetric, if the radius of the body at the waterline is R, $S_{11} = \int x^2 dS = \frac{\pi R^4}{4}$. From the above matrices, we can see that heave and surge-pitch are uncoupled, meaning that we can solve heave separately from the other two modes.

For heave, the equation of motion reduces to

$$\left[-\omega \left(m + A_{33}\right) - i\omega \left(B_{33} + \beta_3\right) + C_{33}\right] \xi_3 = X_3 \tag{2.2.55}$$

Solving for ξ_3, we get

$$\xi_3 = \frac{X_3}{C_{33} - \omega \left(m + A_{33}\right) - i\omega \left(B_{33} + \beta_3\right)} \tag{2.2.56}$$

For surge-pitch, the equation of motion becomes

$$\left(-\omega^2 \begin{bmatrix} m + A_{11} & A_{15} - m z_G \\ A_{15} - m z_G & I_{55} + A_{55} \end{bmatrix} - i\omega \begin{bmatrix} B_{11} + \beta_1 & B_{15} + \beta_{15} \\ B_{15} + \beta_{15} & B_{55} + \beta_5 \end{bmatrix} + \begin{bmatrix} k_1 & 0 \\ 0 & C_{55} \end{bmatrix}\right) \begin{bmatrix} \xi_1 \\ \xi_5 \end{bmatrix} = \begin{bmatrix} X_1 \\ X_5 \end{bmatrix} \tag{2.2.57}$$

Solving for $[\xi_1, \xi_5]^T$, we get

$$\begin{bmatrix} \xi_1 \\ \xi_5 \end{bmatrix} = \frac{1}{D} \begin{bmatrix} C_{55} - \omega^2 (I_{55} + A_{55}) - i\omega (B_{55} + \beta_5) & \omega^2 (A_{15} - mz_G) + i\omega (B_{15} + \beta_{15}) \\ \omega^2 (A_{15} - mz_G) + i\omega (B_{15} + \beta_{15}) & k_1 - \omega^2 (m + A_{11}) - i\omega (B_{11} + \beta_1) \end{bmatrix} \begin{bmatrix} X_1 \\ X_5 \end{bmatrix} \tag{2.2.58}$$

where

$$D = \left[k_1 - \omega^2 (m + A_{11}) - i\omega (B_{11} + \beta_1)\right] \left[C_{55} - \omega^2 (I_{55} + A_{55}) - i\omega (B_{55} + \beta_5)\right] - \left[\omega^2 (A_{15} - mz_G) + i\omega (B_{15} + \beta_{15})\right]^2 \tag{2.2.59}$$

2.2.3 Extractable power

Using the above theory to describe the WEC, we now calculate the extractable power of a given body and incoming wave.

Heave-only power extraction

For the case where the WEC only moves and extracts power in the heave mode, the linear damper, described with damping coefficient β_3, can produce power equal to its velocity times the force of the linear damper, which is β_3 times velocity. The extractable power is

$$\mathcal{P}_3 = \dot{\Xi}_3 \beta_3 \dot{\Xi}_3 \tag{2.2.60}$$

where, as above,

$$\Xi_3 = Re\left\{\xi_3 e^{-i\omega t}\right\} \tag{2.2.61}$$

ξ_3 is the complex amplitude of heave body motion. It can be written in terms of its amplitude $|\xi_3|$ and phase ϕ_3:

$$\xi_3 = |\xi_3| e^{i\phi_3} \tag{2.2.62}$$

Equation 2.2.61 can also be expressed as

$$\Xi_3 = Re\left\{\xi_3 e^{i\omega t}\right\} = Re\left\{|\xi_3| e^{i\phi_3} e^{i\omega t}\right\} = |\xi_3| cos\left(\omega t + \phi_3\right) \tag{2.2.63}$$

Therefore, putting equation 2.2.63 into equation 2.2.60, we get

$$\mathcal{P}_3 = \beta_3 \omega^2 \xi_3^2 = \beta_3 \omega |\xi_3|^2 cos^2\left(\omega t + \phi_3\right) \tag{2.2.64}$$

From now on, we will talk about average power over one period of the wave, which we will call P_3 for heave. Since $\overline{cos^2\left(\omega t + \phi_3\right)} = \frac{1}{2}$,

$$P_3 \equiv \overline{\mathcal{P}_3} = \frac{1}{2} \beta_3 \omega^2 |\xi_3|^2 \tag{2.2.65}$$

Using equation 2.2.56, we can input the expression for $|\xi_3|$ to find an expression for extractable power in heave:

$$P_3 = \frac{\frac{1}{2} \beta_3 \omega^2 |X_3|^2}{\left[C_{33} - \omega^2 \left(m + A_{33}\right)\right]^2 + \omega^2 \left(\beta_3 + B_{33}\right)^2} \tag{2.2.66}$$

General Multi-degree-of-freedom power extraction

Falnes (2020, 1980) and Evans (1980, 1986) explain the general problem of extracting power in six degrees-of-freedom. In general, power from a harmonic oscillation is

$$\mathcal{P} = F(t) U(t) \tag{2.2.67}$$

where $F(t)$ is a harmonic forcing term, and $U(t)$ is a harmonic velocity:

$$F(t) = Re\left\{f e^{i\omega t}\right\} = \frac{f}{2} e^{i\omega t} + \frac{f^*}{2} e^{i\omega t} \tag{2.2.68}$$

where f is the complex amplitude of the forcing term, and $*$ represents the complex conjugate.

$$f = |f|e^{i\phi_f} \tag{2.2.69}$$

and

$$U(t) = Re\left\{ue^{i\omega t}\right\} = \frac{u}{2}e^{i\omega t} + \frac{u^*}{2}e^{i\omega t} \tag{2.2.70}$$

where u is the complex amplitude of the velocity term:

$$u = |u|e^{i\phi_u} \tag{2.2.71}$$

Putting 2.2.68 and 2.2.70 into 2.2.67:

$$\mathcal{P} = F(t)U(t) = \frac{1}{4}\left(fu^* + f^*u + fue^{i\omega t} + f^*u^*e^{i\omega t}\right) \tag{2.2.72}$$

Again, we will consider average power over one period. The third and fourth terms in the parenthesis in the equation above are equivalent to $2fucos(2\omega t)$, and so this has an average of 0 over one period. Therefore, average power over one period from force F moving with velocity U is

$$P \equiv \overline{\mathcal{P}} = \frac{1}{4}\left(fu^* + f^*u\right) = \frac{1}{2}Re\left\{fu^*\right\} \tag{2.2.73}$$

In general, extractable power from a WEC is equivalent to the exciting power minus the radiated power:

$$P = P_e - P_r \tag{2.2.74}$$

For a body in waves, the exciting power is equal to the exciting force times velocity. As above, the harmonic exciting force in the ith mode is

$$\mathbb{X}_i = Re\left\{X_i e^{i\omega t}\right\} = Re\left\{|X_i|e^{i\phi_{X_i}}e^{i\omega t}\right\} \tag{2.2.75}$$

And, if the harmonic body motion in the ith mode is

$$\Xi_i = Re\left\{\xi_i e^{i\omega t}\right\} \tag{2.2.76}$$

then the harmonic velocity is

$$\mathbb{U}_i = \dot{\Xi}_i = \omega \Xi_i = Re\left\{\omega \xi_3 e^{i\omega t}\right\} \tag{2.2.77}$$

Therefore, using equations 2.2.73, 2.2.75 and 2.2.77, the exciting power in the ith mode will be

$$P_{e,i} = \frac{\omega}{4}\left(X_i \xi_i^* + X_i^* \xi_i\right) \tag{2.2.78}$$

So the total exciting power is

$$P_e = \sum_{i=1}^{6} P_{e,i} = \frac{\omega}{4}\sum_{i=1}^{6}\left(X_i \xi_i^* + X_i^* \xi_i\right) = \frac{\omega}{4}\left(\underline{X}^T \underline{\xi}^* + \underline{X}^{*T} \underline{\xi}\right) \tag{2.2.79}$$

The radiated power in the ith mode is equal to the radiation force times the velocity. Again using equation 2.2.73 we find an expression for average radiated power over one period in the ith mode:

$$P_{r,i} = \frac{1}{4}\sum_{j=1}^{6}\left(Z_{ij} u_j u_i^* + Z_{ij}^* u_j^* u_i\right) \tag{2.2.80}$$

where Z_{ij} is the radiation impedance matrix:

$$Z_{ij} = i\omega A_{ij} + B_{ij} \tag{2.2.81}$$

From equation 2.2.73, we see that we can instead express the average power in terms of the real part of the force times complex conjugate of velocity. We see that

$$Re\left\{Z_{ij}\right\} = \frac{1}{2}\left(Z_{ij} + Z_{ij}^*\right) = B_{ij} \tag{2.2.82}$$

So equation 2.2.80 becomes

$$P_{r,i} = \frac{\omega^2}{2} \sum_{j=1}^{6} Re\left\{Z_{ij}\xi_j\xi_i^*\right\} = \frac{\omega^2}{2} \sum_{j=1}^{6} B_{ij}\xi_j\xi_i^* \tag{2.2.83}$$

And the total radiated force is

$$P_r = \sum_{i=1}^{6} P_{r,i} = \frac{\omega^2}{2} \sum_{i=1}^{6}\sum_{j=1}^{6} Re\left\{Z_{ij}\xi_j\xi_i^*\right\} = \frac{\omega}{2}\underline{\xi}^{*T}[B]\underline{\xi} \tag{2.2.84}$$

Extractable power for mode i is then equal to the exciting power in mode i minus radiated power in mode i:

$$P_i = P_{e,i} - P_{r,i} = \frac{\omega}{4}\left(X_i\xi_i^* + X_i^*\xi_i\right) - \frac{\omega^2}{2}\sum_{j=1}^{6} B_{ij}\xi_j\xi_i^* \tag{2.2.85}$$

Finally, total extractable power is

$$P = P_e - P_r = \frac{\omega}{4}\left(\underline{X}^T\underline{\xi}^* + \underline{X}^{*T}\underline{\xi}\right) - \frac{\omega^2}{2}\underline{\xi}^{*T}[B]\underline{\xi} \tag{2.2.86}$$

2.2.4 Maximum power

Heave maximum power

Extractable power in the heave mode only is shown in equation 2.2.66. To find the maximum extractable power, we set the derivative with respect to β_3 equal to zero, and the derivative with respect to $C_{33} - \omega^2(m + A_{33})$ equal to 0. The latter requirement, which is the *resonance condition* is not always possible, so we solve the former first:

$$\frac{\partial P}{\partial \beta_3} = \frac{\left[C_{33} - \omega^2(m + A_{33})\right]\left[\frac{1}{2}\omega^2|X_3|^2\right] - \left[\frac{1}{2}\beta_3\omega^2|X_3|^2\right]\left[2\omega^2(\beta_3 + B_{33})\right]}{\left\{\left[C_{33} - \omega^2(m + A_{33})\right]^2 + \omega^2(\beta_3 + B_{33})\right\}^2} = 0 \tag{2.2.87}$$

Solving this equation for β_3, we get an expression for the optimal power take-off damping coefficient, β_3^{opt}, which is a function of frequency and geometry:

$$\beta_3^{opt} = \sqrt{\frac{C_{33} - \omega^2(m + A_{33})}{\omega^2} + B_{33}^2} \tag{2.2.88}$$

Then, we set the derivative of 2.2.66 with respect to $C_{33} - \omega^2 (m + A_{33})$ equal to 0:

$$\frac{\partial P_3}{\partial \left[C_{33} - \omega^2 (m + A_{33})\right]} = \frac{2 \left[C_{33} - \omega^2 (m + A_{33})\right]}{\left\{\left[C_{33} - \omega^2 (m + A_{33})\right]^2 + \omega^2 (\beta_3 + B_{33})\right\}^2} = 0 \quad (2.2.89)$$

This condition results in what will be called the 'heave resonance equation':

$$C_{33} - \omega^2 (m + A_{33}) = 0 \quad (2.2.90)$$

Putting this heave resonance condition into equation 2.2.66, we get an expression for heave extractable power when the body is in resonance.

$$P_3^r = \frac{\frac{1}{2}\beta_3 |X_3|^2}{(\beta_3 + B_{33})^2} \quad (2.2.91)$$

Putting the heave resonance condition (equation 2.2.90) into the expression for optimal POT coefficient (equation 2.2.88), we get an expression for the optimal PTO coefficient when the body is in resonance:

$$\beta_3^{opt,r} = B_{33} \quad (2.2.92)$$

That is, when the body is in resonance, the optimal PTO coefficient is equal to the damping coefficient due to radiation. Note: if other damping existed in the system (for example, from mooring lines), the optimal β_3 would be the sum of all other damping in the system. Putting this expression into equation 2.2.91, we get an expression for the maximum extractable power, assuming the body is in resonance and the PTO coefficient is equal to the radiation damping coefficient:

$$P_3^{max} = P_3^{opt,r} = \frac{|X_3|^2}{8B_{33}} \quad (2.2.93)$$

Since our WEC is an axisymmetric body, we can use the following version of the Haskind relation (Mei et al., 2005):

$$B_{33} = \frac{k|X_3|^2}{4\rho g V_g A^2} \tag{2.2.94}$$

where V_g is the group velocity. Putting this into equation 2.2.93, we see that the maximum extractable power does not depend on shape:

$$P_3^{max} = \frac{\rho g V_g}{2k} \tag{2.2.95}$$

It is convenient to define a *capture width*, which is the ratio of the extractable power to the incident power per unit crest length. In other words, the capture width is the width of the incoming wave such that the WEC extracts all of the energy from it. In heave, this capture width is

$$W_3 = \frac{P_3}{P_I} \tag{2.2.96}$$

Incident power per unit width of crest of the incident wave is

$$P_I = \frac{1}{2}\rho g A^2 V_g \tag{2.2.97}$$

To non-dimensionalize, the capture width is multiplied by k. Therefore, putting equations 2.2.95 and 2.2.97 into equation 2.2.96, we see that the optimal nondimensional capture width in heave is

$$kW_3^{max} = 1 \tag{2.2.98}$$

General multi-degree-of-freedom maximum power

To find the maximum extractable power for a multi-degree-of-freedom system, we define a vector

$$\overline{\delta} = \overline{\xi} - \overline{\zeta} \tag{2.2.99}$$

where ζ is the solution of

$$\frac{1}{2}\overline{X} = \omega[B]\overline{\zeta} \tag{2.2.100}$$

We know that $[B]$ is symmetric and real, so when we take the complex conjugate transpose of the above equation it becomes

$$\frac{1}{2}\overline{X}^{*T} = \omega\overline{\zeta}^{*T}[B]^{*T} = \omega\overline{\zeta}^{*T}[B] \tag{2.2.101}$$

Putting $\overline{\xi} = \overline{\delta}+\overline{\zeta}$ into the equation for extractable power for a multi-degree-of-freedom WEC (equation 2.2.86) and expanding, we get

$$\begin{aligned} P = &\frac{\omega}{4}\overline{X}^{T}\overline{\zeta}^{*} + \frac{\omega}{4}\overline{X}^{*T}\overline{\zeta} + \frac{\omega}{4}\overline{X}^{T}\overline{\delta}^{*} + \frac{\omega}{4}\overline{X}^{*T}\overline{\delta} - \frac{\omega^2}{2}\overline{\zeta}^{*T}[B]\overline{\zeta} \\ &- \frac{\omega^2}{2}\overline{\delta}^{*T}[B]\overline{\zeta} - \frac{\omega^2}{2}\overline{\zeta}^{*T}[B]\overline{\delta} - \frac{\omega^2}{2}\overline{\delta}^{*T}[B]\overline{\delta} \end{aligned} \tag{2.2.102}$$

The second term cancels the fifth term, the third term cancels the sixth term, and the fourth term cancels the seventh term, so only the first and last terms remain:

$$P = \frac{\omega}{4}\overline{X}^{T}\overline{\zeta}^{*} - \frac{\omega^2}{2}\overline{\delta}^{*T}[B]\overline{\delta} \tag{2.2.103}$$

Since $[B]$ is positive definite, the second term is strictly positive, therefore

$$P^{max} = \frac{\omega}{4}\overline{X}^{T}\overline{\zeta}^{*} \tag{2.2.104}$$

Which occurs when $\overline{\delta} = 0$, meaning that

$$\overline{\xi}^{opt} = \overline{\zeta} \tag{2.2.105}$$

So, when $[B]$ is non-singular, we get an expression for the vector of body motion that results in the maximal extractable power:

$$\overline{\xi}^{opt} = \frac{1}{2\omega}[B]^{-1}\overline{X} \tag{2.2.106}$$

Since P^{max} is a scalar, it is equal to its transpose, so, using equation 2.2.100, the expression for P^{max} in equation 2.2.104 becomes

$$P^{max} = \frac{\omega^2}{2}\overline{\zeta}^{*T}[B]\overline{\zeta} \tag{2.2.107}$$

And when $\overline{\xi} = \overline{\xi}^{opt} = \overline{\zeta}$, we get an expression for the maximal extractable power for a general 6 degree of freedom system in terms of the body motion vector, frequency, and the radiation damping matrix:

$$P^{max} = \frac{\omega^2}{2}\overline{\xi}^{*T}[B]\overline{\xi} \tag{2.2.108}$$

Surge-pitch

Here we use the general 6 degree-of-freedom derivation in the previous section to show the maximum extractable power for surge-pitch motion. When $\overline{\xi} = \overline{\xi}^{opt} = \overline{\zeta}$, equation 2.2.106 gives us an expression for optimal motion in the surge and pitch modes

$$\begin{bmatrix} \xi_1^{opt} \\ \xi_5^{opt} \end{bmatrix} = \frac{1}{2\omega\left(B_{11}B_{55} - B_{15}^2\right)} \begin{bmatrix} B_{55} & -B_{15} \\ -B_{15} & B_{11} \end{bmatrix} \begin{bmatrix} X_1 \\ X_5 \end{bmatrix} \tag{2.2.109}$$

$$= \frac{1}{2\omega\left(B_{11}B_{55} - B_{15}^2\right)} \begin{bmatrix} B_{55}X_1 - B_{15}X_5 \\ B_{11}X_5 - B_{15}X_1 \end{bmatrix} \tag{2.2.110}$$

We can find a more explicit expression for body motion. To do so, ξ_1, ξ_5, X_1 and X_5 can be expressed in the complex amplitude form:

$$\xi_1 = |\xi_1|e^{i\phi_1} \tag{2.2.111}$$

$$\xi_5 = |\xi_5|e^{i\phi_5} \tag{2.2.112}$$

$$X_1 = |X_1|e^{i\psi_1} \tag{2.2.113}$$

$$X_5 = |X_5|e^{i\psi_5} \tag{2.2.114}$$

We wish to find $|\xi_1|, \phi_1, |\xi_5|$ and ϕ_5 in terms of damping coefficients and exciting forces. We will prove in section 2.2.6 the following facts, which will be used in our derivations of body motion amplitude and phases:

1. $\psi_1 - \psi_5$ can only take the values $2\pi n$ or $2\pi n + \pi$.
2. $\psi_1 - \psi_5 = 2\pi n$ if and only if $B_{15} > 0$
3. $\psi_1 - \psi_5 = 2\pi n + \pi$ if and only if $B_{15} < 0$

Using equation 2.2.109, ξ_1 can be expressed as

$$\xi_1 = |\xi_1|e^{i\phi_1} = \frac{B_{55}X_1 - B_{15}X_5}{2\omega\left(B_{11}B_{55} - B_{15}^2\right)} = \frac{N_1}{Q} = \frac{|N_1|}{|Q|}e^{i\phi_1} \tag{2.2.115}$$

where

$$N_1 = B_{55}X_1 - B_{15}X_5 \tag{2.2.116}$$

$$Q = |Q| = 2\omega\left(B_{11}B_{55} - B_{15}^2\right) \tag{2.2.117}$$

To find N_1, we can use the complex amplitude form of X_1 and X_5 given in equations 2.2.113 and 2.2.114 to get

$$N_1 = B_{55}|X_1|e^{i\psi_1} - B_{15}|X_5|e^{i\psi_5} = B_{55}|X_1|(cos\psi_1 + isin\psi_1) - B_{15}|X_5|(cos\psi_5 + isin\psi_5) \tag{2.2.118}$$

So that the square of the amplitude is

$$|N_1|^2 = B_{55}^2|X_1|^2 + B_{15}^2|X_5|^2 - 2B_{55}B_{15}|X_1||X_5|cos\left(\psi_1 - \psi_5\right) \tag{2.2.119}$$

Since when $\psi_1 - \psi_5 = 2\pi n, B_{15} > 0$ and when $\psi_1 - \psi_5 = 2\pi n + \pi, B_{15} < 0$ (and those are the only two options for $\psi - \psi_5$), we can say

$$|N_1|^2 = B_{55}^2|X_1|^2 + B_{15}^2|X_5|^2 - 2B_{55}|B_{15}||X_1||X_5| \tag{2.2.120}$$

and therefore

$$|N_1| = B_{55}|X_1| - |B_{15}||X_5| \tag{2.2.121}$$

Putting equations 2.2.121 and 2.2.117 into equation 2.2.115, we find an expression for $|\xi_1|$:

$$|\xi_1| = \frac{B_{55}|X_1| - |B_{15}||X_5|}{2\omega\left(B_{11}B_{55} - B_{15}^2\right)} \tag{2.2.122}$$

To find ϕ_1, we see that

$$cos\phi_1 = \frac{B_{55}|X_1|cos\psi_1 - B_{15}|X_5|cos\psi_5}{|N_1|} \tag{2.2.123}$$

and/or

$$sin\phi_1 = \frac{B_{55}|X_1|sin\psi_1 - B_{15}|X_5|sin\psi_5}{|N_1|} \tag{2.2.124}$$

Similarly, we can perform the same analysis on ξ_5. We define

$$\xi_5 = |\xi_5|e^{i\phi_5} = \frac{B_{11}X_5 - B_{15}X_1}{2\omega\left(B_{11}B_{55} - B_{15}^2\right)} = \frac{N_5}{Q} = \frac{|N_1|}{|Q|}e^{i\phi_5} \tag{2.2.125}$$

where

$$N_5 = B_{11}X_5 - B_{15}X_1 \tag{2.2.126}$$

and, following the same steps as for ξ_1, we get

$$|\xi_5| = \frac{B_{11}|X_5| - |B_{15}||X_1|}{2\omega\left(B_{11}B_{55} - B_{15}^2\right)} \tag{2.2.127}$$

To find ϕ_5, we see that

$$cos\phi_5 = \frac{B_{11}|X_5|cos\psi_5 - B_{15}|X_1|cos\psi_1}{|N_5|} \tag{2.2.128}$$

and/or

$$sin\phi_5 = \frac{B_{11}|X_5|sin\psi_5 - B_{15}|X_1|sin\psi_1}{|N_5|} \tag{2.2.129}$$

Now that we have expressions for $|\xi_1|, |\xi_5|, \phi_1$ and ϕ_5, we can input these into the expression for maximal power for a multi-degree-of-freedom WEC, given by equation 2.2.108. For surge-pitch motion only, the simplified expression is:

$$P_{1+5}^{max} = \frac{\omega^2}{2}\begin{bmatrix}\xi_1^* & \xi_5^*\end{bmatrix}\begin{bmatrix}B_{11} & B_{15}\\ B_{15} & B_{55}\end{bmatrix}\begin{bmatrix}\xi_1\\ \xi_5\end{bmatrix} \tag{2.2.130}$$

$$= \frac{1}{2}\omega^2\left[B_{11}|\xi_1|^2 + B_{55}|\xi_5|^2 + 2B_{15}|\xi_1||\xi_5|cos\left(\phi_1 - \phi_5\right)\right] \tag{2.2.131}$$

We use equations 2.2.123, 2.2.124, 2.2.128 and 2.2.129 to find an expression for $cos(\phi_1 - \phi_5)$:

$$cos(\phi_1 - \phi_5) = cos\phi_1 cos\phi_5 + sin\phi_1 sin\phi_5 \tag{2.2.132}$$

$$= \frac{-B_{11}B_{15}|X_5|^2 - B_{15}B_{55}|X_1|^2 + \left(B_{11}B_{55}|X_1||X_5| + B_{15}^2|X_1||X_5|\right)cos(\psi_1 - \psi_5)}{B_{11}B_{55}|X_1||X_5| - B_{11}|B_{15}||X_5|^2 - |B_{15}|B_{55}|X_1|^2 + |B_{15}|^2|X_1||X_5|} \tag{2.2.133}$$

When $\psi_1 - \psi_5 = 2\pi n, cos(\psi_1 - \psi_5) = 1$ and $B_{15} > 0$ (so $|B_{15}| = B_{15}$), and therefore $cos(\phi_1 - \phi_5) = 1$. When $\psi_1 - \psi_5 = 2\pi n + \pi, cos(\psi_1 - \psi_5) = -1$ and $B_{15} < 0$ (so $-|B_{15}| = B_{15}$), and therefore $cos(\phi_1 - \phi_5) = -1$. Therefore, the expression for the maximum extractable power for a WEC moving and extracting power in surge and pitch is

$$P_{1+5}^{max} = \frac{\omega^2}{2}\left(B_{11}|\xi_1|^2 + B_{55}|\xi_5|^2 + 2|B_{15}||\xi_1||\xi_5|\right) \tag{2.2.134}$$

We will show in section 2.2.6, using far field analysis, that this corresponds to a capture width of

$$kW_{1+5}^{max} = 2 \tag{2.2.135}$$

Equations 2.2.98 and 2.2.135 show the maximum capture widths for the heave and surge-pitch problems, respectively. These results, which were originally derived by Mei (1976), Newman (1976), Evans (1975) and Budal and Falnes (1975), show that *maximum power does not depend on geometric size or shape.*

2.2.5 Matching equation of motion with optimal motion

Heave

For a heaving-only WEC to achieve maximum power the body must be in resonance (equation 2.2.90) and the PTO coefficient must be equal to the radiation damping coefficient (equation 2.2.92). Therefore, for our first problem, shown in figure 2-1, ensuring these two requirements results in maximum power extracted.

Heave-surge-pitch

Since heave motion is uncoupled from surge-pitch motion, for our second problem, shown in figure 2-2, we must again ensure that the power is maximum in heave, as described in section 2.2.4, but then we must separately determine the requirements to achieve maximum power in surge-pitch.

To determine how to extract the maximum power in surge-pitch, we must compare the analysis done to find the equation of motion in section 2.2.2 with the expressions for the theoretical maximum extractable power in section 2.2.4. Consider the equation of motion in equation 2.2.58 and the expression for the optimal body motion in equation

2.2.109. To match these expressions, we must enforce the following three equations, which we will call the surge-pitch resonance equations:

$$k_1 - \omega^2 (m + A_{11}) = 0 \tag{2.2.136}$$

$$A_{15} - m z_G = 0 \tag{2.2.137}$$

$$C_{55} - \omega^2 (I_{55} + A_{55}) = 0 \tag{2.2.138}$$

Further, the PTO coefficients must be equal to the corresponding resonance damping coefficients:

$$\beta_1 = B_{11} \tag{2.2.139}$$

$$\beta_5 = B_{55} \tag{2.2.140}$$

$$\beta_{15} = B_{15} \tag{2.2.141}$$

Putting these 6 equations into equation 2.2.58 results in equation 2.2.109, the optimal body motion in surge-pitch. Therefore, ensuring these 6 requirements results in maximum power extracted in surge-pitch. Additionally, ensuring equations 2.2.90 and 2.2.92 results in maximum power extracted in heave-surge-pitch.

2.2.6 Far-field analysis

Newman (1976 and 1979) and Mei (Mei et al., 2005) have shown that coupled surge-pitch motion for an axisymmetric body can result in a maximum nondimensional capture width of $kW_{1+5}^{max} = 2$. As shown in section 2.2.4, the maximum capture width for heave is $kW_3^{max} = 1$. Since heave motion is uncoupled from surge-pitch for our axisymmetric body, the total maximum capture width is $kW_T^{max} = 3$. The derivation of maximum surge-pitch capture, using far-field analysis, is summarized here. Also, we look at the capture width from the surge mode, the pitch mode, and the surge-pitch mode.

The maximum extractable power for a multi-degree-of-freedom WEC is given by equation 2.2.108. Putting the expression for optimal motion, equation 2.2.106, into this equation, we get an alternative equation for maximal power:

$$P^{max} = \frac{1}{8}\overline{X}^{*T}[B]^{-1}\overline{X} \tag{2.2.142}$$

For surge-pitch motion, the expression simplifies to

$$P_{1+5}^{max} = \frac{B_{55}|X_1|^2 - B_{15}X_1X_5^* - B_{15}X_1^*X_5 + B_{11}|X_5|^2}{2\left(B_{11}B_{55} - B_{15}^2\right)} \tag{2.2.143}$$

We will use this equation to derive the maximum capture width. If $\mathcal{A}_j(\theta)$ is the angular variation of the forced wave in mode j, we can use expressions that relate the exciting force and radiation damping coefficients to the far-field expressions (derived in Mei et al., 2005):

$$X_i = -\frac{4}{k}\rho g A V_g \mathcal{A}_i\left(\theta_I + \pi\right) \tag{2.2.144}$$

$$B_{ij} = \frac{2}{\pi k}\rho g C_g \int_0^{2\pi} \mathcal{A}_i\left(\theta\right)\mathcal{A}_j^*\left(\theta\right) d\theta \tag{2.2.145}$$

where θ_I is the incident wave angle. Since our body is axisymmetric,

$$\mathcal{A}_1\left(\pi\right) = -\mathcal{A}_1\left(0\right) \equiv -\mathcal{A}_1 \tag{2.2.146}$$

$$\mathcal{A}_5\left(\pi\right) = -\mathcal{A}_5\left(0\right) \equiv -\mathcal{A}_5 \tag{2.2.147}$$

$$\mathcal{A}_1\left(\theta\right) = \mathcal{A}cos\theta \tag{2.2.148}$$

Putting equations 2.2.146, 2.2.147, and 2.2.148 into equations 2.2.144 and 2.2.145, and assuming $\theta_I = 0$, we get the following expressions for surge exciting force and damping coefficient, pitch exciting force and damping coefficient, and surge-pitch damping coefficient:

$$X_1 = \frac{4}{k}\rho g A C_g \mathcal{A}_1 \tag{2.2.149}$$

$$X_5 = \frac{4}{k}\rho g A C_g \mathcal{A}_5 \tag{2.2.150}$$

$$B_{11} = \frac{2}{\pi k}\rho g V_g \int_0^{2\pi} |\mathcal{A}_1|^2 cos\theta d\theta = \frac{2}{\pi k}\rho g V_g \pi |\mathcal{A}_1|^2 = \frac{2}{k}\rho g V_g |\mathcal{A}_1|^2 \tag{2.2.151}$$

$$B_{55} = \frac{2}{k}\rho g V_g |\mathcal{A}_5|^2 \tag{2.2.152}$$

$$B_{15} = \frac{2}{k}\rho g V_g \mathcal{A}_1 \mathcal{A}_5^* \tag{2.2.153}$$

Putting equations 2.2.149-2.2.149 into 2.2.143, we get

$$P_{1+5}^{max} = \frac{\left(\frac{2}{k}\rho g V_g\right)\left(\frac{4}{k}\rho g A V_g\right)^2 \left[|\mathcal{A}_5|^2|\mathcal{A}_1|^2 - \mathcal{A}_1\mathcal{A}_5^*\mathcal{A}_1\mathcal{A}_5^* - \mathcal{A}_1\mathcal{A}_5^*\mathcal{A}_1^*\mathcal{A}_5 + |\mathcal{A}_1|^2|\mathcal{A}_5|^2\right]}{8\left(\frac{2}{k}\rho g V_g\right)^2 \left[|\mathcal{A}_5|^2|\mathcal{A}_1|^2 - \mathcal{A}_1^2\mathcal{A}_5^{*2}\right]} \tag{2.2.154}$$

Therefore, the maximum extractable surge-pitch power is

$$P_{1+5}^{max} = \frac{1}{k}\rho g V_g A^2 \tag{2.2.155}$$

As shown in equation 2.2.97, the energy flux from an incoming unit-crest-length wave is

$$P_I = \frac{1}{2}\rho g A^2 V_g \tag{2.2.156}$$

So the maximum capture width for surge-pitch extraction is

$$kW_{1+5}^{max} = 2 \tag{2.2.157}$$

Surge-pitch damping coefficient

The coupled surge-pitch damping coefficient, in terms of far-field quantities, as shown in equation 2.2.153, is

$$B_{15} = \frac{2}{k}\rho g V_g \mathcal{A}_1 \mathcal{A}_5^* \tag{2.2.158}$$

Showing $\mathcal{A}_1$ and $\mathcal{A}_5$ in terms of complex amplitudes and phases ψ_1 and ψ_5:

$$B_{15} = \frac{2}{k}\rho g V_g |\mathcal{A}_1||\mathcal{A}_5| e^{\psi_1 - \psi_5} \tag{2.2.159}$$

We know that B_{15} must be real, so we see that the only options for $\psi_1 - \psi_5$ are $2\pi n$, in which case $B_{15} > 0$, or $2\pi n + \pi$, in which case $B_{15} < 0$. This is used in section 2.2.4 to find expressions for surge-pitch power.

Capture width from surge, pitch, and coupled, separated

We previously proved that $kW_{1+5} = 2$. In this section we will prove that

$$kW_1 = \frac{1}{2} \tag{2.2.160}$$

$$kW_5 = \frac{1}{2} \tag{2.2.161}$$

$$kW_{15} = 1 \tag{2.2.162}$$

where

$$kW_1 = k\frac{P_1}{P_I} \tag{2.2.163}$$

$$kW_5 = k\frac{P_5}{P_I} \tag{2.2.164}$$

$$kW_{15} = k\frac{P_{15}}{P_I} \tag{2.2.165}$$

Here, P_1 is the extracable power from the surge PTO, P_5 is extracable power from pitch PTO, and P_{15} is the extractable power from the coupled surge-pitch PTO. From equation 2.2.134, we separate P_{1+5}^{max} into three parts:

$$P_1 = \frac{\omega^2}{2} B_{11} |\xi_1|^2 \tag{2.2.166}$$

$$P_5 = \frac{\omega^2}{2} B_{55} |\xi_5|^2 \tag{2.2.167}$$

$$P_{15} = \omega |B_{15}||\xi_1||\xi_5| \tag{2.2.168}$$

To prove equations 2.2.160-2.2.162, it is sufficient to show the following:

$$P_1 + P_5 = P_{15} \tag{2.2.169}$$

and

$$P_1 = P_5 \tag{2.2.170}$$

Putting equations 2.2.122 and 2.2.127 for $|\xi_1|$ and $|\xi_5|$ into these three equations, we see that P_1, P_5 and P_{15} all have the same denominator, $(B_{11}B_{55} - B_{15}^2)^2$, which we will set equal to R, so we can further simplify the objectives. If we set

$$P_1 = \frac{M_1}{R} \tag{2.2.171}$$

$$P_5 = \frac{M_5}{R} \tag{2.2.172}$$

$$P_{15} = \frac{M_{15}}{R} \tag{2.2.173}$$

We must prove that

$$M_1 + M_5 = M_{15} \tag{2.2.174}$$

$$M_1 = M_5 \tag{2.2.175}$$

We again use the far-field relations for X's and B's: equations 2.2.149- 2.2.153. Putting these far-field relations, as well as equation 2.2.122 for $|\xi_1|$, into equation 2.2.166 for P_1, and looking at the numerator, we get

$$M_1 = B_{11}B_{55}^2 |X_1|^2 - 2B_{11}B_{15}B_{55} |X_1| |X_5| + B_{11}B_{15}^2 |X_5|^2 \tag{2.2.176}$$

$$= \left(\frac{2}{k}\rho g V_g\right)^3 \left(\frac{4}{k}\rho g V_g A\right)^2 \left[|\mathcal{A}_1|^2 |\mathcal{A}_5|^4 |\mathcal{A}_1|^2 - 2|\mathcal{A}_1|^2 \mathcal{A}_1\mathcal{A}_5^* |\mathcal{A}_5|^2 |\mathcal{A}_1| |\mathcal{A}_5| + |\mathcal{A}_1|^2 (\mathcal{A}_1\mathcal{A}_5^*)^2 |\mathcal{A}_5|^2\right] \quad (2.2.177)$$

Similarly, putting the far-field relations 2.2.149-2.2.153, as well as equation 2.2.127 for $|\xi_1|$ into equation 2.2.167 for P_5, and looking at the numerator, we get

$$M_5 = B_{11}^2 B_{55} |X_5|^2 - 2B_{11}B_{15}B_{55} |X_1| |X_5| + B_{15}^2 B_{55} |X_1|^2 \quad (2.2.178)$$

$$= \left(\frac{2}{k}\rho g V_g\right)^3 \left(\frac{4}{k}\rho g V_g A\right)^2 \left[|\mathcal{A}_1|^4 |\mathcal{A}_5|^2 |\mathcal{A}_5|^2 - 2|\mathcal{A}_1|^2 \mathcal{A}_1\mathcal{A}_5^* |\mathcal{A}_5|^2 |\mathcal{A}_1| |\mathcal{A}_5| + (\mathcal{A}_1\mathcal{A}_5^*)^2 |\mathcal{A}_1|^2 |\mathcal{A}_5|^2\right] \quad (2.2.179)$$

Looking at equations 2.2.177 and 2.2.179, we can see that $M_1 = M_5$. This proves 2.2.175.

Finally, after putting far-field relations 2.2.149-2.2.153, as well as both equation 2.2.122 and 2.2.127 in to equation 2.2.168 for P_{15} and looking at the numerator, we get

$$M_{15} = 2B_{11}B_{15}B_{55} |X_1| |X_5| - 2B_{15}^2 B_{55} |X_1|^2 - 2B_{11}B_{15}^2 |X_5|^2 + 2B_{15}^3 |X_1| |X_5| \quad (2.2.180)$$

$$= \left(\frac{2}{k}\rho g V_g\right)^3 \left(\frac{4}{k}\rho g V_g A\right)^2 \left[2|\mathcal{A}_1|^3 |\mathcal{A}_5|^3 \mathcal{A}_1\mathcal{A}_5^* - 4|\mathcal{A}_5|^2 |\mathcal{A}_1|^2 (\mathcal{A}_1\mathcal{A}_5^*)^2 + 2|\mathcal{A}_1| |\mathcal{A}_5| (\mathcal{A}_1\mathcal{A}_5^*)^3\right] \quad (2.2.181)$$

Comparing 2.2.181 to 2.2.177 and 2.2.179, we see that

$$M_{15} = \frac{\mathcal{A}_1\mathcal{A}_5^*}{|\mathcal{A}_1| |\mathcal{A}_5|} (M_1 + M_5) = M_1 + M_5 \quad (2.2.182)$$

This proves 2.2.174. We have included this proof because we have not seen it in literature before, and it adds to our understanding of how much energy is extracted

from the surge PTO, the pitch PTO, and the surge-pitch PTO. Note that this does not mean that they can operate separately: each mode must be extracting the specified amount of power for the entire system to work correctly.

2.3 Summary

In this chapter, we derived and explained the relevant hydrodynamic theory for our problem. We started by defining the assumptions made, which are summarized as follows:

- Linear potential flow
- Single monochromatic unit-amplitude incoming wave
- Three-dimensional axisymmetric body
- Two separate problems:
    1. Body only moving and extracting energy in heave
    2. Body moving and extracting energy in surge, heave and pitch
- PTO mechanisms modeled as linear dampers
- Mooring force modeled as a spring force in surge

To derive the equation of motion for the body, we initially derived the general six degree of freedom equation of motion for a freely floating body in a monochromatic wave. Adding in the forces specific to wave energy extraction, including PTO forces and the spring force in surge, and limiting to the three modes of motion of interest, we arrived at the equations of motion for both of the separate (heave only vs. heave-surge-pitch) problems, noticing that heave is uncoupled from surge-pitch.

Next, we derived equations for extractable power for both problems and then maximum power. We emphasized that the way to achieve maximum power in for the

heave-only problem is to ensure the body solves the heave resonance equation (equation 2.2.90) and set the heave PTO damping coefficient equal to the heave radiation damping coefficient at resonance. We showed that this results in a maximum capture width (extractable power over incident power per unit crest length, nondimensionalized by wavenumber k) of $kW_3^{max} = 1$. To achieve maximum power in heave-surge-pitch, it is necessary to again ensure the same conditions as for heave, but additionally all three surge-pitch resonance equations (equations 2.2.136, 2.2.137 and 2.2.138) must be satisfied, and finally each surge, pitch and surge-pitch PTO coefficient must be equal to the corresponding radiation damping coefficient. We showed

Finally, we looked at far-field analysis to show that the maximum capture width for the heave-surge-pitch problem is $kW_{1+5}^{max} = 2$. With all eight (heave and surge-pitch) conditions satisfied, the maximum capture width of $kW_T^{max} = 3$ is achieved. We emphasized that the maximum capture width for heave and surge-pitch do not depend on geometric shape or size.

We also showed that the capture width from the surge PTO is $kW_1 = 0.5$, the capture width from the pitch PTO is $kW_5 = 0.5$ and the capture width from the surge-pitch PTO is $kW_{15} = 1$, when the body moves in both surge and pitch. To the best of our knowledge, this derivation is novel, and it adds to our understanding of the problem.

Chapter 3

Optimization Framework

In the previous chapter, the equations of motion for our problems were derived, and limits for maximum extractable power, along with necessary conditions to achieve those limits, were discussed. In this chapter, the goals and framework of our optimization are motivated and explained.

In the first section, main considerations that must be examined when optimizing a wave energy converter are broadly discussed. Then, these concepts are expanded upon and explained more in the second section, with specific equations, diagrams and symbols. In the third section, other frameworks considered are discussed to further motivate the validity of the chosen framework. Finally, the framework and contributions from this framework are summarized in the final section.

3.1 Main concepts involved for optimizing a WEC

In this section, we discuss broadly what it means to optimize a WEC, and our general optimization question is stated.

As motivated in the introduction, when looking to optimize a wave energy converter, the main objectives are to maximize power and minimize cost. For the latter, this not only refers to minimizing material used, but also ensuring that shapes are practically feasible.

Heave-only extraction:

As shown in the previous chapter, for a WEC moving and extracting power in the heave mode only, the way to achieve maximum extractable power is to force the body to be in resonance and set the power take-off (PTO) damping coefficient equal to the radiation damping coefficient at resonance. This idea of how to achieve resonance, then, becomes very important. We are assuming that an incoming wave frequency is given, so the geometric shape becomes the changing parameter in the resonance equation. However, requiring the body to be in resonance introduces the need for a motion constraint since resonance also corresponds to the largest motion amplitude. This motion constraint is required to ensure that shapes are practically feasible.

Heave-surge-pitch extraction:

To achieve optimal motion, and thus maximum extractable power, a WEC moving and extracting power in heave, surge, and pitch must solve four resonance equations, if active controls, such as latching, are not used. One of these resonance equations is the heave resonance equation, already discussed. However, the other 3 resonance equations, referred to as the surge, pitch, and surge-pitch resonance equations, all contain passively controllable terms. These design parameters do not depend on geometric shapes, so they can be changed after the geometry is chosen. In surge, it is the mooring forces modeled as a linear spring, in surge-pitch, it is the center of gravity, and in pitch, it is the weight distribution through the pitch moment of inertia. Since the heave resonance equation does not have any passively controllable parameters, the heave resonance equation must be solved first to get the geometric shape. Then, the passively controllable parameters can be changed to ensure the other three resonance equations are met. These controllable parameters introduce more constraints. Namely, the center of gravity cannot be outside of the body, the body must be in stable equilibrium, and the radius of gyration must be contained within the body. Furthermore, the same motion constraints as in the heave-only case must be applied to the surge and pitch motion.

Minimizing cost:

As discussed in the introduction chapter, a large concern in realizing wave energy as a viable renewable energy resource is cost. The constraints to the motion and the controllable parameters are important to minimizing cost and making sure the bodies are practically feasible, but additionally we need to minimize the amount of material used. A multi-objective optimization allows us to simultaneously minimize surface area and volume, and the result is a set of optimal solutions that developers could choose from depending on further constraints or budget.

Optimization question: What practically feasible shapes maximize power while minimizing cost?

With this motivation for the optimization statement, we will now discuss the specifics of how to achieve these goals.

3.2 Optimization framework

3.2.1 Multi-objective optimizations and Pareto Fronts

In this section, multi-objective optimization algorithms are explained, and the population and the Pareto Front are defined. Given the constraints of the problem, the set of all possible solutions is known as the **population**. A multi-objective optimization has two or more competing optimization functions. For our optimization problem, we have two optimization functions, so we will limit the explanation to two. For more information on multi-objective optimization problems, see Deb (2011) or Deb et al. (2005).

If the two objective functions are called f_1 and f_2, where the objective is to minimize both f_1 and f_2, and two solutions ('organisms') within the population are $\overline{x_1}$ and $\overline{x_2}$, it is said that organism $\overline{x_1}$ **dominates** $\overline{x_2}$ if

1. $f_i(\overline{x_1}) \leq f_i(\overline{x_2})$ for $i = 1, 2$

2. $f_1(\overline{x_1}) < f_1(\overline{x_2})$ and/or $f_2(\overline{x_1}) < f_2(\overline{x_2})$

The set of *non*-dominated solutions is called the **Pareto Front**, which is the set of optimal solutions for the problem. To visualize the population and and what it means for one point to dominate another, consider figure 3-1. The x-axis is the first objective function, f_1, and the y-axis is the second objective function, f_2. The entire population can be plotted as points on this plot. Consider points $\overline{x_1}$ and $\overline{x_2}$. Point $\overline{x_1}$ dominates point $\overline{x_2}$ since it is not 'worse' in either objective function ($f_1(\overline{x_1}) = f_1(\overline{x_2})$) and is strictly better in one objective function ($f_2(\overline{x_1}) < f_2(\overline{x_2})$). The set of non-dominated solutions are the set of solutions along the 'bottom left' curve, shown in blue in figure 3-2.

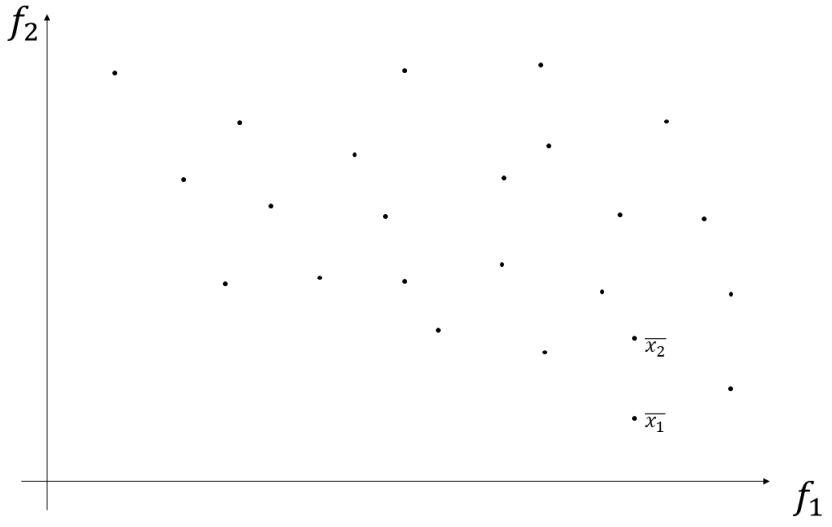

Figure 3-1: Example of plotting a **population**. f_1 and f_2 are the two objective functions, where the objectives are both minimization.

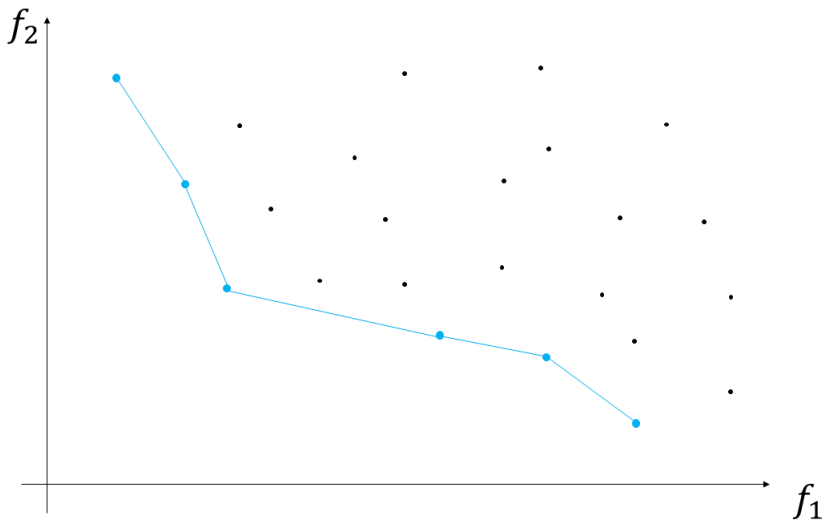

Figure 3-2: The **Pareto Front** of the population shown in figure 3-1, shown in blue.

Multi-objective optimizations are used in this thesis to optimize two objective functions simultaneously, resulting in a *set* of optimal solutions. Next, we will describe how the populations are formed for our problem. Later, objective functions which determine the Pareto Front will be defined.

3.2.2 Constraints in our problem

In this section, the formation of the population is described, using constraints governing the problem. We wish to optimize a body given *any* incoming wave, so we will assume wavenumber k is given and nondimensionalize size parameters to k.

Heave resonance

As shown in the previous chapter, to achieve maximum power in heave, the body must move with optimal motion, which is done by satisfying the heave resonance equation:

$$C_{33} - \omega^2 (m + A_{33}) = 0 \tag{3.2.1}$$

where C_{33} is the buoyancy restoring force, m is mass, and A_{33} is added mass. Since

frequency is given, the parameter in this equation now becomes the geometric shape. We will discuss in chapter 4 how to solve this equation. The set of shapes that solve this equation will be defined as $\mathbb{R}_3$.

Since wave frequency is given, the independent parameter of the heave resonance equation is now geometric shape. Therefore, this is a nonlinear equation, due to the nonlinearity of the heave added mass coefficient on geometry.

Heave motion constraint

In many engineering contexts the goal of looking at resonance equations is to avoid resonance, since this is when the amplitude of motion is maximum, but we have shown that resonance is a necessary condition to achieve maximum power. However, to avoid shapes where the body motion at resonance would be too large, we introduce a motion constraint. This constraint was motivated by Evans (1981). The constraint is given by

$$\frac{|\xi_3|}{A} \leq \alpha \tag{3.2.2}$$

where $|\xi_3|$ is the amplitude of heave body motion and A is incoming wave amplitude. α should be of order 1 so that the body does not move much more than amplitude of wave. In this thesis, we look at $\alpha = 1$ and $\alpha = 3$. As shown in section 4.3, the motion constraint disallows deep SPAR-like shapes who satisfy the heave resonance equation but whose body motion at resonance is unrealistically large. This motion constraint ensures that the body is practically feasible. Bodies moving too much will result in more fatigue and thus a shorter lifespan. Therefore, this constraint also helps minimize costs. Given α, the set of shapes that adhere to the heave motion constraint, and thus satisfy equation 3.2.2, is called $\mathbb{A}_3$.

Heave steepness constraint

Another practical consideration is to make sure that the body does not leave the

ocean surface. If H is the body's draft at the vertical centerline, the body motion in heave must be less than H: $H > |\xi_3|$. Multiplying each side by k and then dividing and multiplying by A on the right-hand-side, we get $kH > kA\frac{|\xi_3|}{A}$. kA is often used in hydrodynamics to specify steepness of the ocean, and is defined by $\epsilon \equiv kA$. Therefore the heave 'steepness constraint' is given by

$$kH > \epsilon\frac{|\xi_3|}{A} \tag{3.2.3}$$

Without this steepness constraint, very thin disk-like objects that satisfy both the resonance equation and the heave motion constraint would be allowed. However, in reality they would leave the ocean surface, creating problems such as slamming. For linear theory, we require $\epsilon << 1$, so we consider small but finite values of ϵ. In this thesis, we consider $\epsilon = 0.1$ and $\epsilon = 0.2$. Given ϵ, the set of shapes that adhere to the heave steepness constraint, and thus satisfy equation 3.2.3, is called $\mathbb{E}_3$.

Forming heave population and Pareto Front

If we define the set of all possible shapes to be $\mathbb{B}$, then the sets $\mathbb{R}_3, \mathbb{A}_3$ and $\mathbb{E}_3$ are all subsets of $\mathbb{B}$. This is shown in figure 3-3, where $\mathbb{R}_3$ is shown in light green, $\mathbb{E}_3$ in light purple and $\mathbb{A}_3$ in light teal. Shown with horizontal lines, the intersection of these sets is $\mathbb{P}_3$, the **heave population**, since this is the set of all shapes that adhere to the constraints of the problem. The **heave Pareto Front**, $\mathbb{PF}_3$, shown as a dark blue circle in figure 3-3, is a subset of $\mathbb{P}_3$.

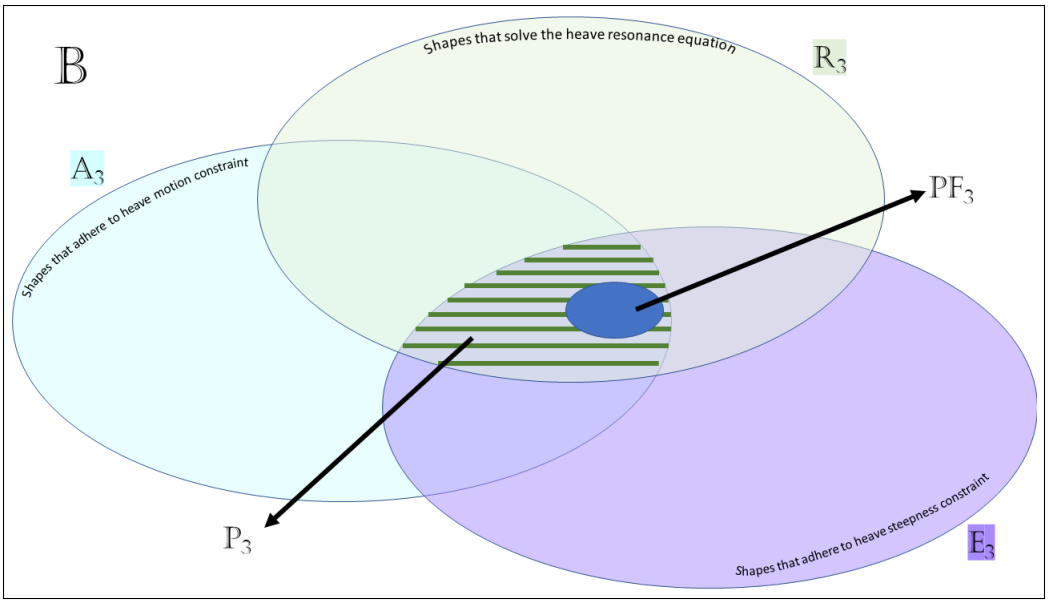

Figure 3-3: Formation of the population for the heave-only problem, given α and ϵ

For different values of α and ϵ the population, and resulting Pareto Front, will be different. Stricter motion constraints (smaller values of α) and/or stricter steepness constraints (larger values of ϵ) will result in smaller sets $\mathbb{A}_3$ and $\mathbb{E}_3$, respectively, resulting in a smaller $\mathbb{P}_3$ set and a smaller $\mathbb{PF}_3$. This is shown in figure 3-4. $\mathbb{R}_3$ will not change. The darker purple represents the set which adheres to a stricter steepness constraint, and darker teal represents the set which adheres to a stricter motion constraint. The new population, represented with red horizontal lines, is a subset of the old population (green horizontal lines). The new Pareto Front, represented by yellow vertical lines, is the intersection of the new population and the old Pareto Front.

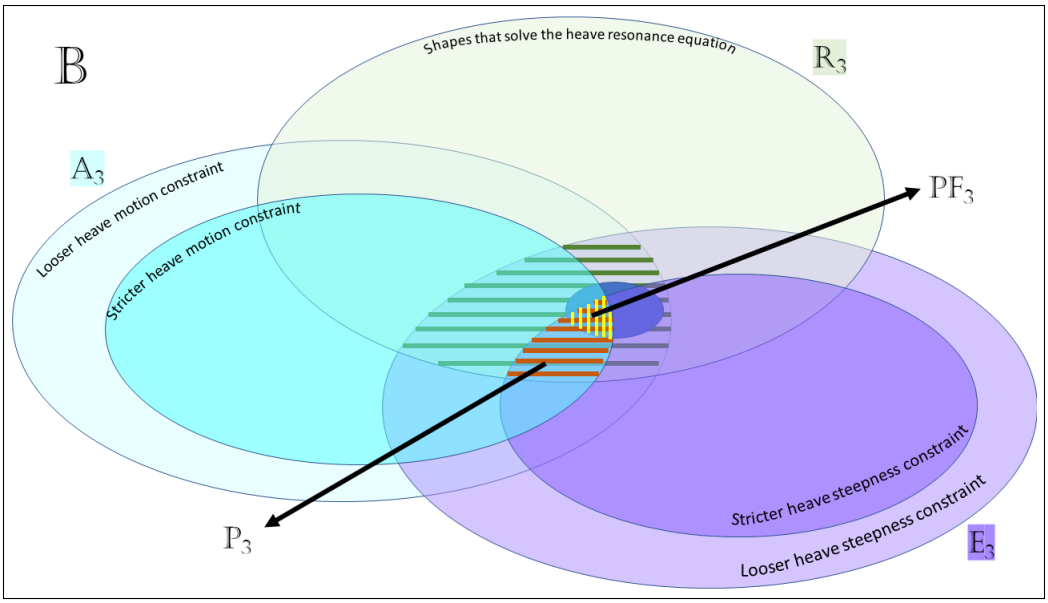

Figure 3-4: How stricter motion and steepness constraints affect the heave population and Pareto Front

Heave-surge-pitch resonance

To achieve maximum power for WECs moving and extracting power in heave, surge, and pitch, the body must move with optimal motion (equation 2.2.106). To achieve this optimal motion without active controls, the body must solve four resonance equations. One of these is the heave resonance equation (3.2.1). The other three will be called the surge resonance equation, the surge-pitch resonance equation, and the pitch resonance equation.

$$k_1 - \omega^2 (m + A_{11}) = 0 \tag{3.2.4}$$

$$A_{15} - m z_G = 0 \tag{3.2.5}$$

$$C_{55} - \omega^2 (I_{55} + A_{55}) = 0 \tag{3.2.6}$$

Here, k_1 is the surge spring coefficient, representing mooring forces, A_{11} is surge added mass, A_{15} is coupled surge-pitch added mass, z_G is the center of gravity, C_{55} is the

pitch buoyancy restoring coefficient, I_{55} is the pitch moment of inertia, and A_{55} is pitch added mass.

Unlike the heave resonance equation, there are now 'controllable' parameters in each of these three equations. That is, there are parameters that do not depend on the shape (or frequency). In equation 3.2.4, k_1 is controllable, in equation 3.2.5, z_G is controllable, and in equation 3.2.6, I_{55} is controllable. For a freely floating WEC, the k_1 term is not needed. However, not only is the inclusion of the k_1 practically correct, since it means that there is a term for mooring force, but also we can see from equation 3.2.4 that it is necessary to be able to solve the resonance equation and ensure that optimal motion, and thus maximal power, is being realized. No other resonance equation has any added terms.

With the addition of these controllable parameters, we no longer need to solve for shape. Given a shape and frequency, we can control these parameters to solve all three resonance equations. From equation 3.2.4, we can solve for k_1 to get the value that would ensure the body was in resonance in surge:

$$k_1^r = \omega^2 \left(m + A_{11}\right) \tag{3.2.7}$$

Given a shape and frequency, the right-hand-side will be fully known. We can solve 3.2.5 for z_G to determine the value of the center of gravity that would ensure the surge-pitch resonance equation was solved:

$$z_G^r = \frac{A_{15}}{m} \tag{3.2.8}$$

where, again, given a shape and frequency the right-hand-side is fully known. Finally, equation 3.2.6 can be solved for I_{55} to determine the value of the pitch moment of inertia to ensure that the pitch resonance equation was solved:

$$I_{55}^r = \frac{C_{55}}{\omega^2} - A_{55} \tag{3.2.9}$$

Here, C_{55} is

$$C_{55}^r = \rho g \pi R^4/4 + \rho g l_V^3 \left(z_B - z_G\right) \tag{3.2.10}$$

Putting equation 3.2.8 for z_G, this becomes

$$C_{55} = \rho g \pi R^4/4 + \rho g l_V^3 z_B - g A_{15} \tag{3.2.11}$$

And after putting this expression for C_{55} into equation 3.2.9, the expression for I_{55}^r becomes

$$I_{55}^r = \frac{\rho g \pi R^4/4 + \rho g l_V^3 z_B - g A_{15}}{\omega^2} - A_{55} \tag{3.2.12}$$

This section explained how to achieve resonance in surge, pitch and surge-pitch, given a frequency and shape.

Stability and center of gravity constraint

Center of gravity is a controllable parameter, but we must introduce constraints to what z_G can be. Firstly, the center of gravity cannot be below the draft at the centerline, H. And secondly, there is a maximum value of z_G, called z_G^{max}, above which the body will no longer be in stable equilibrium.

Stability analysis is explained more in Appendix A. For more information, see Principles of Naval Architecture (1988). A body is in stable equilibrium if

1. The center of mass and center of buoyancy are on the same vertical line
2. If an external moment acts on the body, the body returns to its original position once the moment is removed.

The first is automatically true in our problem since the body is assumed to be axisymmetric. For second requirement to be true, point z_M, the transverse metacenter, must be higher than z_G, vertical center of gravity. As explained in Appendix A, this results in the following expression for z_G^{max}:

$$z_G^{max} = \frac{8R^4}{9\forall} + z_B \tag{3.2.13}$$

The set of shapes such that $-H < z_G^r < z_G^{max}$ is called $\mathbb{Z}_{15}$.

Pitch moment of inertia constraint

Similarly, even though I_{55} is a controllable parameter, we must introduce constraints on the values of I_{55}. Looking at equation 3.2.9, we can deduce that for some shapes (with larger A_{55} or A_{15} values), the expression for I_{55}^r would be negative. This, of course, is not physically possible, so we must enforce the following constraint:

$$\frac{\rho g \pi R^4/4 + \rho g l_V^3 z_B - g A_{15}}{\omega^2} - A_{55} > 0 \tag{3.2.14}$$

Furthermore, we also need to make sure radius of gyration is not so big that it would not be possible to distribute the weight within the body. To simplify, we can assume weight to be located at z_G. If $z_G < 0$, the radius of gyration, $r_g^r = \frac{I_{55}^r}{m}$, must not be greater than radius of the body at z_G, denoted $r(z_G)$. The set of shapes for which $0 < r_g^r < r(z_G)$ will be called $\mathbb{I}_{15}$.

Surge motion constraint

We must enforce a surge motion constraint, similar to the heave one:

$$\frac{|\xi_1|}{A} \leq \alpha \tag{3.2.15}$$

Again, we consider $\alpha = 1, 3$ in this thesis. Given α, the set of shapes that adhere to the surge motion constraint, and thus solve equation 3.2.15, is called $\mathbb{A}_1$.

Pitch motion constraint

Similarly, we must enforce a pitch motion constraint:

$$\frac{|\xi_5|}{A/R} \leq \alpha \tag{3.2.16}$$

Where, again, we consider $\alpha = 1, 3$. Given α, the set of shapes that adhere to the pitch motion constraint, and thus solve equation 3.2.16, is called $\mathbb{A}_5$.

Pitch steepness constraint

There is again a risk of the body leaving the ocean surface for pitch motion, so we must enforce a pitch steepness constraint similar to the one in heave:

$$kH > \epsilon \frac{|\xi_5|}{A/R} \tag{3.2.17}$$

We again consider $\epsilon = 0.1, 0.2$. Given ϵ, the set of shapes that adhere to the pitch steepness constraint, and thus solve equation 3.2.17, is called $\mathbb{E}_5$.

Forming the heave-surge-pitch population and Pareto Front

The set of all shapes that adhere to the five constraints for WECs moving and extracting energy in surge and pitch defined above will be called $\mathbb{P}_{15}$. The formation of this set is shown in figure 3-5. The set of all possible shapes, $\mathbb{B}$, is represented by the white rectangle. Given α, the sets of shapes that adhere to surge and pitch motion constraints, respectively, are $\mathbb{A}_1$ (represented in red) and $\mathbb{A}_5$ (yellow). Given ϵ, the set of shapes that adhere to the pitch steepness constraint is $\mathbb{E}_5$ (orange). And finally, the sets of shapes that adhere to the center of gravity constraint and the pitch motion of inertia constraint are, respectively, $\mathbb{Z}_{15}$ (pink) and $\mathbb{I}_{15}$ (green). The intersection of the five sets, $\mathbb{P}_{15}$, is shown with vertical blue lines.

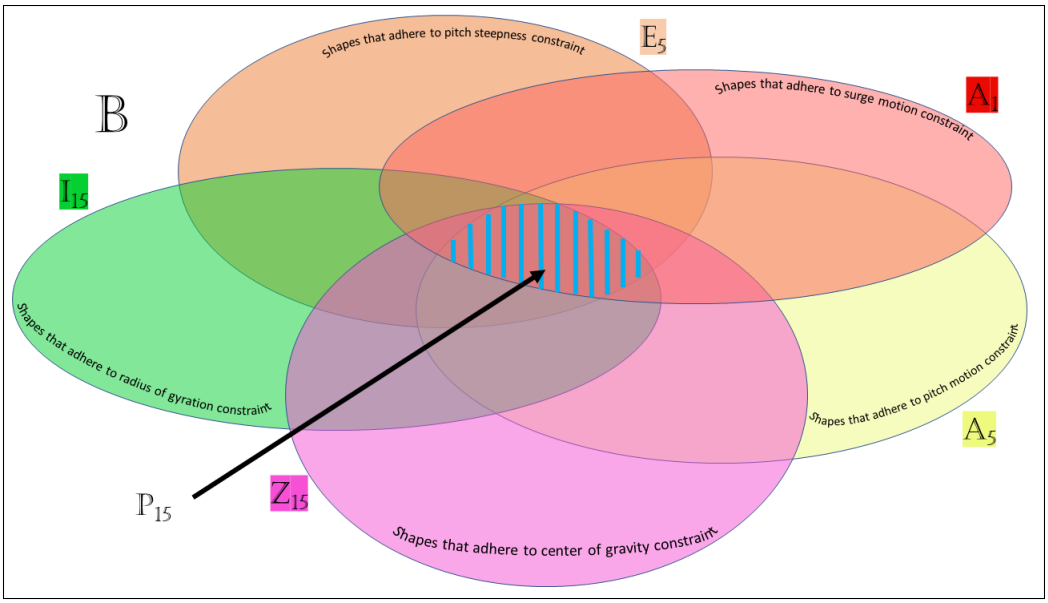

Figure 3-5: The formation of the set of shapes that adhere to the five constraints for WECs moving and extracting energy in surge and pitch, $\mathbb{P}_{15}$

The population for shapes moving and extracting energy in heave, surge, and pitch, which will be called the **heave-surge-pitch population**, $\mathbb{P}_{135}$, is the intersection of the heave population, $\mathbb{P}_3$ and the set of shapes that adhere to the five constraints for surge-pitch, $\mathbb{P}_{15}$. This is shown in figure 3-6. The heave population, $\mathbb{P}_3$ is shown by horizontal green lines, and the set of shapes adhering to all five surge-pitch constraints, $\mathbb{P}_{15}$ is shown by vertical blue lines. The intersection of these two sets, represented by the checkered area, is the heave-surge-pitch population. The **heave-surge-pitch Pareto Front**, $\mathbb{PF}_{135}$ is a subset of $\mathbb{P}_{135}$, shown by a purple circle.

Because of the controllable parameters, we no longer need to solve for a shape to enforce resonance in surge, pitch and surge-pitch. However, to enforce resonance in heave, we do need to solve for a shape. Therefore, to form the heave-surge-pitch population, $\mathbb{P}_{135}$, we must use the heave resonance equation to solve for shape, and then use the controllable parameters to enforce resonance in surge, pitch, and surge-pitch. Then, we can use the constraints (i.e. heave, surge and pitch motion constraints, heave and pitch steepness constraints, and the center of gravity and pitch motion of inertia constraints) to eliminate shapes that are not practical. This subtle idea of solving the heave resonance equation first is crucial to our set up.

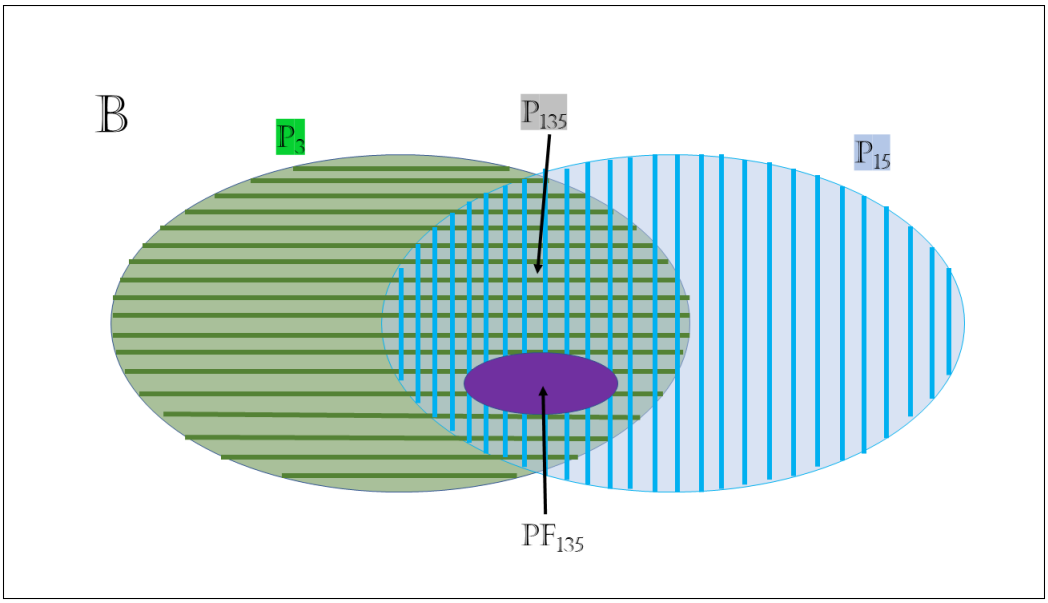

Figure 3-6: Finding $\mathbb{PF}_{135}$, the **heave-surge-pitch Pareto Front**: The intersection of the heave population, $\mathbb{P}_3$, and the set of shapes that adhere to the surge-pitch constraints, $\mathbb{P}_{15}$, is the **heave-surge-pitch population**. The heave-surge-pitch Pareto Front is a subset of the population

Similar to the heave-only case, $\mathscr{P}_{135}$ and PF_{15} depend on α and ϵ. The populations, and resulting Pareto Fronts, for smaller α (or larger ϵ) will be subsets of the corresponding sets for larger α (or smaller ϵ, respectively).

Summary

We discussed how to find shapes that produce maximum power in heave, by ensuring they are in resonance in heave. We defined the heave motion and steepness constraints to ensure that the body does not move much more than the incident wave amplitude, and that the body does not leave the ocean surface. We discussed how these three constraints (resonance, motion, and steepness) formed the population for the heave-only problem, of which the Pareto Front is a subset.

We saw that, unlike for heave, where *shape* was the parameter to solve for in the resonance equation, there exist 'controllable parameters' in the surge, pitch and surge-pitch resonance equations, which can be changed given any shape to enforce resonance, and hence maximum power, in these modes. We defined constraints involving

these controllable parameters (the center of gravity must be within the body, the body must be in stable equilibrium, and the radius of gyration must be within the body). We defined the surge motion constraint, pitch motion constraint, and pitch steepness constraint. We showed that, in order to form the heave-surge-pitch population and the resulting Pareto Front, we must solve for the shape using the heave resonance equation, change the controllable parameters to enforce resonance in surge, pitch and surge-pitch, and then use the constraints to make sure the body is practically feasible.

3.2.3 Optimization statement summary

Objective functions

In the previous section, we described how the heave population and heave-surge-pitch population are formed. The Pareto Front is the set of optimal solutions from that population. To define 'optimal,' we must define the two objective functions. As discussed in the introduction chapter, cost must be reduced to make wave energy a viable source of energy. The constraints listed in the previous chapter help minimize cost by reducing fatigue and ensuring feasibility. Another way to minimize cost is to minimize material used. Therefore, our two objective functions minimize surface area and volume. Because we want to optimize the WEC given any incoming wave, we nondimensionalize these two values by wavenumber k. To measure surface area, we use

$$kl_S = k\sqrt{S_W} \tag{3.2.18}$$

where S_W is wetted surface area. To measure volume, we use

$$kl_V = k\sqrt[3]{\forall} \tag{3.2.19}$$

where $\forall$ is volume of submerged body

Heave only

Our optimization problem for the problem of a heaving-only WEC is summarized in the following box:

Given k, ϵ, and α, minimize

1. kl_S
2. kl_V

such that each body is in resonance, $kH > \epsilon\frac{|\xi_3|}{A}$, and $\frac{|\xi_3|}{A} \leq \alpha$

Heave-surge-pitch

Our optimization problem for the problem of a WEC moving and extracting power in heave, surge and pitch is summarized in the following box:

Given k, ϵ, and α, minimize

1. kl_S
2. kl_V

such that for each body:

1. It is in resonance in heave, surge, pitch, and surge-pitch coupled. That is,
   (a) $C_{33} - \omega^2 (m + A_{33})$
   (b) $k_1 - \omega^2 (m + A_{11})$
   (c) $A_{15} - mz_G$
   (d) $C_{55} - \omega^2 (I_{22} + A_{55})$
2. $\frac{|\xi_3|}{A} \leq \alpha$
3. $kH > \epsilon \frac{|\xi_3|}{A}$
4. $\frac{|\xi_1|}{A} \leq \alpha$
5. $\frac{|\xi_5|}{A/R} \leq \alpha$
6. $-H < z_G < z_G^{max}$
7. If $z_G < 0, r_g < r(z_G)$
8. $kH > \epsilon \frac{|\xi_5|}{A/R}$

The result of each of these optimizations is a Pareto Front, which is a set of optimal shapes. The benefit of having a *set* of shapes is that someone interested in building a WEC can look at this set and decide what is most important to them. This refers to the two objective functions, surface area or volume, but also looking at other parameters, for example mooring forces, design options, and material stiffness. These factors are not the focus of this thesis, but some of the differences within sets will be

discussed in the results section.

The optimization framework that has been developed is summarized in the two boxes above. This framework ensures that the resulting shapes will extract maximum power, while minimizing surface area and volume. Further, the constraints that were included in the framework limit the resulting shapes to be practically feasible.

3.3 Other frameworks considered

To motivate our optimization framework, we will discuss other options for frameworks that were considered before this framework was decided upon.

3.3.1 Maximizing power, minimizing volume or surface area

A first thought when the goal is to maximize power and minimize cost would be to maximize kW, the nondimensional capture width, and minimize either volume or surface area. However, with no constraint this forms an ill-posed multi-objective optimization. In a multi-objective optimization, all objective functions must be able to stand alone as a valid single-objective optimization. The objective of minimizing volume or surface area without any constraint would result in the absence of a body as the answer.

3.3.2 Given volume, maximize power and minimize surface area

Therefore, the next logical step is to enforce a constraint. We tried to look at multiple values of kl_V, and given that kl_V maximize kW and minimize kl_S/kl_V. Due to the nature of the resonance equation, for each kl_V, there would be many shapes which achieved the maximum value of $kW = 1$ (for heave). Looking across multiple values of kl_V, the best would be the shape which achieves $kW = 1$ and minimum kl_S/kl_V, which would be the resonating hemisphere. However, this answer is not very enlightening

since, though it minimizes the ratio of surface area to volume it minimizes neither surface are nor volume, so does not in fact minimize cost.

3.3.3 Minimizing motion and volume or surface area

Seeing all of the shapes able to achieve $kW = 1$, we decided to only look at shapes that maximize power (i.e. all resonating shapes). However, there becomes a problem of large amplitude of body motion. A first thought was to minimize surface area or volume alongside body amplitude. However, minimizing body motion amplitude versus just keeping it small does not really matter to the cost/ performance. So, we decided on the motion constraint described above instead.
These other frameworks that were considered give motivation for our optimization framework that has been discussed in this chapter.

3.4 Summary

In this chapter, our optimization framework was defined and described. In the first section, we discussed the overarching question of 'what make a good WEC' to guide us in defining an optimization goal: to find what practically feasible shapes maximize power while minimizing cost. Next, we introduced the main concepts of a multi-objective optimization algorithm, including the population and Pareto Front.

We then explained how the populations are formed in our problems (heave-only vs. heave-surge-pitch). For WECs moving in heave only, we solve the heave resonance equation (equation 3.2.1) with *shape* as the parameter to find shapes that resonance in heave, thus extracting maximum power. The heave motion constraint and heave steepness constraint must be enforced to ensure that the body does not move much more than the incoming wave amplitude and does not leave the ocean surface, with a small but finite steepness, respectively. Bodies that solve the heave resonance equation and adhere to the heave motion constraint and heave steepness constraint form the population.

To form the population for WECs moving and extracting energy in heave, surge and pitch, we *first* solve the heave resonance equation to find shapes that resonate in heave. Then, we use controllable parameters – surge mooring force modeled as a linear spring, center of gravity, and pitch moment of inertia – to ensure that the body is in resonance in surge, pitch and surge-pitch. The values of these parameters to enforce resonance are shown in equations 3.2.7, 3.2.8 and 3.2.9. Surge and pitch motion constraints, and a pitch steepness constraint, similar to in heave, must be used. In addition, there are constraints that arise from the controllable parameters: the center of gravity must be within the body, the body must be in stable equilibrium, and the radius of gyration must be within the body. Bodies that solve the heave resonance equation, adhere to the heave, surge and pitch motion constraints, the heave and pitch steepness constraints, and the constraints on the center of gravity and pitch moment of inertia, form the heave-surge pitch population.

For each population, the Pareto Front is the set of optimal solutions based on minimizing the two objective functions, defined in equations 3.2.18 and 3.2.19, measuring surface area and volume. The optimization statements for heave-only and for heave-surge-pitch are summarized in section 3.2.3. Finally, other frameworks considered were discussed to motivate our framework.

A novel idea described in this chapter is how to get maximum power from WECs moving and extracting power in heave, surge, and pitch without the use of external controls. The heave resonance equation is used to solve for shape, and then surge mooring force modeled as a linear spring, the center of gravity, and pitch moment of inertia are all used to force resonance in surge, pitch and surge-pitch.

The framework developed in this chapter for finding optimal shapes is theoretically rigorous, comprehensive and realistic. In the next chapter, we detail the methods used in the procedure of how to define possible geometries, get hydrodynamic quantities, and the multi-objective evolutionary algorithm. Also, we show how to find heave resonating shapes using a novel theorem for finding root of the heave resonance

equation.

Chapter 4

Approach to obtain constrained optimized shapes

In the last chapter, our original optimization framework was motivated and presented. In this chapter, the approach we developed to solve this optimization problem is detailed.

In the first section, we explain how we can define any general geometry, by representing it by polynomial basis functions. Using this description of geometry, we can put the coefficients of the basis functions into our optimization. In this way, we can vary geometry by just a few parameters. We also introduce a few terms we use in the rest of the thesis: a class of shapes and a group of shapes. A class of shapes is a set of shapes that have all other parameters other than waterline radius and volume given. A group of shapes is a set of multiple classes of shapes.

In the second section, we present a novel theorem for finding roots of the heave resonance equation and its corresponding proof. As detailed in the previous chapter, solving the heave resonance equation is an essential part of our optimization framework. This theorem allows us to semi-analytically solve the heave resonance equation. We show how this theorem adds to our understanding of optimal shapes for wave energy conversion, but also how this theorem significantly speeds up the optimization

process by reducing the order of the optimization by one. Without the theorem, there would be a computational burden on solving the heave resonance equation.

In the third section, we present general observations and conclusions for any given class of shapes. We use insights from our geometric description, our heave resonance theorem, observations made, and hydrodynamic insights to form general truths about the nature of the population and resulting Pareto Front for any given class of shapes. These insights are used in the subsequent chapters to given reasoning to why certain shapes lie on the Pareto Front.

In the fourth section, we outline our multi-objective evolutionary algorithm, and how it is used to optimize groups of shapes. We detail how our theorem is used in the algorithm, and how the evolutionary algorithm produces the final set of optimal solutions.

Finally, in the fifth section we summarize our robust, complete and efficient approach to finding optimal wave energy converters that minimize cost while maximizing power and ensuring feasibility.

4.1 Geometric description of shapes

In this section, we describe how we represent a large number of shapes by only changing a few parameters, so that we can optimize these shape parameters in our multi-objective optimization. We also introduce the ways we classify shapes into different sets in this thesis: classes and groups of shapes.

4.1.1 Chebyshev polynomial basis functions

Our goal in coming up with a way to describe geometry was to be able to describe the entire geometry using a function with changeable parameters, instead of using panel or node locations as the parameters in the optimize. Additionally, we want to be able to input the radius at the waterline, R, and the draft at the centerline, H, as

parameters.

One way to achieve this goal is to use polynomial basis functions, and to use the coefficients of such functions as the parameters to optimize. We use the Chebyshev polynomials of the first kind, which are defined using the following recursive relation:

$$T_0(x) = 1 \tag{4.1.1}$$

$$T_1(x) = x \tag{4.1.2}$$

$$T_{n+1}(x) = 2xT_n(x) - T_{n-1}(x) \tag{4.1.3}$$

The set of Chebyshev polynomials form an orthonormal basis, defined in $x \in [-1, 1]$, which can be expressed by the infinite sum

$$f(x) = \sum_{n=0}^{\infty} a_n T_n(x) \tag{4.1.4}$$

4.1.2 Parametric description of the body geometry

Since all the bodies considered in this thesis are axisymmetric, the geometry is completely defined in $r - z$ plane. For example, figure 4-1 shows an example of the 2D cross-section in the $r - z$ plane:

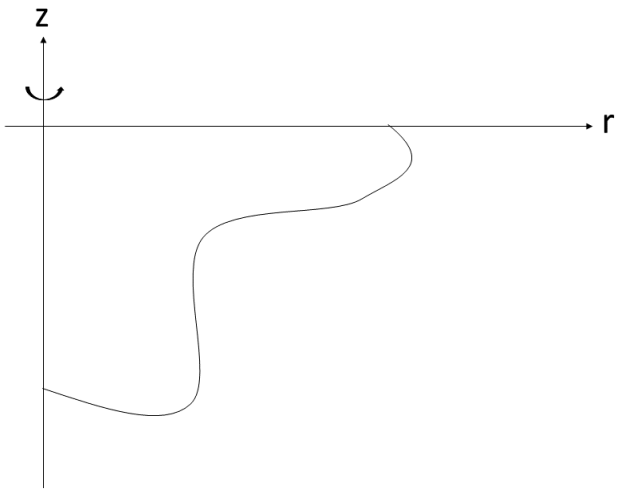

Figure 4-1: Example of the 2D cross-section, in the $r-z$ plane, of a 3D axisymmetric shape

To make geometries more general, we use a parametric description: r and z are described by separate series, with Chebyshev polynomials as basis functions for each separate function. And to further generalize the allowable shapes, we allow slope discontinuities ('kinks') in the body geometry. Each kink coordinates are described by the points $(r_1, z_1), (r_2, z_2)$, etc. For example, figure 4-2 shows a one-kink shape:

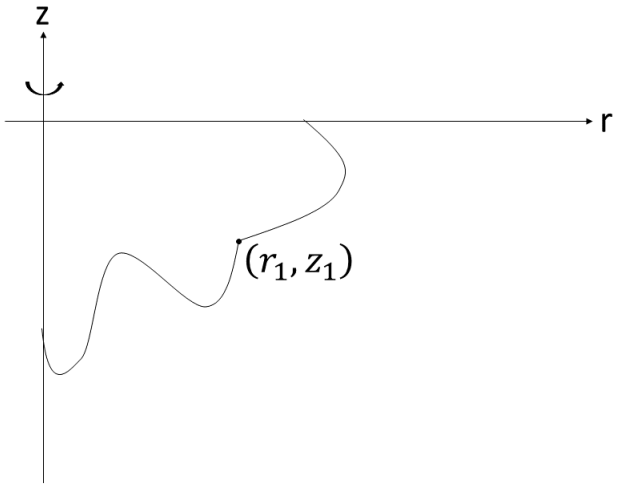

Figure 4-2: Example of a 'one-kink' shape (i.e. a shape with a slope discontinuity)

Each piecewise continuous segment j of the body is described by the following parametric equations:

$$r^j(s) = \sum_{i=0}^{N_j} a_{ji} T_i(s) = a_{j0}T_0(s) + a_{j1}T_1(s) + a_{j2}T_2(s) + ... \tag{4.1.5}$$

$$z^j(s) = \sum_{i=0}^{M_j} b_{ji} T_i(s) = b_{j0}T_0(s) + b_{j1}T_1(s) + b_{j2}T_2(s) + ... \tag{4.1.6}$$

Where s is a parameter in the range $[0, 1]$ so that $x = 2s - 1$, and $j = 1$ refers to the segment closest to the waterline.

As mentioned, one of the requirements is to be able use the radius at the waterline, R, and the draft at the centerline, H, as two input parameters. Additionally, the coordinates of the slope discontinuities (if they exist) need to be parameters. Therefore, we need to use them as boundary conditions. For a shape with no slope discontinuities, $s = 0$ at the waterline and $s = 1$ at the z centerline. That is, $s = 0$ when $r = R$ and $z = 0$, and $s = 1$ when $r = 0$, $z = -H$, as shown in figure 4-3.

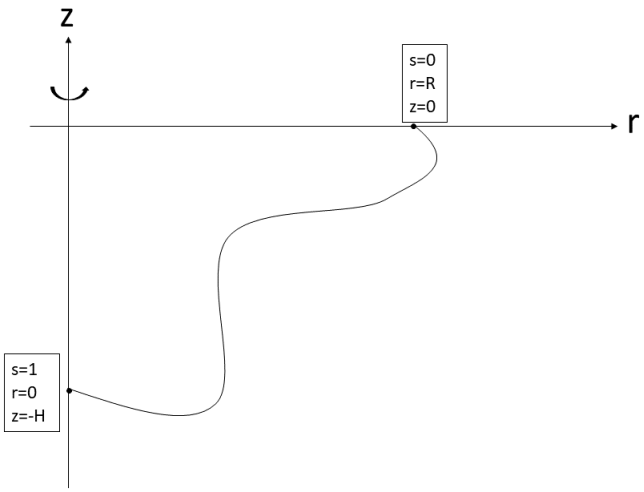

Figure 4-3: Showing boundary values for a shape described by continuous parametric functions

For a shape with one slope discontinuity, for $j = 1$ (the segment closest to the waterline), $s = 0$ at the waterline, and $s = 1$ at the slope discontinuity. Then, $j = 2$,

$s = 0$ at the slope discontinuity and $s = 1$ at the centerline. That is, for piece $j = 1$, $s = 0$ when $r = R$ and $z = 0$, and $s = 1$ when $r = r_1$ and $z = z_1$. For piece $j = 2$, $s = 0$ when $r = r_1$ and $z = z_1$, and $s = 1$ when $r = 0$ and $z = -H$. This is shown in figure 4-4.

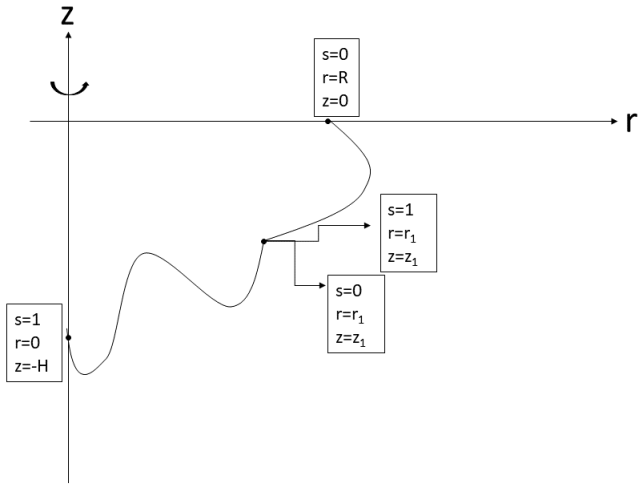

Figure 4-4: Showing boundary values for a shape with one slope discontinuity. Each piecewise continuous segment is described by unique parametric equations.

Note: for $j = 1$, the 1-subscript is dropped, so that the coefficients are $a_0, a_1, a_2, ..., b_0, b_1, b_2, ...$

The coefficients a_{j0}, a_{j1}, b_{j0} and b_{j1} must be defined to ensure the boundary conditions described above and shown in the figures. To generalize, we can describe these boundary conditions by saying that $s = 0$ when $r = \gamma_{j1}, z = \zeta_{j1}$ and $s = 1$ when $r = \gamma_{j2}, z = \zeta_{j2}$. For a shape with no slope discontinuity, $\gamma_1 = R, \gamma_2 = 0, \zeta_1 = 0, \zeta_2 = -H$. For a shape with one slope discontinuity, for $j = 1$, $\gamma_{11} = R, \gamma_{12} = r_1, \zeta_{11} = 0, \zeta_{12} = z_1$, and for $j = 2$, $\gamma_{21} = r_1, \gamma_{22} = 0, \zeta_{21} = z_1, \zeta_{22} = -H$.
Therefore, to ensure boundary conditions, a_{j0} and b_{j0} must be defined as

$$a_{j0} = \frac{\gamma_{j2}}{2} + \frac{\gamma_{j1}}{2} - a_{j2} - a_{j4} - ... \text{ all other even terms} \tag{4.1.7}$$

$$b_{j0} = \frac{\zeta_{j2}}{2} + \frac{\zeta_{j1}}{2} - b_{j2} - b_{j4} - ... \text{ all other even terms} \tag{4.1.8}$$

And a_{j1} and b_{j1} must be defined as

$$a_{j1} = \frac{\gamma_{j2}}{2} - \frac{\gamma_{j1}}{2} - a_{j3} - a_{j5} - ... \text{ all other odd terms} \tag{4.1.9}$$

$$b_{j1} = \frac{\zeta_{j2}}{2} - \frac{\zeta_{j1}}{2} - b_{j3} - b_{j5} - ... \text{ all other odd terms} \tag{4.1.10}$$

Therefore, putting equations 4.1.7, 4.1.8, 4.1.9 and 4.1.10 into equation 4.1.5, we see that $r^j(s)$ can be expressed as

$$r^j(s) = \gamma_{j2}s + \gamma_{j1}(1-s) + a_{j2}(T_2(s)-1) + a_{j3}(T_3(s)-2s+1) + ... \tag{4.1.11}$$

$$r^j(s) = \begin{cases} \gamma_2 s + \gamma_{j1}(1-s) + \sum_{i=1}^{N/2}\left(a_{j2i}(T_{2i}(s)-1)\right) + \sum_{i=1}^{N/2-1}\left(a_{j(2i+1)}(T_{2i+1}(s)-2s+1)\right) & N \text{ even} \\ \gamma_2 s + \gamma_{j1}(1-s) + \sum_{i=1}^{(N-1)/2}\left(a_{j2i}(T_{2i}(s)-1) + a_{j(2i+1)}(T_{2i+1}(s)-2s+1)\right) & N \text{ odd} \end{cases} \tag{4.1.12}$$

We can verify that at $s = 0, r = \gamma_{j1}$ and at $s = 1, r = \gamma_{j2}$, and therefore it satisfies the boundary conditions. Similarly, $z^j(s)$ can be expressed as

$$z^j(s) = \zeta_{j2}s + \zeta_{j1}(1-s) + b_{j2}(T_2(s)-1) + b_{j3}(T_3(s)-2s+1) + ... \tag{4.1.13}$$

$$z^j(s) = \begin{cases} \zeta_{j2} s + \zeta_{j1}(1-s) + \sum_{i=1}^{M/2}\left(b_{j2i}(T_{2i}(s)-1)\right) + \sum_{i=1}^{M/2-1}\left(b_{j(2i+1)}(T_{2i+1}(s)-2s+1)\right) & M \text{ even} \\ \zeta_{j2} s + \zeta_{j1}(1-s) + \sum_{i=1}^{(M-1)/2}\left(b_{j2i}(T_{2i}(s)-1) + b_{j(2i+1)}(T_{2i+1}(s)-2s+1)\right) & M \text{ odd} \end{cases} \tag{4.1.14}$$

We can verify that at $s = 0, z = \zeta_{j1}$ and at $s = 1, z = \zeta_{j2}$, so therefore it satisfies the boundary conditions.

To summarize, for a no-kink shape with up to 4th order polynomials, the parametric

equations would be

$$r(s) = R\,(1-s) + a_2\,(T_2(s)-1) + a_3\,(T_3(s)-2s+1) + a_4\,(T_4(s)-1) \tag{4.1.15}$$

$$z(s) = -Hs + b_2\,(T_2(s)-1) + b_3\,(T_3(s)-2s+1) + b_4\,(T_4(s)-1) \tag{4.1.16}$$

For a shape with one slope discontinuity and two piecewise continuous segments with up to 4th order polynomials, the parametric equations would be

$$r(s) = \begin{cases} r_1 s + R\,(1-s) + a_2\,(T_2(s)-1) + a_3\,(T_3(s)-2s+1) + a_4\,(T_4(s)-1)\,, & \text{piece 1} \\ r_1\,(1-s) + a_{22}\,(T_2(s)-1) + a_{23}\,(T_3(s)-2s+1) + a_{24}\,(T_4(s)-1)\,, & \text{piece 2} \end{cases} \tag{4.1.17}$$

$$z(s) = \begin{cases} z_1 s + b_2\,(T_2(s)-1) + b_3\,(T_3(s)-2s+1) + b_4\,(T_4(s)-1)\,, & \text{piece 1} \\ -Hs + b_{22}\,(T_2(s)-1) + b_{23}\,(T_3(s)-2s+1) + b_{24}\,(T_4(s)-1)\,, & \text{piece 2} \end{cases} \tag{4.1.18}$$

Nondimensionalization

To nondimensionalize the geometric parameters, we will use the cube-root of volume, l_V, for R and H, and then use R for all radial parameters and H for all depth parameters. Therefore,

$$\overline{R} = \frac{R}{l_V} \tag{4.1.19}$$

$$\overline{H} = \frac{H}{l_V} \tag{4.1.20}$$

For all coordinates of the slope discontinuities,

$$\overline{r_j} = \frac{r_j}{R} \tag{4.1.21}$$

$$\overline{z^j} = \frac{z_j}{H} \tag{4.1.22}$$

For all coefficients,

$$\overline{a_{ji}} = \frac{a_{ji}}{R} \tag{4.1.23}$$

$$\overline{b_{ji}} = \frac{b_{ji}}{H} \tag{4.1.24}$$

And, for the functions,

$$\overline{r^j(s)} = \frac{r^j(s)}{R} \tag{4.1.25}$$

$$\overline{z^j(s)} = \frac{z^j(s)}{H} \tag{4.1.26}$$

Equations 4.1.15, 4.1.16, 4.1.17 and 4.1.18 summarize the parametric equations used in this thesis to represent a wide range of shapes. The coefficients a_2, a_3, a_4, a_{22}, a_{23}, a_{24}, b_2, b_3, b_4, b_{22}, b_{23}, and b_{24}, as well as the coordinates of the slope discontinuity (r_1, z_1), become the parameters to optimize in the multi-objective optimization.

4.1.3 Introducing classes of shapes

Given the description of geometric shapes above, there are many ways to group the parameters to describe different shapes. For example, you could compare all shapes with a given volume. As explained more in section 4.2, we need a way to represent the set of all shapes with all geometric parameters other than radius and volume fixed. We call these sets **classes** of shapes.

From the geometric description described above, we see that given the following

vector, $\overline{B}$, the shape is fully defined:

$$\overline{B} = \left\{R, H, \overline{a_2}, \overline{b_2}, \overline{a_3}, \overline{b_3}, ..., \overline{r_1}, \overline{z_1}, \overline{a_{22}}, \overline{b_{22}}, \overline{a_{23}}, \overline{b_{23}}, ..., ...\right\} \tag{4.1.27}$$

Consider the following vector, $\overline{\mathscr{B}_E}$, which contains all of the parameters other than R and H:

$$\overline{\mathscr{B}_E} = \begin{cases} \left\{\overline{a_2}, \overline{b_2}, \overline{a_3}, \overline{b_3}, \overline{a_4}, \overline{b_4}\right\} & \text{0 kinks} \\ \left\{\overline{a_2}, \overline{b_2}, \overline{a_3}, \overline{b_3}, \overline{a_4}, \overline{b_4}, \overline{r_1}, \overline{z_1}, \overline{a_{22}}, \overline{b_{22}}, \overline{a_{23}}, \overline{b_{23}}, \overline{a_{24}}, \overline{b_{24}}\right\} & \text{1 kink} \end{cases} \tag{4.1.28}$$

Therefore, $\overline{B} = \left\{R, H, \overline{\mathscr{B}_E}\right\}$. Since the shape is axisymmetric and described by parametric equations, volume can be expressed as

$$l_V^3 = R^2 H \sum_j \int_0^1 \overline{r^j}^2 \overline{z^{j'}} ds \tag{4.1.29}$$

where $z^{j'}$ is the derivative of z^j. The summation of the integral, which we will call I, depends only on the terms in $\overline{\mathscr{B}_E}$. That is,

$$I\left(\overline{\mathscr{B}_E}\right) = \sum_j \int_0^1 \overline{r^j}^2 \overline{z^{j'}} ds \tag{4.1.30}$$

We can use the expressions from equations 4.1.19 and 4.1.20 to see that $\overline{H}$ can be expressed in terms of $\overline{R}$ and $\overline{\mathscr{B}_E}$:

$$\overline{H} = \frac{1}{\pi \overline{R}^2 I\left(\overline{\mathscr{B}_E}\right)} \tag{4.1.31}$$

Therefore, $\overline{B} = \left\{\overline{R}, l_V, \overline{\mathscr{B}_E}\right\}$.

We define a **class** of shapes as the set of all possible values of $\overline{R}$ and l_V, with a fixed $\overline{\mathscr{B}_E}$. That is, if k is given, class $\mathscr{C}^k$ is

$$\mathscr{C}^k \equiv \left\{l_V, \overline{R} \mid \overline{\mathscr{B}_E} = \overline{\mathscr{B}_E}^k \text{ fixed}\right\} \tag{4.1.32}$$

We have defined a class of shapes to be all shapes with a fixed $\overline{\mathscr{B}_E}$, which is defined

in equation 4.1.28. We came up with the idea of classes to use them, as explained in section 4.2, to find roots of the heave resonance equation.

4.1.4 Examples of classes of shapes

In this section, we will look at example of classes to help demonstrate the principle.

Cylinders

This class consists of all possible cylinders and so is the simplest class to understand. We set $\overline{r_1} = 1$ and $\overline{z_1} = -1$ and all other terms in $\overline{\mathscr{B}_E}$ equal to 0:

$$\begin{aligned} \overline{\mathscr{B}_E}^{cylinder} &= \left\{\overline{a_2}, \overline{b_2}, \overline{a_3}, \overline{b_3}, ..., \overline{r_1}, \overline{z_1}, \overline{a_{22}}, \overline{b_{22}}, \overline{a_{23}}, \overline{b_{23}}, ...\right\} \\ &= \{0, 0, 0, 0, ..., 1, -1, 0, 0, 0, 0, ...\} \end{aligned} \tag{4.1.33}$$

and so the class is

$$\mathscr{C}^{cylinder} = \left\{l_V, \overline{R} \mid \overline{\mathscr{B}_E} = \overline{\mathscr{B}_E}^{cylinder}\right\} \tag{4.1.34}$$

All cylinders are describable by l_V and $\overline{R}$. Figure 4-5 demonstrates some of the cylinders in this set. Note that the x-axis is $\frac{r}{l_V}$ and y-axis is $\frac{z}{l_V}$. The full class of shapes consists of all values of $\overline{R}$ and all values of l_V. That is, it consists of all cylinders. Given l_V, increasing $\overline{R}$, as shown in the figure, decreases $\overline{H}$.

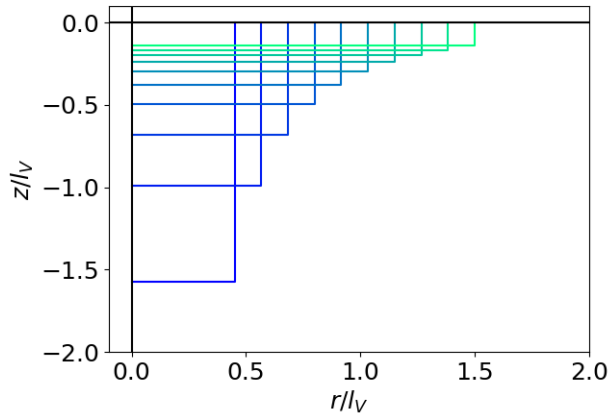

Figure 4-5: Example of a class of shapes: cylinders

Class $\overline{r_1} = 2$

Another class of shapes is all shapes with $\overline{r_1} = 2, \overline{z_1} = -1$ and all other parameters in $\overline{\mathscr{B}_E}$ equal to 0:

$$\begin{aligned} \overline{\mathscr{B}_E}^{\overline{r_1}=2} &= \left\{\overline{a_2}, \overline{b_2}, \overline{a_3}, \overline{b_3}, ..., \overline{r_1}, \overline{z_1}, \overline{a_{22}}, \overline{b_{22}}, \overline{a_{23}}, \overline{b_{23}}, ...\right\} \\ &= \{0, 0, 0, 0, ..., 2, -1, 0, 0, 0, 0, ...\} \end{aligned} \tag{4.1.35}$$

and so the class is

$$\mathscr{C}^{\overline{r_1}=2} = \left\{l_V, \overline{R} \mid \overline{\mathscr{B}_E} = \overline{\mathscr{B}_E}^{\overline{r_1}=2}\right\} \tag{4.1.36}$$

Figure 4-6 shows associated shapes for this class. The ratio of the maximum radial dimension (at the coordinate of the slope discontinuity) to the radius at the waterline is fixed at 2, and the bottom remains flat. For a given l_V as $\overline{R}$ increases, $\overline{H}$ decreases.

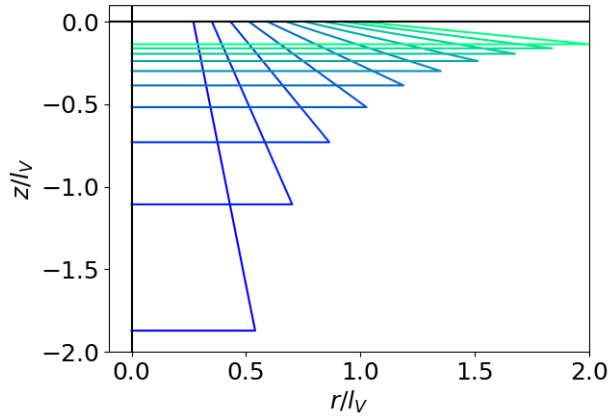

Figure 4-6: Example of class of shapes: $\overline{r_1} = 2, \overline{z_1} = -1$

Class $\overline{z_1} = -2$

Another class of shapes is all shapes with $\overline{r_1} = 1, \overline{z_1} = -2$ and all other parameters in $\overline{\mathscr{B}_E}$ equal to 0:

$$\begin{aligned} \overline{\mathscr{B}_E}^{\overline{z_1}=-2} &= \left\{\overline{a_2}, \overline{b_2}, \overline{a_3}, \overline{b_3}, ..., \overline{r_1}, \overline{z_1}, \overline{a_{22}}, \overline{b_{22}}, \overline{a_{23}}, \overline{b_{23}}, ...\right\} \\ &= \{0, 0, 0, 0, ..., 1, -2, 0, 0, 0, 0, ...\} \end{aligned} \tag{4.1.37}$$

and so the class is

$$\mathscr{C}^{\overline{z_1}=-2} = \left\{ l_V, \overline{R} \mid \overline{\mathscr{B}_E} = \overline{\mathscr{B}_E}^{\overline{z_1}=-2} \right\} \tag{4.1.38}$$

Figure 4-7 shows associated shapes for this class.

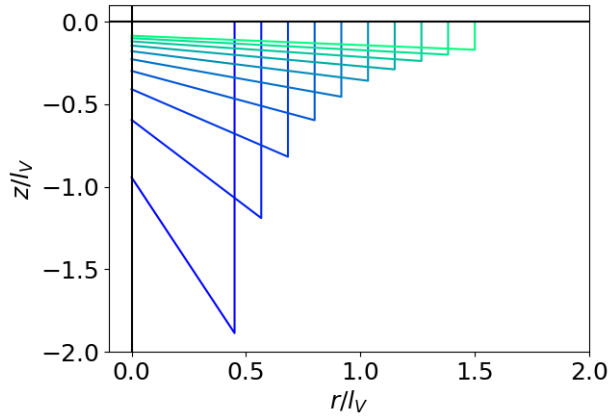

Figure 4-7: Example of class of shapes: $\overline{r_1} = 1, \overline{z_1} = -2$

Class $\bar{a_2} = -0.25$

A class of shapes can be defined by a given coefficient of the parametric equations. For example, a certain class of shapes could be all shapes with no slope discontinuities, with $\overline{a_2} = -0.25$ with all other coefficients equal to 0:

$$\begin{aligned} \overline{\mathscr{B}_E}^{\overline{a_2}=-0.25} &= \left\{ \overline{a_2}, \overline{b_2}, \overline{a_3}, \overline{b_3}, ... \right\} \\ &= \{-0.25, 0, 0, 0, ...\} \end{aligned} \tag{4.1.39}$$

and so the class is

$$\mathscr{C}^{\overline{a_2}=-0.25} = \left\{ l_V, \overline{R} \mid \overline{\mathscr{B}_E} = \overline{\mathscr{B}_E}^{\overline{a_2}=-0.25} \right\} \tag{4.1.40}$$

Figure 4-8 shows associated shapes for this class. The ratio of the maximum radial dimension (this time not occurring at a slope discontinuity) to the radius at the waterline is again fixed. For a given l_V, as $\overline{R}$ increases, $\overline{H}$ decreases.

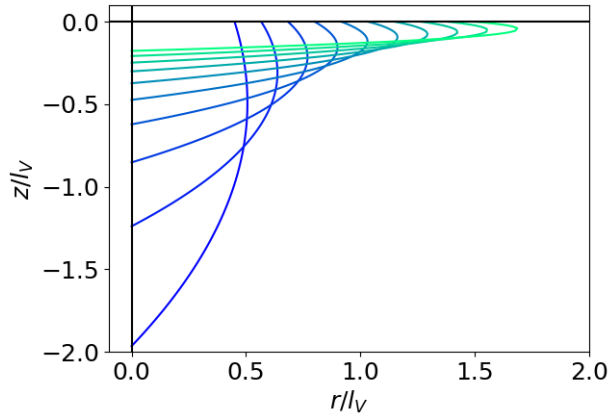

Figure 4-8: Example of class of shape: $\overline{a_2} = -0.25$

Class $\overline{b_2} = 0.25$

Similarly, a class of shapes could be defined by the vector

$$\begin{aligned} \overline{\mathscr{B}_E}^{\overline{b_2}=0.25} &= \left\{\overline{a_2}, \overline{b_2}, \overline{a_3}, \overline{b_3}, ...\right\} \\ &= \{0, 0.25, 0, 0, ...\} \end{aligned} \tag{4.1.41}$$

and so the class is

$$\mathscr{C}^{\overline{b_2}=0.25} = \left\{ l_V, \overline{R} \mid \overline{\mathscr{B}_E} = \overline{\mathscr{B}_E}^{\overline{b_2}=0.25} \right\} \tag{4.1.42}$$

Figure 4-9 shows associated shapes for this class.

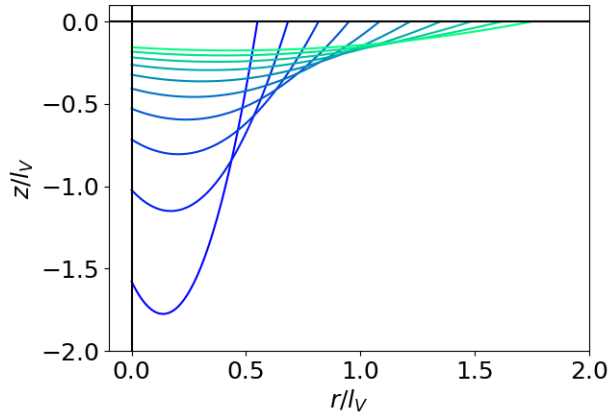

Figure 4-9: Example of class of shape: $\overline{b_2} = 0.25$

4.1.5 Groups of shapes

A group of shapes is a set of multiple classes of shapes, and our optimizations consider entire groups at once, instead of just individual classes. We use the symbol $\mathscr{G}$ to represent a group of shapes. In this section, the groups that are optimized.

Flat-bottomed shapes

The 'flat-bottomed' group contains all shapes consisting of two piecewise-linear segments with one slope discontinuity, with the bottom segment being horizontal. That is, $\overline{z_1} = -1$ and $\overline{r_1} > 0$.

We showed one of the classes belonging to this group in figure 4-6. Class $\mathscr{C}^{\overline{r_1}=2}$ is defined in equation 4.1.38, with $\overline{\mathscr{B}_E}$ shown in equation 4.1.37. The group is defined as

$$\mathscr{G}^{FB} = \left\{\mathscr{C}^{\overline{r_1}=\overline{r_1}^1}, \mathscr{C}^{\overline{r_1}=\overline{r_1}^2}, ...\right\} \tag{4.1.43}$$

where $\mathscr{C}^{\overline{r_1}=\overline{r_1}^i}$ is

$$\mathscr{C}^{\overline{r_1}=\overline{r_1}^i} = \left\{\overline{R}, kl_V | \overline{\mathscr{B}_E} = \overline{\mathscr{B}_E}^{\overline{r_1}=r_1^i}\right\} \tag{4.1.44}$$

where $\overline{\mathscr{B}_E}^{\overline{r_1}=\overline{r_1}^i}$ is

$$\overline{\mathscr{B}_E}^{\overline{r_1}=\overline{r_1}^i} = \left\{0, 0, 0, 0, ..., \overline{r_1}^i, -1, 0, 0, 0, 0, ...\right\} \tag{4.1.45}$$

Figure 4-10 illustrates shapes included in this group. Each column represents one class of shapes. The figures show one example shape in each class.

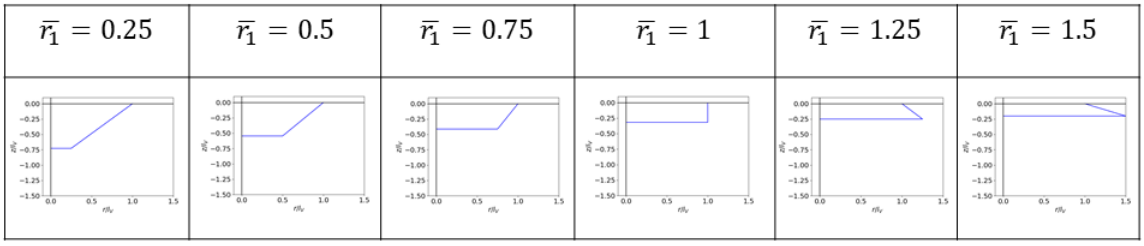

Figure 4-10: 'Flat-bottomed' group of shapes: linear piecewise segments with one slope discontinuity at (r_1, z_1). $\overline{z_1} = \frac{z_1}{H} = -1$, so that the segment from the centerline to the slope discontinuity is horizontal. $\overline{r_1} = \frac{r_1}{R} > 1$ represents a 'protruding outwards' shape

Flat-sided shapes

Another group of shapes, called 'flat-sided shapes' consists of all classes of shapes with $\overline{r_1} = 1$ and $\overline{z_1} < 0$. That is, the walls are vertical from the waterline to the slope discontinuity. The group is defined as

$$\mathscr{G}^{FS} = \left\{ \mathscr{C}^{\overline{z_1}=\overline{z_1}^1}, \mathscr{C}^{\overline{z_1}=\overline{z_1}^2}, ... \right\} \tag{4.1.46}$$

where $\mathscr{C}^{\overline{z_1}=\overline{z_1}^i}$ is

$$\mathscr{C}^{\overline{z_1}=\overline{z_1}^i} = \left\{ \overline{R}, kl_V | \overline{\mathscr{B}_E} = \overline{\mathscr{B}_E}^{\overline{z_1}=z_1^i} \right\} \tag{4.1.47}$$

where $\overline{\mathscr{B}_E}^{\overline{z_1}=\overline{z_1}^i}$ is

$$\overline{\mathscr{B}_E}^{\overline{z_1}=\overline{z_1}^i} = \left\{ 0, 0, 0, 0, ..., 1, \overline{z_1}^i, 0, 0, 0, 0, ... \right\} \tag{4.1.48}$$

Figure 4-11 shows examples of shapes in each class to form the group.

$\overline{z_1} = -0.25$	$\overline{z_1} = -0.5$	$\overline{z_1} = -0.75$	$\overline{z_1} = -1$	$\overline{z_1} = -1.25$	$\overline{z_1} = -1.5$
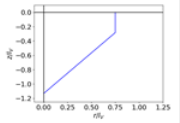	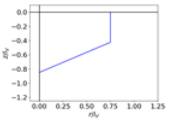	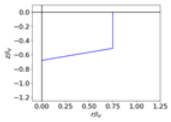	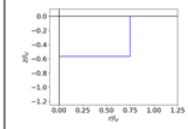	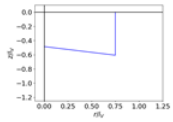	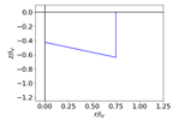

Figure 4-11: 'Flat-sided' group of shapes: piecewise linear segments with one slope discontinuity at (r_1, z_1). $\overline{r_1} = \frac{r_1}{R} = 1$, so that the segment from the waterline to the slope discontinuity is vertical. $\overline{z_1} = \frac{z_1}{H} < -1$ represents a 'dipping down' shape

All 'one-kink' shapes

The group of shapes with one slope discontinuity, with two piecewise linear segments, is called 'one-kink shapes.' This group consists of all classes with different values of $\overline{r_1}$ and $\overline{z_1}$, with all other shape parameters 0. The group is defined as

$$\mathscr{G}^{OK} = \left\{ \mathscr{C}^{(\overline{r_1},\overline{z_1})=(\overline{r_1}^1,\overline{z_1}^1)}, \mathscr{C}^{(\overline{r_1},\overline{z_1})=(\overline{r_1}^2,\overline{z_1}^2)}, ... \right\} \tag{4.1.49}$$

where $\mathscr{C}^{(\overline{r_1},\overline{z_1})=(\overline{r_1}^i,\overline{z_1}^i)}$ is

$$\mathscr{C}^{(\overline{r_1},\overline{z_1})=(\overline{r_1}^i,\overline{z_1}^i)} = \left\{ \overline{R}, kl_V | \overline{\mathscr{B}_E} = \overline{\mathscr{B}_E}^{(\overline{r_1},\overline{z_1})=(\overline{r_1}^i,\overline{z_1}^i)} \right\} \tag{4.1.50}$$

where $\overline{\mathscr{B}_E}^{(\overline{r_1},\overline{z_1})=(\overline{r_1}^i,\overline{z_1}^i)}$ is

$$\overline{\mathscr{B}_E}^{(\overline{r_1},\overline{z_1})=(\overline{r_1}^i,\overline{z_1}^i)} = \left\{ 0, 0, 0, 0, ..., \overline{r_1}^i, \overline{z_1}^i, 0, 0, 0, 0, ... \right\} \tag{4.1.51}$$

Figure 4-12 shows example shapes, with one example shape from a range of classes with $\overline{r_1}$ from 0.25 to 1.5 and $\overline{z_1}$ from -0.25 to -1.5.

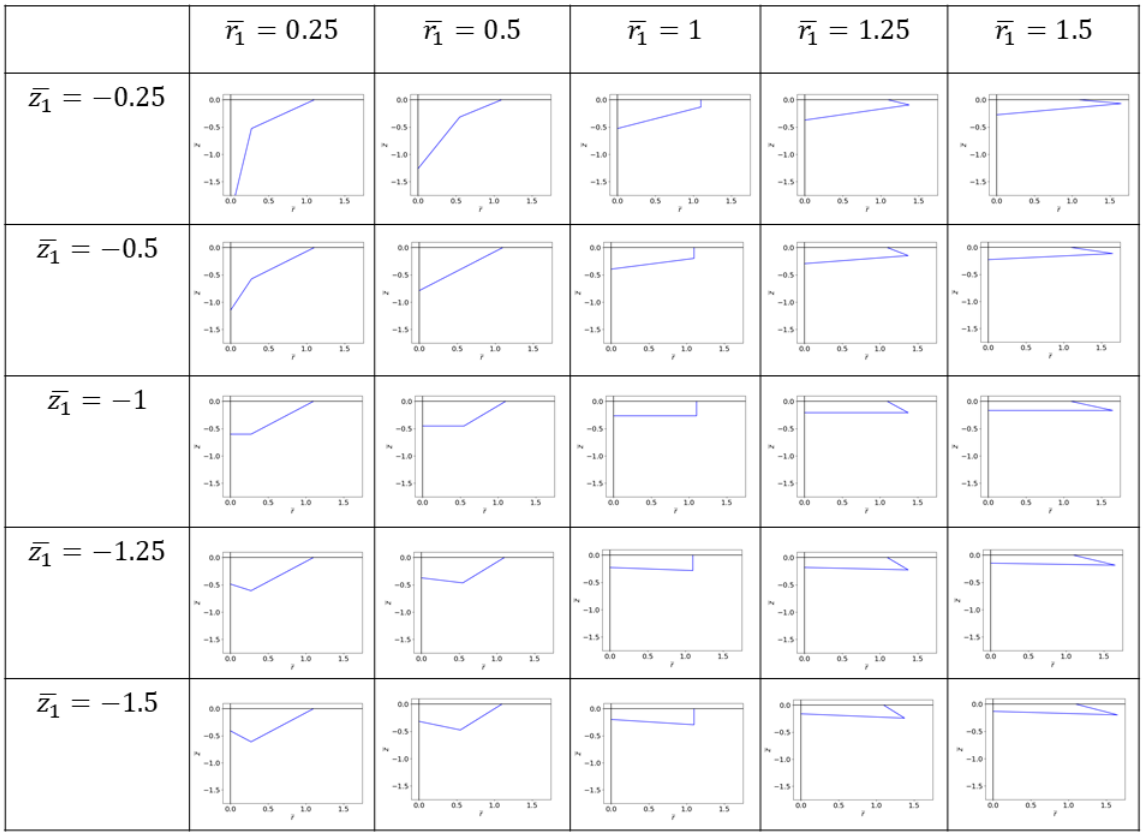

Figure 4-12: 'One-kink' group of shapes: piecewise linear segments with one slope discontinuity at (r_1, z_1). $\overline{z_1} = \frac{z_1}{H} < -1$ represents a 'dipping down' shape, and $\overline{r_1} = \frac{r_1}{R} > 1$ represents a 'protruding outward' shape

Compound cylinders

Another group of shapes is the compound cylinder. This is the group of shapes that can be made from two cylinders of differing widths being stacked one on top of the other. Therefore, the shape is known if $l_V, \overline{R}, \overline{r_2}$ and $\overline{z_2}$ are known, where $(\overline{r_2 z_2})$ is the coordinate of the intersection of the two cylinders. The group is defined as

$$\mathscr{G}^{CC} = \left\{ \mathscr{C}^{(\overline{r_2},\overline{z_2})=(\overline{r_2}^1,\overline{z_2}^1)}, \mathscr{C}^{(\overline{r_2},\overline{z_2})=(\overline{r_2}^2,\overline{z_2}^2)}, ... \right\} \tag{4.1.52}$$

where $\mathscr{C}^{(\overline{r_2},\overline{z_2})=(\overline{r_2}^i,\overline{z_2}^i)}$ is

$$\mathscr{C}^{(\overline{r_2},\overline{z_2})=(\overline{r_2}^i,\overline{z_2}^i)} = \left\{ \overline{R}, kl_V | \overline{\mathscr{B}_E} = \overline{\mathscr{B}_E}^{(\overline{r_2},\overline{z_2})=(\overline{r_2}^i,\overline{z_2}^i)} \right\} \tag{4.1.53}$$

where $\overline{\mathscr{B}_E}^{(\overline{r_2},\overline{z_2})=(\overline{r_2}^i,\overline{z_2}^i)}$ is

$$\overline{\mathscr{B}_E}^{(\overline{r_2},\overline{z_2})=(\overline{r_2}^i,\overline{z_2}^i)} = \left\{0,0,0,0,...,\overline{r_2}^i,\overline{z_2}^i,0,0,0,0,...\right\} \tag{4.1.54}$$

These shapes have three slope discontinuities, and 4 piecewise-linear segments. $\overline{r_2}$ can be any number greater than 0, and $\overline{z_2}$ must be between -1 and 0. Figure 4-13 shows example shapes from a range of classes in the group.

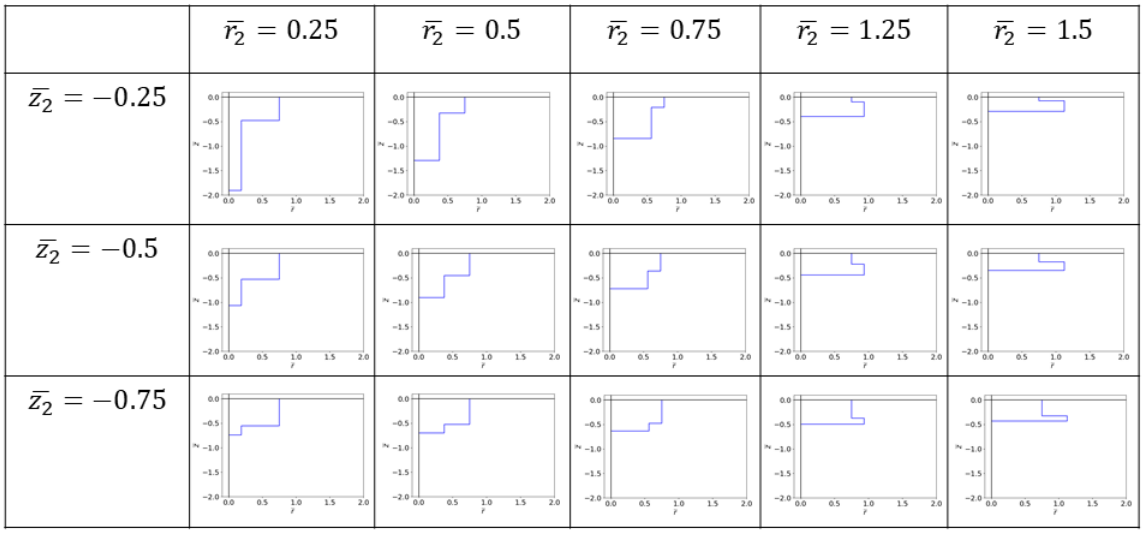

Figure 4-13: Compound cylinder group of shapes: shapes consisting of one cylinder on top of another. $\overline{r_2} = \frac{r_2}{R}$ is the ratio of the radius of the bottom cylinder to the radius of the top cylinder. Therefore, $\overline{r_2} > 1$ represents a larger bottom cylinder. $\overline{z_2} = \frac{z_2}{H}$ is the ratio of the draft of the top cylinder to the total draft.

All no-kink 2nd-order shapes

The final group of shapes we optimize in this thesis is called 'no-kink 2nd-order' shapes. This group consists of all shapes with no slope discontinuities, with nonzero 2nd-order coefficients of both parametric equations. It is defined by

$$\mathscr{G}^{NK2O} = \left\{\mathscr{C}^{(\overline{a_2},\overline{b_2})=(\overline{a_2}^1,\overline{b_2}^1)}, \mathscr{C}^{(\overline{a_2},\overline{b_2})=(\overline{a_2}^2,\overline{b_2}^2)}, ...\right\} \tag{4.1.55}$$

where $\mathscr{C}^{(\overline{a_2},\overline{b_2})=(\overline{a_2}^i,\overline{b_2}^i)}$ is

$$\mathscr{C}^{(\overline{a_2},\overline{b_2})=(\overline{a_2}^i,\overline{b_2}^i)} = \left\{\overline{R}, kl_V | \overline{\mathscr{B}_E} = \overline{\mathscr{B}_E}^{(\overline{a_2},\overline{b_2})=(\overline{a_2}^i,\overline{b_2}^i)}\right\} \tag{4.1.56}$$

where $\overline{\mathscr{B}_E}^{(\overline{a_2},\overline{b_2})=(\overline{a_2}^i,\overline{b_2}^i)}$ is

$$\overline{\mathscr{B}_E}^{(\overline{a_2},\overline{b_2})=(\overline{a_2}^i,\overline{b_2}^i)} = \left\{\overline{a_2}, \overline{b_2}, 0, 0, ...\right\} \tag{4.1.57}$$

Figure 4-14 shows example shapes from a range of classes in the group.

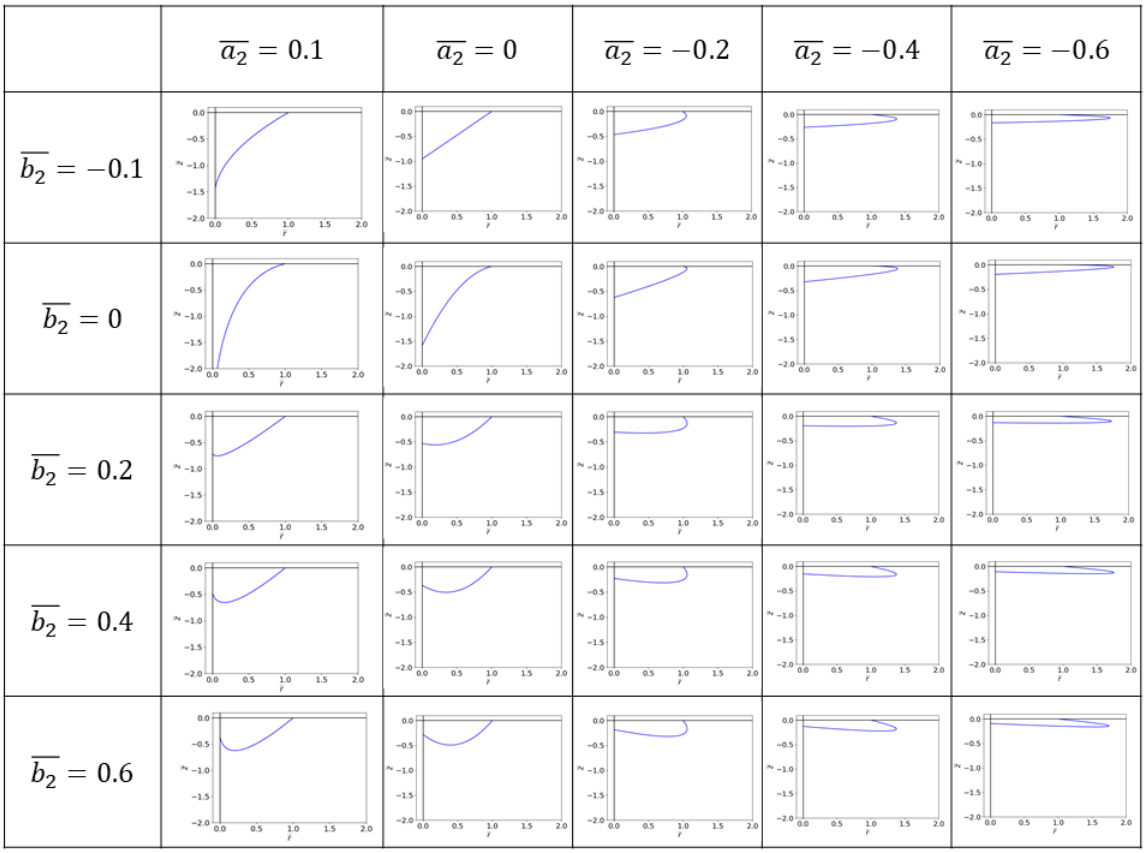

Figure 4-14: 'No-kinks-2nd-order' group of shapes: one second-order continuous segment with no slope discontinuities. The parametric equations ahve coefficients of the second-order polynomial basis function a_2 and b_2 (in the r and z directions, respectively). $\overline{a_2} = \frac{a_2}{R} < -0.1$ signifies a 'protruding outward' shape and $\overline{b_2} = \frac{b_2}{H} > 0.1$ signifies a 'dipping down' shape

In this section, the geometric description of shapes that we developed to be able to represent many geometries by changing few parameters was presented. These

parameters are the radius at the waterline, R, the draft at the centerline, H, the coordinates of any slope discontinuities and the coefficients of parametric polynomial basis functions. Then, the idea of a class of shapes was introduced. A class of shapes is the set of shapes with all geometric parameters other than R and H fixed, and we showed some examples of different classes. Finally, the groups of shapes (sets of multiple classes of shapes) that are optimized in this thesis were defined and illustrated.

4.2 Theorem for finding roots of heave resonance equation

In this section, a novel theorem for finding roots of the heave resonance equation is presented and proved. This theorem adds to our understanding of resonating heave bodies, and it significantly decreases computational burden in our optimization by allowing us to semi-analytically solve for resonating shapes, instead of looking for them with brute-force methods.

4.2.1 Theorem

Consider a WEC of volume l_V^3, with an incoming wave of unit-amplitude and wavenumber k. Suppose body class vector $\overline{\mathscr{B}_E}$ is given. If nondimensional added-mass coefficient, $\overline{A_{33}} = \frac{A_{33}}{\rho l_V^3}$, where A_{33} is the dimensional added mass coefficient, can be approximated by the function

$$\overline{A_{33}} = f(\overline{R}, kl_V) = A(kl_V)\overline{R}^3 \tag{4.2.1}$$

with the following restrictions on $A(kl_V)$:

1. $A(kl_V) > 0$ for all $kl_V > 0$
2. $\Delta = kl_V \left[-27\left(A(kl_V)\right)^2 (kl_V)^3 + 4\pi^3\right]$ must have 1 positive real root, $(kl_V)^{max}$, such that $\Delta > 0$ for $kl_V < (kl_V)^{max}$ and $\Delta < 0$ for $kl_V > (kl_V)^{max}$

then for $kl_V < (kl_V)^{max}$ there are two shapes, with R-values $\overline{R}_1$ and $\overline{R}_2$, that achieve resonance, and for $kl_V > (kl_V)^{max}$ there are no shapes that achieve resonance.

4.2.2 Proof

For a shape to achieve resonance, it must solve the resonance equation:

$$C_{33} - \omega^2 (m + A_{33}) = 0 \tag{4.2.2}$$

For a floating body in deep water, and assuming small motion, this becomes

$$\pi g R^2 - kg \left(\rho a^3 + A_{33} \right) = 0 \tag{4.2.3}$$

Dividing this equation by $g\rho l_V^2$, the resonance condition can be defined by:

$$\pi \overline{R}^2 - kl_V \left(1 + \overline{A_{33}} \right) = 0 \tag{4.2.4}$$

Putting the expression for $\overline{A_{33}}$ from equation 4.2.1, into this version of the resonance condition, we get

$$G(\overline{R}, kl_V) = \pi \overline{R}^2 - kl_V \left(1 + A(kl_V) \overline{R}^3 \right) = 0 \tag{4.2.5}$$

Since $A(kl_V) > 0$ for all $kl_V > 0$, the Descartes' rule of signs tells us that there is always one real negative root and either 0 or 2 real positive roots.
It is known that the sign of the cubic discriminant, Δ, reveals the number of real roots:

- If $\Delta > 0$ the equation has 3 real roots (in our case, 1 negative and 2 positive),
- If $\Delta < 0$ the equation has 1 real root (in our case, 1 negative) and 2 complex conjugate roots.

Therefore, if Δ has one positive real root, $(kl_V)^{max}$, and for $0 < kl_V < (kl_V)^{max}, \Delta > 0$ and for $kl_V > (kl_V)^{max}, \Delta < 0$, then we can say that for $0 < kl_V < (kl_V)^{max}$ there are two resonant shapes, defined by the two positive real roots of equation 4.2.5, $\overline{R}_1(kl_V)$

and $\overline{R}_2(kl_V)$, and for $kl_V > (kl_V)^{max}$ there are no resonant shapes, since there are no positive real roots of equation 4.2.5.

Note: We could equivalently solve the equation $\frac{\Delta}{kl_V} = 0$ to find $(kl_V)^{max}$, and if we show that for $0 < kl_V < (kl_V)^{max}, \frac{\Delta}{kl_V} > 0$ and for $kl_V > (kl_V)^{max}, \frac{\Delta}{kl_V} < 0$, this is equivalent to showing that for $0 < kl_V < (kl_V)^{max}, \Delta > 0$ and for $kl_V > (kl_V)^{max}, \Delta < 0$.

4.2.3 Discussion of theorem and its use

From equation 4.2.5, it becomes apparent why defining a class of shapes is important: we need all other geometric parameters to be defined other than ł$_V$ and $\overline{R}$ so that $G(\overline{R}, kl_V)$ was only a function of those two variables. Every organism in our optimization algorithm is defined by a vector $\overline{V}$:

$$\overline{V} = \left\{kl_V \overline{\mathscr{B}_E}\right\} \tag{4.2.6}$$

So for each $\overline{V}_i$, we get $\overline{A_{33}}$ values for a 'few' (around 10) values of $\overline{R}$. Then, this data is fit to the the curve

$$\overline{A_{33}} = A_c \overline{R}^3 \tag{4.2.7}$$

where A_c is a constant, since kl_V is given. Then, we calculate $\Delta = (kl_V)\left[-27\,(A_c)^2\,(kl_V)^3 + 4\pi^3\right]$, to determine if there are 0 (if $\Delta < 0$) or 2 (if $\Delta > 0$) positive real roots to the resonance equation. If there are two, we find them by putting equation 4.2.7 into 4.2.5 which becomes

$$-(kl_V)A_c\overline{R}^3 + \pi\overline{R}^2 - kl_V = 0 \tag{4.2.8}$$

which is just a cubic equation for $\overline{R}$ and can be solved explicitly. From our theorem, we know that the solution will give one negative root and two positive roots, $\overline{R}_1(\overline{V}_i)$ and $\overline{R}_2(\overline{V}_i)$. The resonating shapes are defined by $\overline{B}_1 = \left\{\overline{R}_1(\overline{V}_i), \overline{V}_i\right\}$ and $\overline{B}_2 = \left\{\overline{R}_2(\overline{V}_i), \overline{V}_i\right\}$. Note that this theorem is not specific to Chebyshev polynomials. For

example, if shapes were described by a Fourier basis, it would still be valid.

This theorem essentially speeds up our optimization algorithm by removing one degree of freedom from the algorithm, using formulas and semi-analytic theory. Without the theorem, we would need to search many values of $\overline{R}$ to find where the resonance equation is true. Due to the nature of the resonance equation, these roots are hard to find without prior knowledge of (1) how many there will be, and (2) where they might be. Because of this theorem, our process is **100x more efficient than brute-force tests**.

Additionally, if for a given $\overline{V}^* = \left\{kl_V^*, \overline{\mathscr{B}_E}^*\right\}$, there are 0 roots of the resonance equation, from the theorem we know that for any $kl_V > kl_V^*$, for the given $\overline{\mathscr{B}_E} = \overline{\mathscr{B}_E}^*$, there are also 0 roots of the resonance equation, so we can automatically disregard any $\overline{V}_i$ with $\overline{\mathscr{B}_E} = \overline{\mathscr{B}_E}^*$ and $kl_V > kl_V^*$. This also significantly increases our optimization computation time.

In this section, we presented a novel theorem to find roots of the heave resonance equation, which adds to our understanding of the problem and significantly reduces our computational time to solve the optimization problem.

4.2.4 Computational notes

All hydrodynamic parameters are from WAMIT (Lee, 1996; Lee and Newman, 2006), a linear frequency-domain panel method. To ensure that our grids are well suited to the method, we ensure close to square panels. Furthermore, we have a wrapper around each run to make sure the hydrodynamic parameters do not differ by more than 3 % after adding another panel to the smallest arclength, and also adding corresponding panels to other arclengths to keep the panels close to squares.

For thin, shallow shapes, we interpolate the functions to pure disks ($H = 0$). For heave hydrodynamic parameters, we use a linear interpolation, and for surge and pitch parameters we use a quadratic interpolation. In both cases we found that this

interpolation converged to the actual parameters. For asymptotic values (for $H = 0$), for heave hydrodynamic parameters we use the values from Miles (1987), and for pitch hydrodynamic parameters we use the values from Kim (1963).

To speed up the optimization, we use a 2D+ interpolation among each group of shapes for the roots of the resonance equations, $\overline{R}_1$ and $\overline{R}_2$, as well as the body motion for the shape with $\overline{R}_2$, $\xi_3(\overline{R})$. For example, for one-kink shapes, the interpolation is for $\overline{r_1}, \overline{z_1}$ and kl_V. For each group of shapes, we verified that the interpolation was well defined and produced accurate values of the three parameters. This interpolation sped up the process of finding the Pareto Front considerably, and once the final Pareto Front was determined, the shapes on the Pareto Front were checked by running WAMIT to ensure the accuracy.

4.3 General observations and conclusions for any given class of shapes

In our optimization runs, we run the optimization for entire groups of shapes, but it is informative to look at general observations and conclusions that can be made for *any* given class of shapes.

The populations and Pareto Fronts will be plotted in the $kl_V - kl_S$ space. The plot of the shape of the curve of the population in $kl_V - kl_S$ will directly impact the resulting Pareto Front, so determining a general pattern in the curve of the population in the $kl_V - kl_S$ plot will enable us to make conclusions about the resulting Pareto Front. The symbol $\mathcal{S}$ will symbolize the curve of a set in the $kl_V - kl_S$ space. For example, the curve of the heave population would be represented as $\mathcal{S}(\mathbb{P}_3)$.

We start with the set of shapes that solve the heave resonance equation, $\mathbb{R}_3$, since the population is the intersection of $\mathbb{R}_3$ with the sets of shapes that adhere to the heave motion constraint, $\mathbb{A}_3$, and heave steepness constraint, $\mathbb{E}_3$. Given $\overline{\mathscr{B}_E}$, the set of shapes in $\mathscr{C}^{\overline{\mathscr{B}_E}}$ that solve the heave resonance equation will be called $\mathbb{R}_3^{\overline{\mathscr{B}_E}}$. That

is, $\mathscr{C}^{\overline{\mathscr{B}_E}} \cap \mathbb{R}_3 = \mathbb{R}_3^{\overline{\mathscr{B}_E}}$. Given α and ϵ, the heave population for $\mathscr{C}^{\overline{\mathscr{B}_E}}$ will then be $\mathbb{P}_{3,\alpha,\epsilon}^{\overline{\mathscr{B}_E}} = \mathbb{R}_3^{\overline{\mathscr{B}_E}} \cap \mathbb{A}_3(\alpha) \cap \mathbb{E}_3(\epsilon)$

To form the heave-surge-pitch population, we again start with $\mathbb{R}_3^{\overline{\mathscr{B}_E}}$, since the population is the intersection of $\mathbb{R}_3^{\overline{\mathscr{B}_E}}$ with the set of shapes that adhere to the heave motion constraint, $\mathbb{A}_3$, the heave steepness constraint, $\mathbb{E}_3$, the surge motion constraint, $\mathbb{A}_1$, the pitch motion constraint, $\mathbb{A}_5$, the pitch steepness constraint, $\mathbb{E}_5$, the pitch moment of inertia constraint, $\mathbb{I}_{15}$, and the center of gravity constraint, $\mathbb{Z}_{15}$. That is, for a given α and ϵ, the heave-surge-pitch population for $\mathscr{C}^{\overline{\mathscr{B}_E}}$ will be $\mathbb{P}_{135,\alpha,\epsilon}^{\overline{\mathscr{B}_E}} = \mathbb{R}_3^{\overline{\mathscr{B}_E}} \cap \mathbb{A}_3(\alpha) \cap \mathbb{E}_3(\epsilon) \cap \mathbb{A}_5(\alpha) \cap \mathbb{A}_1(\alpha) \cap \mathbb{E}_5(\epsilon) \cap \mathbb{I}_{15} \cap \mathbb{Z}_{15}$.

Therefore, we first need to examine $\mathcal{S}(\mathbb{R}_3^{\overline{\mathscr{B}_E}})$, the curve of the plot of $\mathbb{R}_3^{\overline{\mathscr{B}_E}}$ in the $kl_V - kl_S$ space, and then see how $\mathcal{S}(\mathbb{R}_3^{\overline{\mathscr{B}_E}})$ is affected by the different constraints. In the next chapter, we use the cylinder as an example to demonstrate these principles with an easily describable shape.

4.3.1 The set of all shapes in a class that solve the heave resonance equation

To understand the shape of $\mathcal{S}(\mathbb{R}_3^{\overline{\mathscr{B}_E}})$, we look at the equations for kl_V and kl_S of resonating bodies, given $\overline{\mathscr{B}_E}$. We can solve the heave resonance equation, with the approximation for added mass, given in equation 4.2.5, for kl_V, to get an implicit expression for kl_V^{res}, in terms of $A(kl_V^{res})$

$$kl_V^{res} = \frac{\pi \overline{R}^2}{1 + A(kl_V^{res})\overline{R}^3} \tag{4.3.1}$$

Since the geometry is described by piecewise parametric equations, and since the body is axisymmetric, we know that kl_S can be expressed as

$$kl_S = kl_V \sqrt{2\pi \overline{R} \sum_j^J \int_0^1 \overline{r^j(s)} \sqrt{\overline{R}^2 \overline{r^j(s)}'^2 + \frac{\overline{z^j(s)}'^2}{\pi^2 \overline{R}^4 I(\overline{\mathscr{B}_E})^2}} ds} \tag{4.3.2}$$

where J is the number of piecewise continuous segments of the shape, $r^j(s)$ and $z^j(s)$ are the parametric equations for piece j, and $I(\overline{\mathscr{B}_E})$ is defined in equation 4.1.30. $\overline{r^j(s)} = \frac{r^j(s)}{R}$ and $\overline{z^j(s)} = \frac{z^j(s)}{H}$, so given $\overline{\mathscr{B}_E}$, everything in the square-root expression in equation 4.3.2 is known besides $\overline{R}$.

We can put equation 4.3.1 into equation 4.3.2 for kl_V to get an expression for kl_S of resonating bodies in terms of $\overline{R}$ and $A(kl_V)$:

$$kl_S^{res} = \frac{\pi \overline{R}^2}{1 + A(kl_V^{res})\overline{R}^3} \sqrt{2\pi \overline{R} \sum_j^J \int_0^1 \overline{r^j(s)} \sqrt{\overline{R}^2 \overline{r^j(s)}'^2 + \frac{\overline{z^j(s)}'^2}{\pi^2 \overline{R}^4 I(\overline{\mathscr{B}_E})^2}} ds} \qquad (4.3.3)$$

Therefore, equations 4.3.1 and 4.3.3 give parametric equations for kl_V and kl_S in terms of parameter $\overline{R}$. These are equations for the cube-root of volume and square-root of surface area of *heave-resonating* bodies.

For all $\overline{\mathscr{B}_E}$ considered in this thesis, we have observed that equations 4.3.1 and 4.3.3 result in a curve in the $kl_V - kl_S$ space such as the one shown in figure 4-15.

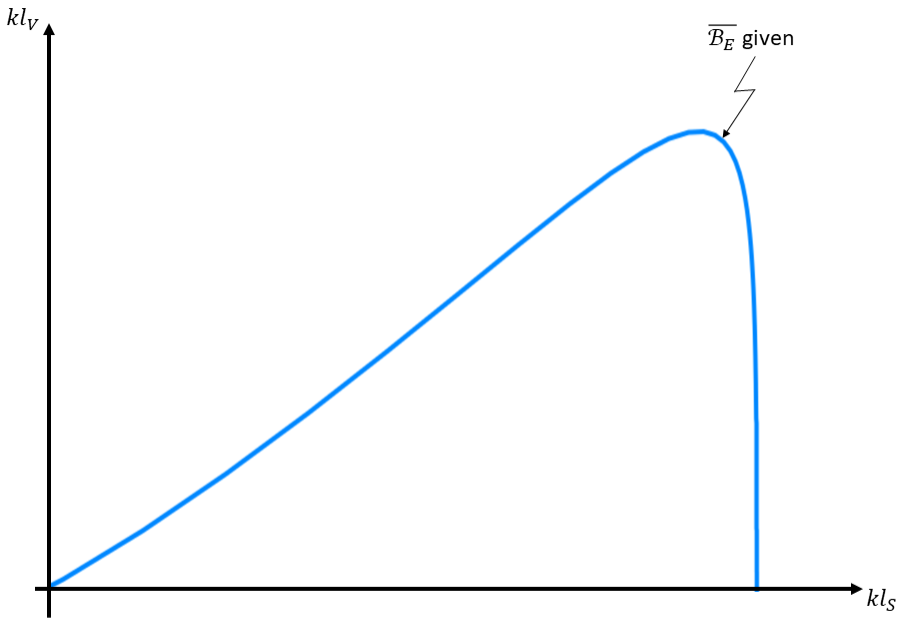

Figure 4-15: Example of $\mathcal{S}(\mathbb{R}_3^{\overline{\mathscr{B}_E}})$, the curve of the set of all shapes in class $\mathscr{C}^{\overline{\mathscr{B}_E}}$ that solve the heave resonance equation in the $kl_V - kl_S$ space

The characteristics of this curve, labeled $\mathcal{S}(\mathbb{R}_3^{\overline{\mathscr{B}_E}})$, which are true for any given $\overline{\mathscr{B}_E}$, are that it

- Is one-to-one
- Is concave down
- Starts at (0,0)
- Has a maximum at kl_V^{max}
- Has a positive slope for the left 'branch,' consisting of the lower roots of the resonance equation, $\overline{R}_1$, and a negative slope for the right 'branch,' consisting of the larger roots of the resonance equation, $\overline{R}_2$.

Recall the relation between $\overline{H}$ and $\overline{R}$, given $\overline{\mathscr{B}_E}$ (equation 4.1.31). Therefore, for $\overline{R} = 0$ (and thus $\overline{H} = \infty$), $kl_S = kl_V = 0$. As $\overline{R}$ increases (and thus $\overline{H}$ decreases), we have observed that kl_S increases as well, so we can think of the curve as a parametric

equation curve, with the parameter being $\overline{R}$. Progressing along the curve, $\overline{R}$ gets larger and $\overline{H}$ gets smaller. Therefore, for the lowest left part of the curve the shapes are deep and narrow (like a SPAR buoy), and for the lowest right part of the curve the shapes are shallow and wide (like a disk). This is illustrated in figure 4-16.

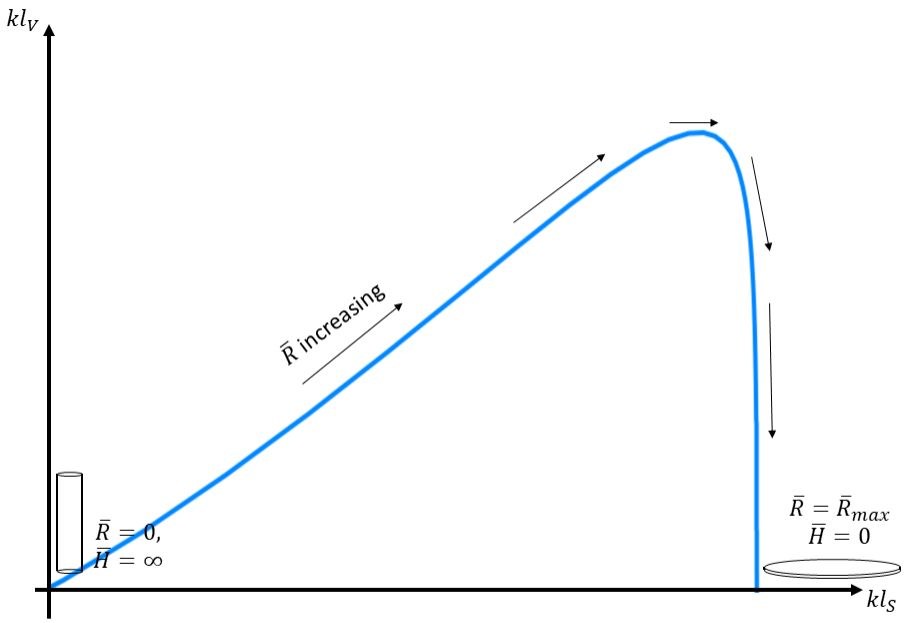

Figure 4-16: Some general characteristics observed for the set of all shapes of a given class that solve the heave resonance equation, plotted in the $kl_V - kl_S$ space: for $kl_V = kl_S = 0$, the shape is deep and narrow. Progressing along the curve, $\overline{R}$ increases and $\overline{H}$ decreases, until the bottom left where the shape is wide and shallow (like a disk)

These observations and resulting conclusions are true for any given class of shape that we considered in this thesis. For a different class, the value of $(kl_V)^{max}$ will change, as well as the value of kl_S when $kl_V = (kl_V)^{max}$, and the slopes of the left and right branches. Figure 4-17 shows a few examples of $\mathcal{S}(\mathbb{R}^{\overline{\mathscr{B}_E}}_3)$ for different $\overline{\mathscr{B}_E}$. But the general characteristics of the curve (one-to-one, concave down, with a maximum at $(kl_V)^{max}$) are true for each class.

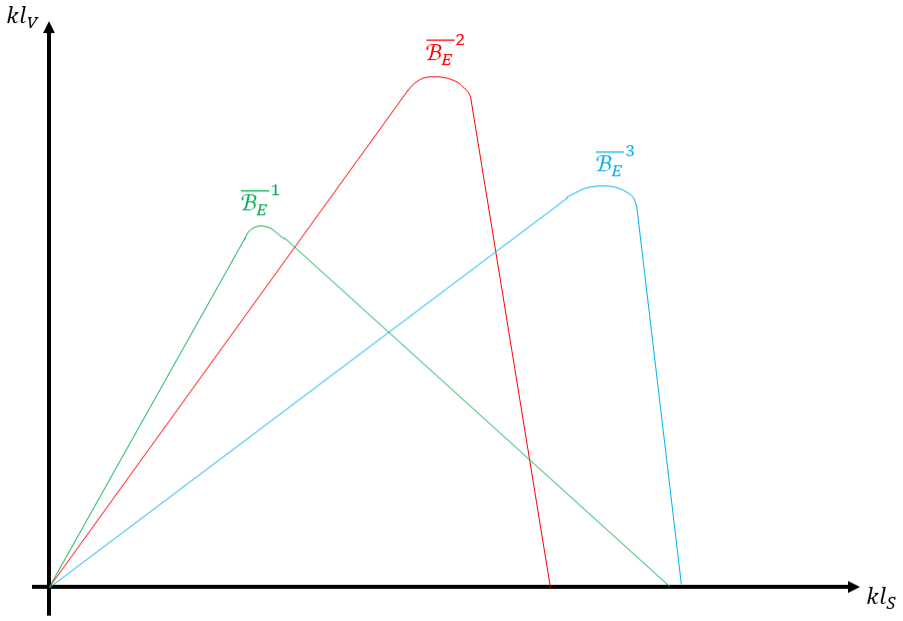

Figure 4-17: Examples of $\mathcal{S}(\mathbb{R}_3^{\overline{\mathscr{B}_E}})$ for different $\overline{\mathscr{B}_E}$

Therefore, we have shown general observations about the general shape of $\mathcal{S}(\mathbb{R}_3^{\overline{\mathscr{B}_E}})$, the curve of the set of shapes in class $\mathscr{C}^{\overline{\mathscr{B}_E}}$ that solve the heave resonance equation, plotted in the $kl_V - kl_S$ space. Knowing these general characteristics of $\mathcal{S}(\mathbb{R}_3^{\overline{\mathscr{B}_E}})$, we can now determine how and where the constraints affect it, to be able to determine the shape of the final heave population.

4.3.2 Heave motion constraint

The heave motion constraint is, given α,

$$\frac{|\xi_3|}{A} < \alpha \tag{4.3.4}$$

In this section, we will consider the case of a SPAR buoy to show that deep, narrow shapes move the most at resonance. From this fact, we can conclude that the heave motion constraint will eliminate shapes from the bottom left branch of $\mathcal{S}(\mathbb{R}_3^{\overline{\mathscr{B}_E}})$.

Consider a long, thin vertical cylinder. If we assume $R/H << 1$, with $\lambda/H = O(1)$,

slender-body theory tells us that we can approximate exciting force by the Froude-Krylov force. The heave exciting force is

$$X_3 = \iint p n_3 dS \tag{4.3.5}$$

Since we assume the shape is a cylinder, the only surface with $n_3 \neq 0$ is the bottom. Therefore, the force will be:

$$X_3^{FK} = (\pi R^2) p|_{z=-H, x=y=0} \tag{4.3.6}$$

The Froude-Krylov force uses the incident potential. For deep water, the incident wave potential is

$$\phi_I = Re\left\{ i\frac{gA}{\omega} e^{kz} e^{i(kx-\omega t)} \right\} \tag{4.3.7}$$

From the linear Bernoulli equation, pressure is

$$p = -\rho \frac{\partial \phi}{\partial t} \tag{4.3.8}$$

Putting equation 4.3.7 into equation 4.3.8, and calculating the value at $z = -H$ and $x = y = 0$, and inputting that into equation 4.3.6, we get

$$X_3^{FK} = Re\left\{ \pi R^2 \rho g A e^{-kH} e^{i\omega t} \right\} \tag{4.3.9}$$

Using the Haskind relation (Haskind, 1957), the heave damping coefficient can be expressed as

$$B_{33} = \frac{k|X_3|^2}{4A^2 \rho g V_g} \tag{4.3.10}$$

Since we are approximating exciting force by the Froude-Krylov force, $|X_3|$ will be $|X_3^{FK}|$. Therefore, the damping coefficient will be

$$B_{33} = \frac{k\left(\pi R\right)^2 \rho g A^2 e^{-2kH}}{4V_g} \tag{4.3.11}$$

The square of the amplitude of heave body motion at resonance is

$$\frac{|\xi_3|^2}{A^2} = \frac{|X_3|^2}{4\omega^2 B_{33}^2} \tag{4.3.12}$$

Using the Haskind relation again, this becomes

$$\frac{|\xi_3|^2}{A^2} = \frac{\rho g V_g}{k\omega^2 B_{33}} \tag{4.3.13}$$

Therefore, putting in our expression for approximate heave damping coefficient, given by equation 4.3.11, taking the square-root, and assuming unit-amplitude, we get an expression for the amplitude of heave body motion for a long vertical body:

$$|\xi_3| = \frac{V_g e^{kH}}{k\omega\pi R^2} \tag{4.3.14}$$

We can see from this equation that as R decreases and H increases, this motion will increase. In the limit, all long slender bodies can be approximated by a cylinder, so we justify the approximation that as shapes become deeper and narrower, their resonance motion becomes larger.

The heave motion constraint eliminates any shape for which $\frac{|\xi_3|}{A} > \alpha$, for a given α. Therefore, it will eliminate the shapes which have the largest heave motion value. As mentioned earlier, the shapes at the lower left branch of $\mathcal{S}(\mathbb{R}_3^{\overline{\mathscr{B}_E}})$ are the ones that are deepest and narrowest, so these are the shapes that will be eliminated first by the heave motion constraint. This is illustrated in figure 4-18. As α decreases (and thus the motion constraint becomes more restrictive), more of the lower left branch of $\mathcal{S}(\mathbb{R}_3^{\overline{\mathscr{B}_E}})$ is eliminated.

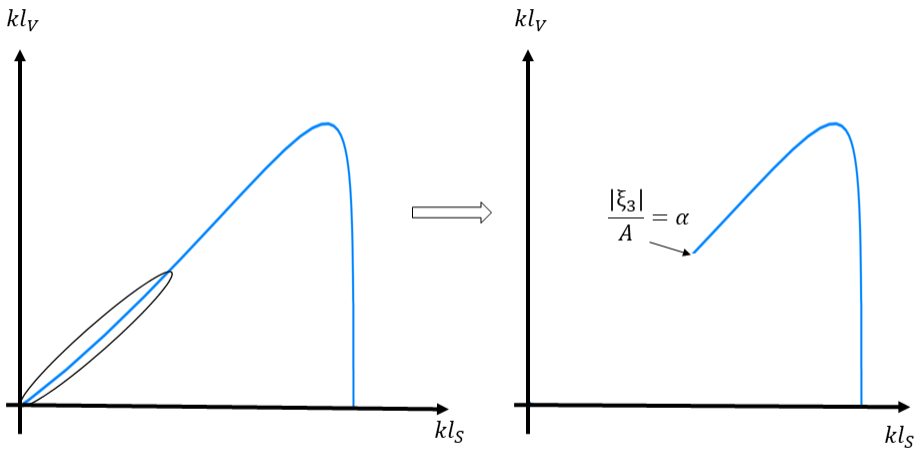

Figure 4-18: The effect of the heave motion constraint: as α decreases (so that the constraint becomes more restrictive), more of the left branch of $\mathcal{S}(\mathbb{R}_3^{\overline{\mathscr{B}_E}})$ will be eliminated.

This shows how the heave motion constraint affects $\mathcal{S}(\mathbb{R}_3^{\overline{\mathscr{B}_E}})$: it eliminates shapes from the bottom left branch.

4.3.3 Heave steepness constraint

The heave steepness constraint is, given ϵ,

$$kH > \epsilon \frac{|\xi_3|}{A} \tag{4.3.15}$$

This constraint will affect shapes that are shallow (with a small H) and shapes with a large resonance motion (large $\frac{|\xi_3|}{A}$). As shown in the previous section, the shapes with the largest $\frac{|\xi_3|}{A}$ are the ones on the bottom left branch of $\mathcal{S}(\mathbb{R}_3^{\overline{\mathscr{B}_E}})$. The shapes with the smallest kH values are those at the bottom right branch. Therefore, as illustrated in figure 4-19, the heave steepness constraint eliminates shapes from the bottom left and bottom right branch. Larger ϵ gives a more restrictive constraint, so the higher ϵ will eliminate more from each side.

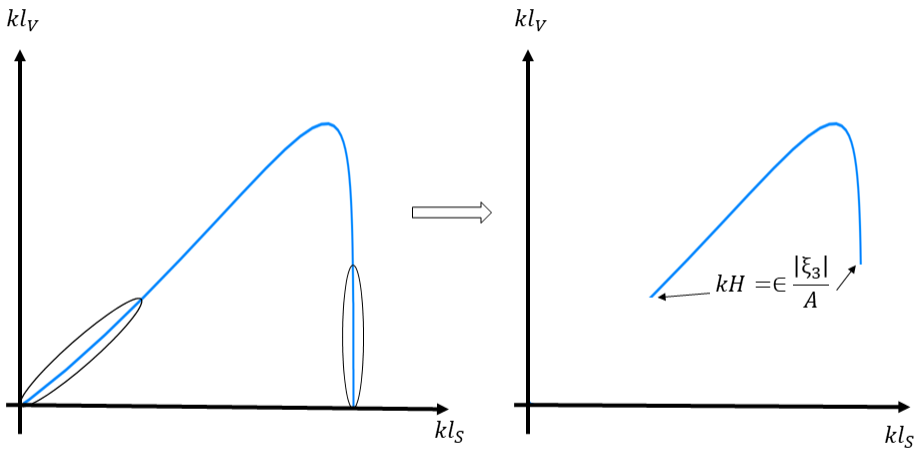

Figure 4-19: The effect of the heave steepness constraint on $\mathcal{S}(\mathbb{R}_3^{\overline{\mathscr{B}_E}})$. The heave steepness constraint eliminates shapes where $kH < \epsilon\frac{|\xi_3|}{A}$, so as ϵ increases (so that the constraint becomes more restrictive), more from the ends of both branches will be eliminated.

This shows how the heave motion constraint affects $\mathcal{S}(\mathbb{R}_3^{\overline{\mathscr{B}_E}})$: it eliminates shapes from the bottom left branch and the bottom right branch.

4.3.4 Resulting shape of the heave population curve and Pareto Front

The heave population for class $\mathscr{C}^{\overline{\mathscr{B}_E}}$ is made up of all shapes in $\mathscr{C}^{\overline{\mathscr{B}_E}}$ that are in resonance in heave and adhere to the heave motion constraint and the heave steepness constraint. $\mathcal{S}(\mathbb{R}_3^{\overline{\mathscr{B}_E}})$, the curve of the set of all shapes from class $\mathscr{C}^{\overline{\mathscr{B}_E}}$ that resonate in heave in the $kl_V - kl_S$ space looks something like the ones shown in figure 4-17. The α constraint affects the graph as shown in figure 4-18, and the ϵ constraint affects the graph as shown in figure 4-19.

Therefore, given $\overline{\mathscr{B}_E}$ the shape of the final heave population, $\mathbb{P}_3$, will be one of the

three general shapes shown in figure 4-20. Which of these shapes $\mathbb{P}_3$ will take depends on the shape of $\mathcal{S}(\mathbb{R}_3^{\overline{\mathscr{B}_E}})$, and where the constraints affect the particular class of shapes. The shapes of these curves for the population in the $kl_V - kl_S$ space will be referred to as $\mathbb{P}_A$, $\mathbb{P}_B$, and $\mathbb{P}_C$.

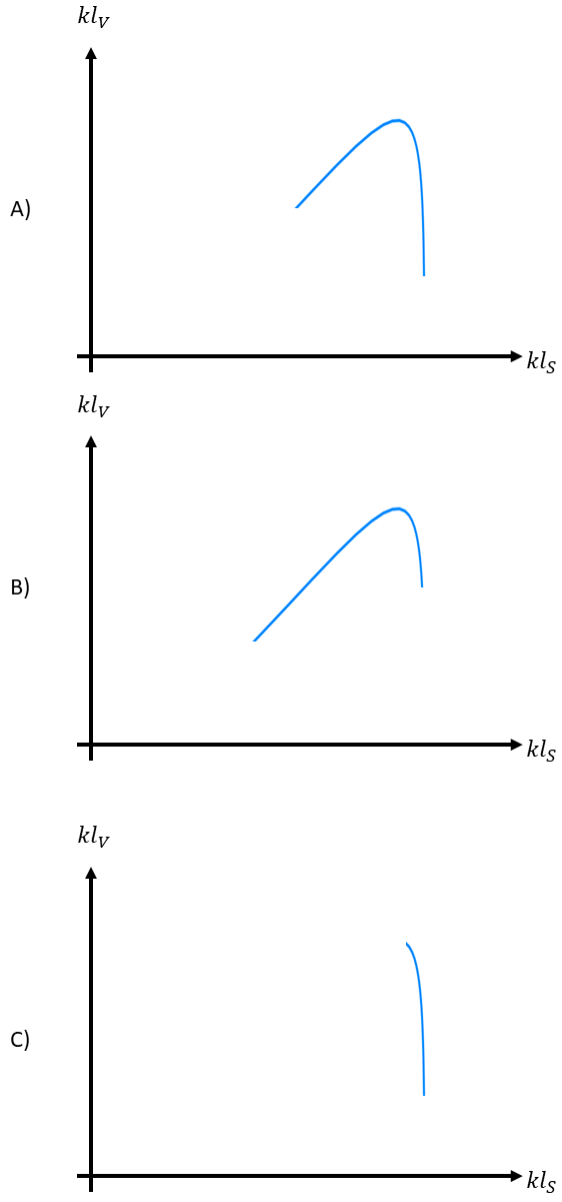

Figure 4-20: Different options for the shape of $\mathbb{P}_3$, the final heave population curves, for a given class of shapes. The shapes of curves for the population will be referred to as $\mathbb{P}_A$, $\mathbb{P}_B$, and $\mathbb{P}_C$

The resulting Pareto Fronts for each of these three options for the population shape

are given in figure 4-21. For option A, the PF is a single dot from the left branch and a cluster of points from the right branch. For option B, it is just the single dot from the left branch. For option C, it is a cluster of shapes from the right branch. The shapes of these curves for the Pareto Front in the $kl_V - kl_S$ space will be referred to as $\mathbb{PF}_A$, $\mathbb{PF}_B$, and $\mathbb{PF}_C$.

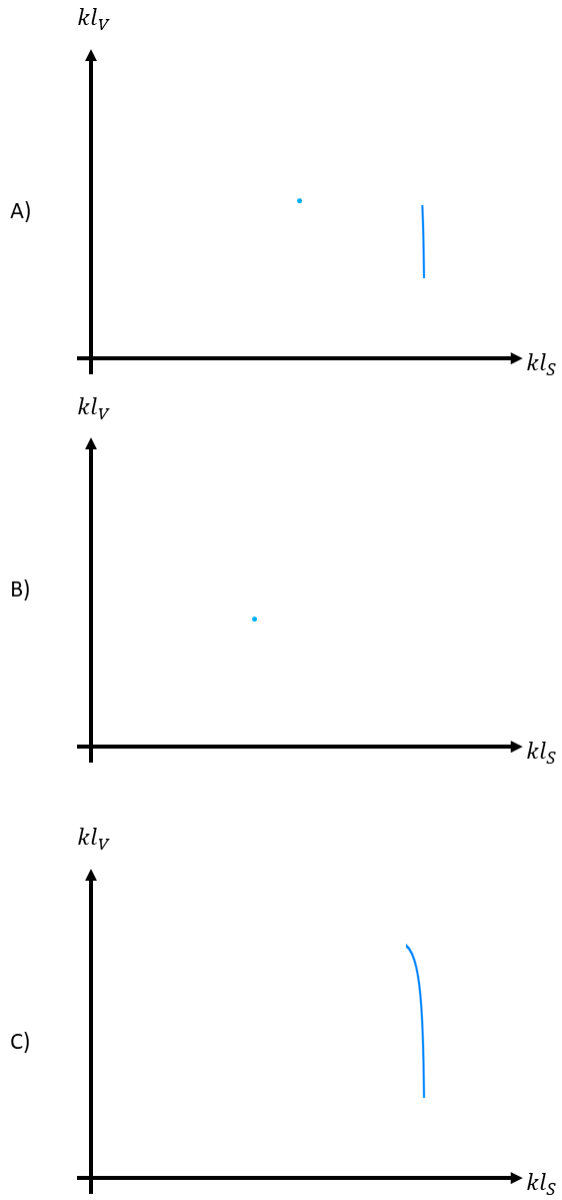

Figure 4-21: Corresponding Pareto Fronts for the options for the shape of the final heave population curve, shown in figure 4-20. The shapes of curves for the Pareto Front will be referred to as $\mathbb{PF}_A$, $\mathbb{PF}_B$, and $\mathbb{PF}_C$

Following the observation of the shape of curve $\mathcal{S}(\mathbb{R}_3^{\overline{\mathscr{B}_E}})$, we have shown in this section that, after eliminating shapes that do not adhere to the heave constraints, the shape of the final heave population, $\mathbb{P}_{3,\alpha,\epsilon}$, will fall into one of three categories, called $\mathbb{P}_A, \mathbb{P}_B$ and $\mathbb{P}_C$, shown in figure 4-20, and the corresponding shapes of the Pareto Fronts, called $\mathbb{PF}_A, \mathbb{PF}_B$ and $\mathbb{PF}_C$, are shown in figure 4-21.

If $\mathbb{PF}_3$ has shape $\mathbb{PF}_A$ or $\mathbb{PF}_B$, we know that the lone point is determined by one of the two constraints. Since both the heave motion constraint as well as the heave steepness constraint eliminate shapes from the lower left branch of $\mathcal{S}(\mathbb{R}_3^{\overline{\mathscr{B}_E}})$, we cannot predict which constraint will determine this point. Furthermore, we do not know what the geometry of the WEC represented by this point will be since it depends on its added mass and damping coefficients. In fact, we cannot say *a priori* which shape – $\mathbb{PF}_A, \mathbb{PF}_B$ or $\mathbb{PF}_C$ – the Pareto Front will take for a given $\overline{\mathscr{B}_E}$ because we cannot know the shape of $\mathcal{S}(\mathbb{R}_3^{\overline{\mathscr{B}_E}})$, and furthermore we cannot say how much of $\mathcal{S}(\mathbb{R}_3^{\overline{\mathscr{B}_E}})$ the constraints will eliminate.

An interesting, somewhat counter-intuitive phenomenon occurs because of the nature of the shape of $\mathcal{S}(\mathbb{R}_3^{\overline{\mathscr{B}_E}})$ and how the constraint affect it: as the constraints affecting the lower left branch become stricter, more of the lower left branch is eliminated. So, the Pareto Front could go from $\mathbb{PF}_B$ to $\mathbb{PF}_A$ to $\mathbb{PF}_C$. Therefore, as the constraints become stricter, the Pareto Front becomes *fuller*: there are more shapes on the Pareto Front, and less determined by the constraints. This conclusion, which is true for any given class of shapes, was enabled by the observation of the general shape of $\mathcal{S}(\mathbb{R}_3^{\overline{\mathscr{B}_E}})$, as well as our conclusions about the how the constraints form the shapes of the population and resulting Pareto Front.

4.3.5 Resulting shape of the heave-surge-pitch population curve and Pareto Front

Given $\overline{\mathscr{B}_E}$, α and ϵ, the final population for the heave-surge-pitch case, called $\mathbb{P}_{135,\alpha,\epsilon}$, is formed by eliminating shapes from $\mathbb{R}_3^{\overline{\mathscr{B}_E}}$ that do not adhere to the heave-surge-pitch

constraints. We know that the stability of the shape will increase with increasing $\overline{R}$, so we can say that the upper-bound of the center of gravity constraint ($z_G < z_G^{max}$) will affect the lower left branch. The pitch moment of inertia constraint (that the expression for I_{55} must be greater than 0) will affect shapes with large A_{55}, large A_{15}, small R, small volume and/or small z_B. Otherwise, however, generally determining the shape of the populations and Pareto Fronts for the heave-surge-pitch case is much more difficult than for the heave-only case. This is because the constraints do not only affect the ends of the curves. Since they can affect the middle, the populations in the end could be disjointed, making it impossible to generalize what the shape of the curve will be. We go through each constraint in the next chapter for the case of the cylinder and show where and how they affect the shape of the final heave-surge-pitch population.

4.3.6 Summary

In this section, we examined the behavior of the population of any given class of shapes in the context of our optimization process and goals. Because our optimization functions are to minimize kl_V and kl_S, we examined the population in the $kl_V - kl_S$ space.

Given $\overline{\mathscr{B}_E}$, the curve of the set of shapes in $\mathscr{C}^{\overline{\mathscr{B}_E}}$ that solve the heave resonance equation in the $kl_V - kl_S$ space is called $\mathcal{S}(\mathbb{R}_3^{\overline{\mathscr{B}_E}})$. We observed that, for any given $\overline{\mathscr{B}_E}$, $\mathcal{S}(\mathbb{R}_3^{\overline{\mathscr{B}_E}})$ has certain common characteristics: the curve is one-to-one and concave down, with a maximum kl_V value at $(kl_V)^{max}$, a positive slope before this maximum point and a negative slope after the maximum point. Examples are shown in figure 4-17.

The left branch of $\mathcal{S}(\mathbb{R}_3^{\overline{\mathscr{B}_E}})$ corresponds to the shape with $\overline{R}$ value given by the smaller of the two roots of the heave resonance equation, and the right branch of $\mathcal{S}(\mathbb{R}_3^{\overline{\mathscr{B}_E}})$ corresponds to the shape with $\overline{R}$ value given by the larger of the two roots of the heave resonance equation.

The lower left branch of $\mathcal{S}(\mathbb{R}_3^{\overline{\mathscr{B}_E}})$ corresponds to shapes with small $\overline{R}$, and thus large $\overline{H}$, meaning that the shapes are deep and narrow. Along the curve, $\overline{R}$ increases and $\overline{H}$ decreases, meaning that the shapes become wider and thinner, until the lower right branch which corresponds to an infinitely thin disk.

As shown in section 4.3.2, deeper, narrower shapes move more at resonance. Therefore, the heave motion constraint will affect the lower left branch of $\mathcal{S}(\mathbb{R}_3^{\overline{\mathscr{B}_E}})$. The heave steepness constraint affects shapes with small kH or large $\frac{|\xi_3|}{A}$ values. Therefore, it affects both the lower right branch and the lower left branch of $\mathcal{S}(\mathbb{R}_3^{\overline{\mathscr{B}_E}})$.

The heave population consists of all the resonating shapes that adhere to the heave motion constraint and the heave steepness constraint, so we concluded that the three possible general shapes of the curve of the population in the $kl_V - kl_S$ plane are shown in figure 4-20. The corresponding Pareto Front curves are shown in figure 4-21.

In the next chapter, we look at the cylinder class. This will give a concrete example to all of the observations and conclusions we discussed in this section. We will show what $\mathcal{S}(\mathbb{R}_3^{\overline{\mathscr{B}_E}})$ looks like and how each constraint affects this curve to form the populations.

4.4 Forming heave and heave-surge-pitch populations and Pareto Fronts for groups of shapes

In the previous section, we examined populations and Pareto Fronts for a single class of shapes. In this section, we will discuss how populations and Pareto Fronts are formed when looking at *groups* of classes of shapes, since that is what we optimize and present in chapter 6.

Recall from section 4.1.5 that a group of shapes is a set of classes of shapes. For example, group $\mathscr{G}^{FB}$ contains all shapes consisting of two piecewise linear sections with one kink with a flat bottom. Class $\mathscr{C}^{\overline{r_1}=\overline{r_1}^i}$, defined in equation 4.1.44, is the set of shapes with $\overline{z_1} = -1$ and $\overline{r_1} = \overline{r_1}^i$. The group of flat-bottomed shapes contains all

such shapes: that is, it is the set of classes of shapes with different $\overline{r_1}$ values.

In the previous section, we looked at a single class of shapes, given by $\overline{\mathscr{B}_E}$, and we examined the shape of $\mathcal{S}(\mathbb{R}_3^{\overline{\mathscr{B}_E}})$, the entire set of shapes that solve the heave resonance equation, and the shapes of the final heave and heave-surge-pitch populations, $\mathbb{P}_3$ and $\mathbb{P}_{135}$, and the resulting Pareto Fronts, $\mathbb{PF}_3$ and $\mathbb{PF}_{135}$.

These conclusions aid in describing populations and Pareto Fronts for groups of shapes, too. For example, consider figure 4-22, which shows an example of a population from three classes of shapes: $\overline{\mathscr{B}_E}^1$, $\overline{\mathscr{B}_E}^2$ and $\overline{\mathscr{B}_E}^3$. The population for the group consisting of these three classes consists of all of the shapes from all three curves.

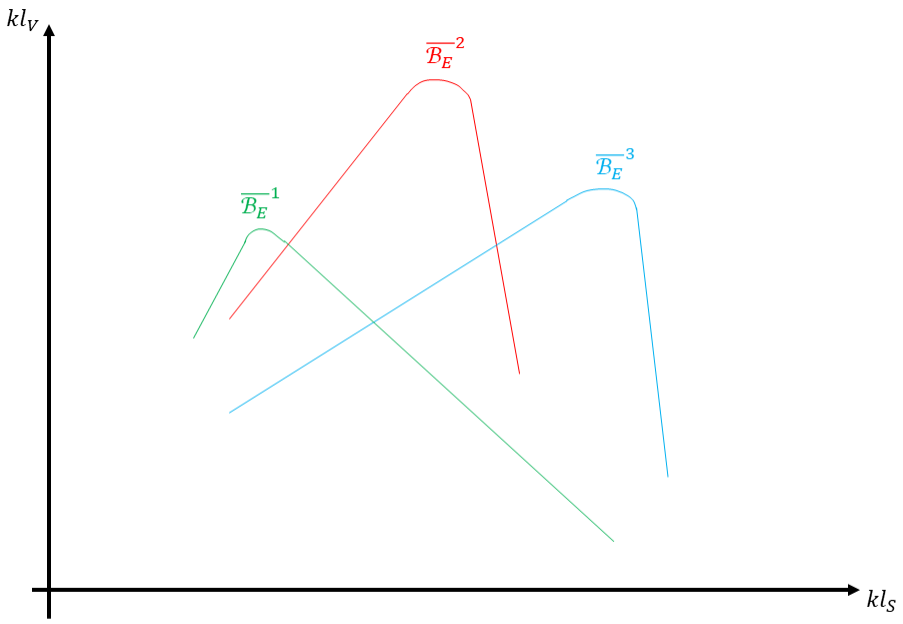

Figure 4-22: Examples of a population from a group of shapes consisting of three classes: $\overline{\mathscr{B}_E}^1$, $\overline{\mathscr{B}_E}^2$ and $\overline{\mathscr{B}_E}^3$

The resulting Pareto Front for this group is shown in figure 4-23. We see that none of the shapes from $\overline{\mathscr{B}_E}^2$ are in the Pareto Front. The Pareto Front consists of a single dot from the left branch of $\overline{\mathscr{B}_E}^1$, a single dot from the left branch of $\overline{\mathscr{B}_E}^3$, and a cluster from the right branch of $\overline{\mathscr{B}_E}^1$. The observations and conclusions we made

about any given class of shapes enables us to know that the single points are from the left branch, and from different classes, and that the cluster is from the right branch.

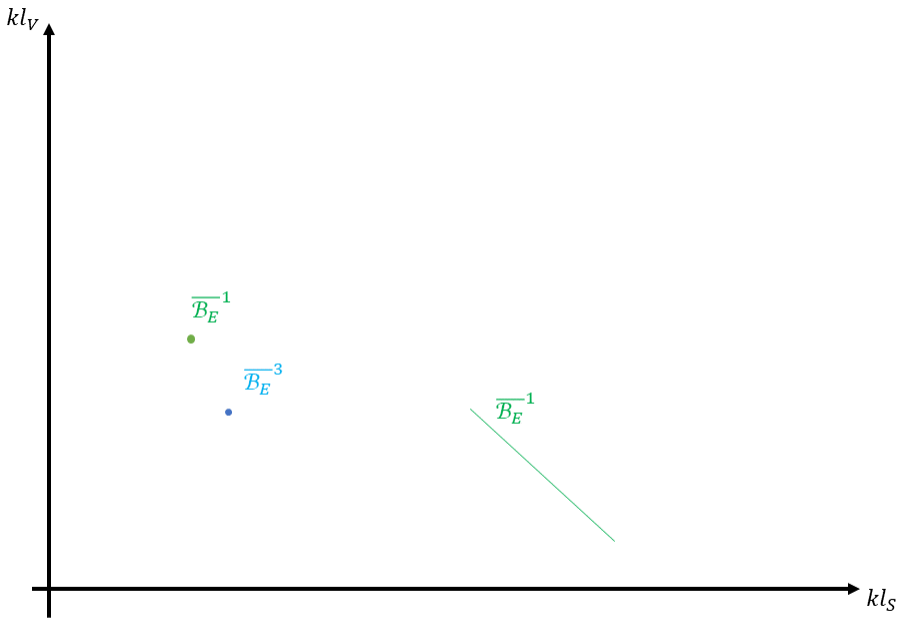

Figure 4-23: Resulting Pareto Front for the population shown in figure 4-22

In the next chapter, we show the example of a single class of shapes: cylinders. But in chapter 6, we look at groups of shapes, so the Pareto Fronts will not have the same easily describable characteristics as for a single class.

Figure 4-24 shows a flow chart of the optimization process for a group of shapes. The details of the multi-objective evolutionary algorithm are described in the next section. But figure 4-24 shows the overall process. Firstly we specify the group we are optimizing, the α value, the ϵ value, and if it is a heave-only optimization or a heave-surge-pitch optimization. Within the optimization algorithm, each organism is specified by a vector $\overline{V_i}$:

$$\overline{V_i} = \left\{(kl_V)_i, (\overline{\mathscr{B}_E})_i\right\} \tag{4.4.1}$$

The theorem from section 4.2 is then used to find the roots, given V_i, if they exist: $\overline{R}_1(\overline{V_i}), \overline{R}_2(\overline{V_i})$. The relevant parameters for the shapes defined by $\overline{B}_1 = \left\{\overline{R}_1, kl_V, \overline{\mathscr{B}_E}\right\}$

and $\overline{B}_2 = \left\{\overline{R}_2, kl_V, \overline{\mathscr{B}_E}\right\}$ are tested to determine if they adhere to the constraints (for the heave-only optimizations, this is the heave motion constraint and heave steepness constraint, and for the heave-surge-pitch optimizations, this is the heave motion constraint, heave steepness constraint, surge motion constraint, pitch motion constraint, pitch steepness constraint, the center of gravity constraint, and the pitch moment of inertia constraint). For each shape, if it adheres to the constraints of the specified problem, it is added to the population. Otherwise, it is discarded. Therefore, the population does not correspond to the number of organisms: for each generation, sometimes there are 0 shapes added to the population, sometimes 1, and sometimes 2.

The optimization optimizes $\overline{V_i}$ vectors to find the best kl_V and $\overline{\mathscr{B}_E}$'s to minimize kl_V and kl_S. The details of this optimization algorithm are found the next section.

Here, we highlight another benefit of the theorem described in section 4.2. For a given $\overline{V}^* = \left\{kl_V^*, \overline{\mathscr{B}_E}^*\right\}$ there are 0 roots of the heave resonance equation, we know that kl_V^* is greater than $(kl_V)^{max}$ for $\overline{\mathscr{B}_E}^*$, so we can disregard any $\overline{V_i}$ with $kl_V > kl_V^*$ and $\overline{\mathscr{B}_{Ei}} = \overline{\mathscr{B}_E}^*$.

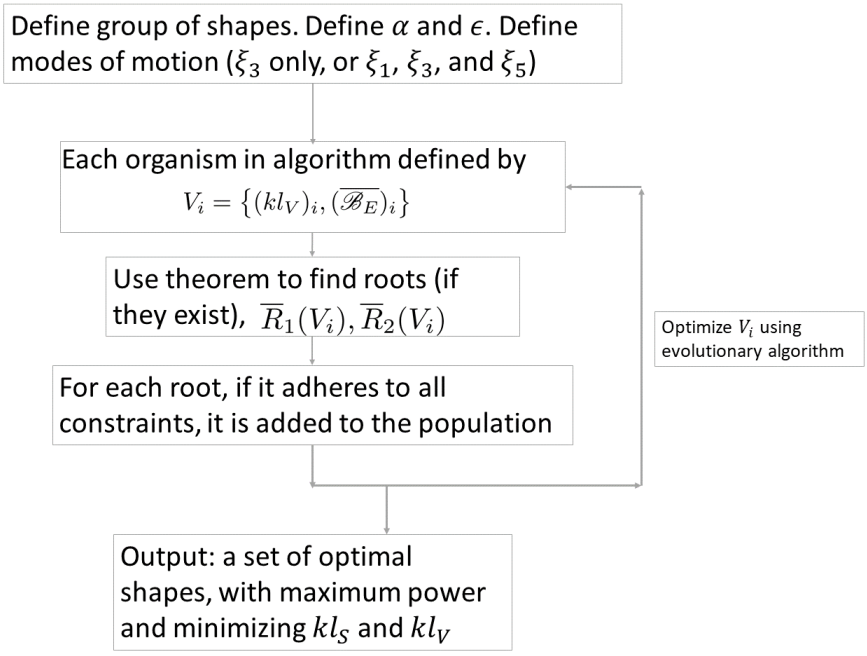

Figure 4-24: Flow chart of optimization process (not algorithm)

4.5 Multi-objective evolutionary algorithm

We use a multi-objective evolutionary algorithm. For more information, see (Deb, 2011). This algorithm is a genetic algorithm for multiple objective functions. In this section, we will summarize the algorithm. We did a sensitivity study for the algorithm, which is shown in Appendix C. The multi-objective evolutionary algorithm is based on the algorithm developed by Deb (2011) but has been adapted to our problem.

4.5.1 Flow chart and explanation

The flow chart of the optimization is shown in figure 4-25. For each optimization run, the group to optimize is defined, as well as α and ϵ. For a given group, the range of values of each parameter in $\overline{\mathscr{B}_E}$, as well as the range of values of kl_V are specified.

For example, for flat-bottomed shapes, the changing parameter in $\overline{\mathscr{B}_E}$ is $\overline{r_1}$, since $\overline{z_1} = -1$ and all coefficients of the parametric polynomial basis functions are 0. So, the range of $\overline{r_1}$ could be specified as all values between 0.1 and 2, with a stepsize of 0.02, and the range of kl_V could be specified as all values between 0.3 and 1.7, with a stepsize of 0.05.

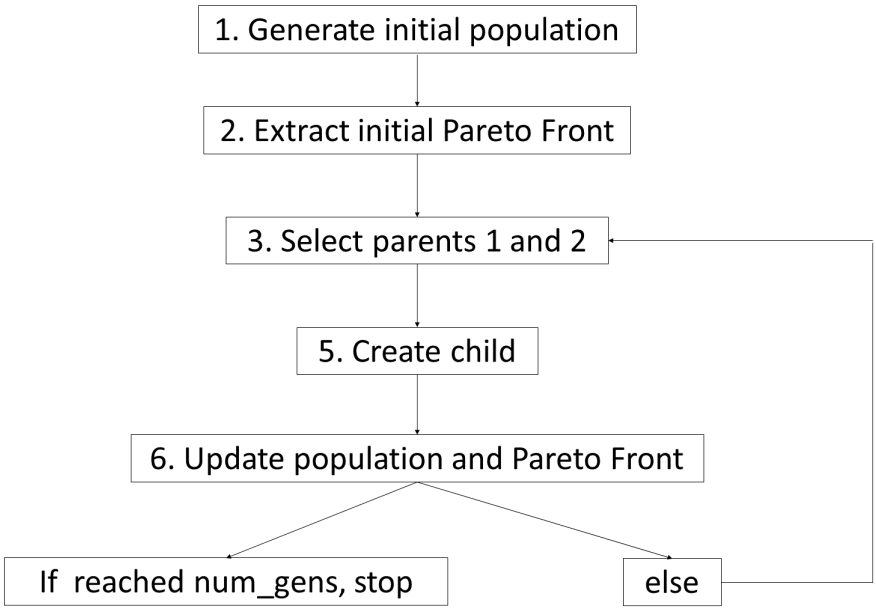

Figure 4-25: Flow chart of optimization algorithm

1. Generate initial population

   The initial population size, *popsize*, specifies how many organisms are randomly selected, given the ranges of the parameters. Each organism is specified by $\overline{V_i} = \left\{(kl_V)_i, (\overline{\mathscr{B}_E})_i\right\}$, so for flat-bottomed shapes it would be $\overline{V_i} = \{(kl_V)_i, (\overline{r_1})_i\}$. For one-kink shapes, it would be $\overline{V_i} = \{(kl_V)_i, (\overline{r_1})_i, (\overline{z_1})_i\}$.

   For $i = \{1, 2, ..., popsize\}$, we find the roots of the heave resonance equation, using the theorem described in section 4.2, labeled $\overline{R}_1(\overline{V_i})$ and $\overline{R}_2(\overline{V_i})$, if they exist. For the resulting shapes, $\overline{B}_1 = \left\{\overline{R}_1(\overline{V_i}), \overline{V_i}\right\}$ and $\overline{B}_2 = \left\{\overline{R}_2(\overline{V_i}), \overline{V_i}\right\}$, the parameters needed to determine if they adhere to the constraints are found. If

they do adhere to the constraints, they are added to the population. If not, they are disregarded. Therefore, the size of the population will not necessarily be *popsize*, since for each $\overline{V_i}$ there could be 0, 1, or 2 shapes added to the population. For each optimization run, the initial population size, *popsize*, the mutation probability, $\mathbb{P}_M$, and the number of generations, num_gens, are specified.

2. Extract initial Pareto Front

   The Pareto Front is the set of *nondominated* $\overline{B}$ vectors. For two vectors $\overline{B}_1$ and $\overline{B}_2$, vector $\overline{B}_1$ *dominates* vector $\overline{B}_2$ if $kl_V(\overline{B}_1) \leq kl_V(\overline{B}_2)$, $kl_S(\overline{B}_1) \leq kl_S(\overline{B}_2)$ and $kl_V(\overline{B}_1) < kl_V(\overline{B}_2)$ or $kl_S(\overline{B}_1) < kl_S(\overline{B}_2)$.

   For each $\overline{B}$ in the initial population, we test it against the rest of the population. If it is dominated by any other organism, it is eliminated. Once these tests are done for the entire population, the set of all nondominated organisms is the Pareto Front.

3. Select parent 1

   Then, the optimization loop begins. Two $\overline{B}$ vectors are chosen randomly from the current population. If one dominates the other, choose the dominant one. If neither dominates the other, we choose randomly among them. The result is Parent 1.

4. Select parent 2

   One $\overline{B}$ vector is chosen randomly from the current Pareto Front. This is Parent 1.

5. Create child

   Parent 1's $\overline{V}$ vector is labeled $\overline{V}_{p1}$ and parent 2's is $\overline{V}_{p2}$. We first perform crossover to create $\overline{V}_c$. A number between 1 and the length of $\overline{V}$ minus 1 is randomly chosen, labeled *c_idx*. For example, for the one-kink group, since

each $\overline{V}$ has length 3, *c_idx* can be either 1 or 2. $\overline{V}_c$ is defined as the first *c_idx* values from $\overline{V}_{p1}$ and the rest from $\overline{V}_{p2}$.

Then, a biased coin is flipped with probability $\mathbb{P}_M$. If the coin is a head, mutation is performed. Otherwise, the final child $\overline{V}$ vector is defined to be $\overline{V}_c$. If mutation is performed, a number between 1 and the length of $\overline{V}$ is randomly chosen, labeled *m_idx*. The parameter in position *m_idx* is then mutated: the resulting $\overline{V}$ vector, $\overline{V}_m$, takes its values from $\overline{V}_c$ except for in position *m_idx*, where a new value is randomly selected within the constraints of the parameter. The final child $\overline{V}$ vector, $\overline{V}_o$, is defined by $\overline{V}_c$ if mutation is not performed, and $\overline{V}_m$ otherwise.

6. Update population and Pareto Front:

   Using a similar procedure to in the initial population, the roots of the heave resonance equation are found for the given $\overline{V}_o$, and if they adhere to the heave constraints, it is added to the population. So for each generation, there could be 0, 1, or 2 shapes added to the population. The updated Pareto Front is found from the updated population.

   If we have reached *num_gens*, output the current population and Pareto Front. If not, return to step 3 to go through another generation.

This section describes the multi-objective evolutionary algorithm specific to our optimization. We show convergence using the sensitivity study in Appendix C. This is an efficient procedure, and is made more efficient by using our new theorem to find roots of the resonance equation, which essentially decreases the degree of freedom of the optimization.

4.6 Summary

In chapter 3, we described our optimization framework. We showed why we defined optimality by requiring maximum power for all shapes and minimizing surface area

and volume, and why we introduce constraints to the problem.

In this chapter, we described the procedure to execute this optimization. In section 4.1, we outlined our description of geometric shape by piecewise parametric polynomial basis functions. In this way, we can represent very general geometries by entire functions, with the coefficients of the basis functions to be the parameters to put into the optimization, instead of panel locations, for example. We then introduced the definitions of a class of shapes and a group of shapes.

In section 4.2, we introduce a novel theorem to find roots of the heave resonance equation, using an approximation for added mass which turns the equation into a cubic equation for $\overline{R}$ which can be solved explicitly. This approximation and theorem add to our understanding of the heave resonance equation and the dependence on geometric shape, and it also significantly reduces the computational effort required for optimization. Using the theorem we essentially reduced the degrees of freedom of the optimization by one, increasing the efficiency 100x compared to brute-force tests

In section 4.3, we presented some general observations and conclusions for any given class of shapes. Given $\overline{\mathscr{B}_E}$, we know that $\mathcal{S}(\mathbb{R}_3^{\overline{\mathscr{B}_E}})$, the curve of the set of shapes in class $\mathscr{C}^{\overline{\mathscr{B}_E}}$ that solve the heave resonance equation in the $kl_V - kl_S$ space will have certain characteristics: it will be a one-to-one, concave down curve, starting at the origin with maximum at $(kl_V)^{max}$. The left and right branches correspond to the smaller and larger roots of the heave resonance equation, respectively. The lower left branch has deep, narrow shapes and the bottom right branch has wide, shallow shapes. Consequently, the heave motion constraint will affect the lower left branch and the heave steepness constraint will affect the lower left and lower right branches. We can conclude that there are three possible shapes of the heave population for a given class of shapes, as shown in figure 4-20, with corresponding Pareto Fronts shown in figure 4-21. We also saw the counter-intuitive phenomenon that, as the motion constraint becomes stricter, and thus more of the lower left branch is eliminated, the Pareto Front becomes fuller and less determined by the constraint.

In section 4.4 we describe the procedure for forming populations of groups of shapes, showing how using the theorem from section 4.2 increases efficiency, and how we can perform systematic investigations of a broad range of shapes and see how constraints affect the optimal shapes.

In section 4.5 we presented the details for the multi-objective evolutionary algorithm, showing a flow chart and explaining each step of the algorithm.

In this chapter, we presented our general, efficient and efficacious procedure to execute the optimization and provide insights. In the next chapter, we use the cylinder to showcase the optimization framework and procedure.

Chapter 5

Optimizing the dimensions of a cylinder

In chapter 3, the framework of our optimization problem was presented, while in chapter 4 the specific approach that we take to solve the optimization was explained. In this chapter, the framework and optimization approach will be demonstrated for the case of a simple set of shapes: cylinders.

The goal is to optimize the dimensions of the cylinder to minimize the volume and surface area, while keeping extractable power maximum, under different constraint regimes. Limiting the scope of this chapter to only cylinders allows for a physically intuitive and relevant exploration of the process to be developed, without overcomplication. We will look at how the population is formed, first by finding roots to the heave resonance equation and then by studying how each constraint affects the population and the resulting Pareto Front.

In addition to being a helpful aid which demonstrates our framework and optimization, the results of the cylinder are of significant interest themselves, since the cylinder is one of the simplest and most common shapes used in ocean engineering. Therefore, this chapter yields the dimensions of *the best* cylinders that should be used under differing constraints to minimize volume and surface area, while keeping extractable

power maximum. Since this is a multi-objective optimization, the results of the optimization for different constraint values are *sets* of optimal cylinders. Information about the dimensions, body motions and some other physical parameters is provided, which could aid a developer in deciding which cylinder would be ideal. Within these sets, other parameters could be used to find an optimal engineering design (for example cost, manufacturing techniques, survivability, etc.) but it is outside the scope of this thesis to decide within these sets which specific cylinder should be used.

The focus on cylinders only in this chapter also provides us with a useful benchmark to which other shapes may be compared. Therefore, when detailing the results from more complicated optimizations with multiple shape classes in the next chapter, we will compare the results to the cylinders found in this chapter. This allows us to determine how much 'better' (i.e. how much smaller is the surface area and/or volume) than the cylinder it is possible to achieve with more general geometries.

In the first section of this chapter, the approach described in the previous chapter is applied to cylinders, showing how populations are formed by finding roots to the heave resonance equation and eliminating shapes that do not adhere to the constraints. In the second section, the results for the heave-only optimization are presented and the results discussed. In the third section, the results for the heave-surge-pitch optimization are presented and the results are again discussed.

5.1 Detailed example of approach

In this section, the optimization framework, described in chapter 3, and the approach we developed, described in chapter 4, are demonstrated for cylinders. We will first show how the theorem described and proved in section 4.2 enables us to find the roots of the heave resonance equation, thus giving us shapes that are in resonance in heave.

As discussed in chapter 3, to form the population for the optimization for a WEC moving and extracting energy in the heave mode only, we consider all shapes that

are in resonance in heave and then eliminate shapes that do not adhere to the heave constraints. To form the population for the case of a WEC moving and extracting energy in heave, surge and pitch, we consider all shapes that are in resonance in heave and then eliminate shapes that do not adhere to the heave, surge and pitch constraints. The reason that we start with shapes that solve the *heave* resonance equation is because there are passively controllable terms in the surge and pitch resonance equations, so the geometric shape can be defined first (by the heave resonance equation), and then these controllable terms ensure resonance in surge and pitch, and the constraints eliminate impractical shapes.

In this section, we demonstrate this process by first showing the set of all truncated cylinders that solve the heave resonance equation, and then going through each heave, surge and pitch constraint individually to demonstrate which shapes are eliminated by each constraint.

5.1.1 Finding roots of the heave resonance equation

In the previous chapter we presented a novel theorem that uses an approximation for heave added mass to get solutions to the heave resonance equation for any class of shape. In addition to aiding our understanding of the problem generally, one benefit of this theorem is that it allows us to decrease the optimization by one parameter. Since the heave resonance equation depends on heave added mass, which does not have an analytic form for most geometries, without this theorem we would need to solve the heave resonance equation by the brute-force testing of many shapes. However, using this theorem allows us to approximate the roots and then perform a local optimization to find more accurate values, speeding up the process tremendously.

The theorem states that if, given a class of shapes – that is, given $\overline{\mathscr{B}_E}$ – the nondimensional heave added mass coefficient, $\overline{A_{33}} = \frac{A_{33}}{\rho l_V^3}$ can be approximated as

$$\overline{A_{33}} = A(kl_V)\overline{R}^3 \tag{5.1.1}$$

with further restrictions on $A(kl_V)$, given in section 4.2), then there will be two roots to the heave resonance equation for $kl_V < (kl_V)^{max}$, and none for $kl_V > (kl_V)^{max}$. The heave resonance equation, using the approximation given in equation 5.1.1 is

$$\pi\overline{R}^2 - kl_V\left(1 + A(kl_V)\overline{R}^3\right) = 0 \tag{5.1.2}$$

Given kl_V, this is simply a cubic equation for $\overline{R}$. In our optimization, each organism is defined by kl_V and $\overline{\mathscr{B}_E}$. So, we can use this theorem, and the resulting simplification of the heave resonance equation, for each organism:

- Given kl_V and $\overline{\mathscr{B}_E}$, look at 10 values of $\overline{R}$. Run WAMIT for these 10 shapes to get $\overline{A_{33}}$ values.
- Fit the curve $\overline{A_{33}} = A_c\overline{R}^3$ to the data points to find the constant A_c.
- Use this constant in equation 5.1.2, which becomes

$$\pi\overline{R}^2 - kl_V\left(1 + A_c\overline{R}^3\right) = 0 \tag{5.1.3}$$

  where kl_V is given. This is a cubic equation which can be solved analytically to find the roots of the equation. When $kl_V < (kl_V)^{max}$, there are two real roots, which will be called $\overline{R}_1^a$ and $\overline{R}_2^a$.
- From the theorem, we saw that there will either be 0 or 2 roots.

Once we have $\overline{R}_1^a$ and $\overline{R}_2^a$, we can perform local optimizations using $\overline{A_{33}}$ from WAMIT instead of the approximation $A_c\overline{R}^3$ to find more accurate values for the roots, which will be called $\overline{R}_1$ and $\overline{R}_2$. Figure 5-1 helps to illustrates this procedure. The plot shows the heave resonance equation as a function of $\overline{R}$. Each color represents a different kl_V value. The solid curve shows the resonance equation using $\overline{A_{33}}$ values from WAMIT, whereas the dashed curve shows the equation with the added mass approximation (given by equation 5.1.3). The solid vertical lines show the roots of the resonance equation which were found by brute-force evaluation, and the dashed vertical lines

show the approximate values, found by solving the cubic equation for $\overline{R}$. The roots represented by the dashed lines are then used to perform local optimizations which finds more accurate values of the roots

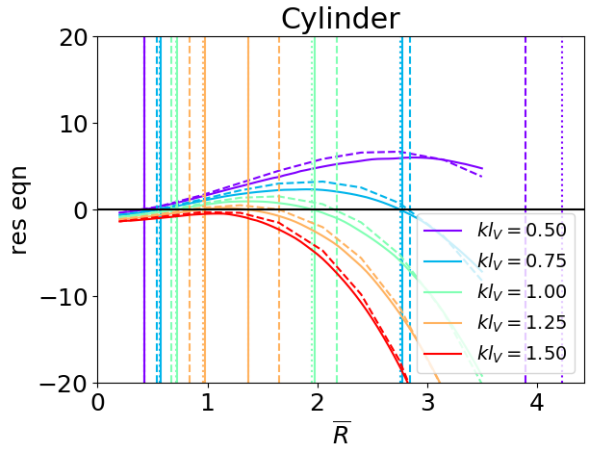

Figure 5-1: Illustrating how roots of the heave resonance equation are found by using the added mass approximation and theorem presented in the previous chapter

Figure 5-1 is also helpful in visualizing the heave resonance equation. For smaller kl_V, the roots of the resonance equation are far apart from each other. As kl_V increases, the resonance equation curve moves down, and the roots approach one another. Eventually, at $kl_V = (kl_V)^{max}$, the roots become a double root, and the resonance equation meets the y-axis once, at that double root. For $kl_V > (kl_V)^{max}$, the resonance equation does not cross the y-axis and there are no roots to the resonance equation.

For each kl_V, the above procedure is performed. The result is $\mathbb{R}_3^{cyl}$, the set of all cylinders that solve the heave resonance equation. In figure 5-2, we plot this set. In the left plot, each organism in the set is plotted in a $kl_V - kl_S$ scatter plot. This curve is called $\mathcal{S}(\mathbb{R}_3^{cyl})$. Each organism is given a color, ranging from purple to red, corresponding to increasing kl_S. The right plot shows the shape of some of the cylinders in $\mathbb{R}_3^{cyl}$. The colors correspond to the left plot, so the deeper narrow purple cylinder corresponds to an organism on the lower left branch of $\mathcal{S}(\mathbb{R}_3^{cyl})$, whereas the wide shallow orange cylinder corresponds to the lower left branch of $\mathcal{S}(\mathbb{R}_3^{cyl})$.

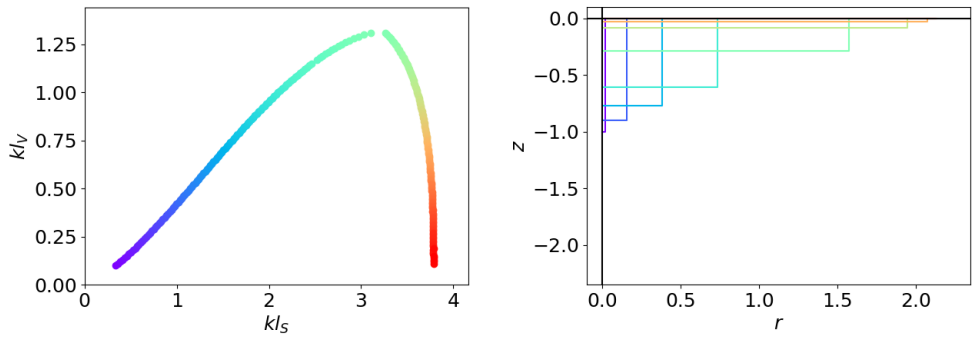

Figure 5-2: $\mathbb{R}_3^{cyl}$, the set of cylinders that solve the heave resonance equation. The left plot shows $\mathcal{S}(\mathbb{R}_3^{cyl})$, the curve of $\mathbb{R}_3^{cyl}$ in the $kl_V - kl_S$ space, where the colors, from purple to red, correspond to increasing kl_S. The right plot shows the shape, in the $r - z$ plane of some of the cylinders in the set, with colors corresponding to the left plot. Shapes at the lower left branch of $\mathcal{S}(\mathbb{R}_3^{cyl})$ correspond to deep, narrow cylinders. Along the curve, $\overline{R}$ increases and $\overline{H}$ decreases, so the shapes at the lower right branch correspond to wide, shallow cylinders.

Section 4.3 discusses general observations and conclusions the shape of the curve of $\mathbb{R}_3$ in the $kl_V - kl_S$ space, $\mathcal{S}(\mathbb{R}_3^{\overline{\mathscr{B}_E}})$. $\mathcal{S}(\mathbb{R}_3^{cyl})$, shown in figure 5-2, is a real example of this observation. The characteristics of this curve that are general to any given class are that it is a one-to-one concave down curve with a maximum value of $(kl_V)^{max}$. The left branch corresponds to the smaller roots of resonance equation, $\overline{R}_1$, and the right branch corresponds to larger roots of the resonance equation, $\overline{R}_2$.

5.1.2 Heave constraints and where they affect the population

From $\mathbb{R}_3^{cyl}$, the heave population, $\mathbb{P}_3$ is formed by eliminating shapes that do not adhere to the two heave constraints: the heave motion constraint and the heave steepness constraint. We will now who which cylinders these constraints eliminate. We look at each constraint starting from $\mathbb{R}_3$, instead of considering them cumulatively.

Heave motion constraint

The heave motion constraint is, given α,

$$\frac{|\xi_3|}{A} < \alpha \tag{5.1.4}$$

As shown in section 4.3, the heave motion constraint will affect the lower left branch of $\mathcal{S}(\mathbb{R}^{cyl}_3)$, since these deep, narrow shapes are the ones that move the most at resonance. Figure 5-3 shows which regions are eliminated for a few different α values: $\alpha = 3$, 2, and 1. As α becomes smaller, the motion constraint becomes more restrictive, therefore eliminating shapes further up the left branch. All of the shapes given a red color will be eliminated when $\alpha = 3$ – that is, if you require that $\frac{|\xi_3|}{A} < 3$. If $\alpha = 2$, all shapes given a green or red color would be eliminated. If $\alpha = 1$, shapes given a purple, red or green color will be eliminated. All shapes given a blue color, then, have $\frac{|\xi_3|}{A} < 1$.

Figure 5-3 also labels the H/R value of the cylinders at transitions from one constraint 'regime' to another. For example, if $\alpha = 3$, the cylinder with $H/R = 1.18$ is the deepest cylinder that is in $\mathbb{R}^{cyl}_3$ and adheres to the constraint $\frac{|\xi_3|}{A} < \alpha$. Therefore, we know that $\frac{|\xi_3|}{A} = 3$ for this cylinder. When $\alpha = 2$, the deepest shape in $\mathbb{R}^{cyl}_3$ adhering to the constraint $\frac{|\xi_3|}{A} < 2$ has an H/R value of 0.85, and when $\alpha = 1$, the corresponding cylinder has $H/R = 0.47$. As α decreases, the point where $\frac{|\xi_3|}{A} = \alpha$ is further up the left branch, corresponding to a larger kl_V and kl_S and a smaller H/R.

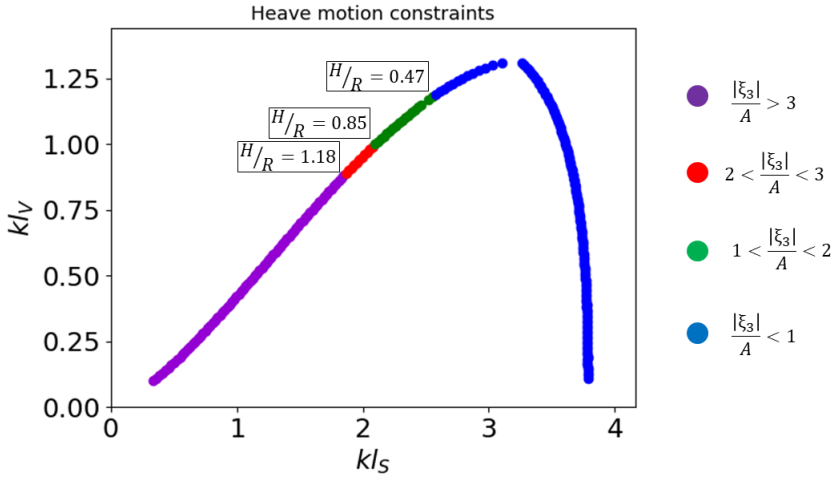

Figure 5-3: Illustration of the effect of the heave motion constraint on $\mathcal{S}(\mathbb{R}^{cyl}_3)$. The purple shapes are eliminated when $\alpha = 3$. The red and purple shapes are eliminated when $\alpha = 2$. The green, red, and purple shapes are eliminated when $\alpha = 1$.

Heave steepness constraint

The heave steepness constraint is, given ϵ,

$$kH > \epsilon \frac{|\xi_3|}{A} \tag{5.1.5}$$

The heave steepness constraint will affect both the lower left and lower right branches of the $\mathcal{S}(\mathbb{R}_3^{cyl})$, as explained in section 4.3. Figure 5-4 demonstrates the specific regions that are eliminated for a few different ϵ values: $\epsilon = 0.1$ and 0.2. As ϵ increases, the constraint is more restrictive. All shapes given a purple color will be eliminated if $\epsilon = 0.1$ – that is, if you require that $kH > 0.1\frac{|\xi_3|}{A}$. If $\epsilon = 0.2$, all shapes given a purple or orange color will be eliminated. For all shapes that are blue, therefore, $kH > 0.2\frac{|\xi_3|}{A}$.

Since this constraint affects shapes with larger $\frac{|\xi_3|}{A}$, a similar effect to $\mathcal{S}(\mathbb{R}_3^{cyl})$ as for the α constraint occurs: the more restrictive the constraint, the shallower the deepest shape not eliminated will be. However, we know that the ϵ constraint also affects the lower right branch of $\mathcal{S}(\mathbb{R}_3^{cyl})$, where the shallowest shapes are, and thus the more restrictive the constraint, the deeper the shallowest shapes not eliminated with be. Therefore, the range of H/R will be limited from both ends, as labeled in figure 5-4.

For $\epsilon = 0.1$, the deepest shape has $H/R = 2.28$, and for $\epsilon = 0.2$ the deepest shape has $H/R = 1.29$. For $\epsilon = 0.1$, the shallowest shape has $H/R = 0.01$ and for $\epsilon = 0.2$, the shallowest shape has $H/R = 0.03$

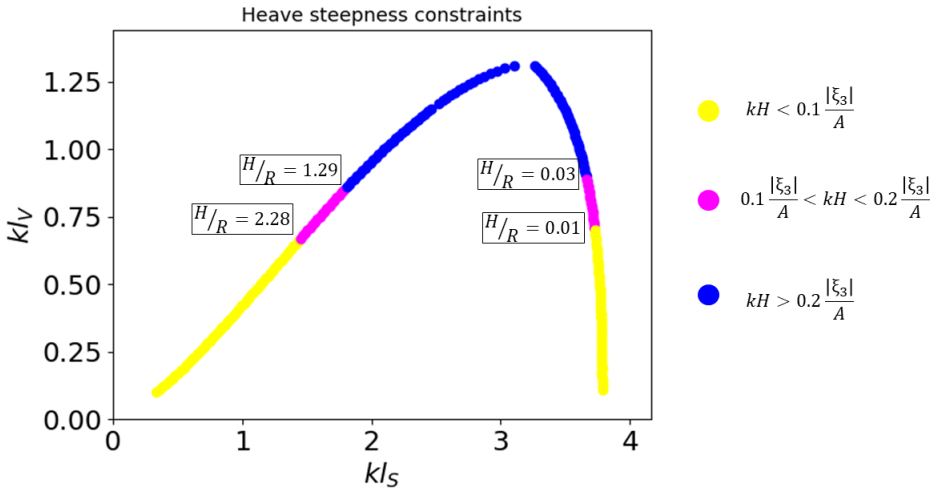

Figure 5-4: Illustration of the effect of the heave steepness constraint on $\mathcal{S}(\mathbb{R}_3^{cyl})$. The yellow shapes are eliminated when $\epsilon = 0.1$, and the pink and yellow shapes are eliminated when $\epsilon = 0.2$.

5.1.3 Surge pitch constraints and where they affect the population

As discussed in detail in section 3.2, the heave-surge-pitch population is formed by starting with $\mathbb{R}_3$, the set of shapes that solve the heave resonance equation, and then eliminating shapes that do not adhere to the heave, surge, and pitch constraints.

In addition to the heave motion constraint and the heave steepness constraint, the five additional constraints to consider when looking at WECs that move and extract energy in surge and pitch, are the surge and pitch motion constraints, the pitch steepness constraint, the pitch moment of inertia constraint, and the center of gravity constraint. Section 3.2 discusses the motivation behind all of these constraints. In this section, we will go through each one for the cylinder to show which parts of $\mathcal{S}(\mathbb{R}_3^{cyl})$ each constraint eliminates.

Surge motion constraint

The surge motion constraint is, given α,

$$\frac{|\xi_1|}{A} < \alpha \tag{5.1.6}$$

Figure 5-5 shows the specific regions on $\mathcal{S}(\mathbb{R}^{cyl}_3)$ that are eliminated for a few α values: $\alpha = 3$, 2 and 1. The purple shapes are eliminated when $\alpha = 3$. That is, all of the shapes given a purple color have $\frac{|\xi_1|}{A} > 3$. The shapes given a red color have $2 < \frac{|\xi_1|}{A} < 1$, so if $\alpha = 2$ all purple and red shapes are eliminated. Shapes given a green color have $1 < \frac{|\xi_1|}{A} < 2$, so if $\alpha = 1$ all purple, red and green shapes are eliminated. All blue shapes have $\frac{|\xi_1|}{A} < 1$.

We see that the surge motion constraint affects both ends of the population curve. As α decreases (so the motion constraint becomes more restrictive), the constraint eliminates shapes further up each branch, meaning that the range of H/R becomes more limited. For $\alpha = 3$, the cylinders have H/R values ranging from 0.02 to 2.59. For $\alpha = 2$, this reduces to 0.03 to 1.89, and for $\alpha = 1$ it is reduced further to 0.09 to 1.02. We notice that the surge motion constraint does not affect the left branch as much as the heave motion constraint did. For the heave motion constraint, the deepest cylinder left when $\alpha = 3$ had an H/R value of 1.18 (compared to 2.59 here).

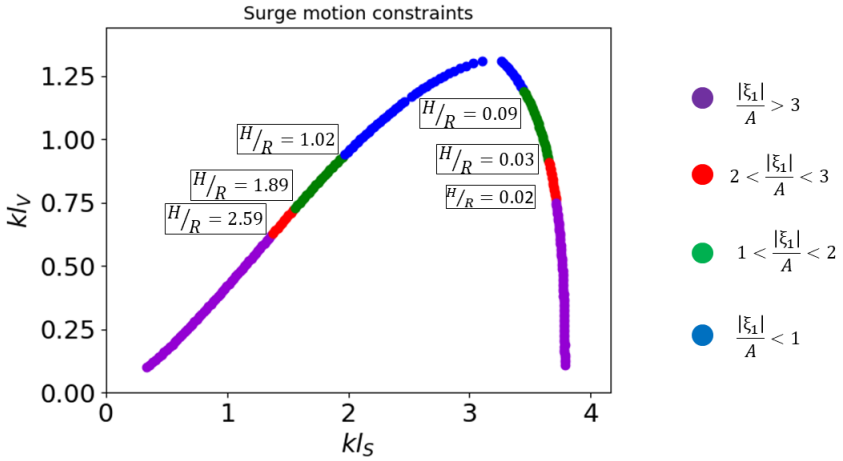

Figure 5-5: Illustration of the effect of the surge motion constraint on $\mathcal{S}(\mathbb{R}^{cyl}_3)$. The purple shapes are eliminated when $\alpha = 3$, the red and purple shapes are eliminated when $\alpha = 2$, and the green, red and purple shapes are eliminated when $\alpha = 1$.

Pitch motion constraint

The pitch motion constraint is, given α,

$$\frac{|\xi_5|}{A/R} < \alpha \tag{5.1.7}$$

Figure 5-6 shows where the pitch motion constraint affects $\mathcal{S}(\mathbb{R}^{cyl}_3)$. Compared to the constraints so far, the pitch motion constraint affects $\mathcal{S}(\mathbb{R}^{cyl}_3)$ in the least straightforward way.

When $\alpha = 3$, the purple shapes are eliminated. That means that there is a hole in the middle of the $\mathcal{S}(\mathbb{R}^{cyl}_3)$, with a continuous section from $H/R = 2.85$ to $H/R = 0.96$, a missing chunk, and then another continuous section from $H/R = 0.34$ and below. For $\alpha = 2$, purple and red shapes are eliminated. That means that the section from $H/R = 2.85$ and $H/R = 0.96$ is eliminated, as is the section from $H/R = 0.34$ to $H/R = 0.29$. For $H/R < 0.29$, there is a continuous section. For $\alpha = 1$, purple, red and green shapes are eliminated. Therefore, any shapes with $H/R > 0.16$ are eliminated.

We see that this does not follow the pattern of any of the constraints we have discussed so far because it does not only affect the ends of $\mathcal{S}(\mathbb{R}^{cyl}_3)$ (aka the deepest and shallowest ones). It seems to affect the 'intermediate' shapes, too.

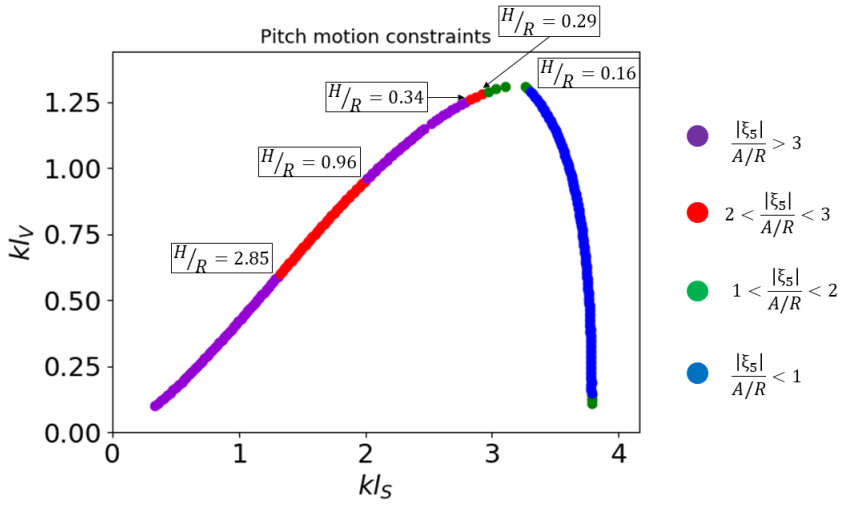

Figure 5-6: Illustration of the effect of the pitch motion constraint on $\mathcal{S}(\mathbb{R}^{cyl}_3)$

Pitch steepness constraint

The pitch steepness constraint is, given ϵ,

$$kH > \epsilon \frac{|\xi_5|}{A/R} \tag{5.1.8}$$

Figure 5-7 shows where the pitch steepness constraint affects $\mathcal{S}(\mathbb{R}^{cyl}_3)$ for a few different values of ϵ: $\epsilon = 0.1$ and 0.2.

We see that the pitch steepness constraint affects the ends of each branch of $\mathcal{S}(\mathbb{R}^{cyl}_3)$, but it also affects the middle of the curve, where there are 'intermediate' (neither very shallow nor very deep) shapes.

When $\epsilon = 0.1$, the yellow shapes will be eliminated. We can see that the deepest shapes ($H/R > 13.2$), the shallowest shapes ($H/R < 0.04$), and a section of the 'intermediate' shapes ($0.68 < H/R < 0.39$) are all affected, leaving two continuous sections of the curve with a gap from $H/R = 0.68$ to $H/R = 0.39$). When $\epsilon = 0.2$, the yellow and pink shapes are eliminated. We see that the pink forms an 'extension' of the where the yellow shapes are– more of the left branch is eliminated, so that

the deepest shape is now $H/R = 5.31$), more of the right branch is eliminated, so that the shallowest shape is now $H/R = 0.08$, and more of the intermediate shapes are eliminated, so that the two continuous segments that are allowed are $0.91 < H/R < 5.31$ and $0.08 < H/R < 0.27$.

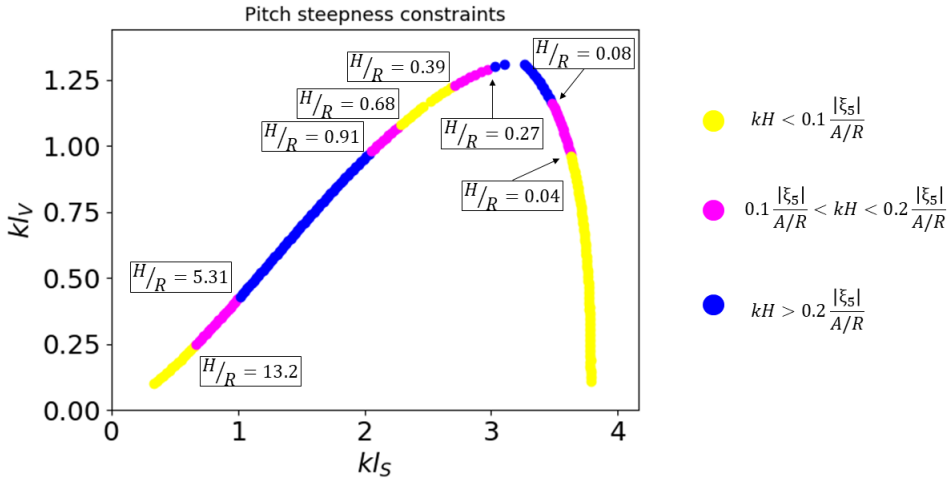

Figure 5-7: Illustration of the effect of the pitch steepness constraint on $\mathcal{S}(\mathbb{R}^{cyl}_3)$. The yellow shapes are eliminated if $\epsilon = 0.1$. If $\epsilon = 0.2$, the yellow and pink shapes are eliminated.

Pitch moment of inertia constraint

As discussed in section 3.2.2, when using I_{55} as a passively controllable parameter in the pitch resonance equation, it is necessary to enforce that I_{55} is greater than 0. For resonance in pitch, we set

$$I^r_{55} = \frac{\rho g \pi R^4/4 + \rho g l_v^3 z_B - g A_{15}}{\omega^2} - A_{55} \tag{5.1.9}$$

However, we must enforce that

$$I^r_{55} > 0 \tag{5.1.10}$$

which is the pitch moment of inertia constraint. As shown in figure 5-8, this constraint affects deep shapes, for $H/R > 0.78$, marked with pink in the figure. For $H/R < 0.78$,

the expression in equation 5.1.9 is greater than 0. From looking at equation 5.1.9, we can say that the reasons why it may affect deeper shapes is that they have larger A_{55}, larger A_{15}, smaller R and/ore a more negative z_B.

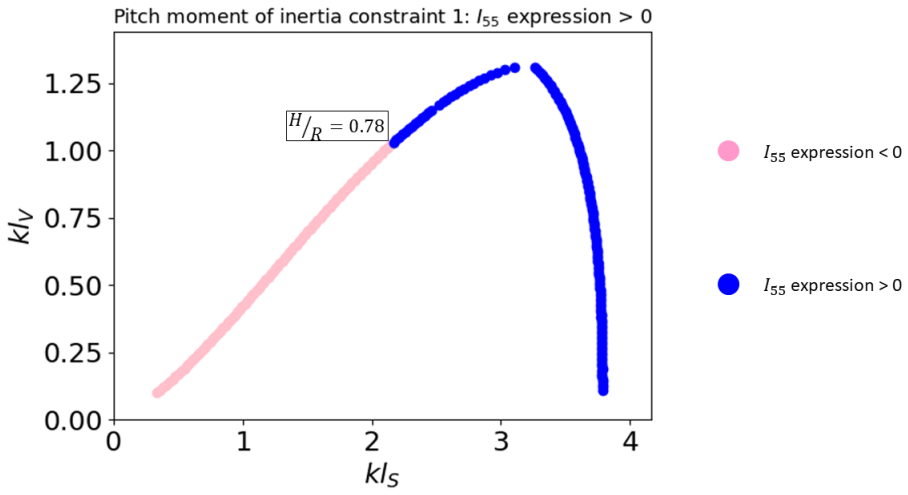

Figure 5-8: Illustration of the effect of the pitch moment of inertia constraint on $\mathcal{S}(\mathbb{R}_3^{cyl})$. The pink shapes will be eliminated due to this constraint.

Center of gravity constraint

In the surge-pitch resonance equation, we use z_G as the passively controllable parameter, so we must ensure that the value for z_G that enforces resonance is also practically feasible. The center of gravity constraint is

$$-H < z_G < z_G^{max} \tag{5.1.11}$$

where z_G^{max} is determined by stability, as explained in appendix A. Figure 5-9 show that for $H/R > 1.41$ this constraints all the shapes. We anticipated this because of stability: deeper, narrow shapes are less stable, so the maximum value that the center of gravity can be to ensure stability will be smaller. For $H/R < 1.41$, z_G^r, the value for z_G needed to enforce surge-pitch resonance, is greater than z_G^{max}, so these shapes are eliminated.

The other part of the center of gravity constraint is that the center of gravity cannot be below the bottom of the shape: $z_G^r > -H$. We found that this is always true for the cylinder, so it does not eliminate any shapes.

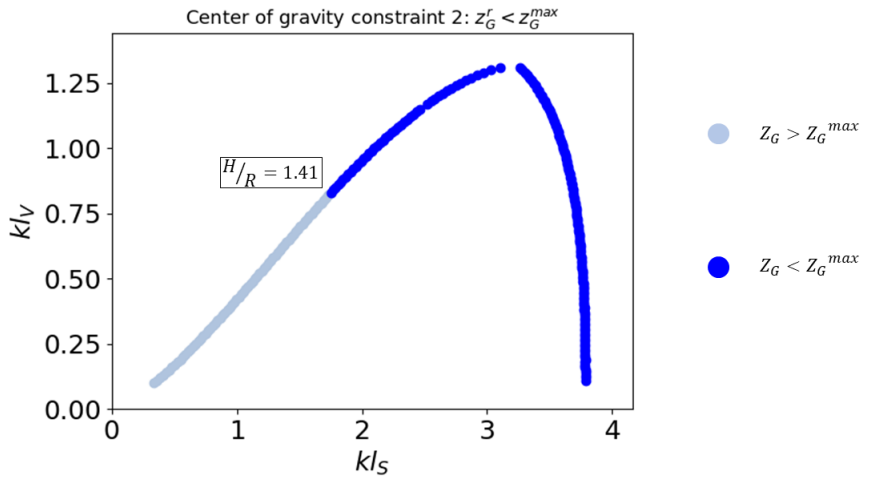

Figure 5-9: Illustration of the effect of the center of gravity constraint on $\mathcal{S}(\mathbb{R}_3^{cyl})$. The light blue shapes will be eliminated due to this constraint.

In this section, the framework discussed in chapter 3 and the approach discussed in chapter 4 were applied on the simple case of the cylinder. The theorem discussed and proved in section 4.2 was demonstrated to find the set of all cylinders resonating in heave, $\mathbb{R}_3^{cyl}$. The curve of this set in the $kl_V - kl_S$ space was discussed, as an illustration of the general conclusions for such curves, made in section 4.3. Each heave, surge, and pitch constraint were considered, and we showed which cylinders from $\mathbb{R}_{cyl}$ were eliminated by each one, for a few values of each constraint value. We will now look at the full optimizations for the cylinder for heave and heave-surge-pitch, for two different values of α and two different values of ϵ.

5.2 Heave-only optimization

In this section the results of the optimizations for the case of a WEC moving and extracting energy in the heave mode only are presented. Two values of α are considered: $\alpha = 3$ and $\alpha = 1$. Since the heave motion constraint eliminates shapes such

that $\frac{|\xi_3|}{A} > \alpha$, a smaller value of α corresponds to a stricter motion constraint, thus eliminating more shapes. Additionally, two values of ϵ are considered: $\epsilon = 0.1$ and $\epsilon = 0.2$. Since the heave steepness constraint eliminates shapes such that $kH > \epsilon\frac{|\xi_3|}{A}$, a larger value of ϵ corresponds to a stricter steepness constraint, thus eliminating more shapes.

5.2.1 Populations

Each population will be labeled first by mode (heave is 3, heave-surge-pitch is 135), then by α, then by ϵ. For example, the population for heave for $\alpha = 3$ and $\epsilon = 0.1$ will be $\mathbb{P}_{3,3,0.1}$

Figure 5-10 shows the populations for the four cases as four rows: $\mathbb{P}_{3,3,0.1}$, $\mathbb{P}_{3,3,0.2}$, $\mathbb{P}_{3,1,0.1}$, and $\mathbb{P}_{3,1,0.2}$. The left column shows $\mathcal{S}(\mathbb{P}_3)$, the population in the $kl_V - kl_S$ space. The right column shows the 2D shapes of the cylinders in the population in the $r - z$ plane. Each unique cylinder is designated a color in this figure, which do not correspond to the colors in figure 5-2. Colors progress in a rainbow, where purple corresponds to the shapes with the smallest kl_S value in $\mathbb{P}_{3,3,0.1}$) and the red correspond to the largest kl_S value in $\mathbb{P}_{3,3,0.1}$), since this is the least restrictive case. The colors are consistent between the different populations. That is, the cylinder with $kR = kR^*$ and $kH = kH^*$ will be the same color in the first row as in the second row, if it is in both populations.

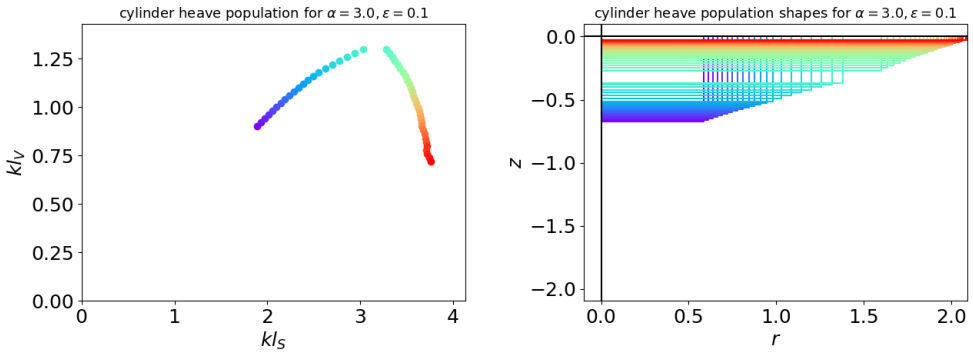

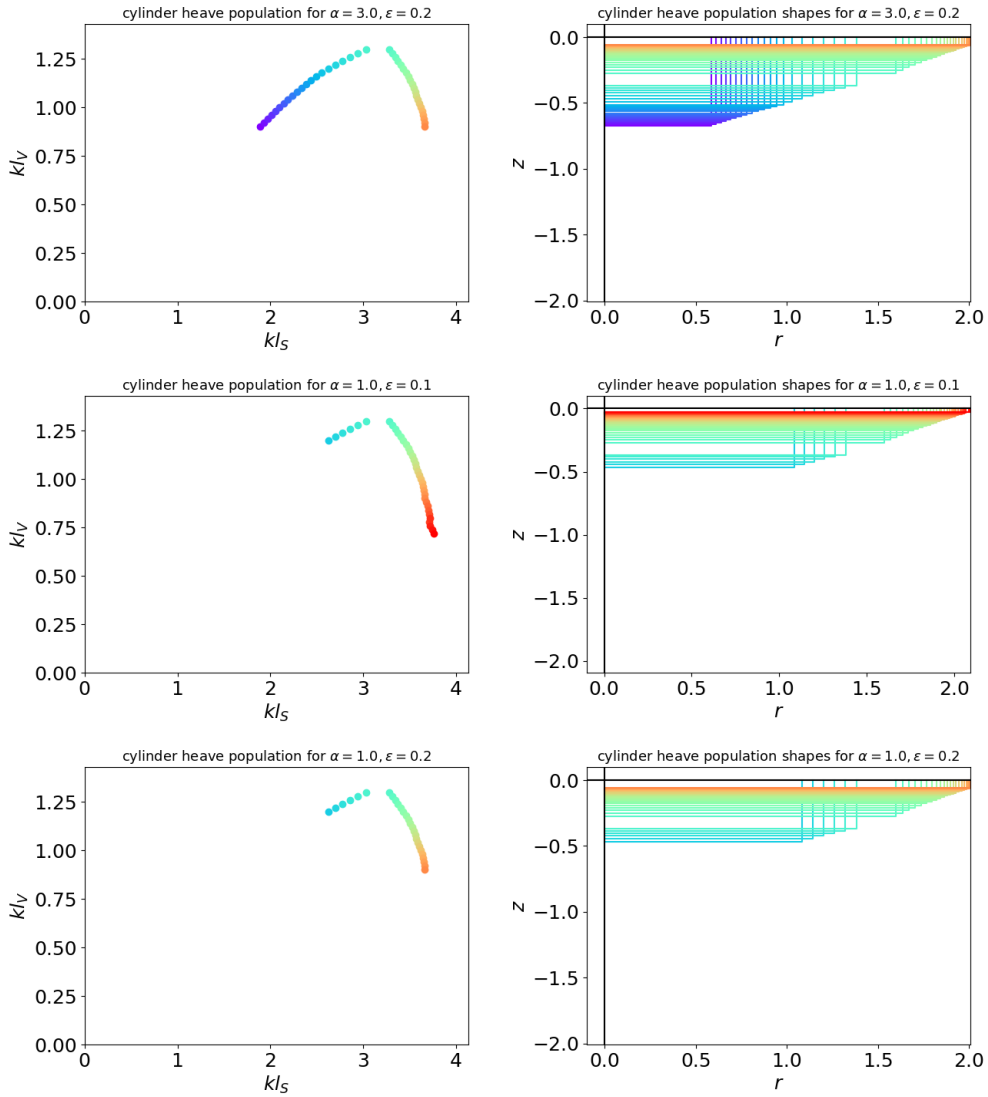

Figure 5-10: Heave-only populations of cylinders for different constraint values. Row 1 is the population for $\alpha = 3, \epsilon = 0.1$, row 2 is for $\alpha = 3, \epsilon = 0.2$, row 3 is for $\alpha = 1, \epsilon = 0.1$ and row 4 is for $\alpha = 1, \epsilon = 0.2$. In each row, the left figure shows a scatter plot of the population in the $kl_V - kl_S$ space, and the right figure shows the corresponding shapes of the cylinders in 2D $r - z$ space. The colors range from smaller kl_S (purple) to larger kl_S (red).

We can relate the shape of each population back to the three general categories that a heave population can take given $\overline{\mathscr{B}_E}$, as discussed in section 4.3. $\mathbb{P}_{3,3,0.1}, \mathbb{P}_{3,1,0.1}$ and $\mathbb{P}_{3,1,0.2}$ are $\mathbb{P}_A$ shape, $\mathbb{P}_{3,3,0.2}$ is $\mathbb{P}_B$ shape.

As we discussed above in section 5.1.2, changing α from 3 to 1 eliminates the deepest cylinders. It was also discussed in section 5.1.2 that increasing ϵ will eliminate the

deepest shapes and the shallowest shapes. However, we see that the $\alpha = 3$ constraint eliminates more shapes from the left branch of $\mathcal{S}(\mathbb{R}^{cyl}_3)$ than the $\epsilon = 0.2$ constraint does, meaning that no further shapes are eliminated from the left branch as a consequence of the steepness constraint.

5.2.2 Pareto Fronts

The Pareto Fronts corresponding to the heave-only populations shown in figure 5-10 are now presented. Similar to the populations, the Pareto Fronts will be labeled first by mode, then by α, then by ϵ. For example, the Pareto Front for heave for $\alpha = 3$ and $\epsilon = 0.1$ will be called $\mathbb{PF}_{3,3,0.1}$.

To determine the effect of the constraints on the Pareto Front, we will consider how the shape of the curve of the Pareto Front in the $kl_V - kl_S$ space, $\mathcal{S}(\mathbb{PF}_3)$, changes with changing constraints. Additionally, we will determine how the shapes of the cylinders on the Pareto Front change with changing constraints. And finally, we will determine how the performance changes with changing constraints by comparing two points across Pareto Fronts: the minimum kl_S value, $(kl_S)^{min}$, and the minimum kl_V value, $(kl_V)^{min}$.

$\underline{\alpha = 3, \epsilon = 0.1}$

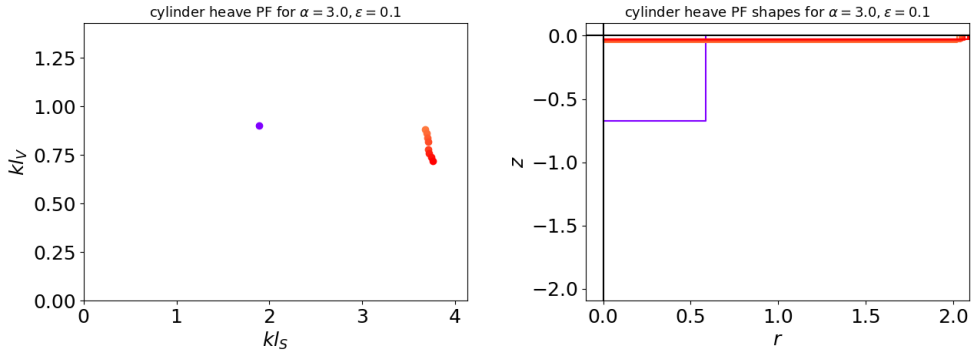

Figure 5-11: $\mathbb{PF}_{3,3,0.1}$, the Pareto Front for the heave-only case of cylinders with an α constraint value of 3 and ϵ constraint value of 0.1

This Pareto Front, called $\mathbb{PF}_{3,3,0.1}$ follows the $\mathbb{PF}_B$ shape, with a lone dot left from the left branch and a cluster of shapes left from the right branch. The cylinder represented by purple has an H/R value of 1.14, and its dimensions and body motion are shown in table 5.1.

kl_S	kl_V	kR	kH	$\frac{\lvert\xi_3\rvert}{A}$
1.89	0.9	0.59	0.67	2.89

Table 5.1: Dimensions and body motion of the cylinder represented by a purple dot in figure 5-11

The cylinders shown in the cluster from the right branch, with orange to red colors, corresponding to increasing kl_S, have H/R values from 0.025 to 0.014. The dimensions and body motion values for all of the shapes in this cluster are shown in table 5.2.

kl_S	kl_V	kR	kH	$\frac{\lvert\xi_3\rvert}{A}$
3.68	0.88	2.02	0.05	0.28
3.69	0.86	2.04	0.05	0.28
3.71	0.84	2.05	0.05	0.27
3.71	0.82	2.05	0.04	0.27
3.71	0.78	2.06	0.04	0.27
3.72	0.76	2.07	0.03	0.27
3.74	0.74	2.08	0.03	0.27
3.76	0.72	2.09	0.03	0.26

Table 5.2: Dimensions and body motion of the cylinders in the orange-red cluster in figure 5-11

The lone purple dot was determined by the α constraint, and the darkest red dot was determined by the ϵ constraint. The Pareto Front provides a set of optimal shapes that is the answer to the optimization problem. The purple dot has minimum surface area, so if it is decided that minimizing surface area is the most important thing, that would be the shape that would be built. The orange-red shapes have larger surface area but smaller volume. There also may be other parameters that a developer would

consider, such as survivability, ease of build, etc. It is beyond the scope of this thesis to discuss these aspects further or recommend a specific shapes from this set.

$\underline{\alpha = 3, \epsilon = 0.2}$

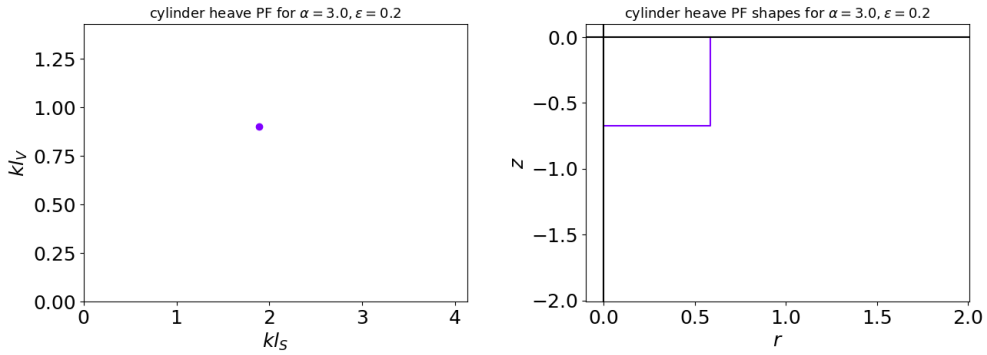

Figure 5-12: Pareto Front for the heave-only case of cylinders with a α constraint value of 3 and ϵ constraint value of 0.2

This Pareto Front follows a $\mathbb{PF}_A$ shape: it consists of only a single dot. The dimensions and body motion are shown in table 5.3.

kl_S	kl_V	kR	kH	$\frac{\lvert\xi_3\rvert}{A}$
1.89	0.9	0.59	0.67	2.89

Table 5.3: Dimensions and body motion of the cylinder represented in figure 5-12

We see that this cylinder is the same as the purple one in figure 5-11. All of the orange-red cylinders from that figure were eliminated by the stricter ϵ constraint. Going from $\epsilon = 0.1$ to $\epsilon = 0.2$, the minimum kl_S does not change. The minimum kl_V changes from 0.72 to 0.9 – a 25 % increase.

$\underline{\alpha = 1, \epsilon = 0.1}$

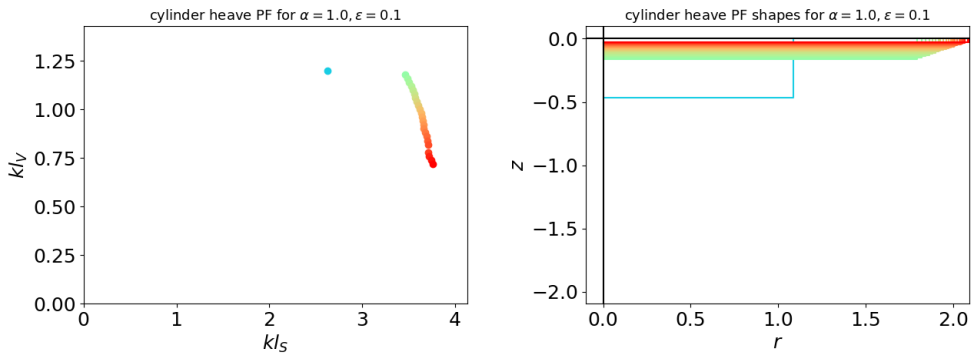

Figure 5-13: Pareto Front for the heave-only case of cylinders with a α constraint value of 1 and ϵ constraint value of 0.1

Figure 5-14 shows that $\mathbb{PF}_{3,1,0.1}$ is a $\mathbb{PF}_B$ shape, like $\mathbb{PF}_{3,3,0.1}$ was. The purple dot shown in figure 5-11 is eliminated because $\frac{|\xi_3|}{A} > \alpha = 1$. The lone dot in this Pareto Front, shown in teal in figure 5-13, has H/R value 0.43. The dimensions and body motion value are shown in table 5.4.

kl_S	kl_V	kR	kH	$\frac{\lvert\xi_3\rvert}{A}$
2.62	1.2	1.09	0.47	0.92

Table 5.4: Dimensions and body motion of the cylinder represented by a teal dot in figure 5-13

We see that the teal cylinder is wider and shallower than the purple dot was in figure 5-11. The cluster of points from the right branch, which in figure 5-13 range from light green to red, with increasing kl_S value, is a larger, more inclusive cluster of shapes than the cluster in figure 5-11. It shows a wider range of shapes, with the lightest green cylinder having a H/R value of 0.089, and including a range of shapes to the same red cylinder as from figure 5-11 and table 5.2, which has a H/R value of 0.014. The dimensions of the lightest green cylinder and the darkest red cylinder are shown in table 5.5. Between these two ends of the cluster, kl_S increases, kl_V decreases, kR increases, kH decreases, and $\frac{|\xi_3|}{A}$ decreases.

kl_S	kl_V	kR	kH	$\frac{\lvert\xi_3\rvert}{A}$
3.46	1.18	1.8	0.16	0.35
3.76	0.72	2.09	0.03	0.26

Table 5.5: Dimensions and body motion of the cylinders on the ends of the green-yellow-orange-red cluster in figure 5-13. The first row shows the values for the lightest green cylinder, and the second row shows the values for the darkest red cylinder.

So, a more restrictive motion constraint (α value going from 3 to 1) means that the Pareto Front becomes more inclusive and expansive. Because of the nature of the shape of the population (a one-to-one, concave down shape with a maximum value at $(kl_V)^{max}$, with positive slope before this and negative slope after this, and the fact that $\overline{R}$ is increasing as you go along the curve), decreasing α will always result in a larger minimum kl_S and shallower shapes on the Pareto Front. Going from $\alpha = 3$ to $\alpha = 1$, the shape of the cylinder with the smallest kl_S gets shallower, going from having a H/R value of 1.14 to 0.43. The value of the minimum kl_S goes from 1.89 to 2.62 – a 39 % increase.

$\underline{\alpha = 1, \epsilon = 0.2}$

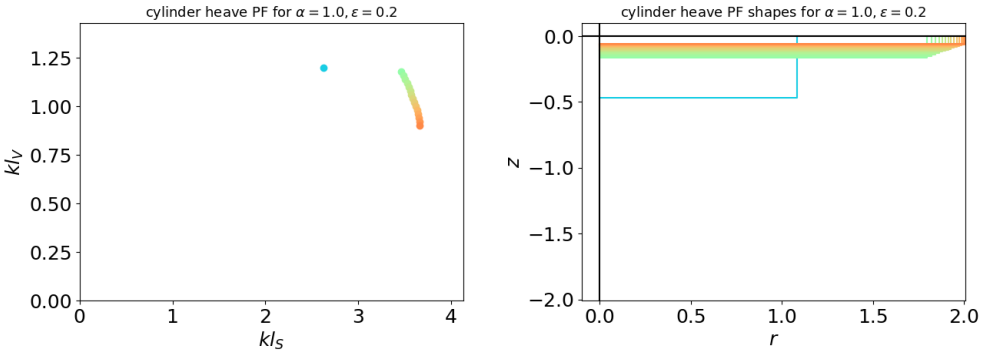

Figure 5-14: Pareto Front for the heave-only case of cylinders with a α constraint value of 1 and ϵ constraint value of 0.2

$\mathbb{PF}_{3,1,0.2}$ again shows a $\mathbb{PF}_A$ shape. As shown in table 5.6, the teal point in figure 5-14 is the same as the teal point from figure 5-13. However, the cluster of points in figure 5-14 is smaller than the cluster in figure 5-13. This is because the ϵ constraint eliminates the bottom right branch.

kl_S	kl_V	kR	kH	$\frac{\lvert\xi_3\rvert}{A}$
2.62	1.2	1.09	0.47	0.92
3.46	1.18	1.8	0.16	0.35
3.66	0.9	2.01	0.06	0.28

Table 5.6: Dimensions and body motion of three of the cylinders in figure 5-14. The first row shows the values for the lone teal dot. The second row shows the values for the cylinder on the upper left of the green-yellow-orange cluster: the lightest green one. The third row shows the values for the cylinder on the lower right of the cluster: the darkest orange one.

Table 5.6 shows the dimensions and body motion values for the teal dot, the lightest green dot, and the darkest orange dot (the latter two being the two ends of the green-yellow-orange cluster). As was the case when increasing ϵ from 0.1 to 0.2 when α was 3, increasing ϵ from 0.1 to 0.2 when $\alpha = 1$ results in the minimum kl_V value increasing. $(kl_V)^{min}$ increases from 0.72 to 0.9 – a 25 % increase.

General trends/ observations

1. How the $\mathcal{S}(\mathbb{PF}_3)$ changes

   - $\mathbb{PF}_{3,3,0.1}, \mathbb{PF}_{3,1,0.1}$ and $\mathbb{PF}_{3,1,0.2}$ are of the shape $\mathbb{PF}_A$, and $\mathbb{PF}_{3,3,0.2}$ is of the shape $\mathbb{PF}_B$
   - Somewhat counter-intuitively, as α decreases (and thus the motion constraint becomes more restrictive), the Pareto Front becomes fuller and less dominated by the motion constraint. There are more cylinders on $\mathbb{PF}_{3,1,0.1}$ than there are on $\mathbb{PF}_{3,3,0.1}$.

2. How the dimensions of the cylinders on the Pareto Fronts change

   - For $\alpha = 3$, the Pareto Fronts are a pretty limited set, as shown in tables 5.1, 5.2 and 5.3 and figure 5-11 and 5-12, consisting of one point from the left branch with $kR = 0.59$ and $kH = 0.67$, and either a small cluster of very think disk-like shapes (with $0.014 < H/R0.025$) for $\epsilon = 0.1$, or

no cluster for $\epsilon = 0.1$. Decreasing α to 1 eliminates the cylinder given a purple color, and the cylinder with minimum kl_S now has an H/R value of 0.43, but it also enables many more cylinders from the population to be on the Pareto Front, by 'pushing' the left branch up.

- Increasing ϵ results in the shape with the minimum kl_V being slightly deeper and not as wide.

3. How the performance changes

   - As α decreases, $(kl_S)^{min}$ increases; $(kl_V)^{min}$ does not change. This is because the deeper shapes had smaller kl_S and they were eliminated for the smaller α. From $\alpha = 3$ to $\alpha = 1$, the minimum kl_S increases from 1.89 to 2.62 – a 39 % increase.
   - As ϵ increases, the $(kl_S)^{min}$ does not change but $(kl_V)^{min}$ increases. This means that the ϵ constraint is only affecting the lower right branch (the shallowest shapes). We can see from figure 5-4 that the ϵ constraint does affect the lower left branch but at a point below the minimum value for which the α constraint affects it. The minimum kl_V value goes from 0.72 to 0.9 – a 25 % increase.

In this section, the results of the heave-only optimization were presented and discussed.

5.3 Heave-surge-pitch optimization

In this section, the results of the heave-surge-pitch optimization are presented and discussed. We again use two values of α and two values of ϵ: $\alpha = 3$ and 1 and $\epsilon = 0.1$ and 0.2. We use the same α and ϵ across all modes. That is, if $\alpha = 3$, then $\frac{|\xi_3|}{A} < 3$, $\frac{|\xi_1|}{A} < 3$ and $\frac{|\xi_5|}{A/R} < 3$. And if $\epsilon = 0.1$, $kH > 0.1\frac{|\xi_3|}{A}$ and $kH > 0.2\frac{|\xi_5|}{A/R}$. The center of gravity constraint and the pitch moment of inertia constraint are always applied.

5.3.1 Populations

Figure 5-15 shows the populations for the four cases as four rows: $\mathbb{P}_{135,3,0.1}, \mathbb{P}_{135,3,0.2}, \mathbb{P}_{135,1,0.1}$, and $\mathbb{P}_{135,1,0.2}$. The left column shows $\mathcal{S}(\mathbb{P}_{135})$, the population in the $kl_V - kl_S$ space. The right column shows the 2D shapes of the cylinders in the population in the $r - z$ plane. The colors correspond to the same colors as in the heave-only populations in figure 5-10. Keeping the colors the same allows us to examine how these populations are different than the heave-only ones.

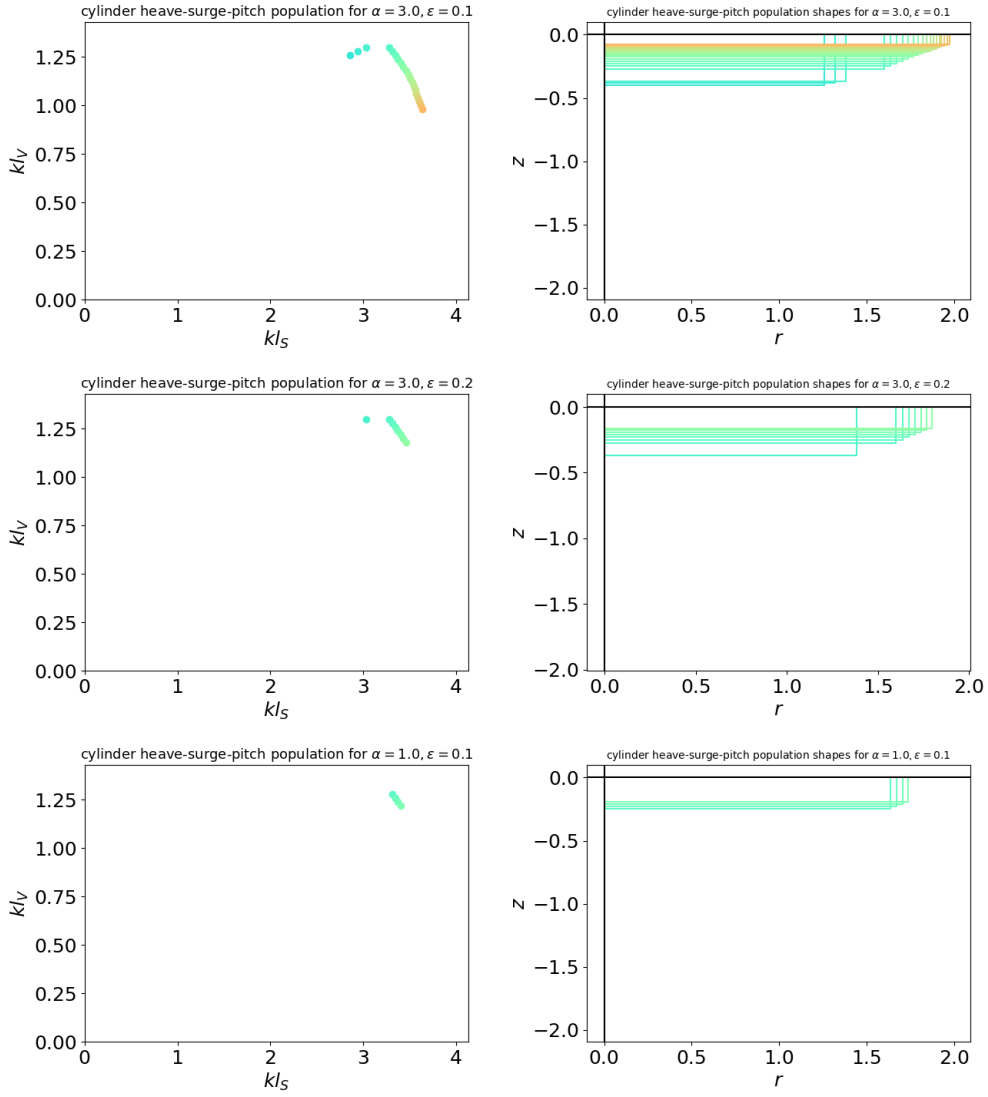

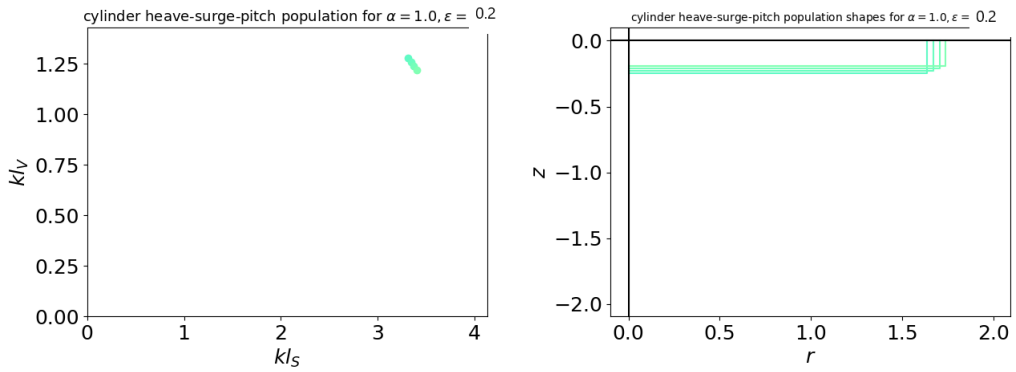

Figure 5-15: Heave-surge-pitch populations of cylinders for different constraint values. Row 1 is the population for $\alpha = 3, \epsilon = 0.1$, row 2 is for $\alpha = 3, \epsilon = 0.2$, row 3 is for $\alpha = 1, \epsilon = 0.1$ and row 4 is for $\alpha = 1, \epsilon = 0.2$. In each row, the left figure shows a scatter plot of the population in the $kl_V - kl_S$ space, and the right figure shows the corresponding shapes of the cylinders. The colors correspond to the same colors in figure 5-10.

$\mathbb{P}_{135,3,0.1}$ and $\mathbb{P}_{135,3,0.2}$ are of shape $\mathbb{P}_B$. $\mathbb{P}_{135,1,0.1}$ and $\mathbb{P}_{135,1,0.2}$ are of shape $\mathbb{P}_C$.

5.3.2 Pareto Fronts

The Pareto Fronts corresponding to the heave-surge-pitch populations shown in figure 5-15 will be presented and discussed in this section. We will discuss how $\mathcal{S}(\mathbb{PF}_{135})$ changes with differing constraint values, how the shapes of cylinders on the Pareto Front change with constraints, and how the performance changes with the constraints by comparing $(kl_S)^{min}$ and $(kl_V)^{min}$ across the constraints. Additionally, we will compare these Pareto Fronts to the corresponding ones in the heave-only case, under the same constraint values. For example, we will compare $\mathbb{PF}_{3,3,0.1}$ to $\mathbb{PF}_{135,3,0.1}$.

$\underline{\alpha = 3, \epsilon = 0.1}$

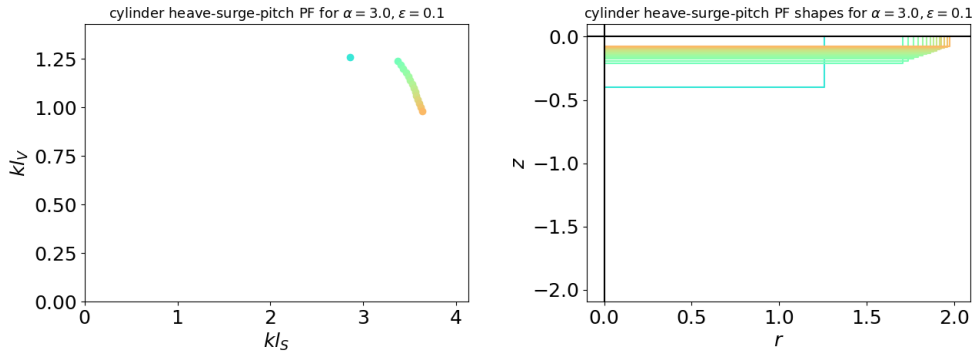

Figure 5-16: Pareto Front for the heave-surge-pitch case of cylinders with a α constraint value of 3 and ϵ constraint value of 0.1

$\mathbb{PF}_{135,3,0.1}$ is shown in figure 5-16. The Pareto Front has a $\mathbb{PF}_B$ shape: the lone point is teal, and then there is a green-yellow-orange cluster. Table 5.7 shows some of the relevant parameters for the heave-surge-pitch problem. Column 8 shows the nondimensional surge spring coefficient:

$$\overline{k_1} \equiv \frac{k_1}{\rho\omega^2 l_V^3} \tag{5.3.1}$$

Column 9 shows the nondimensional center of gravity:

$$\overline{z_G} \equiv \frac{z_G}{H} \tag{5.3.2}$$

Column 10 shows the nondimensional radius of gyration for pitch

$$\overline{r_g} \equiv \frac{r_g}{R} \tag{5.3.3}$$

kl_S	kl_V	kR	kH	$\frac{\lvert\xi_1\rvert}{A}$	$\frac{\lvert\xi_3\rvert}{A}$	$\frac{\lvert\xi_5\rvert}{A/R}$	$\overline{k_1}$	$\overline{z_G}$	$\overline{r_g}$
2.86	1.26	1.26	0.4	0.66	0.7	2.41	1.39	0.12	0.5
3.37	1.24	1.71	0.21	0.91	0.39	0.87	1.24	0.82	0.71
3.4	1.22	1.74	0.19	0.94	0.37	0.82	1.24	0.93	0.73
3.43	1.2	1.77	0.18	1.01	0.36	0.8	1.24	1.02	0.77
3.46	1.18	1.8	0.16	1.05	0.35	0.78	1.24	1.13	0.79
3.48	1.16	1.82	0.15	1.12	0.34	0.76	1.23	1.24	0.82
3.5	1.14	1.84	0.14	1.15	0.33	0.75	1.24	1.35	0.84
3.52	1.12	1.86	0.13	1.19	0.32	0.75	1.24	1.39	0.86
3.54	1.1	1.88	0.12	1.3	0.32	0.73	1.23	1.58	0.9
3.56	1.08	1.9	0.11	1.34	0.31	0.73	1.23	1.71	0.93
3.57	1.06	1.91	0.1	1.43	0.31	0.72	1.23	1.85	0.96
3.58	1.04	1.93	0.1	1.49	0.3	0.72	1.23	1.98	0.99
3.6	1.02	1.94	0.09	1.58	0.3	0.72	1.23	2.14	1.02
3.62	1.0	1.96	0.08	1.61	0.29	0.72	1.23	2.3	1.05
3.63	0.98	1.97	0.08	1.69	0.29	0.72	1.23	2.32	1.08

Table 5.7: Characteristics of the heave-surge-pitch Pareto Front for $\alpha = 3, \epsilon = 0.1$, called $\mathbb{PF}_{135,3,0.1}$. Columns 1, 2, 3, and 4 are the same as for the heave-only case: they show kl_S, kl_V, kR and kH. Columns 5, 6 and 7 show the body motion for the three modes: surge, heave and pitch, respectively. Column 8 shows the nondimensional surge spring coefficient. Column 9 shows the nondimensional center of gravity. Column 10 shows the nondimensional radius of gyration for pitch

We see that, for this Pareto Front, as kl_S increases, $\frac{\lvert\xi_1\rvert}{A}$ increases, $\frac{\lvert\xi_3\rvert}{A}$ decreases, $\frac{\lvert\xi_5\rvert}{A/R}$ decreases, $\overline{k_1}$ decreases, $\overline{z_G}$ increases and $\overline{r_g}$ increases.

The minimum kl_S value in this Pareto Front is 2.86 and the minimum kl_V is 0.98. The corresponding heave-only PF, $\mathbb{PF}_{3,3,0.1}$, had a minimum kl_S of 1.89 and a minimum kl_V of 0.72. That is an increase of kl_S by 51 % and an increase of kl_V by 36 %. The other difference between these two Pareto Fronts is that $\mathbb{PF}_{135,3,0.1}$ has more shapes on the Pareto Front than $\mathbb{PF}_{3,3,0.1}$. So we again see that eliminating shapes from the left branch enables more shapes on the Pareto Front.

The shape of the cylinder with the minimum kl_S on the Pareto Front for heave-only, $\mathbb{PF}_{3,3,0.1}$ had a H/R value of 1.14, and the shape with the minimum kl_S in this Pareto Front has an H/R value of 0.32, so it is shallower (which makes sense since more of the left branch is eliminated). The shape of the cylinder with the minimum kl_V on the Pareto Front for heave-only, $\mathbb{PF}_{3,3,0.1}$ had an $H/R = 0.041$. On this Pareto Front, the cylinder with minimum kl_V has $H/R = 0.014$ to 0.041.

We see from figures 5-8, 5-6 and 5-5 that for $H/R > 0.78$, the shape are eliminated by the I_{55} constraint. For $0.34 < H/R < 0.96$, the pitch motion is too large. The right branch is determined by surge motion: for $H/R < 0.04$, the surge motion is too large. The amount of extractable power for the heave-surge-pitch WECs is three times more than that of the heave-only case. So, the increases to $(kl_V)^{min}$ and $(kl_S)^{min}$ must be weighed with the increase in power.

$\underline{\alpha = 3, \epsilon = 0.2}$

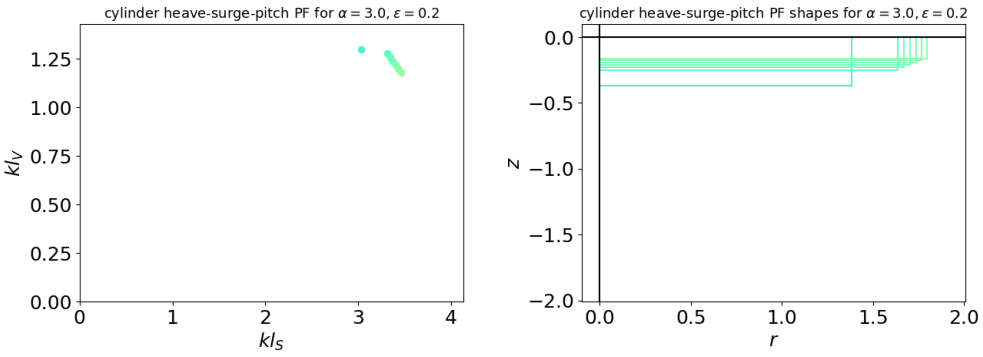

Figure 5-17: Pareto Front for the heave-surge-pitch case of cylinders with a α constraint value of 3 and ϵ constraint value of 0.2

Figure 5-17 shows $\mathbb{PF}_{135,3,0.2}$. Table 5.8 shows the characteristics of the cylinders on the Pareto Front. From the table, we see that the lone point in this PF (teal) is not the same as the one in $\mathbb{PF}_{135,3,0.1}$.

kl_S	kl_V	kR	kH	$\frac{\lvert\xi_1\rvert}{A}$	$\frac{\lvert\xi_3\rvert}{A}$	$\frac{\lvert\xi_5\rvert}{A/R}$	$\overline{k_1}$	$\overline{z_G}$	$\overline{r_g}$
3.03	1.3	1.38	0.37	0.67	0.6	1.69	1.34	0.22	0.53
3.31	1.28	1.64	0.25	0.82	0.43	0.97	1.25	0.62	0.66
3.34	1.26	1.67	0.23	0.86	0.41	0.91	1.25	0.72	0.69
3.37	1.24	1.71	0.21	0.91	0.39	0.87	1.24	0.82	0.71
3.4	1.22	1.74	0.19	0.94	0.37	0.82	1.24	0.93	0.73
3.43	1.2	1.77	0.18	1.01	0.36	0.8	1.24	1.02	0.77
3.46	1.18	1.8	0.16	1.05	0.35	0.78	1.24	1.13	0.79

Table 5.8: Characteristics of the heave-surge-pitch Pareto Front for $\alpha = 3, \epsilon = 0.2$, called $\mathbb{PF}_{135,3,0.2}$, shown in figure 5-17.

We see from figure 5-7 that the lone point from $\mathbb{PF}_{135,3,0.1}$ was eliminated because of the pitch steepness constraint. So in contrast to the heave-only case, increasing ϵ causes an increase in the minimum kl_S value. It increases from 2.86 to 3.03 – a 6 % increase. The cylinder with the minimum kl_S value is shallower for the higher ϵ value.

We also see from table 5.8, compared to table 5.7 that the yellow-orange shapes from the bottom right of the cluster from the right branch are eliminated. From figure 5-7, we see that this is also because of the pitch steepness constraint. As ϵ increase, the minimum kl_V value increases from 0.98 to 1.18 – a 20 % increase. The shape of the cylinder with the minimum kl_V value gets deeper: the H/R value goes from 0.041 to 0.89. Compared to heave-only, $\mathbb{PF}_{3,3,0.2}$, the minimum kl_S increases from 1.89 to 3.03 – a 60 % increase, and the minimum kl_V increases from 0.9 to 1.18 – a 31 % increase. $\mathbb{PF}_{3,3,0.1}$ only had one point on it, so this Pareto Front is more extensive.

$\underline{\alpha = 1, \epsilon = 0.1}$

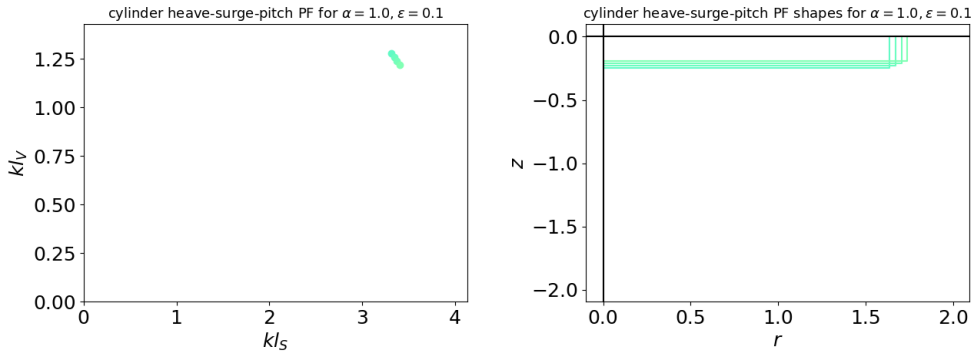

Figure 5-18: Pareto Front for the heave-surge-pitch case of cylinders with a α constraint value of 1 and ϵ constraint value of 0.1

Figure 5-18 shows $\mathbb{PF}_{135,1,0.1}$. This is a $\mathbb{PF}_C$ shape. Table 5.9 shows the characteristics for this Pareto Front.

kl_S	kl_V	kR	kH	$\frac{\lvert\xi_1\rvert}{A}$	$\frac{\lvert\xi_3\rvert}{A}$	$\frac{\lvert\xi_5\rvert}{A/R}$	$\overline{k_1}$	$\overline{z_G}$	$\overline{r_g}$
3.31	1.28	1.64	0.25	0.82	0.43	0.97	1.25	0.62	0.66
3.34	1.26	1.67	0.23	0.86	0.41	0.91	1.25	0.72	0.69
3.37	1.24	1.71	0.21	0.91	0.39	0.87	1.24	0.82	0.71
3.4	1.22	1.74	0.19	0.94	0.37	0.82	1.24	0.93	0.73

Table 5.9: Characteristics of the heave-surge-pitch Pareto Front for $\alpha = 1, \epsilon = 0.1$, called $\mathbb{PF}_{135,1,0.1}$, shown in figure 5-18.

Compared to $\mathbb{PF}_{135,3,0.1}$, decreasing α from 3 to 1 increases the minimum kl_S from 2.86 to 3.31 – a 16 % increase. We see from figures 5-6 that the decrease in α value meant the teal shapes were eliminated because of the pitch motion constraint. The shallowest shapes from $\mathbb{PF}_{135,3,0.1}$, shown in yellow-orange in figure 5-16, are eliminated. We can see from figure 5-5 that this is due to the surge motion constraint. Consequently, the minimum kl_V value increases from 0.98 to 1.22 – a 24 % increase. Compared the $\mathbb{PF}_{3,1,0.1}$, the minimum kl_S has increased from 2.62 to 3.31 – a 26 % increase, and the minimum kl_V has increased from 0.72 to 1.22 – a 69 % increase.

$\underline{\alpha = 1, \epsilon = 0.2}$

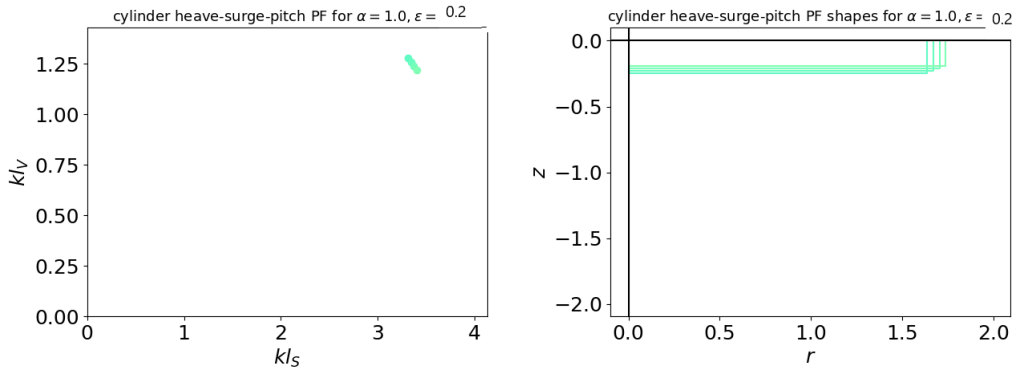

Figure 5-19: Pareto Front for the heave-surge-pitch case of cylinders with a α constraint value of 1 and ϵ constraint value of 0.2

Figure 5-19 shows $\mathbb{PF}_{135,1,0.2}$. We see that this is the same as $\mathbb{PF}_{135,1,0.1}$. Therefore, increasing ϵ does not change the Pareto Front at all, when $\alpha = 1$.

kl_S	kl_V	kR	kH	$\frac{\lvert\xi_1\rvert}{A}$	$\frac{\lvert\xi_3\rvert}{A}$	$\frac{\lvert\xi_5\rvert}{A/R}$	$\overline{k_1}$	$\overline{z_G}$	$\overline{r_g}$
3.31	1.28	1.64	0.25	0.82	0.43	0.97	1.25	0.62	0.66
3.34	1.26	1.67	0.23	0.86	0.41	0.91	1.25	0.72	0.69
3.37	1.24	1.71	0.21	0.91	0.39	0.87	1.24	0.82	0.71
3.4	1.22	1.74	0.19	0.94	0.37	0.82	1.24	0.93	0.73

Table 5.10: Characteristics of the heave-surge-pitch Pareto Front for $\alpha = 1, \epsilon = 0.2$, called $\mathbb{PF}_{135,1,0.2}$, shown in figure 5-19.

Comparing this to $\mathbb{PF}_{135,3,0.2}$ to show how decreasing α from 3 to 1, we see that the minimum kl_S value increases from 3.03 to 3.31 – a 9% increase, and the minimum kl_V value increases from 1.18 to 1.22 – a 3% increase. Compared to $\mathbb{PF}_{3,3,0.1}$, the minimum kl_S value increase from 2.62 to 3.31 – a 26 % increase, and the minimum kl_V value increases from 0.9 to 1.22 – a 35 % increase.

General trends/ observations

1. How $\mathcal{S}(\mathbb{PF}_{135})$ changes from the heave-only case to the heave-surge-pitch case

    - Compared to the heave-only problem, more shapes are eliminated from the populations.

- However, for some constraint values (for example, $\alpha = 3, \epsilon = 0.2$), there are more shapes on the Pareto Front for the heave-surge-pitch case than for the heave-only case.
- How $\mathcal{S}(\mathbb{P}_{135})$ and $\mathcal{S}(\mathbb{PF}_{135})$ changes for different α and ϵ is not as straight forward as in the heave-only case. For example, if $\alpha = 3$, changing ϵ from 0.1 to 0.2 eliminates shapes on both ends of $\mathcal{S}(\mathbb{P}_{135,3,0.1})$ because of the pitch steepness constraint. However, if $\alpha = 1$, changing ϵ from 0.1 to 0.2 does not change the population or Pareto Front at all.
- It is not the case that a stricter constraint means a fuller PF, like it was for heave.

2. How the performance changed from heave

   Table 5.11 shows the increase in $(kl_S)^{min}$ and $(kl_V)^{min}$ when going from the heave-only case to the heave-surge-pitch case.

constraint values	% increase of $(kl_S)^{min}$	% increase of $(kl_V)^{min}$
$\alpha = 3, \epsilon = 0.1$	51 %	36%
$\alpha = 3, \epsilon = 0.2$	60 %	31%
$\alpha = 1, \epsilon = 0.1$	26 %	69%
$\alpha = 1, \epsilon = 0.2$	26 %	35%

Table 5.11: The percent increase in minimum kl_V and minimum kl_S values from the heave-only case to the heave-surge-pitch case, for each constraint regime

3. How the performance changes with α
   - From $\mathbb{PF}_{135,3,0.1}$ to $\mathbb{PF}_{135,1,0.1}$, $(kl_S)^{min}$ increased by 16 % and $(kl_V)^{min}$ increased by 16 %.
   - From $\mathbb{PF}_{135,3,0.2}$ to $\mathbb{PF}_{135,1,0.2}$, $(kl_S)^{min}$ increased by 9 % and $(kl_V)^{min}$ increased by 3 %.

4. How the performance changes with ϵ

5. From $\mathbb{PF}_{135,3,0.1}$ to $\mathbb{PF}_{135,3,0.2}$, $(kl_S)^{min}$ increased by 6 % and $(kl_V)^{min}$ increased by 20 %.

6. From $\mathbb{PF}_{135,1,0.1}$ to $\mathbb{PF}_{135,1,0.2}$, $(kl_S)^{min}$ and $(kl_V)^{min}$ do not change.

7. How the shapes change from heave

   - The deepest shapes in $\mathbb{PF}_3$'s are eliminated in $\mathbb{PF}_{135}$'s
   - This is due to the I_{55} constraint, the pitch motion constraint and the pitch steepness constraint.
   - Also, the shallowest shapes are eliminated. This is due to the surge motion constraint and the pitch steepness constraint.
   - Therefore, for each case, $H/R\left((kl_S)^{min}\right)$ is smaller in $\mathbb{PF}_{135}$ compared to $\mathbb{PF}_{135}$, and $H/R\left((kl_V)^{min}\right)$ is larger.

In this section, results of the heave-surge-pitch optimization were presented and discussed.

5.4 Summary

In this chapter, we used the cylinder as an example to show the optimization framework and approach that we developed in this thesis, which were explained in chapters 3 and 4. But also, the cylinder is the simplest shape to build, and is often the preferred shape in ocean engineering, so these results show the dimensions of the *the best* cylinders under our optimization definition, and also physical insights into why they are the best shapes.

In section 5.1, we gave a detailed example of the approach. We showed how we used the theorem developed and proved in chapter 4 to find $\mathbb{R}_3^{cyl}$, the set of all cylinders that solve the heave resonance equation. We showed the plot of $\mathcal{S}(\mathbb{R}_3^{cyl})$, which is $\mathbb{R}_3^{cyl}$ in the $kl_V - kl_S$ space, in figure 5-2, which also showed the physical dimensions of a few of the cylinders in $\mathbb{R}_3^{cyl}$ by plotting them in the $r - z$ plane.

We discussed in chapter 4 that we observed that, for every shape of WEC discussed in this thesis, the shape of the curve of each $\mathbb{R}_3$ in the $kl_V - kl_S$ space followed a similar pattern: they are all one-to-one, concave down curves, with a maximum at $(kl_V)^{max}$. Figure 5-2 confirmed these aspects for $\mathbb{R}_3^{cyl}$. We then showed how each constraint affected the shape of $\mathcal{S}(\mathbb{R}_3^{cyl})$ to form the populations for the heave-only problem ($\mathbb{P}_3$'s). We proved in chapter 4 that the heave motion constraint would eliminate shapes from the lower left branch of $\mathbb{R}_3$, and figure 5-3 demonstrated this for the cylinders. Additionally, we proved that the heave steepness constraint would eliminate shapes from both the lower left branch as well as from the lower right branch, and figure 5-4 demonstrated this for the cylinders.

We then showed how each constraint affected the shape of $\mathcal{S}(\mathbb{R}_3^{cyl})$ to form the populations for the heave-surge-pitch problem ($\mathbb{P}_{135}$'s). Figures 5-5, 5-6, 5-7, 5-8 and 5-9 show which parts of $\mathbb{R}_3^{cyl}$ are eliminated by the surge motion constraint, the pitch motion constraint, the pitch steepness constraint, the pitch moment of inertia constraint, and the center of gravity constraint, respectively.

In section 5.2, we showed the results of the optimization for the heave-only case. Figure 5-10 shows the populations for four different cases: $\alpha = 3, \epsilon = 0.1$, $\alpha = 3, \epsilon = 0.2$, $\alpha = 1, \epsilon = 0.1$ and $\alpha = 1, \epsilon = 0.2$. The resulting Pareto Fronts – $\mathbb{PF}_{3,3,0.1}$, $\mathbb{PF}_{3,3,0.2}$, $\mathbb{PF}_{3,1,0.1}$, $\mathbb{PF}_{3,1,0.2}$ are shown in figures 5-11, 5-12, 5-13 and 5-14. Their dimensions and heave body motion amplitudes are recorded in tables 5.1, 5.2, 5.3, 5.4, 5.5, and 5.6.

As α decreases (so the motion constraint becomes more restrictive), the Pareto Front becomes 'fuller' (there are more options, less constrained), since elimination of more of the left branch opens up more of the right branch. As α decreases from 3 to 1, $(kl_S)^{min}$ increases by 39 %, but $(kl_V)^{min}$ does not change. As ϵ increases from 0.1 to 0.2, $(kl_S)^{min}$ does not change, but $(kl_V)^{min}$ increases by 25 %. As α decreases, the cylinder with $(kl_S)^{min}$ is shallower. As ϵ increase, the cylinder with $(kl_V)^{min}$ is deeper.

In section 5.3, we showed the results of the optimization for the heave-surge-pitch case. Figure 5-15 shows the populations for four different cases: $\alpha = 3, \epsilon = 0.1$, $\alpha = 3, \epsilon = 0.2$, $\alpha = 1, \epsilon = 0.1$ and $\alpha = 1, \epsilon = 0.2$.

The resulting Pareto Fronts – $\mathbb{PF}_{135,3,0.1}$, $\mathbb{PF}_{135,3,0.2}$, $\mathbb{PF}_{135,1,0.1}$, $\mathbb{PF}_{135,1,0.2}$ are shown in figures 5-16, 5-17, 5-18 and 5-19. Their dimensions, heave, surge and pitch body motion amplitudes, nondimensional surge spring coefficient, nondimensional center of gravity, and nondimensional radius of gyration are recorded in tables 5.7, 5.8, 5.9, and 5.10.

There are fewer shapes in the populations than for heave, because more shapes are eliminated from $\mathbb{R}_3^{cyl}$ by the surge-pitch constraints. In every case, $(kl_V)^{min}$ and $(kl_S)^{min}$ increased from $\mathbb{PF}_3$ to $\mathbb{PF}_{135}$: specific numbers given in table 5.11. The cylinders on the heave-surge-pitch Pareto Fronts are generally less optimal than those in the heave-only case, but it is important to recognize that the extractable power for the heave-surge-pitch case is three times more than that for the heave-only case.

Decreasing α increases $(kl_S)^{min}$ and $(kl_V)^{min}$. Increasing ϵ increases $(kl_S)^{min}$ when $\alpha = 3$ but does not change the population when $\alpha = 1$. As α decreases, the cylinder with $(kl_S)^{min}$ is shallower, and the cylinder with $(kl_V)^{min}$ is deeper. As ϵ increases, the cylinder with $(kl_S)^{min}$ is shallower; for $\alpha = 3$ the cylinder with $klVmin$ is deeper but for $\alpha = 1$ it does not change. Compared to heave, the cylinders with minimum $(kl_S)^{min}$ are shallower and the cylinder with minimum $(kl_V)^{min}$ are deeper. The constraints do not change the PFs in as predictable of a way as in heave

We presented Pareto Fronts for eight optimizations in this chapter: four for the heave-only problem, and four for the heave-surge-pitch problem. These Pareto Fronts are sets of optimal solutions, according to our optimization framework. It is not in the scope of this thesis to decide within the sets which cylinder is best. That could be decided by the developer by other parameters, such as cost, survivability, and ease of build.

In the next chapter, we will present the results for the optimizations of groups of shapes. We will use the results from this chapter as a base case to determine how much better (in terms of smaller surface area and/or volume) than a simple cylinder we can achieve by optimizing geometry.

Chapter 6

Optimization of a broad range of general geometries

6.1 Introduction

In the previous chapter, we showed the optimization framework and procedure using the cylinder as an example, and we showed a detailed analysis of the optimal dimensions of the cylinder. In this chapter, we present the optimization results from a systematic investigation of a broad range of shapes.

We studied five different groups of shapes. Groups of shapes are sets of multiple classes of shapes. Since every geometric shape in this thesis is axisymmetric, we describe the properties in the 2D $r - z$ plane. The four groups of shapes that are presented in this chapter are:

1. **'Flat-bottomed' shapes**: Piecewise-linear with one slope discontinuity at (r_1, z_1), where the segment from the centerline to the slope discontinuity is horizontal. That is, $z_1 = -H$. Figure 4-10 shows examples of classes of shapes in this group. The parameters to optimize are kl_V and $\overline{r_1} = \frac{r_1}{R}$. $\overline{r_1}$ can be any number greater than 0. A value of $\overline{r_1} > 1$ would signify a protruding outward shape.

2. **'One-kink' shapes**: Piecewise-linear with one slope discontinuity at (r_1, z_1). Figure 4-12 shows examples of classes of shapes in this group. The parameters to optimize are $kl_V, \overline{r_1} = \frac{r_1}{R}$ and $\overline{z_1} = \frac{z_1}{H}$. $\overline{r_1}$ can be any number greater than 0, and $\overline{z_1}$ can be any number less 0. A value of $\overline{r_1} > 1$ would signify a protruding outward shape. A value of $\overline{z_1} < -1$ would signify a protruding downwards shape.

3. **Compound cylinders**: One cylinder on top of another. The shape can be described by four piecewise-linear segments. The segment from the waterline to the first slope discontinuity is vertical, the segment from the first slope discontinuity to the second slope discontinuity is horizontal, the segment from the second slope discontinuity to the third slope discontinuity is vertical, and the segment from the third slope discontinuity to the centerline is horizontal. Figure 4-13 shows examples of classes of shapes in this group. The coordinates of the second slope discontinuity are (r_2, z_2). Therefore, the parameters to optimize are $kl_V, \overline{r_2} = \frac{r_2}{R}$ and $\overline{z_2} = \frac{z_2}{H}$. $\overline{r_2}$ is the ratio of the radii of the two cylinders and $\overline{z_1}$ is the ratio of the depths of the two cylinders. $\overline{r_2}$ can be any number greater than 0, and $\overline{z_2}$ can be between 0 and -1. A value of $\overline{r_2} < 1$ would signify a larger cylinder on top of a smaller cylinder, and a value of $\overline{r_2} > 1$ would signify a smaller cylinder on top of a larger cylinder.

4. **'No-kink-2nd-order' shapes**: A second-order continuous segment, with no slope discontinuities. The parametric equations have coefficients of the second-order polynomial basis function a_2 (in the r direction) and b_2 (in the z direction). Figure 4-14 shows examples of different classes of shapes in this group. The parameters to be optimized are $kl_V, \overline{a_2} = \frac{a_2}{R}$ and $\overline{b_2} = \frac{b_2}{H}$. $\overline{a_2}$ can be any number less than 0.1, and $\overline{b_2}$ can be any number greater than -0.1. A value of $\overline{a_2} < -0.1$ signifies a protruding outwards shape, and a value of $\overline{b_2} > 0.1$ would signify a protruding downwards shape.

We run these groups separately to observe trends among certain groups, and then we assess overall trends by combining the groups and comparing between the groups.

We also considered 'flat-sided' shapes: piecewise-linear with one slope discontinuity, where the segment from the waterline to the slope discontinuity is vertical (i.e., $\overline{r_1} = 1$). These did not perform well compared to the other groups, so we show them in Appendix D.

Similar to the cylinder analysis, for each group of shapes, we run eight optimizations: four for the heave-only problem, and four for the heave-surge-pitch problem. For each case, we run 2 values of α (3 and 1) and 2 values of ϵ (0.1 and 0.2). Therefore, the Pareto Fronts will be $\mathbb{PF}_{3,3,0.1}$, $\mathbb{PF}_{3,3,0.2}$, $\mathbb{PF}_{3,1,0.1}$, $\mathbb{PF}_{3,1,0.2}$, $\mathbb{PF}_{135,3,0.1}$, $\mathbb{PF}_{135,3,0.2}$, $\mathbb{PF}_{135,1,0.1}$, and $\mathbb{PF}_{135,1,0.2}$. The multi-objective optimization is described in sections 4.5. The sensitivity study, shown in Appendix C, informs us on how large the initial population size should be and how many generations we should run. These numbers for the heave-only problem vs. the heave-surge-pitch problem are very different. Also due to the sensitivity study, we set the mutation probability at 0.1 for all cases. For each group, we describe the possible values of the parameters by their limits and the step-size. For example, if for a specific group we say that the 'possible values' of $\overline{r_1}$ are [0.25,1,0.05], this means that in the optimization algorithm the defined possible values for $\overline{r_1}$ are 0.25, 0.3, 0.35, ..., 0.9,0.95,1. These are the only values that $\overline{r_1}$ can take in the algorithm. For some cases, after running the initial algorithm, we ran all cases for a select range of values. We state these values at the beginning of each section.

For each group, we only show the final Pareto Front and the corresponding shapes for each organism on the Pareto Front. We do not show entire populations like we did in the previous chapter for cylinders. For each run, the colors of the organisms on the Pareto Front on the left plot correspond to the colors of the shapes shown in the right plot. The colors from one run to the next are not related. After each Pareto Front, we show a table with corresponding dimensions and characteristics of the shapes, like we did for the cylinder. For the heave-only case, for each shape on the Pareto Front we show kl_S, kl_V, kR, kH, all other geometric parameters for that group, and $\frac{|\xi_3|}{A}$. For the heave-surge-pitch case, for each shape on the Pareto Front we show

kl_S, kl_V, kR, kH, all other geometric parameters for that group, $\frac{|\xi_3|}{A}, \frac{|\xi_1|}{A}, \frac{|\xi_5|}{A/R}, \overline{k_1}, \overline{z_G}$, and $\overline{r_g}$ where $\overline{k_1} = \frac{k_1}{\rho\omega^2 l_v^3}$, $\overline{z_G} = \frac{z_G}{H}$ and $\overline{r_g} = \frac{r_g}{R}$. The reason we show these tables is to compare different shapes on the Pareto Front. One of the reasons why we present a set of optimal shapes is that a developer could decide among this set which they would want to build, based on the importance of minimizing surface area or volume, but also potentially based on other parameters. The parameters in these tables are among the ones that are potentially interesting to a developer. For example, if stability was the most important thing to them, they could choose the one with the lowest $\overline{z_G}$.

The parameters to optimize are described in each group above. We state that we optimize kl_V and then any parameter that determines its $\overline{\mathscr{B}_E}$ vector. kR is determined from requiring the body to be in resonance in heave, and kH is found once $kR, \overline{\mathscr{B}_E}$ and kl_V are known. Therefore, we optimize the whole shape: we determine the best sizes and dimensions the shape should be to maximize power and minimize surface area and volume, while ensuring shapes are a practically realistic by requiring certain constraints.

In each group, we show the results and discuss observations and trends within the group, including the characteristics of shapes on the Pareto Front and how the motion and steepness constraints affect shapes and performance. We will also compare results from the heave-only problem to those from the heave-surge-pitch problem, and we will compare shapes and performance from these Pareto Fronts to the ones found in the previous chapter for the optimal cylinders.

In section 2, we present the 'flat-bottomed' results, in section 3 we present the 'one-kink' results, in section 4 we present the compound cylinder results, in section 5 we present the 'no-kink-2nd-order' results. In section 6, we combine the results from all five groups to make overall Pareto Fronts for each of the 8 optimizations (heave-only and heave-surge-pitch for the different α and ϵ values). In section 7 we discuss overall observations, trends, and conclusions. We discuss physical insights we gained from these results, and make conclusions and hypotheses about why they are true. In

section 8, we show the benefit of the optimization by showing how much less material optimal shapes have compared to the optimal cylinders, to extract the same power, and we also show physical dimensions and amount of extractable power in a typical sea state. In section 9, we discuss the overall optimal shape. And finally, in section 10 we summarize the chapter.

6.2 Flat-bottomed

Since this was used as the basis for the sensitivity study (see Appendix C), we ran every possible value of each of the parameters. For both the heave-only problem, as well as the heave-surge-pitch problem, the possible values for $\overline{r_1}$ are [0.25,1.45,0.02], and the possible values for kl_V are [0.3,1.7,0.05].

6.2.1 Heave-only

$\alpha = 3, \epsilon = 0.1$

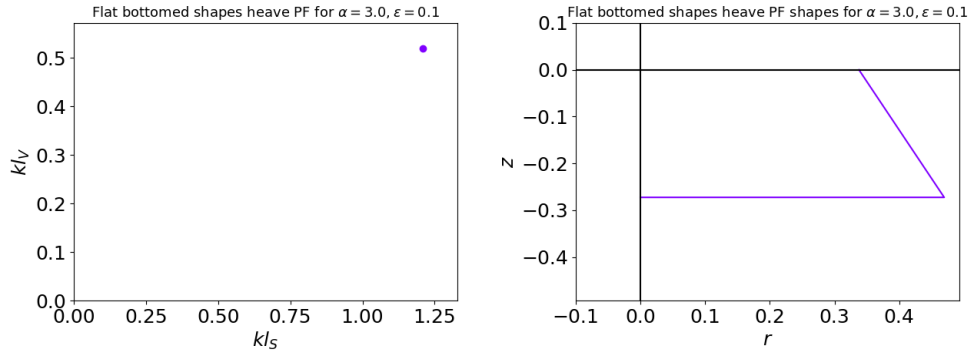

Figure 6-1: Pareto Front (left) and corresponding shapes in the $r - z$ plane (right), resulting from the multi-objective evolutionary algorithm for 'flat-bottomed' shapes for the heave-only problem, with motion constraint $\alpha = 3$ and steepness constraint $\epsilon = 0.1$

kl_S	kl_V	kR	kH	$\overline{r_1}$	$\frac{\lvert\xi_3\rvert}{A}$
1.19	0.52	0.32	0.3	1.39	2.88

Table 6.1: Dimensions and characteristics of the 'flat-bottomed' shapes on the Pareto Front for the heave-only problem, with motion constraint $\alpha = 3$ and steepness constraint $\epsilon = 0.1$ (shown in figure 6-1)

$\alpha = 3, \epsilon = 0.2$

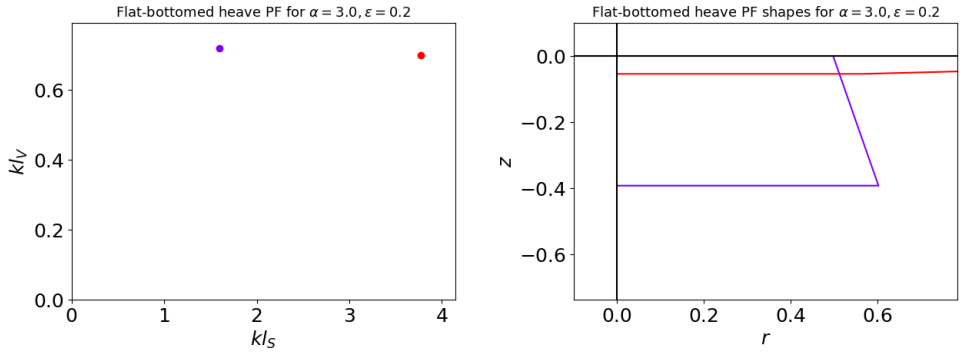

Figure 6-2: Pareto Front (left) and corresponding shapes in the $r - z$ plane (right), resulting from the multi-objective evolutionary algorithm for 'flat-bottomed' shapes for the heave-only problem, with motion constraint $\alpha = 3$ and steepness constraint $\epsilon = 0.2$

kl_S	kl_V	kR	kH	$\overline{r_1}$	$\frac{\lvert\xi_3\rvert}{A}$
1.59	0.72	0.5	0.39	1.21	1.93
3.77	0.7	2.13	0.05	0.27	0.25

Table 6.2: Dimensions and characteristics of the 'flat-bottomed' shapes on the Pareto Front for the heave-only problem, with motion constraint $\alpha = 3$ and steepness constraint $\epsilon = 0.2$ (shown in figure 6-2)

$\alpha = 1, \epsilon = 0.1$

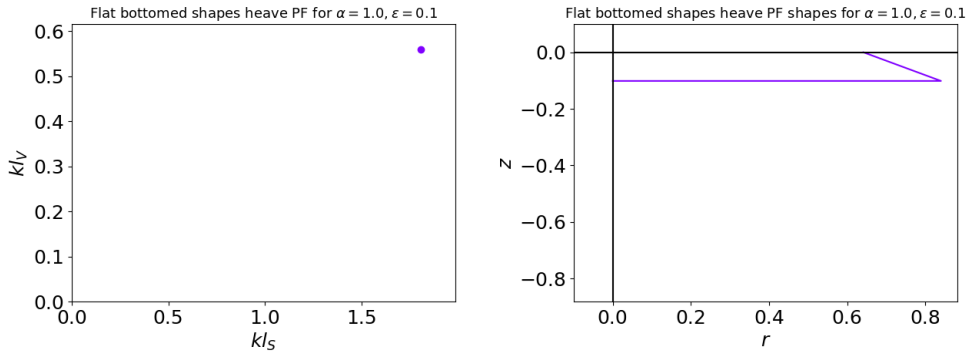

Figure 6-3: Pareto Front (left) and corresponding shapes in the $r - z$ plane (right), resulting from the multi-objective evolutionary algorithm for 'flat-bottomed' shapes for the heave-only problem, with motion constraint $\alpha = 1$ and steepness constraint $\epsilon = 0.1$

kl_S	kl_V	kR	kH	$\overline{r_1}$	$\frac{\lvert\xi_3\rvert}{A}$
1.8	0.56	0.64	0.1	1.31	0.95

Table 6.3: Dimensions and characteristics of the 'flat-bottomed' shapes on the Pareto Front for the heave-only problem, with motion constraint $\alpha = 1$ and steepness constraint $\epsilon = 0.1$ (shown in figure 6-3)

$\alpha = 1, \epsilon = 0.2$

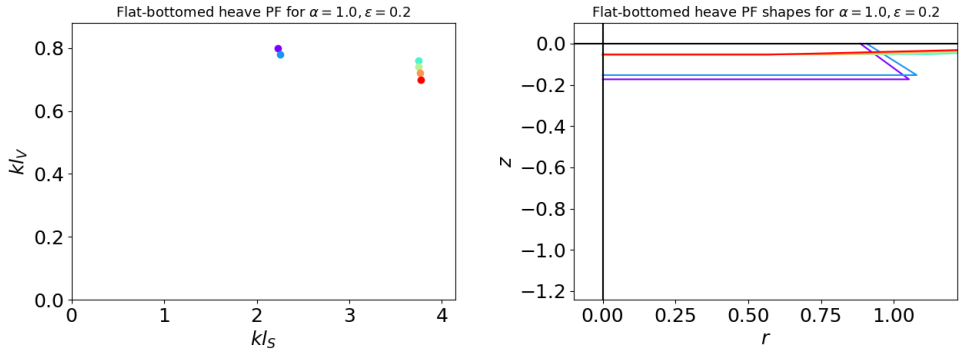

Figure 6-4: Pareto Front (left) and corresponding shapes in the $r - z$ plane (right), resulting from the multi-objective evolutionary algorithm for 'flat-bottomed' shapes for the heave-only problem, with motion constraint $\alpha = 1$ and steepness constraint $\epsilon = 0.2$

kl_S	kl_V	kR	kH	$\overline{r_1}$	$\frac{\lvert\xi_3\rvert}{A}$
2.22	0.8	0.88	0.17	1.19	0.72
2.26	0.78	0.91	0.15	1.19	0.68
3.75	0.76	2.11	0.05	0.53	0.25
3.75	0.74	2.12	0.05	0.45	0.25
3.76	0.72	2.12	0.05	0.37	0.25
3.77	0.7	2.13	0.05	0.27	0.25

Table 6.4: Dimensions and characteristics of the 'flat-bottomed' shapes on the Pareto Front for the heave-only problem, with motion constraint $\alpha = 1$ and steepness constraint $\epsilon = 0.2$ (shown in figure 6-4)

Trends/ observations

- We notice that generally these optimal shapes are *protruding outward*. That is, $\overline{r_1} > 1$. We will see that this is a general trend, and we will show our hypothesis for why this is true in the discussion in section 6.7.

- For a stricter motion constraint (i.e. when α decreases), shapes are wider (kR increases) and shallower (kH decreases), with a similar level of 'protrusion' ($\overline{r_1}$ stays about the same).

- For a stricter steepness constraint (i.e. when ϵ increases), the shapes are larger (both kR and kH increase) and less protruding ($\overline{r_1}$ decreases).

6.2.2 Heave-surge-pitch

$\underline{\alpha = 3, \epsilon = 0.1}$

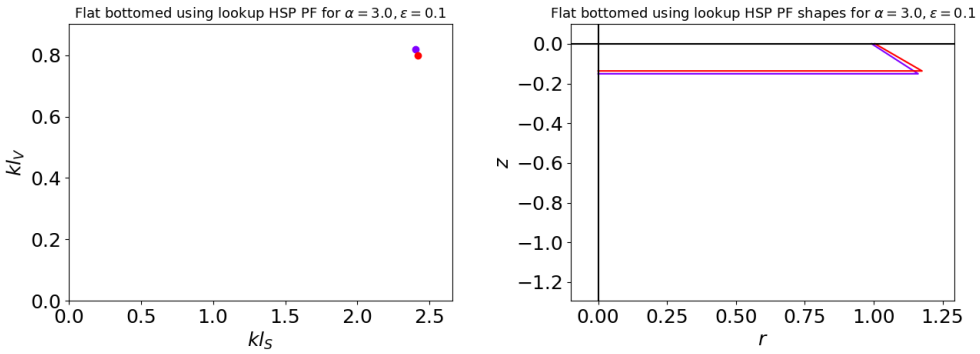

Figure 6-5: Pareto Front (left) and corresponding shapes in the $r-z$ plane (right), resulting from the multi-objective evolutionary algorithm for 'flat-bottomed' shapes for the heave-surge-pitch problem, with motion constraint $\alpha = 3$ and steepness constraint $\epsilon = 0.1$

kl_S	kl_V	kR	kH	$\overline{r_1}$	$\frac{\lvert\xi_3\rvert}{A}$	$\frac{\lvert\xi_1\rvert}{A}$	$\frac{\lvert\xi_5\rvert}{A/R}$	$\overline{k_1}$	$\overline{z_G}$	$\overline{r_g}$
2.37	0.82	0.98	0.16	1.17	0.64	2.3	1.47	1.31	1.28	0.24
2.39	0.8	0.99	0.14	1.17	0.62	2.44	1.37	1.31	1.53	0.19

Table 6.5: Dimensions and characteristics of the 'flat-bottomed' shapes on the Pareto Front for the heave-surge-pitch problem, with motion constraint $\alpha = 3$ and steepness constraint $\epsilon = 0.1$ (shown in figure 6-5)

$\underline{\alpha = 3, \epsilon = 0.2}$

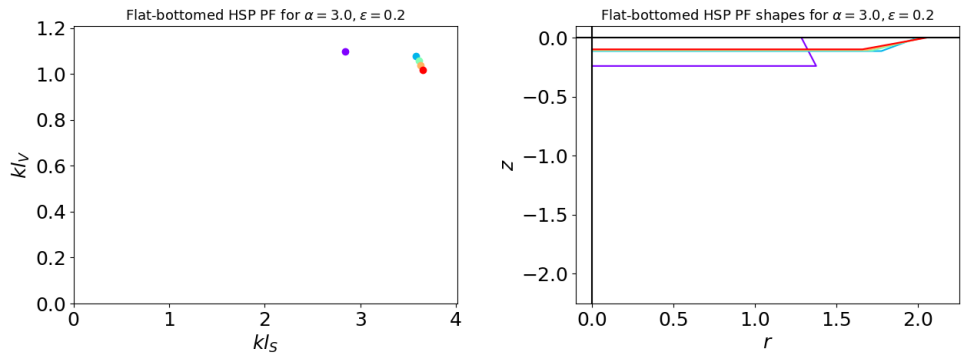

Figure 6-6: Pareto Front (left) and corresponding shapes in the $r-z$ plane (right), resulting from the multi-objective evolutionary algorithm for 'flat-bottomed' shapes for the heave-surge-pitch problem, with motion constraint $\alpha = 3$ and steepness constraint $\epsilon = 0.2$

kl_S	kl_V	kR	kH	$\overline{r_1}$	$\frac{\lvert\xi_3\rvert}{A}$	$\frac{\lvert\xi_1\rvert}{A}$	$\frac{\lvert\xi_5\rvert}{A/R}$	$\overline{k_1}$	$\overline{z_G}$	$\overline{r_g}$
2.84	1.1	1.29	0.24	1.07	0.52	1.11	1.19	1.3	0.75	0.49
3.58	1.08	2.0	0.11	0.89	0.28	1.77	0.56	1.17	4.03	0.93
3.62	1.06	2.02	0.11	0.85	0.28	2.12	0.52	1.14	4.71	0.95
3.63	1.04	2.04	0.1	0.83	0.27	2.36	0.51	1.14	5.19	0.98
3.65	1.02	2.05	0.1	0.81	0.27	2.73	0.48	1.12	5.71	1.01

Table 6.6: Dimensions and characteristics of the 'flat-bottomed' shapes on the Pareto Front for the heave-surge-pitch problem, with motion constraint $\alpha = 3$ and steepness constraint $\epsilon = 0.2$ (shown in figure 6-6)

$\underline{\alpha = 1, \epsilon = 0.1}$

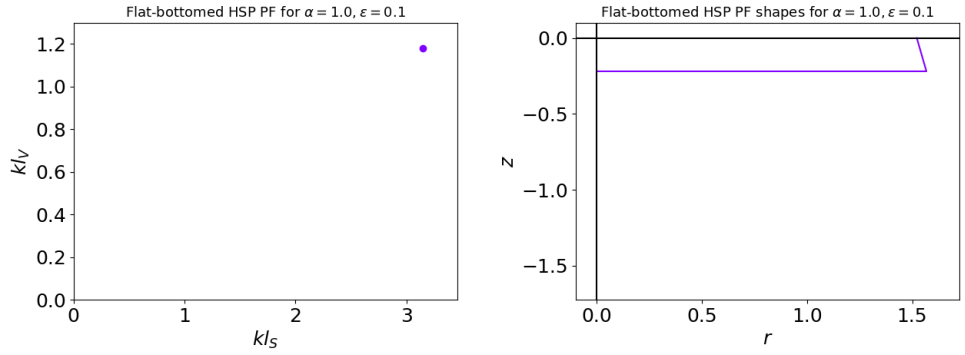

Figure 6-7: Pareto Front (left) and corresponding shapes in the $r-z$ plane (right), resulting from the multi-objective evolutionary algorithm for 'flat-bottomed' shapes for the heave-surge-pitch problem, with motion constraint $\alpha = 1$ and steepness constraint $\epsilon = 0.1$

kl_S	kl_V	kR	kH	$\overline{r_1}$	$\frac{\lvert\xi_3\rvert}{A}$	$\frac{\lvert\xi_1\rvert}{A}$	$\frac{\lvert\xi_5\rvert}{A/R}$	$\overline{k_1}$	$\overline{z_G}$	$\overline{r_g}$
3.15	1.18	1.52	0.22	1.03	0.98	0.43	0.94	1.27	0.86	0.62

Table 6.7: Dimensions and characteristics of the 'flat-bottomed' shapes on the Pareto Front for the heave-surge-pitch problem, with motion constraint $\alpha = 1$ and steepness constraint $\epsilon = 0.1$ (shown in figure 6-7)

$\underline{\alpha = 1, \epsilon = 0.2}$

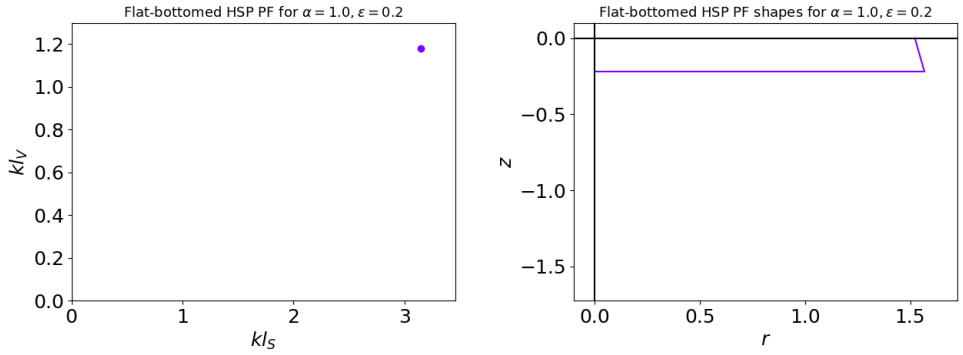

Figure 6-8: Pareto Front (left) and corresponding shapes in the $r-z$ plane (right), resulting from the multi-objective evolutionary algorithm for 'flat-bottomed' shapes for the heave-surge-pitch problem, with motion constraint $\alpha = 1$ and steepness constraint $\epsilon = 0.2$

kl_S	kl_V	kR	kH	$\overline{r_1}$	$\frac{\lvert\xi_3\rvert}{A}$	$\frac{\lvert\xi_1\rvert}{A}$	$\frac{\lvert\xi_5\rvert}{A/R}$	$\overline{k_1}$	$\overline{z_G}$	$\overline{r_g}$
3.15	1.18	1.52	0.22	1.03	0.98	0.43	0.94	1.27	0.86	0.62

Table 6.8: Dimensions and characteristics of the 'flat-bottomed' shapes on the Pareto Front for the heave-surge-pitch problem, with motion constraint $\alpha = 1$ and steepness constraint $\epsilon = 0.2$ (shown in figure 6-8)

Trends/ observations

- We notice again that generally the optimal shapes protrude outwards. Therefore, this is a trend for the heave-only problem as well as the heave-surge-pitch problem.
- Compared to the optimal shapes for the heave-only problem, the optimal shapes on these Pareto Fronts are generally wider and less protruding (i.e., the shapes on the heave-surge-pitch Pareto Fronts have larger kR values and smaller $\overline{r_1}$ values).

- Decreasing α for the heave-surge-pitch problem results in wider shapes (i.e. kR increases), but unlike the heave-only problem, the shape are not shallower.
- The Pareto Fronts are identical for $\alpha = 1, \epsilon = 0.1$ and $\alpha = 1, \epsilon = 0.2$.

6.3 One-kink shapes

6.3.1 Heave-only

For the heave-only problem, the possible values of kl_V were [0.3,1.5,0.05], the possible values of $\overline{r_1}$ were [0.25,1.6,0.05], and the possible values of $\overline{z_1}$ were [-1.5,-0.1,0.05]. The initial population size was 500, and the number of generations was 7500. Once we did this initial optimization and noticed the trend that shapes with $\overline{r_1} > 1$ and $-1 < \overline{z_1} < 0$ were optimal, we evaluated all values of $kl_V = [0.3, 0.75, 0.05], \overline{r_1} = [1, 1.7, 0.05]$ and $\overline{z_1} = [-1, -0.1, 0.05]$.

$\underline{\alpha = 3, \epsilon = 0.1}$

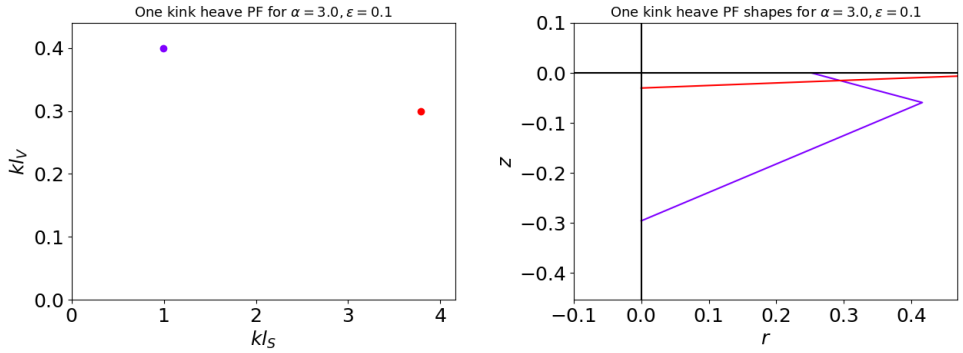

Figure 6-9: Pareto Front (left) and corresponding shapes in the $r - z$ plane (right), resulting from the multi-objective evolutionary algorithm for 'one-kink' shapes for the heave-only problem, with motion constraint $\alpha = 3$ and steepness constraint $\epsilon = 0.1$

kl_S	kl_V	kR	kH	$\overline{r_1}$	$\overline{z_1}$	$\frac{\lvert\xi_3\rvert}{A}$
1.0	0.4	0.25	0.3	1.65	-0.2	2.87
3.79	0.3	2.14	0.03	0.25	-0.1	0.25

Table 6.9: Dimensions and characteristics of the 'one-kink' shapes on the Pareto Front for the heave-only problem, with motion constraint $\alpha = 3$ and steepness constraint $\epsilon = 0.1$ (shown in figure 6-9)

$\alpha = 3, \epsilon = 0.2$

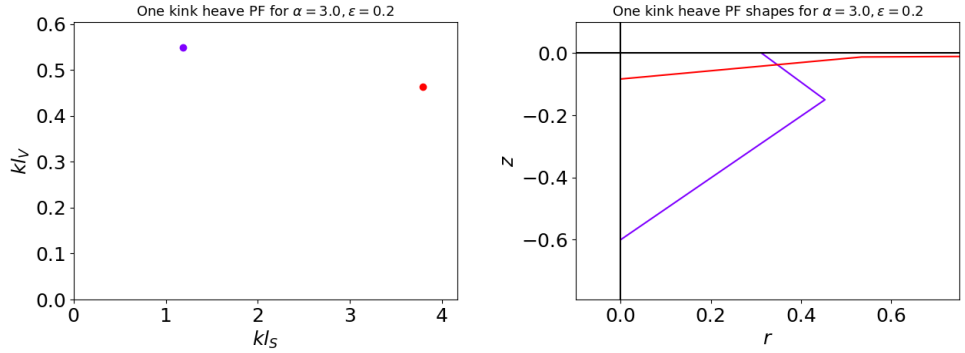

Figure 6-10: Pareto Front (left) and corresponding shapes in the $r - z$ plane (right), resulting from the multi-objective evolutionary algorithm for 'one-kink' shapes for the heave-only problem, with motion constraint $\alpha = 3$ and steepness constraint $\epsilon = 0.2$

kl_S	kl_V	kR	kH	$\overline{r_1}$	$\overline{z_1}$	$\frac{\lvert\xi_3\rvert}{A}$
1.18	0.55	0.31	0.6	1.45	-0.25	2.71
3.79	0.46	2.14	0.08	0.25	-0.15	0.25

Table 6.10: Dimensions and characteristics of the 'one-kink' shapes on the Pareto Front for the heave-only problem, with motion constraint $\alpha = 3$ and steepness constraint $\epsilon = 0.2$ (shown in figure 6-10)

$\alpha = 1, \epsilon = 0.1$

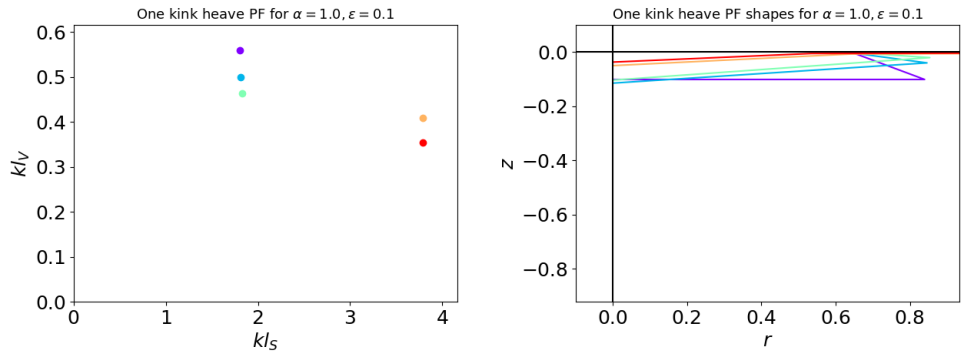

Figure 6-11: Pareto Front (left) and corresponding shapes in the $r - z$ plane (right), resulting from the multi-objective evolutionary algorithm for 'one-kink' shapes for the heave-only problem, with motion constraint $\alpha = 1$ and steepness constraint $\epsilon = 0.1$

kl_S	kl_V	kR	kH	$\overline{r_1}$	$\overline{z_1}$	$\frac{\lvert\xi_3\rvert}{A}$
1.8	0.56	0.64	0.1	1.31	-1.0	0.95
1.81	0.5	0.63	0.11	1.35	-0.35	0.92
1.83	0.46	0.63	0.1	1.35	-0.2	0.89
3.78	0.41	2.14	0.05	0.3	-0.15	0.25
3.79	0.35	2.14	0.04	0.25	-0.15	0.25

Table 6.11: Dimensions and characteristics of the 'one-kink' shapes on the Pareto Front for the heave-only problem, with motion constraint $\alpha = 1$ and steepness constraint $\epsilon = 0.1$ (shown in figure 6-11)

$\underline{\alpha = 1, \epsilon = 0.2}$

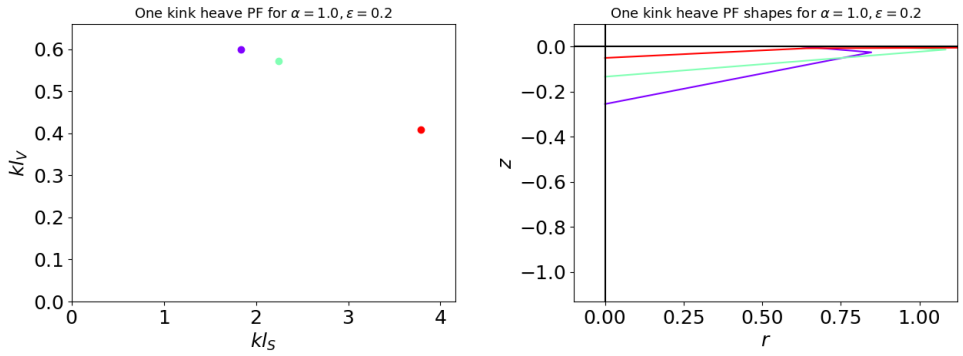

Figure 6-12: Pareto Front (left) and corresponding shapes in the $r - z$ plane (right), resulting from the multi-objective evolutionary algorithm for 'one-kink' shapes for the heave-only problem, with motion constraint $\alpha = 1$ and steepness constraint $\epsilon = 0.2$

kl_S	kl_V	kR	kH	$\overline{r_1}$	$\overline{z_1}$	$\frac{\lvert\xi_3\rvert}{A}$
1.83	0.6	0.63	0.25	1.35	-0.1	0.92
2.24	0.57	0.87	0.13	1.25	-0.1	0.26
3.78	0.41	2.14	0.05	0.3	-0.15	0.26

Table 6.12: Dimensions and characteristics of the 'one-kink' shapes on the Pareto Front for the heave-only problem, with motion constraint $\alpha = 1$ and steepness constraint $\epsilon = 0.2$ (shown in figure 6-12)

Trends/ observations

- Similar to the flat-bottomed shapes, generally the optimal shapes are protruding outwards.

- We also notice that generally $-0.5 < \overline{z_1} < 0$ – that is, the protrusion is closer to the waterline ($z = 0$) than the maximum draft ($z = -H$).

- If we compare these Pareto Fronts to the ones from the flat-bottomed groups, we see that minimum kl_S values and minimum kl_V values for the one-kink group are smaller than the flat-bottomed group. For example, comparing the purple shape in figure 6-1 to the purple shape in figure 6-9, the kl_S values are 1.19 (flat-bottomed) vs. 1 (one-kink), and the kl_V values are 0.52 (flat-bottomed) vs. 0.4 (one-kink).

- For $\mathbb{PF}_{3,1,0.1}$, this includes a flat-bottomed shape, as well as shapes with $-1 < \overline{z_1} < 0$. The flat-bottomed shape has the smallest kl_S value. As $\overline{z_1}$ increases, kl_S increases slightly and kl_V decreases significantly, creating an almost vertical Pareto Front for those shapes.

- As α decreases, kR increases, kH decreases. That is, shapes get wider and shallower.

- As ϵ increases, kR stays about the same, kH increases, $\overline{r_1}$ stays about the same. That is, shapes get deeper but with a similar protrusion.

6.3.2 Heave-surge-pitch

For the heave-surge-pitch problem, the possible values of kl_V were [0.6,1.5,0.05], the possible values of $\overline{r_1}$ were [0.25,1.6,0.05], and the possible values of $\overline{z_1}$ were [-1.5,-0.1,0.05]. The initial population size was 300, and the number of generations was 1500. We also evaluated all values of $kl_V = [0.8, 1.3, 0.05], \overline{r_1} = [1, 1.6, 0.05]$ and $\overline{z_1} = [-1, -0.1, 0.05]$.

$\underline{\alpha = 3, \epsilon = 0.1}$

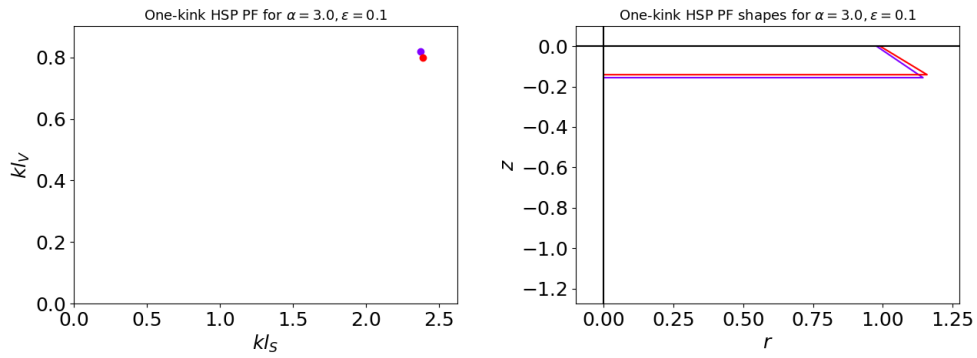

Figure 6-13: Pareto Front (left) and corresponding shapes in the $r - z$ plane (right), resulting from the multi-objective evolutionary algorithm for 'one-kink' shapes for the heave-surge-pitch problem, with motion constraint $\alpha = 3$ and steepness constraint $\epsilon = 0.1$

kl_S	kl_V	kR	kH	$\overline{r_1}$	$\overline{z_1}$	$\frac{\lvert\xi_3\rvert}{A}$	$\frac{\lvert\xi_1\rvert}{A}$	$\frac{\lvert\xi_5\rvert}{A/R}$	$\overline{k_1}$	$\overline{z_G}$	$\overline{r_g}$
2.37	0.82	0.98	0.16	1.17	-1.0	0.64	2.3	1.47	1.31	1.28	0.24
2.39	0.8	0.99	0.14	1.17	-1.0	0.62	2.44	1.37	1.31	1.53	0.19

Table 6.13: Dimensions and characteristics of the 'one-kink' shapes on the Pareto Front for the heave-surge-pitch problem, with motion constraint $\alpha = 3$ and steepness constraint $\epsilon = 0.1$ (shown in figure 6-13)

$\underline{\alpha = 3, \epsilon = 0.2}$

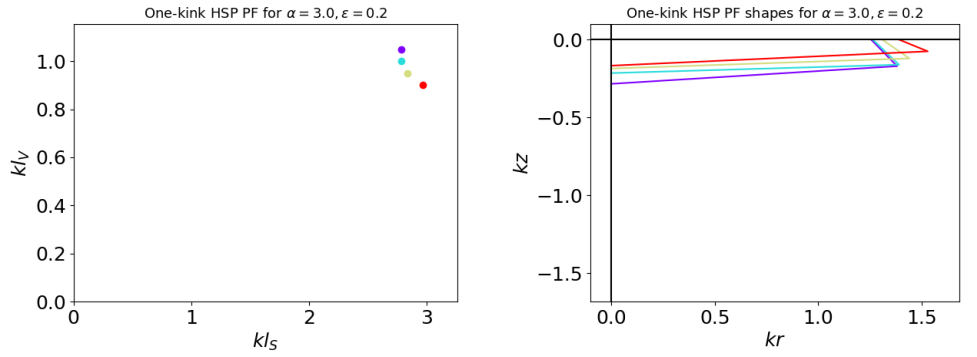

Figure 6-14: Pareto Front (left) and corresponding shapes in the $r - z$ plane (right), resulting from the multi-objective evolutionary algorithm for 'one-kink' shapes for the heave-surge-pitch problem, with motion constraint $\alpha = 3$ and steepness constraint $\epsilon = 0.2$

kl_S	kl_V	kR	kH	$\overline{r_1}$	$\overline{z_1}$	$\frac{\lvert\xi_3\rvert}{A}$	$\frac{\lvert\xi_1\rvert}{A}$	$\frac{\lvert\xi_5\rvert}{A/R}$	$\overline{k_1}$	$\overline{z_G}$	$\overline{r_g}$
2.79	1.05	1.26	0.28	1.1	-0.6	0.5	1.41	1.06	1.24	0.97	0.13
2.79	1.0	1.26	0.22	1.1	-0.75	0.49	1.57	1.04	1.25	1.18	0.3
2.84	0.95	1.31	0.19	1.1	-0.65	0.45	1.91	0.91	1.21	1.72	0.34
2.97	0.9	1.39	0.17	1.1	-0.45	0.41	2.64	0.8	1.15	2.37	0.45

Table 6.14: Dimensions and characteristics of the 'one-kink' shapes on the Pareto Front for the heave-surge-pitch problem, with motion constraint $\alpha = 3$ and steepness constraint $\epsilon = 0.2$ (shown in figure 6-14)

$\underline{\alpha = 1, \epsilon = 0.1}$

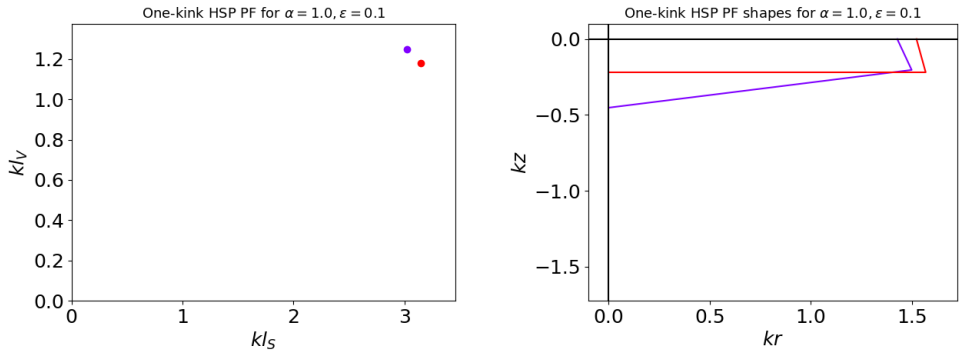

Figure 6-15: Pareto Front (left) and corresponding shapes in the $r - z$ plane (right), resulting from the multi-objective evolutionary algorithm for 'one-kink' shapes for the heave-surge-pitch problem, with motion constraint $\alpha = 1$ and steepness constraint $\epsilon = 0.1$

kl_S	kl_V	kR	kH	$\overline{r_1}$	$\overline{z_1}$	$\frac{\lvert\xi_3\rvert}{A}$	$\frac{\lvert\xi_1\rvert}{A}$	$\frac{\lvert\xi_5\rvert}{A/R}$	$\overline{k_1}$	$\overline{z_G}$	$\overline{r_g}$
3.02	1.25	1.43	0.45	1.05	-0.45	0.46	0.94	0.97	1.24	0.63	0.28
3.15	1.18	1.52	0.22	1.03	-1.0	0.43	0.98	0.94	1.27	0.86	0.62

Table 6.15: Dimensions and characteristics of the 'one-kink' shapes on the Pareto Front for the heave-surge-pitch problem, with motion constraint $\alpha = 1$ and steepness constraint $\epsilon = 0.1$ (shown in figure 6-15)

$\underline{\alpha = 1, \epsilon = 0.2}$

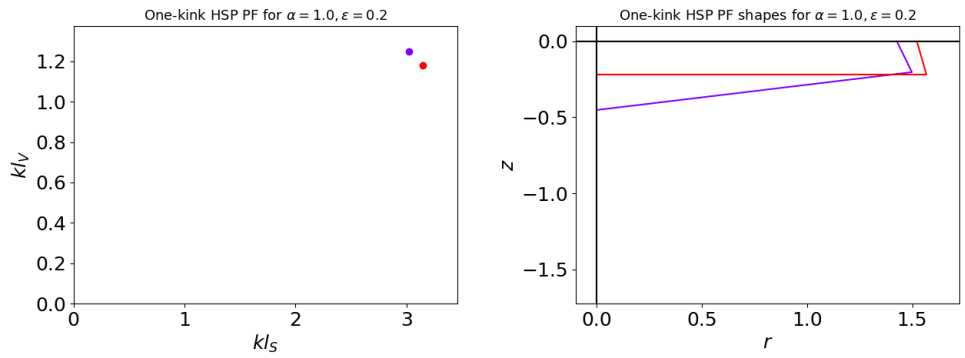

Figure 6-16: Pareto Front (left) and corresponding shapes in the $r - z$ plane (right), resulting from the multi-objective evolutionary algorithm for 'one-kink' shapes for the heave-surge-pitch problem, with motion constraint $\alpha = 1$ and steepness constraint $\epsilon = 0.2$

kl_S	kl_V	kR	kH	$\overline{r_1}$	$\overline{z_1}$	$\frac{\lvert\xi_3\rvert}{A}$	$\frac{\lvert\xi_1\rvert}{A}$	$\frac{\lvert\xi_5\rvert}{A/R}$	$\overline{k_1}$	$\overline{z_G}$	$\overline{r_g}$
3.02	1.25	1.43	0.45	1.05	-0.45	0.46	0.94	0.97	1.24	0.63	0.28
3.15	1.18	1.52	0.22	1.03	-1.0	0.43	0.98	0.94	1.27	0.86	0.62

Table 6.16: Dimensions and characteristics of the 'one-kink' shapes on the Pareto Front for the heave-surge-pitch problem, with motion constraint $\alpha = 1$ and steepness constraint $\epsilon = 0.2$ (shown in figure 6-16)

Trends/ observations

- We once again notice that generally the optimal shapes are protruding outwards.
- We notice that the maximum radius occurs when $-1 < \overline{z_1} < 0$. Compared to the heave-only problem, the $\overline{z_1}$ values are smaller: recall that for the heave-only problem the optimal shapes had $-0.5 < \overline{z_1} < 0$, whereas for the heave-surge-pitch problem $-1 < \overline{z_1} < -0.5$ mostly. We see that shapes that 'protruding downward' (i.e. $\overline{z_1} < -1$) is generally not optimal.
- As α decreases, kR and kH increase, $\overline{r_1}$ decreases. That is, shapes generally get wider, deeper and less protruding outwards.
- Compared to the heave-only problem, the optimal shapes on these Pareto Fronts are wider, shallower, and less outwardly protruding.
- The Pareto Fronts for $\alpha = 1, \epsilon = 0.1$ and for $\alpha = 1, \epsilon = 0.2$ are identical.

6.4 Compound cylinder

6.4.1 Heave-only

For the heave-only problem, the possible values of kl_V were [0.3,1.4,0.05], the possible values of $\overline{r_2}$ were [0.25,1.4,0.05], and the possible values of $\overline{z_2}$ were [-0.9,-0.25,0.05]. The initial population size was 500, and the number of generations was 4300. Additionally, however, we ran every compound cylinder with $\overline{r_2}$ values [1,1.4,0.05] and $\overline{z_2}$ [-0.9,-0.25,0.05].

$\alpha = 3, \epsilon = 0.1$

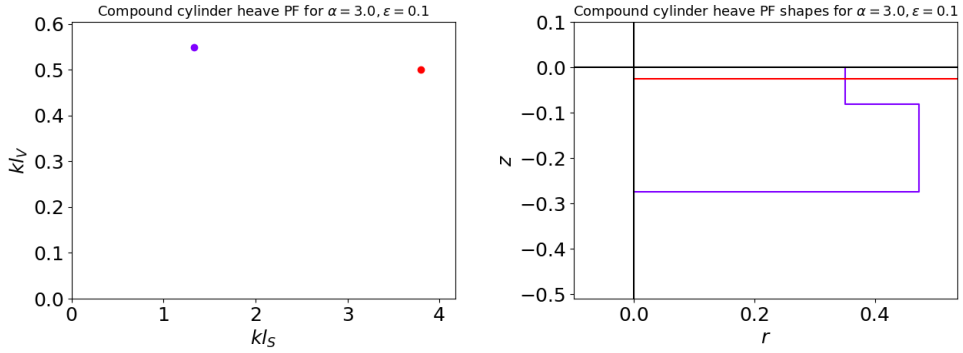

Figure 6-17: Pareto Front (left) and corresponding shapes in the $r - z$ plane (right), resulting from the multi-objective evolutionary algorithm for 'compound-cylinder' shapes for the heave-only problem, with motion constraint $\alpha = 3$ and steepness constraint $\epsilon = 0.1$

kl_S	kl_V	kR	kH	$\overline{r_2}$	$\overline{z_2}$	$\frac{\lvert\xi_3\rvert}{A}$
1.33	0.55	0.35	0.27	1.35	-0.3	2.73
3.79	0.5	2.13	0.03	0.35	-0.25	0.25

Table 6.17: Dimensions and characteristics of the 'compound-cylinder' shapes on the Pareto Front for the heave-only problem, with motion constraint $\alpha = 3$ and steepness constraint $\epsilon = 0.1$ (shown in figure 6-17)

$\alpha = 3, \epsilon = 0.2$

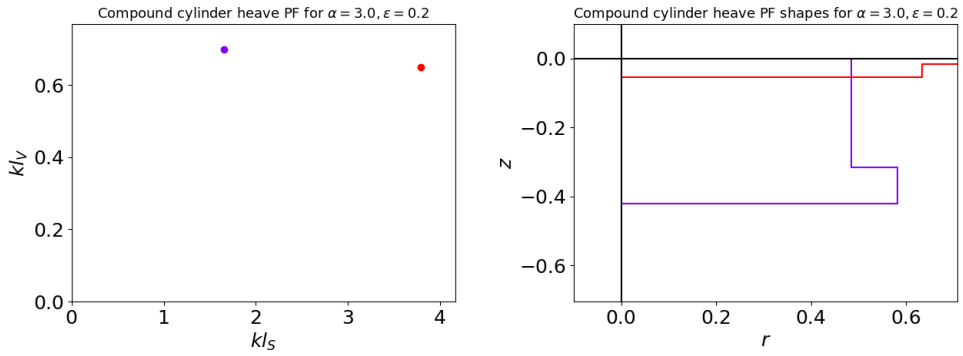

Figure 6-18: Pareto Front (left) and corresponding shapes in the $r - z$ plane (right), resulting from the multi-objective evolutionary algorithm for 'compound-cylinder' shapes for the heave-only problem, with motion constraint $\alpha = 3$ and steepness constraint $\epsilon = 0.2$

kl_S	kl_V	kR	kH	$\overline{r_2}$	$\overline{z_2}$	$\frac{\lvert\xi_3\rvert}{A}$
1.65	0.7	0.48	0.42	1.2	-0.75	2.08
3.79	0.65	2.11	0.05	0.3	-0.3	0.26

Table 6.18: Dimensions and characteristics of the 'compound-cylinder' shapes on the Pareto Front for the heave-only problem, with motion constraint $\alpha = 3$ and steepness constraint $\epsilon = 0.2$ (shown in figure 6-18)

$\alpha = 1, \epsilon = 0.1$

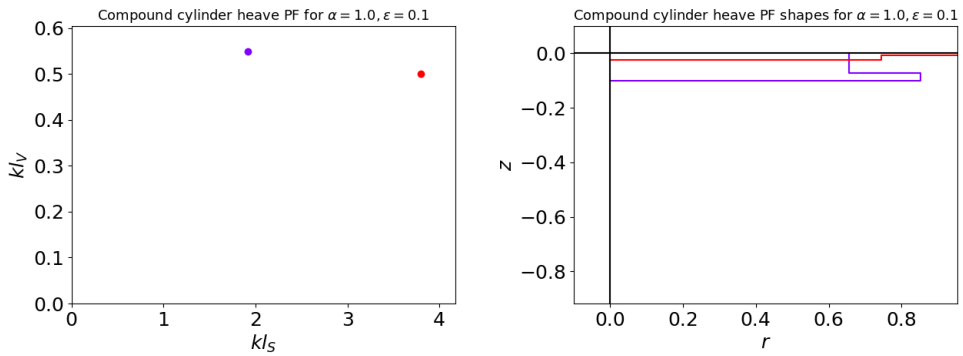

Figure 6-19: Pareto Front (left) and corresponding shapes in the $r - z$ plane (right), resulting from the multi-objective evolutionary algorithm for 'compound-cylinder' shapes for the heave-only problem, with motion constraint $\alpha = 1$ and steepness constraint $\epsilon = 0.1$

kl_S	kl_V	kR	kH	$\overline{r_2}$	$\overline{z_2}$	$\frac{\lvert\xi_3\rvert}{A}$
1.92	0.55	0.66	0.1	1.3	-0.7	0.95
3.79	0.5	2.13	0.03	0.35	-0.25	0.25

Table 6.19: Dimensions and characteristics of the 'compound-cylinder' shapes on the Pareto Front for the heave-only problem, with motion constraint $\alpha = 1$ and steepness constraint $\epsilon = 0.1$ (shown in figure 6-19)

$\underline{\alpha = 1, \epsilon = 0.2}$

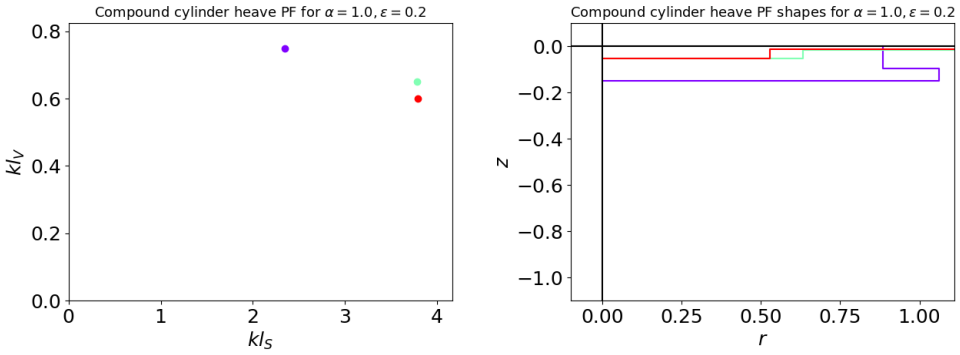

Figure 6-20: Pareto Front (left) and corresponding shapes in the $r - z$ plane (right), resulting from the multi-objective evolutionary algorithm for 'compound-cylinder' shapes for the heave-only problem, with motion constraint $\alpha = 1$ and steepness constraint $\epsilon = 0.2$

kl_S	kl_V	kR	kH	$\overline{r_2}$	$\overline{z_2}$	$\frac{\lvert\xi_3\rvert}{A}$
2.35	0.75	0.88	0.15	1.2	-0.65	0.71
3.79	0.65	2.11	0.05	0.3	-0.3	0.26
3.79	0.6	2.12	0.05	0.25	-0.25	0.26

Table 6.20: Dimensions and characteristics of the 'compound-cylinder' shapes on the Pareto Front for the heave-only problem, with motion constraint $\alpha = 1$ and steepness constraint $\epsilon = 0.2$ (shown in figure 6-20)

Trends/ observations

- Generally the optimal shapes are protruding outwards – that is, $\overline{r_2} > 1$ – so that the bottom cylinder is larger than the top one.

- Compared to the optimal cylinders, the surface area and volume of these optimal compound cylinders are significantly smaller. For example, for $\alpha = 3, \epsilon = 0.1$, kl_S is 30 % smaller (meaning surface area is 50 % smaller) and kl_V is 39 % smaller (meaning volume is 77 % smaller). We point this out because compound cylinders are relatively easy to build (being just one cylinder on top of another),

but the fact that surface area and volume can be decreased so much by simply adding another cylinder shows that (1) geometric optimization is important to decrease the amount of material needed to extract the same power, and (2) allowing the shape to protrude outwards greatly improves the performance (that is, allows the body to resonate at smaller volumes/ surface areas).

- Similarly to the flat-bottomed and one-kink groups, decreasing α increases kR and decreases kH. $\overline{z_2}$ decreases, while $\overline{r_2}$ is similar. That is, for a stricter motion constraint shapes are wider, shallower and similarly protruding.

- As ϵ increases, kR and kH increase, and $\overline{r_2}$ decreases. So generally the shapes get larger and less protruding, which is the same as for the one-kink group and the flat-bottomed group.

- We notice that the kl_S and kl_V values are larger for the compound cylinders than they were for the flat-bottomed and one-kink shapes.

6.4.2 Heave-surge-pitch

For the heave-surge-pitch problem, the possible values of kl_V were [0.6,1.4,0.05], the possible values of $\overline{r_2}$ were [0.25,1.4,0.05], and the possible values of $\overline{z_2}$ were [-0.9,-0.25,0.05]. For the $\alpha = 3$ runs, the initial population size was 110, and the number of generations was 400, and for the $\alpha = 1$ runs, the initial population size was 200, and the number of generations was 500.

$\underline{\alpha = 3, \epsilon = 0.1}$

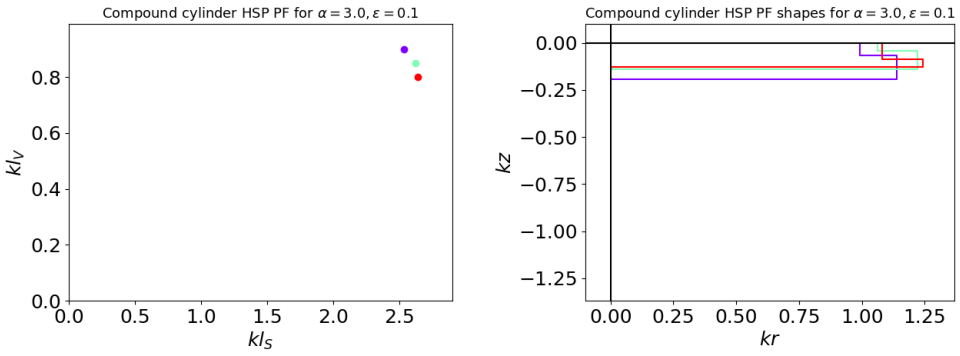

Figure 6-21: Pareto Front (left) and corresponding shapes in the $r-z$ plane (right), resulting from the multi-objective evolutionary algorithm for 'compound-cylinder' shapes for the heave-surge-pitch problem, with motion constraint $\alpha = 3$ and steepness constraint $\epsilon = 0.1$

kl_S	kl_V	kR	kH	$\overline{r_2}$	$\overline{z_2}$	$\frac{\lvert\xi_3\rvert}{A}$	$\frac{\lvert\xi_1\rvert}{A}$	$\frac{\lvert\xi_5\rvert}{A/R}$	$\overline{k_1}$	$\overline{z_G}$	$\overline{r_g}$
2.53	0.9	0.99	0.2	1.15	-0.35	0.67	1.74	1.61	1.31	0.86	0.11
2.62	0.85	1.06	0.14	1.15	-0.3	0.58	2.22	1.27	1.26	1.48	0.37
2.64	0.8	1.08	0.13	1.15	-0.7	0.56	2.48	1.19	1.31	1.89	0.16

Table 6.21: Dimensions and characteristics of the 'compound-cylinder' shapes on the Pareto Front for the heave-surge-pitch problem, with motion constraint $\alpha = 3$ and steepness constraint $\epsilon = 0.1$ (shown in figure 6-21)

$\underline{\alpha = 3, \epsilon = 0.2}$

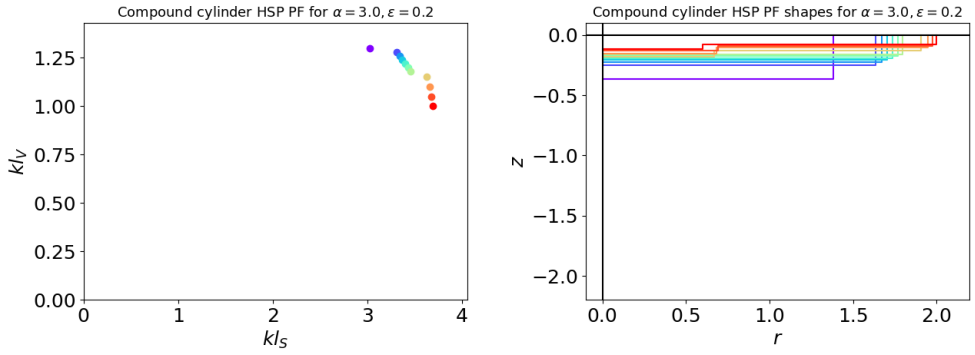

Figure 6-22: Pareto Front (left) and corresponding shapes in the $r-z$ plane (right), resulting from the multi-objective evolutionary algorithm for 'compound-cylinder' shapes for the heave-surge-pitch problem, with motion constraint $\alpha = 3$ and steepness constraint $\epsilon = 0.2$

kl_S	kl_V	kR	kH	$\overline{r_2}$	$\overline{z_2}$	$\frac{\lvert\xi_3\rvert}{A}$	$\frac{\lvert\xi_1\rvert}{A}$	$\frac{\lvert\xi_5\rvert}{A/R}$	$\overline{k_1}$	$\overline{z_G}$	$\overline{r_g}$
3.03	1.3	1.38	0.37	1	-1	0.6	0.67	1.69	1.34	0.22	0.53
3.31	1.28	1.64	0.25	1	-1	0.43	0.82	0.97	1.25	0.62	0.66
3.34	1.26	1.67	0.23	1	-1	0.41	0.86	0.91	1.25	0.72	0.69
3.37	1.24	1.71	0.21	1	-1	0.39	0.91	0.87	1.24	0.82	0.71
3.4	1.22	1.74	0.19	1	-1	0.37	0.94	0.82	1.24	0.93	0.73
3.43	1.2	1.77	0.18	1	-1	0.36	1.01	0.8	1.24	1.02	0.77
3.46	1.18	1.8	0.16	1	-1	0.35	1.05	0.78	1.24	1.13	0.79
3.63	1.15	1.91	0.18	0.35	-0.7	0.32	1.39	0.64	1.18	1.59	0.81
3.66	1.1	1.95	0.15	0.35	-0.7	0.3	1.61	0.62	1.17	1.96	0.88
3.68	1.05	1.97	0.13	0.35	-0.7	0.29	1.78	0.61	1.18	2.41	0.95
3.69	1.0	2.0	0.12	0.3	-0.65	0.29	2.22	0.58	1.16	2.72	1.04

Table 6.22: Dimensions and characteristics of the 'compound-cylinder' shapes on the Pareto Front for the heave-surge-pitch problem, with motion constraint $\alpha = 3$ and steepness constraint $\epsilon = 0.2$ (shown in figure 6-22)

$\underline{\alpha = 1, \epsilon = 0.1}$

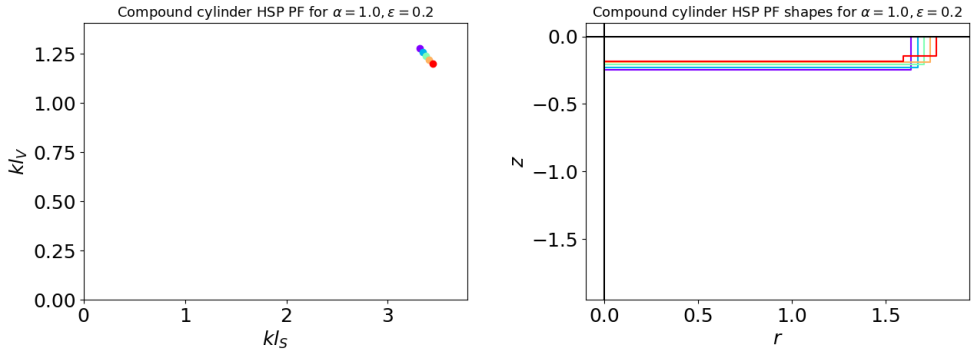

Figure 6-23: Pareto Front (left) and corresponding shapes in the $r - z$ plane (right), resulting from the multi-objective evolutionary algorithm for 'compound-cylinder' shapes for the heave-surge-pitch problem, with motion constraint $\alpha = 1$ and steepness constraint $\epsilon = 0.1$

kl_S	kl_V	kR	kH	$\overline{r_2}$	$\overline{z_2}$	$\frac{\lvert\xi_3\rvert}{A}$	$\frac{\lvert\xi_1\rvert}{A}$	$\frac{\lvert\xi_5\rvert}{A/R}$	$\overline{k_1}$	$\overline{z_G}$	$\overline{r_g}$
3.31	1.28	1.64	0.25	1	-1	0.43	0.82	0.97	1.25	0.62	0.66
3.34	1.26	1.67	0.23	1	-1	0.41	0.86	0.91	1.25	0.72	0.69
3.37	1.24	1.71	0.21	1	-1	0.39	0.91	0.87	1.24	0.82	0.71
3.4	1.22	1.74	0.19	1	-1	0.37	0.94	0.82	1.24	0.93	0.73
3.46	1.2	1.78	0.18	0.85	-0.8	0.35	0.93	0.86	1.26	1.03	0.74

Table 6.23: Dimensions and characteristics of the 'compound-cylinder' shapes on the Pareto Front for the heave-surge-pitch problem, with motion constraint $\alpha = 1$ and steepness constraint $\epsilon = 0.1$ (shown in figure 6-23)

$\underline{\alpha = 1, \epsilon = 0.2}$

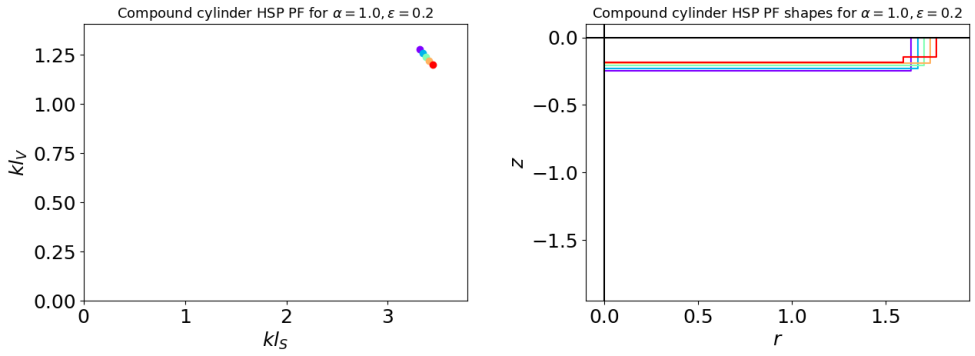

Figure 6-24: Pareto Front (left) and corresponding shapes in the $r - z$ plane (right), resulting from the multi-objective evolutionary algorithm for 'compound-cylinder' shapes for the heave-surge-pitch problem, with motion constraint $\alpha = 1$ and steepness constraint $\epsilon = 0.2$

kl_S	kl_V	kR	kH	$\overline{r_2}$	$\overline{z_2}$	$\frac{\lvert\xi_3\rvert}{A}$	$\frac{\lvert\xi_1\rvert}{A}$	$\frac{\lvert\xi_5\rvert}{A/R}$	$\overline{k_1}$	$\overline{z_G}$	$\overline{r_g}$
3.31	1.28	1.64	0.25	1	-1	0.43	0.82	0.97	1.25	0.62	0.66
3.34	1.26	1.67	0.23	1	-1	0.41	0.86	0.91	1.25	0.72	0.69
3.37	1.24	1.71	0.21	1	-1	0.39	0.91	0.87	1.24	0.82	0.71
3.4	1.22	1.74	0.19	1	-1	0.37	0.94	0.82	1.24	0.93	0.73
3.44	1.2	1.77	0.18	0.9	-0.8	0.35	0.92	0.88	1.26	0.98	0.74

Table 6.24: Dimensions and characteristics of the 'compound-cylinder' shapes on the Pareto Front for the heave-surge-pitch problem, with motion constraint $\alpha = 1$ and steepness constraint $\epsilon = 0.2$ (shown in figure 6-24)

Trends/ observations

- These Pareto Fronts are the first so far in this chapter that are not generally protruding outwards. For $\alpha = 3, \epsilon = 0.1$, the shapes are protruding outwards, but for the other constraint regimes they are not.
- Cylinders are on the Pareto Fronts, for all other constraint regimes besides $\alpha = 3, \epsilon = 0.1$. This suggests that for heave-surge-pitch, as the constraint regimes get stricter, the shape optimization for compound cylinders does not provide a very strong benefit, and that the optimal shapes are similar to cylinders (or *are* cylinders).

6.5 No-kink-2nd-order

6.5.1 Heave-only

For the heave-only problem, the possible values of kl_V were [0.3,1.4,0.05], the possible values of $\overline{a_2}$ were [-0.5,0.1,0.05], and the possible values of $\overline{b_2}$ were [-0.1,0.8,0.05]. The initial population size was 400, and the number of generations was 3500. Once we did this initial optimization and noticed the trend that shapes with $\overline{a_2} < -0.1$ and $\overline{b_2} < 0.1$ were optimal, we evaluated all values of $kl_V = [0.4, 0.75, 0.05], \overline{a_2} = [-0.5, -0.1, 0.05]$ and $\overline{b_2} = [-0.1, 0.1, 0.05]$.

$\alpha = 3, \epsilon = 0.1$

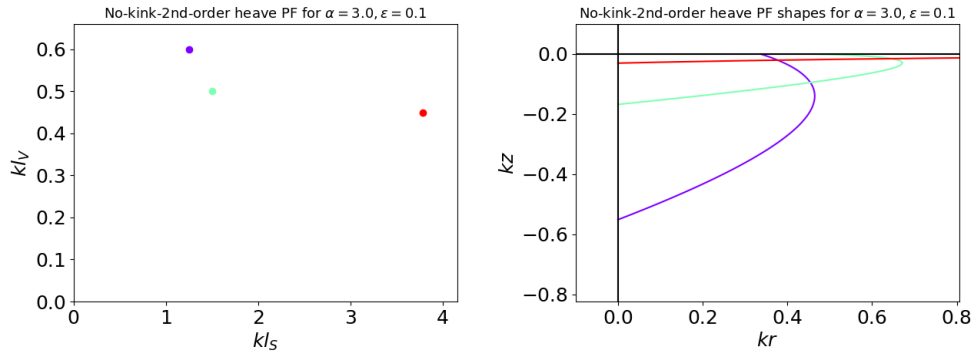

Figure 6-25: Pareto Front (left) and corresponding shapes in the $r-z$ plane (right), resulting from the multi-objective evolutionary algorithm for 'no-kink-2nd-order' shapes for the heave-only problem, with motion constraint $\alpha = 3$ and steepness constraint $\epsilon = 0.1$

kl_S	kl_V	kR	kH	$\overline{a_2}$	$\overline{b_2}$	$\frac{\lvert\xi_3\rvert}{A}$
1.25	0.6	0.34	0.55	-0.4	-0.05	2.7
1.5	0.5	0.46	0.17	-0.45	-0.1	1.33
3.78	0.45	2.13	0.03	0.05	-0.05	0.25

Table 6.25: Dimensions and characteristics of the 'no-kinks-2nd-order' shapes on the Pareto Front for the heave-only problem, with motion constraint $\alpha = 3$ and steepness constraint $\epsilon = 0.1$ (shown in figure 6-25)

$\alpha = 3, \epsilon = 0.2$

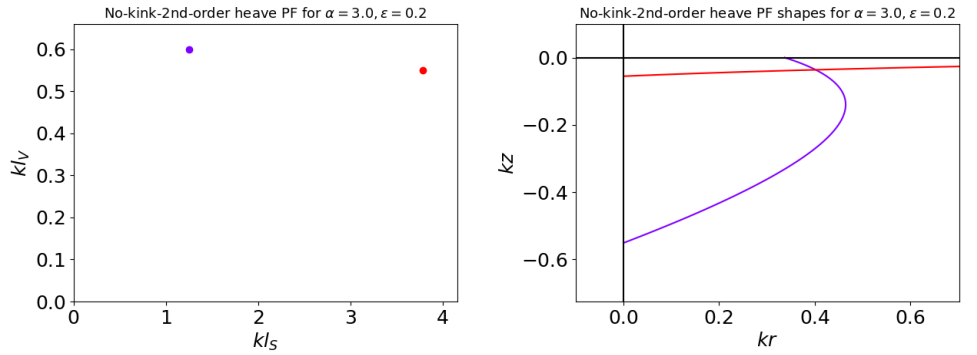

Figure 6-26: Pareto Front (left) and corresponding shapes in the $r-z$ plane (right), resulting from the multi-objective evolutionary algorithm for 'no-kink-2nd-order' shapes for the heave-only problem, with motion constraint $\alpha = 3$ and steepness constraint $\epsilon = 0.2$

kl_S	kl_V	kR	kH	$\overline{a_2}$	$\overline{b_2}$	$\frac{\lvert\xi_3\rvert}{A}$
1.25	0.6	0.34	0.55	-0.4	-0.05	2.7
3.78	0.55	2.13	0.06	0.05	-0.05	0.25

Table 6.26: Dimensions and characteristics of the 'no-kinks-2nd-order' shapes on the Pareto Front for the heave-only problem, with motion constraint $\alpha = 3$ and steepness constraint $\epsilon = 0.2$ (shown in figure 6-26)

$\underline{\alpha = 1, \epsilon = 0.1}$

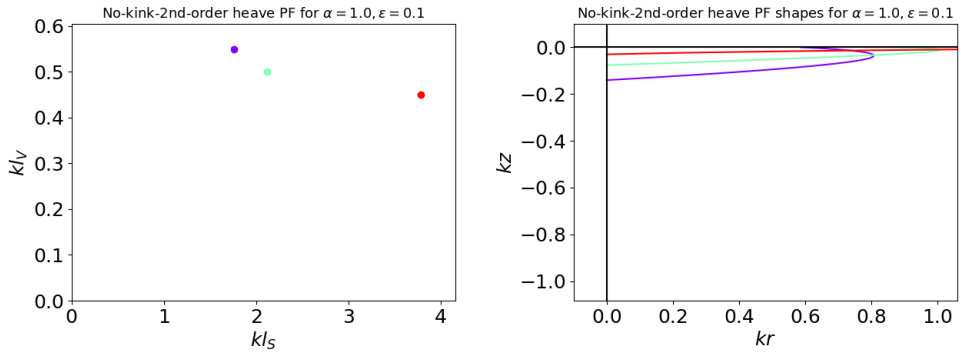

Figure 6-27: Pareto Front (left) and corresponding shapes in the $r-z$ plane (right), resulting from the multi-objective evolutionary algorithm for 'no-kink-2nd-order' shapes for the heave-only problem, with motion constraint $\alpha = 1$ and steepness constraint $\epsilon = 0.1$

kl_S	kl_V	kR	kH	$\overline{a_2}$	$\overline{b_2}$	$\frac{\lvert\xi_3\rvert}{A}$
1.76	0.55	0.59	0.14	-0.4	-0.05	0.99
2.12	0.5	0.78	0.08	-0.35	-0.1	0.7
3.78	0.45	2.13	0.03	0.05	-0.05	0.25

Table 6.27: Dimensions and characteristics of the 'no-kinks-2nd-order' shapes on the Pareto Front for the heave-only problem, with motion constraint $\alpha = 1$ and steepness constraint $\epsilon = 0.1$ (shown in figure 6-27)

$\underline{\alpha = 1, \epsilon = 0.2}$

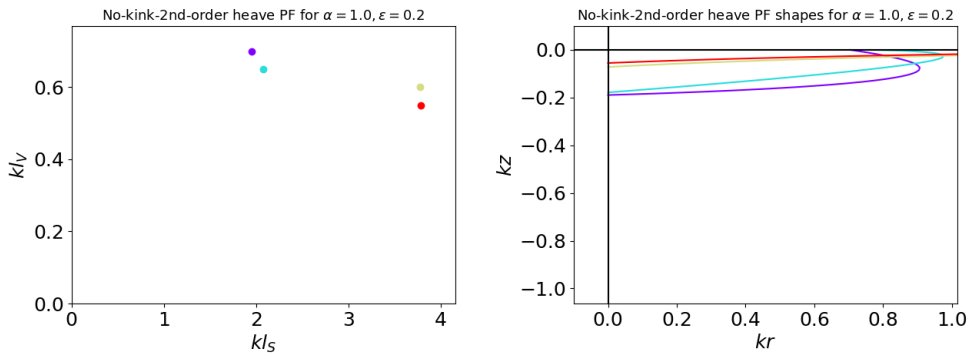

Figure 6-28: Pareto Front (left) and corresponding shapes in the $r-z$ plane (right), resulting from the multi-objective evolutionary algorithm for 'no-kink-2nd-order' shapes for the heave-only problem, with motion constraint $\alpha = 1$ and steepness constraint $\epsilon = 0.2$

kl_S	kl_V	kR	kH	$\overline{a_2}$	$\overline{b_2}$	$\frac{\lvert\xi_3\rvert}{A}$
1.95	0.7	0.7	0.19	-0.35	0.05	0.86
2.07	0.65	0.76	0.18	-0.35	-0.1	0.75
3.78	0.6	2.13	0.07	0.05	-0.05	0.25
3.78	0.55	2.13	0.06	0.05	-0.05	0.25

Table 6.28: Dimensions and characteristics of the 'no-kinks-2nd-order' shapes on the Pareto Front for the heave-only problem, with motion constraint $\alpha = 1$ and steepness constraint $\epsilon = 0.2$ (shown in figure 6-28)

Trends/ observations

- We notice that generally the optimal shapes are protruding outwards. For the 'no-kink-2nd-order' shapes, that corresponds to $\overline{a_2} < -0.1$.

- Similar to the one-kink group, we also notice here that generally the protrusion is close to the waterline (that is, $\overline{b_2} < 0$). And again, we notice that the shapes for which the protrusion is closer to the waterline have smaller kl_V values and slightly larger kl_S values.

- In fact, the shapes on each of these Pareto Fronts look very similar to the ones on the corresponding Pareto Fronts for the one-kink group. This shows that the observed trends are not specific to groups but are generally true.

- As α decreases, as was the case for all previous groups, shapes get wider and shallower.
- The kl_S and kl_V values are generally smaller than for the compound cylinder group and the flat-bottomed group, but slightly larger than for the 'one-kink' group.

6.5.2 Heave-surge-pitch

For the heave-only problem, the possible values of kl_V were [0.6,1.4,0.05], the possible values of $\overline{a_2}$ were [-0.5,0.1,0.05], and the possible values of $\overline{b_2}$ were [-0.1,0.8,0.05]. The initial population size was 100, and the number of generations was 1000. Once we did this initial optimization and noticed the trend that shapes with $\overline{a_2} < -0.1$ and $\overline{b_2} < 0.1$ were optimal, we evaluated all values of $kl_V = [0.8, 1.3, 0.05], \overline{a_2} = [-0.5, -0.1, 0.05]$ and $\overline{b_2} = [-0.1, 0.1, 0.05]$.

$\alpha = 3, \epsilon = 0.1$

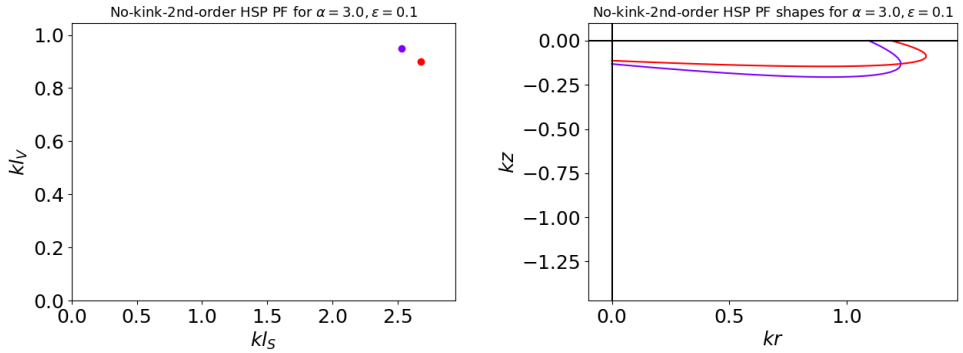

Figure 6-29: Pareto Front (left) and corresponding shapes in the $r-z$ plane (right), resulting from the multi-objective evolutionary algorithm for 'no-kink-2nd-order' shapes for the heave-surge-pitch problem, with motion constraint $\alpha = 3$ and steepness constraint $\epsilon = 0.1$

kl_S	kl_V	kR	kH	$\overline{a_2}$	$\overline{b_2}$	$\frac{\lvert\xi_3\rvert}{A}$	$\frac{\lvert\xi_1\rvert}{A}$	$\frac{\lvert\xi_5\rvert}{A/R}$	$\overline{k_1}$	$\overline{z_G}$	$\overline{r_g}$
2.53	0.95	1.15	0.14	-0.25	0.5	0.59	1.49	1.3	1.31	1.5	0.45
2.68	0.9	1.32	0.13	-0.25	0.35	0.5	1.97	1.05	1.25	2.23	0.52

Table 6.29: Dimensions and characteristics of the 'no-kinks-2nd-order' shapes on the Pareto Front for the heave-surge-pitch problem, with motion constraint $\alpha = 3$ and steepness constraint $\epsilon = 0.1$ (shown in figure 6-29)

$\alpha = 3, \epsilon = 0.2$

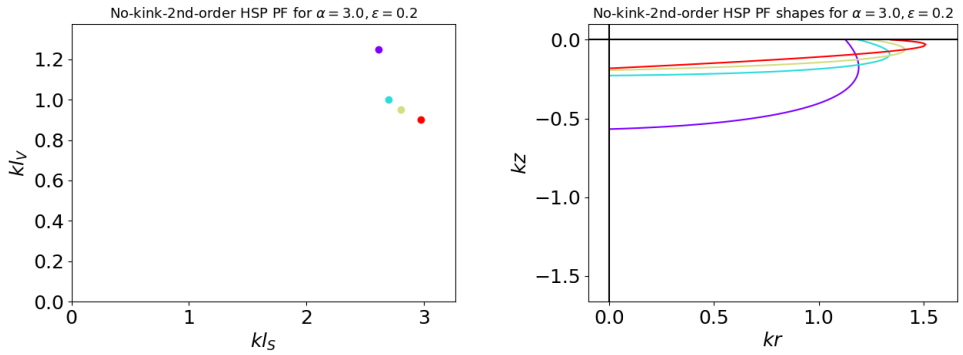

Figure 6-30: Pareto Front (left) and corresponding shapes in the $r-z$ plane (right), resulting from the multi-objective evolutionary algorithm for 'no-kink-2nd-order' shapes for the heave-surge-pitch problem, with motion constraint $\alpha = 3$ and steepness constraint $\epsilon = 0.2$

kl_S	kl_V	kR	kH	$\overline{a_2}$	$\overline{b_2}$	$\frac{\lvert\xi_3\rvert}{A}$	$\frac{\lvert\xi_1\rvert}{A}$	$\frac{\lvert\xi_5\rvert}{A/R}$	$\overline{k_1}$	$\overline{z_G}$	$\overline{r_g}$
2.62	1.25	0.9	0.45	-0.2	0.1	0.69	0.72	1.99	1.38	0.28	0.28
2.7	1.0	1.19	0.23	-0.25	0.1	0.5	1.67	1.03	1.2	1.39	0.21
2.81	0.95	1.32	0.2	-0.25	0.05	0.46	2.12	0.92	1.16	1.85	0.32

Table 6.30: Dimensions and characteristics of the 'no-kinks-2nd-order' shapes on the Pareto Front for the heave-surge-pitch problem, with motion constraint $\alpha = 3$ and steepness constraint $\epsilon = 0.2$ (shown in figure 6-30)

$\alpha = 1, \epsilon = 0.1$

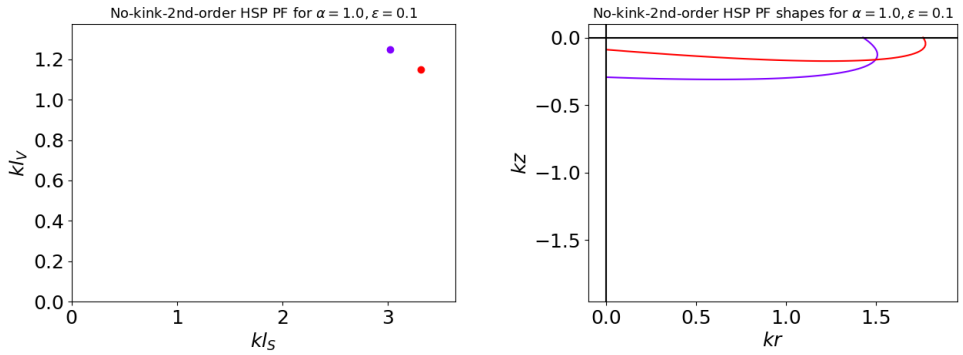

Figure 6-31: Pareto Front (left) and corresponding shapes in the $r-z$ plane (right), resulting from the multi-objective evolutionary algorithm for 'no-kink-2nd-order' shapes for the heave-surge-pitch problem, with motion constraint $\alpha = 1$ and steepness constraint $\epsilon = 0.1$

kl_S	kl_V	kR	kH	$\overline{a_2}$	$\overline{b_2}$	$\frac{\lvert\xi_3\rvert}{A}$	$\frac{\lvert\xi_1\rvert}{A}$	$\frac{\lvert\xi_5\rvert}{A/R}$	$\overline{k_1}$	$\overline{z_G}$	$\overline{r_g}$
3.02	1.25	1.14	0.24	-0.2	0.2	0.46	0.94	0.98	1.22	0.88	0.48
3.31	1.15	1.53	0.08	-0.15	0.7	0.34	0.98	0.9	1.27	2.16	0.82

Table 6.31: Dimensions and characteristics of the 'no-kinks-2nd-order' shapes on the Pareto Front for the heave-surge-pitch problem, with motion constraint $\alpha = 1$ and steepness constraint $\epsilon = 0.1$ (shown in figure 6-31)

$\underline{\alpha = 1, \epsilon = 0.2}$

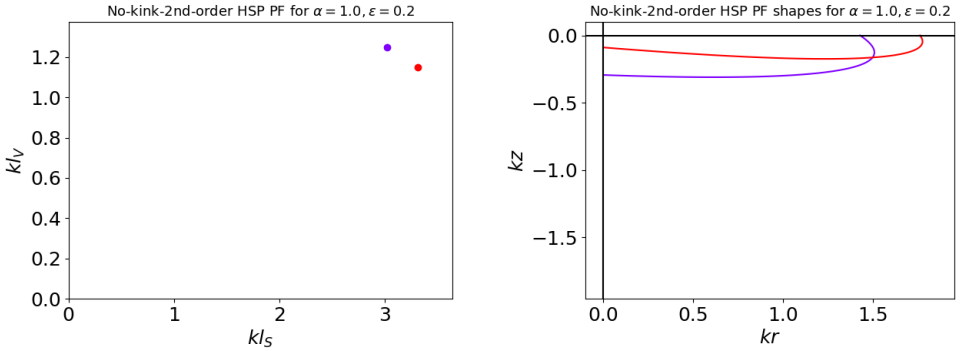

Figure 6-32: Pareto Front (left) and corresponding shapes in the $r-z$ plane (right), resulting from the multi-objective evolutionary algorithm for 'no-kink-2nd-order' shapes for the heave-surge-pitch problem, with motion constraint $\alpha = 1$ and steepness constraint $\epsilon = 0.2$

kl_S	kl_V	kR	kH	$\overline{a_2}$	$\overline{b_2}$	$\frac{\lvert\xi_3\rvert}{A}$	$\frac{\lvert\xi_1\rvert}{A}$	$\frac{\lvert\xi_5\rvert}{A/R}$	$\overline{k_1}$	$\overline{z_G}$	$\overline{r_g}$
3.02	1.25	1.14	0.24	-0.2	0.2	0.46	0.94	0.98	1.22	0.88	0.48
3.31	1.15	1.53	0.08	-0.15	0.7	0.34	0.98	0.9	1.27	2.16	0.82

Table 6.32: Dimensions and characteristics of the 'no-kinks-2nd-order' shapes on the Pareto Front for the heave-surge-pitch problem, with motion constraint $\alpha = 1$ and steepness constraint $\epsilon = 0.2$ (shown in figure 6-32)

Trends/ observations

- These shapes are all protruding outwards, similar to the other groups presented in this chapter.
- However, unlike the other groups, for some of the Pareto Fronts in this group, the shapes are protruding downwards. That is, $\overline{b_2} > 0.1$. The only time this is not true is in $\mathbb{PF}_{135,3,0.2}$.

- Compared to the heave-only problem, the shapes on these Pareto Fronts are wider and less protruding outwards.
- For all of the shapes on these Pareto Fronts, $\overline{a_2} = -0.2$ or -0.25.
- As α decreases, shapes get wider.
- The Pareto Fronts for $\alpha = 1, \epsilon = 0.1$ and for $\alpha = 1, \epsilon = 0.2$ are identical.

6.6 Overall

In this section, we combine all Pareto Fronts, in the corresponding constraint regimes, from all of the groups of shapes shown above (flat-bottomed, one-kink, compound cylinders, no-kink-2nd-order, and flat-sided). For each constraint regime, we present the overall Pareto Front from all shapes considered. Since the only groups represented in these overall Pareto Fronts are one-kink shapes and no-kink-2nd-order, the only geometric parameters in the tables after the plots are $\overline{r_1}, \overline{z_1}, \overline{a_2}$ and $\overline{b_2}$.

6.6.1 Heave

$\alpha = 3, \epsilon = 0.1$

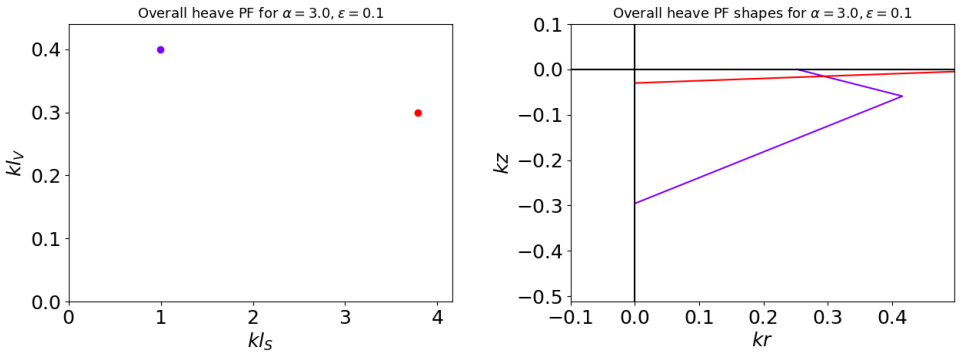

Figure 6-33: The overall Pareto Front (left) and corresponding shapes in the $r - z$ plane (right), after combining the Pareto Fronts from all 6 groups in this chapter, for the heave-only problem with motion constraint $\alpha = 3$ and steepness constraint $\epsilon = 0.1$

kl_S	kl_V	kR	kH	$\overline{r_1}$	$\overline{z_1}$	$\overline{a_2}$	$\overline{b_2}$	$\frac{\lvert\xi_3\rvert}{A}$
1.0	0.4	0.25	0.3	1.65	-0.2	0	0	2.87
3.79	0.3	2.14	0.03	0.25	-0.1	0	0	0.25

Table 6.33: Dimensions and characteristics of the shapes on the *overall* Pareto Front for the heave-only problem, with motion constraint $\alpha = 3$ and steepness constraint $\epsilon = 0.1$ (shown in figure 6-33)

$\underline{\alpha = 3, \epsilon = 0.2}$

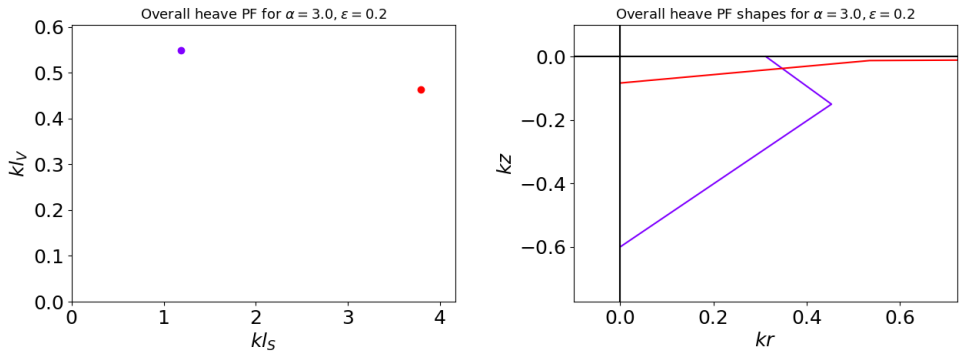

Figure 6-34: The overall Pareto Front (left) and corresponding shapes in the $r - z$ plane (right), after combining the Pareto Fronts from all 6 groups in this chapter, for the heave-only problem with motion constraint $\alpha = 3$ and steepness constraint $\epsilon = 0.2$

kl_S	kl_V	kR	kH	$\overline{r_1}$	$\overline{z_1}$	$\overline{a_2}$	$\overline{b_2}$	$\frac{\lvert\xi_3\rvert}{A}$
1.18	0.55	0.31	0.6	1.45	-0.25	0	0	2.71
3.79	0.46	2.14	0.08	0.25	-0.15	0	0	0.25

Table 6.34: Dimensions and characteristics of the shapes on the *overall* Pareto Front for the heave-only problem, with motion constraint $\alpha = 3$ and steepness constraint $\epsilon = 0.2$ (shown in figure 6-34)

$\underline{\alpha = 1, \epsilon = 0.1}$

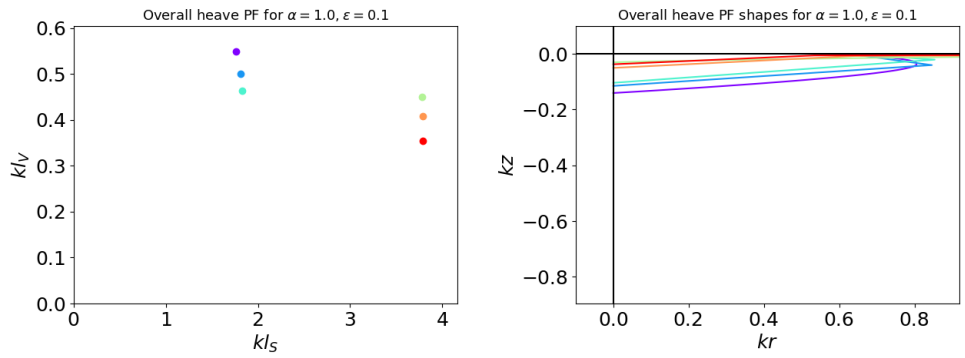

Figure 6-35: The overall Pareto Front (left) and corresponding shapes in the $r - z$ plane (right), after combining the Pareto Fronts from all 6 groups in this chapter, for the heave-only problem with motion constraint $\alpha = 1$ and steepness constraint $\epsilon = 0.1$

kl_S	kl_V	kR	kH	$\overline{r_1}$	$\overline{z_1}$	$\overline{a_2}$	$\overline{b_2}$	$\frac{\lvert\xi_3\rvert}{A}$
1.76	0.55	0.59	0.14	0	0	-0.4	-0.05	0.99
1.81	0.5	0.63	0.11	1.35	-0.35	0	0	0.92
1.83	0.46	0.63	0.1	1.35	-0.2	0	0	0.89
3.78	0.45	2.13	0.03	0	0	0.05	-0.05	0.25
3.78	0.41	2.14	0.05	0.3	-0.15	0	0	0.25
3.79	0.35	2.14	0.04	0.25	-0.15	0	0	0.25

Table 6.35: Dimensions and characteristics of the shapes on the *overall* Pareto Front for the heave-only problem, with motion constraint $\alpha = 1$ and steepness constraint $\epsilon = 0.1$ (shown in figure 6-35)

$\underline{\alpha = 1, \epsilon = 0.2}$

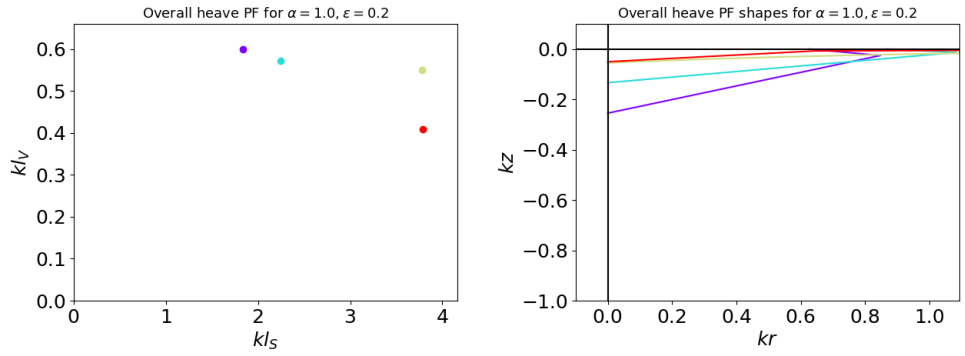

Figure 6-36: The overall Pareto Front (left) and corresponding shapes in the $r-z$ plane (right), after combining the Pareto Fronts from all 6 groups in this chapter, for the heave-only problem with motion constraint $\alpha = 1$ and steepness constraint $\epsilon = 0.2$

kl_S	kl_V	kR	kH	$\overline{r_1}$	$\overline{z_1}$	$\overline{a_2}$	$\overline{b_2}$	$\frac{\lvert\xi_3\rvert}{A}$
1.83	0.6	0.63	0.25	1.35	-0.1	0	0	0.92
2.24	0.57	0.87	0.13	1.25	-0.1	0	0	0.26
3.78	0.55	2.13	0.06	0	0	0.05	-0.05	0.25
3.78	0.41	2.14	0.05	0.3	-0.15	0	0	0.26

Table 6.36: Dimensions and characteristics of the shapes on the *overall* Pareto Front for the heave-only problem, with motion constraint $\alpha = 1$ and steepness constraint $\epsilon = 0.1$ (shown in figure 6-35)

Trends/ observations

- Generally, the optimal shapes are protruding outwards. That is $\overline{r_1} > 1$ or $\overline{a_2} < -0.1$.
- All of the shapes are either 'one-kink' or 'no-kink-2nd-order' shapes.
- As the motion constraint becomes stricter (as α decreases), the optimal shapes are generally wider and shallower.
- As the steepness constraint becomes stricter (as ϵ increases), the optimal shapes are generally deeper. This is more pronounced for $\alpha = 3$.
- None of the shapes are protruding downwards. That is, $-1 < \overline{z_1} < 0$ or $\overline{b_2} < 0.1$. For most of the shapes, the protrusion is closer to the waterline than the maximum draft ($-0.5 < \overline{z_1} < 0$ or $\overline{b_2} < 0$).

6.6.2 Heave-surge-pitch

$\underline{\alpha = 3, \epsilon = 0.1}$

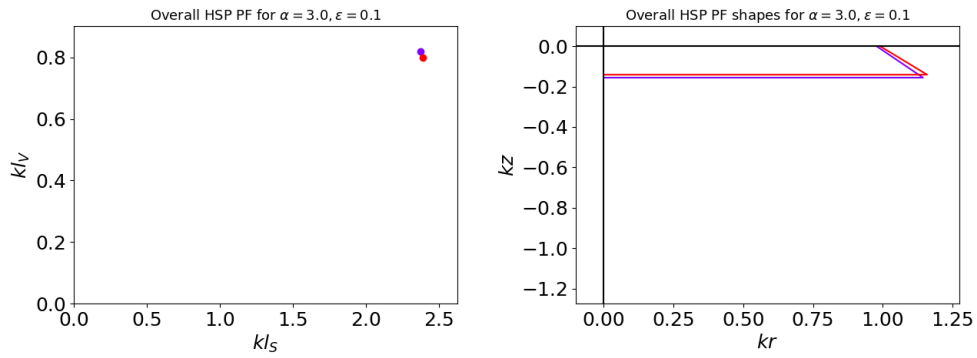

Figure 6-37: The overall Pareto Front (left) and corresponding shapes in the $r - z$ plane (right), after combining the Pareto Fronts from all 6 groups in this chapter, for the heave-surge-pitch problem with motion constraint $\alpha = 3$ and steepness constraint $\epsilon = 0.1$

kl_S	kl_V	kR	kH	$\overline{r_1}$	$\overline{z_1}$	$\overline{a_2}$	$\overline{b_2}$	$\frac{\lvert\xi_3\rvert}{A}$	$\frac{\lvert\xi_1\rvert}{A}$	$\frac{\lvert\xi_5\rvert}{A/R}$	$\overline{k_1}$	$\overline{z_G}$	$\overline{r_g}$
2.37	0.82	0.98	0.16	1.17	-1.0	0	0	0.64	2.3	1.47	1.31	1.28	0.24
2.39	0.8	0.99	0.14	1.17	-1.0	0	0	0.62	2.44	1.37	1.31	1.53	0.19

Table 6.37: Dimensions and characteristics of the shapes on the *overall* Pareto Front for the heave-surge-pitch problem, with motion constraint $\alpha = 3$ and steepness constraint $\epsilon = 0.1$ (shown in figure 6-37)

$\underline{\alpha = 3, \epsilon = 0.2}$

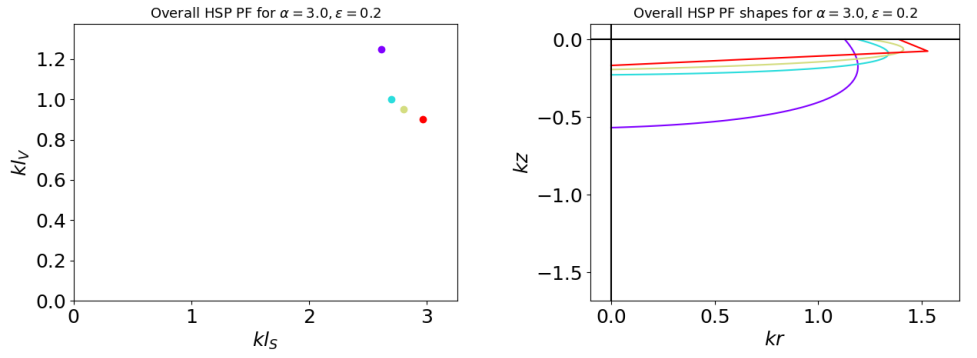

Figure 6-38: The overall Pareto Front (left) and corresponding shapes in the $r - z$ plane (right), after combining the Pareto Fronts from all 6 groups in this chapter, for the heave-surge-pitch problem with motion constraint $\alpha = 3$ and steepness constraint $\epsilon = 0.2$

kl_S	kl_V	kR	kH	$\overline{r_1}$	$\overline{z_1}$	$\overline{a_2}$	$\overline{b_2}$	$\frac{\lvert\xi_3\rvert}{A}$	$\frac{\lvert\xi_1\rvert}{A}$	$\frac{\lvert\xi_5\rvert}{A/R}$	$\overline{k_1}$	$\overline{z_G}$	$\overline{r_g}$
2.62	1.25	1.13	0.57	0	0	-0.2	0.1	0.69	0.72	1.99	1.38	0.28	0.28
2.7	1.0	1.19	0.23	0	0	-0.25	0.1	0.5	1.67	1.03	1.2	1.39	0.21
2.75	0.95	1.23	0.18	0	0	-0.25	0.1	0.48	2.05	0.95	1.17	1.83	0.33
2.8	0.9	1.26	0.15	0	0	-0.25	0.1	0.46	2.61	0.87	1.15	2.36	0.43

Table 6.38: Dimensions and characteristics of the shapes on the *overall* Pareto Front for the heave-surge-pitch problem, with motion constraint $\alpha = 3$ and steepness constraint $\epsilon = 0.2$ (shown in figure 6-38)

$\underline{\alpha = 1, \epsilon = 0.1}$

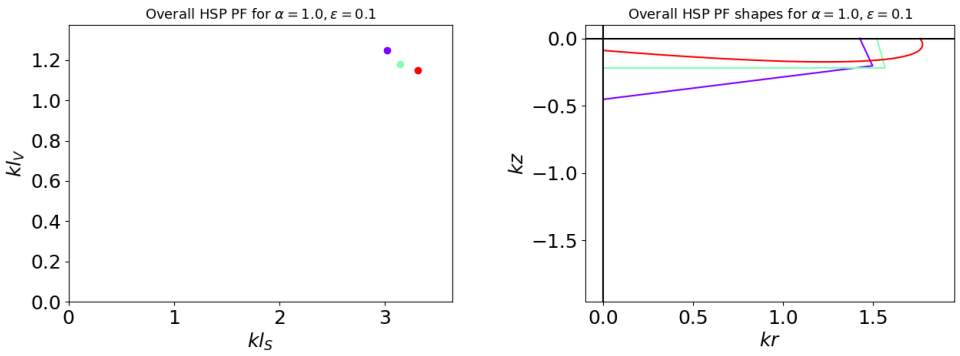

Figure 6-39: The overall Pareto Front (left) and corresponding shapes in the $r - z$ plane (right), after combining the Pareto Fronts from all 6 groups in this chapter, for the heave-surge-pitch problem with motion constraint $\alpha = 1$ and steepness constraint $\epsilon = 0.1$

kl_S	kl_V	kR	kH	$\overline{r_1}$	$\overline{z_1}$	$\overline{a_2}$	$\overline{b_2}$	$\frac{\lvert\xi_3\rvert}{A}$	$\frac{\lvert\xi_1\rvert}{A}$	$\frac{\lvert\xi_5\rvert}{A/R}$	$\overline{k_1}$	$\overline{z_G}$	$\overline{r_g}$
3.02	1.25	1.43	0.45	1.05	-0.45	0	0	0.46	0.94	0.97	1.24	0.63	0.28
3.15	1.18	1.52	0.22	1.03	-1.0	0	0	0.43	0.98	0.94	1.27	0.86	0.62
3.31	1.15	1.76	0.09	0	0	-0.15	0.7	0.34	0.98	0.9	1.27	2.16	0.82

Table 6.39: Dimensions and characteristics of the shapes on the *overall* Pareto Front for the heave-surge-pitch problem, with motion constraint $\alpha = 1$ and steepness constraint $\epsilon = 0.1$ (shown in figure 6-39)

$\underline{\alpha = 1, \epsilon = 0.2}$

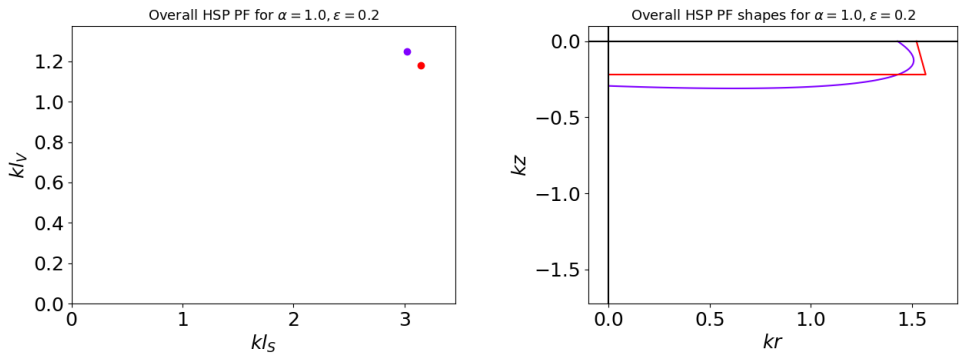

Figure 6-40: The overall Pareto Front (left) and corresponding shapes in the $r - z$ plane (right), after combining the Pareto Fronts from all 6 groups in this chapter, for the heave-surge-pitch problem with motion constraint $\alpha = 1$ and steepness constraint $\epsilon = 0.2$

kl_S	kl_V	kR	kH	$\overline{r_1}$	$\overline{z_1}$	$\overline{a_2}$	$\overline{b_2}$	$\frac{\lvert\xi_3\rvert}{A}$	$\frac{\lvert\xi_1\rvert}{A}$	$\frac{\lvert\xi_5\rvert}{A/R}$	$\overline{k_1}$	$\overline{z_G}$	$\overline{r_g}$
3.02	1.25	1.43	0.29	0	0	-0.2	0.2	0.46	0.94	0.98	1.22	0.88	0.48
3.15	1.18	1.52	0.22	1.03	-1.0	0	0	0.43	0.98	0.94	1.27	0.86	0.62

Table 6.40: Dimensions and characteristics of the shapes on the *overall* Pareto Front for the heave-surge-pitch problem, with motion constraint $\alpha = 1$ and steepness constraint $\epsilon = 0.2$ (shown in figure 6-39)

Trends/ observations

- Generally, the optimal shapes are protruding outward ($\overline{r_1} > 1$ or $\overline{a_2} < -0.1$).
- The shapes are either 'one-kink' shapes or 'no-kink-2nd-order' shapes
- Compared to the heave-only problem optimal shapes, the optimal shapes for the heave-surge-pitch problem are wider, generally shallower, and less protruding (that is, smaller $\overline{r_1}$ values, but still greater than 1 generally).
- As the motion constraint gets stricter (as α decreases), shapes generally get wider.

6.7 Discussion of general trends and physical insights

In this section, we will discuss some of the general trends we noticed from the optimization results. We will make hypotheses of why these trends are true, using hydrodynamics to develop physical insights.

The main insights/ conclusions from the overall results are:

1. The optimal shapes generally protrude outwards.
2. In general, the maximum radius occurs closer to the waterline than the maximum draft (when allowed by the shape definition).
3. The trends that we observe in the optimal shapes are consistent across all the groups of shapes, implying these may be features of a general optimum.
4. As the motion constraint becomes stricter (i.e. α decreases), the optimal shapes for the heave-only problem typically become wider and shallower, and the optimal shapes for the heave-surge-pitch problem typically become wider.
5. Compared to the heave-only problem, the optimal shapes from the heave-surge-pitch problem are generally wider and less protruding outwards, resulting in a larger volume and surface area.
6. Shapes that protrude downwards are generally not optimal

We will now discuss each of these trends separately.

The optimal shapes generally protrude outwards

To determine why shapes that protrude outwards are better, consider figure 6-41. In this figure, we show the heave populations for four flat-bottomed shape classes, for $\alpha = 3, \epsilon = 0.1$. The purple dots show the population for $\overline{r_1} = 1$, the blue for $\overline{r_1} = 1.1$, the green for $\overline{r_1} = 1.2$, and the orange for $\overline{r_1} = 1.25$. In this figure, we see that for a

given kl_V, the class with the smaller $\overline{r_1}$ (i.e. shapes that are less protruding), have a larger kl_S on their right branch but a smaller kl_S on their left branch, compared to a class with larger $\overline{r_1}$ (i.e. shapes that are more protruding).

We know that both the heave motion constraint and the heave steepness constraint eliminate shapes on the lower left branch. We cannot say here which constraint will eliminate more of the lower left branch, but if we call the point on the left branch with minimum kl_V and minimum kl_S point L, we know that L is either where $\frac{|\xi_3|}{A} = \alpha$ or $kH = \epsilon\frac{|\xi_3|}{A}$. We see in figure 6-41 that $(kl_V)_L$ and $(kl_S)_L$ are smaller for larger $\overline{r_1}$ (i.e. shapes that protrude outwards more). That is, less of the left branch is eliminated for the shapes that protrude outwards more.

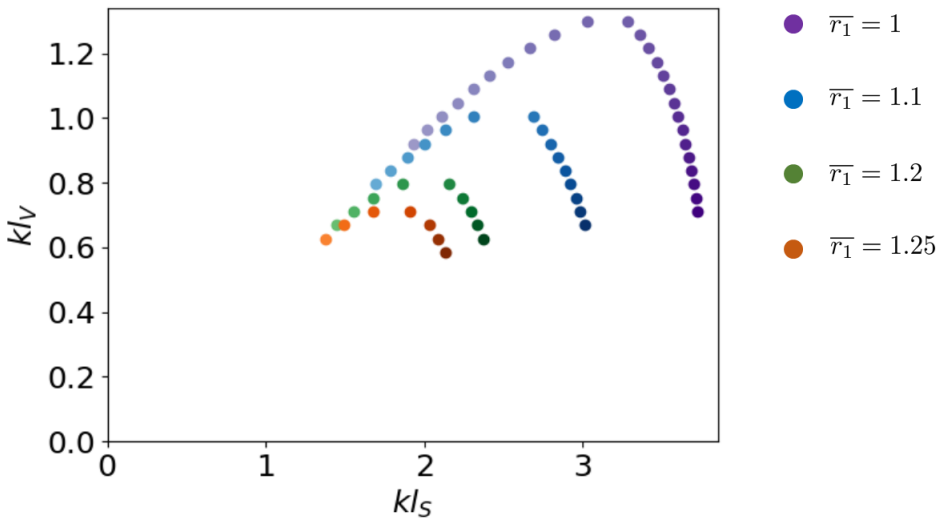

Figure 6-41: Demonstrating populations for 'flat-bottomed' shapes with different $\overline{r_1} = \frac{r_1}{R}$ values, which shows that the shapes that protrude outward more are better since they have smaller minimum kl_V and kl_S values

To see why more of the left branch is eliminated for shapes that protrude outwards more, consider figure 6-42. In this figure, we consider the heave added mass and damping coefficients for six flat-bottomed shapes with constant kH and r_{max}, but varying $\overline{r_1}$ (and thus varying kR). We plot heave added mass and damping as functions of $\overline{r_1}$, and we see that both A_{33} and B_{33} increase with increasing $\overline{r_1}$. But while A_{33} seems to increase linearly, B_{33} seems to be logarithmic or similar (i.e. the rate

of increase is decreasing). We recall that when the body is in resonance the heave motion is

$$\frac{|\xi_3|}{A}^{res} = \sqrt{\frac{\rho g V_g}{k\omega^2 B_{33}}} \tag{6.7.1}$$

Therefore, we can see that a shape with larger B_{33} will have smaller heave body motion at resonance, meaning that it is less likely to be eliminated due to the heave motion constraint or heave steepness constraint. We know that all shapes *can* resonate at smaller kl_V, but they are eliminated due to the motion constraint and/or the steepness constraint. From figure 6-42, and equation 6.7.1, we can hypothesize that shapes that protrude outwards are optimal because they have higher heave damping, but that at a certain $\overline{r_1}$ the benefit of the damping diminishes.

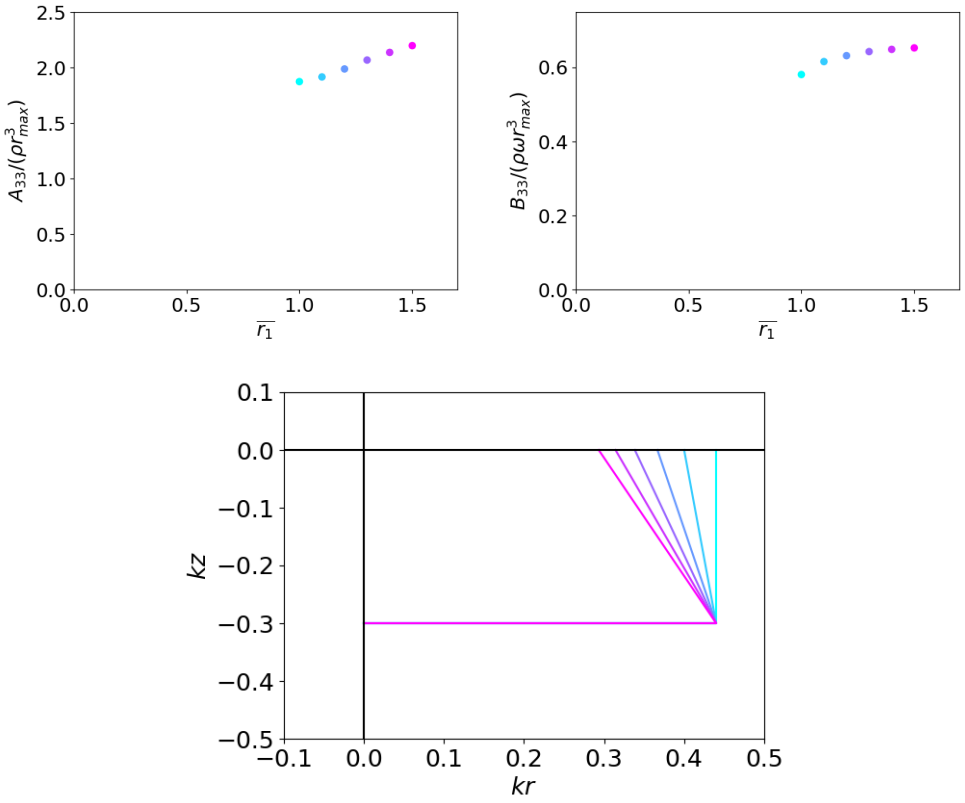

Figure 6-42: Showing how heave added mass (A_{33}) and heave damping (B_{33}) increase with increasing $\overline{r_1}$, keeping r_{max}, $\overline{z_1}$ and kH constant

In general, the maximum radius occurs closer to the waterline than the

maximum draft (when allowed by the shape definition)

Flat-bottomed shapes and compound cylinders by definition must have horizontal segments from the centerline at the body's maximum draft. So for a flat-bottomed shape protruding outwards, the maximum radius would occur at $z = -H$. For a compound cylinder protruding outwards, the maximum radius would be when $-H \leq z \leq z_2$ (since it is a vertical segment). However, for 'one-kink' and 'no-kink-2nd-order' shapes that protrude outwards, the maximum radius could occur for any $z < 0$. We found that, generally, the maximum radius occurs between $z = -H$ and $z = 0$. For the heave-only problem, we saw it generally occurred between $z = -H/2$ and $z = 0$, and for the heave-surge-pitch problem, we saw it generally occurred between $z = -H$ and $z = -H/2$.

To discuss why this trend is true, consider figure 6-43. In this figure, we consider the heave added mass and damping coefficients for five one-kink shapes with constant kH, kR and $\overline{r_1}$, but varying $\overline{z_1}$ from -1 to 0. We plot the heave added mass and damping coefficients as a function of $\overline{z_1}$, and we see that as $\overline{z_1}$ increases (i.e. the protrusion moves closer to the waterline), added mass decreases and damping increases.

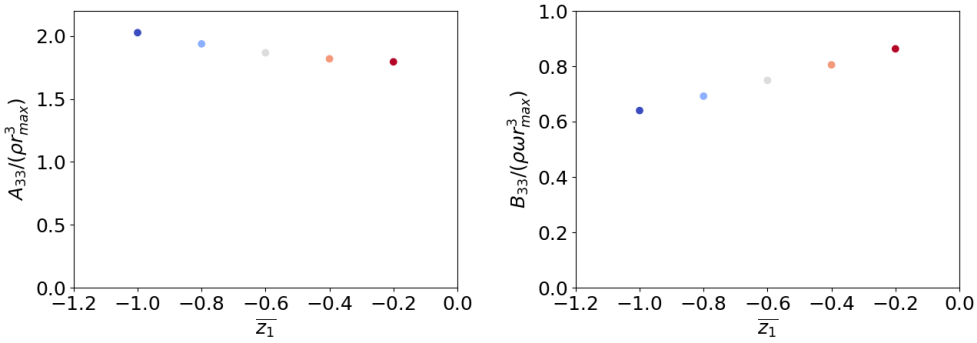

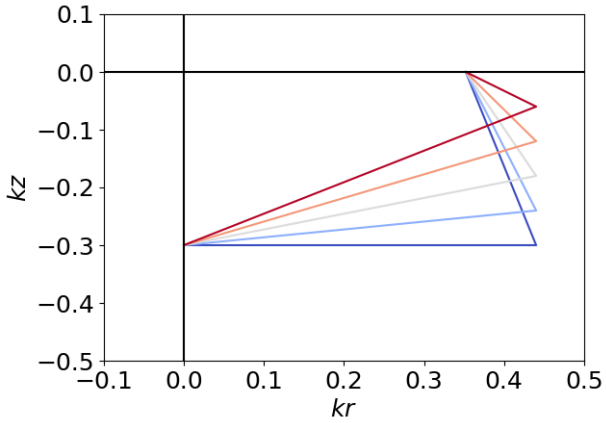

Figure 6-43: Showing how heave added mass (A_{33}) decreases and damping (B_{33}) increases with increasing $\overline{z_1}$, keeping R, $\overline{r_1}$ and kH constant

Therefore, added mass increases as shapes are more protruding but decreases as the protrusion is closer to the waterline, and damping increases in both cases. Since both of these trends are generally optimal, we can conjecture that *increased heave damping generally leads to optimal shapes.*

We must discuss the limitations of this trend and resulting conclusions. Our steepness constraint ensures that $H > |\xi_3|$, but perhaps we should ensure that $|\xi_3|$ is less than the z_1, the z coordinate of the slope discontinuity, to ensure that the protrusion does not leave the ocean surface (with a small but finite steepness).

We are also aware that the uniqueness of the boundary-value problem for shapes that protrude outwards has not been proven. As mentioned in chapter 4, we ensure that the solution is not sensitive to discretization by running a wrapper around it, making sure that the hydrodynamic parameters do not change by more than 3 % when increasing the number of panels. We also ensure that the panels close to the surface are small and close to squares.

In this thesis, we assume potential flow. To show the relative importance of drag forces to inertia forces, the Keulegan–Carpenter number is used:

$$K_c = \frac{\omega \frac{|\xi_3|}{A} AT}{l} \tag{6.7.2}$$

where l is a characteristic length scale. Consider the purple shape in figure 6-33. We use the diameter at the widest part of the shape as the characteristic length scale, so $l = kr/k$, where $kr = 0.41$. For a 10 second wave with amplitude $A = 0.5m$, the K-C number is 0.44. Since $K_c < 1$, this shows that there is no appreciable flow separation, and therefore vortex shedding should not occur. Also, although the corners in these shapes are sharp, in reality they would be rounded to avoid vortex shedding. This shape has the smallest maximum diameter out of all of the shapes on the overall Pareto Fronts, so any other shape would have a smaller K_c number, implying that drag forces are even less important relative to the inertia forces.

The trends that we observe in the optimal shapes are consistent across all the groups of shapes, implying these may be features of a general optimum

When we compare the shapes on Pareto Fronts across different groups, the shapes look very similar, and follow similar patterns of how they change with different constraint values. As we will discuss next, one of these general trends is that as the motion constraint becomes stricter (i.e. α decreases), for the heave-only problem the optimal shapes get wider and shallower and for the heave-surge-pitch problem the optimal shapes get wider. Also, compared to the optimal shapes for the heave-only problem, the optimal shapes for the heave-surge-pitch problem are wider and less protruding. These trends are true for the *overall* Pareto Fronts, but they are also true within *each* group.

But moreover, the actual dimensions of shapes are similar between different groups. For example, consider the heave-only problem for $\alpha = 3, \epsilon = 0.1$. Comparing the shapes with minimum kl_S in all of the four groups presented in this chapter, we see that all kR values are between 0.31 and 0.35, and all r_{max} values are between 0.44 and 0.5. kH values range a bit more: 0.21 to 0.55. The other constraint regimes also have similar dimensions across all of the groups of shapes.

We also see a general trend that for the heave-surge-pitch problem, the shapes on the

Pareto Front for $\alpha = 1, \epsilon = 0.1$ are the same as the shapes on the Pareto Front for $\alpha = 1, \epsilon = 0.2$. This is true for flat-bottomed, one-kink, and for no-kink-2nd-order.

These similarities are evident when just glancing through the different groups. This suggests that these trends are *general*. This suggests that these are features of a general optimum.

As the motion constraint becomes stricter (i.e. α decreases), the optimal shapes for the heave-only problem typically become wider and shallower, and the optimal shapes for the heave-surge-pitch problem typically become wider

We know that as α decreases, for a given class, more of the left branch of $\mathbb{R}_3$ is eliminated, and we know that going along the curve of $\mathcal{S}(\mathbb{R}_3)$, the shapes get shallower and wider. Therefore, we can see why as α decreases, the optimal shapes are shallower and wider, but have similar $\frac{r_{max}}{R}$ values (i.e. are similarly protruding).

We saw in the previous chapter for the cylinder that the surge motion constraint affected the right branch, so that as α decreased more of the right branch was eliminated. And we saw that the pitch motion constraint affected the 'middle' of the $\mathcal{S}(\mathbb{R}_3)$ curve and that as α decreased more from the middle of the left branch was eliminated. Therefore, we hypothesize that as α decreases, entire classes are eliminated. This is why the shapes are deeper.

Compared to the heave-only problem, the optimal shapes from the heave-surge-pitch problem are generally wider and less protruding outwards, resulting in a larger volume and surface area

As we saw with the cylinder in the previous chapter, shapes from the left branch of the population are eliminated due to stability, the pitch moment of inertia constraint (namely, that the expression for I_{55} necessary to achieve resonance is less than 0, and therefore not possible), and the pitch motion constraint.

We also saw with the cylinder that shapes on the heave-surge-pitch Pareto Front were 'moderate' in terms of shapes (that is, they were neither very disk-like nor deep), since both ends of the $\mathcal{S}(\mathbb{R}_3)$ curve were eliminated. This appears to be the case for the general shapes. We believe they are still protruding outwards for the same reasons as in the heave-only case, but that for shapes with larger $\overline{r_1}$, all of the shapes from $\mathbb{R}_3$ were eliminated due to stability, pitch moment of inertia constraint, or pitch motion constraint. Garrison (1974) shows that the pitch motion is very large at resonance for shapes with $H/R \approx 0.5$.

Shapes that protrude downwards are generally not optimal

Looking at the optimal shapes, we see that almost none of them are protruding downwards (that is, almost none of them have $\overline{z_1} < -1$ or $\overline{b_2} > 0.1$. We saw that shapes that protrude outwards have larger heave damping coefficients than those that do not protrude outwards. Additionally, shapes whose protrusion is closer to the waterline have larger heave damping coefficients than those whose protrusion is deeper (further from the waterline). So, we hypothesized that shapes are generally better with larger heave damping coefficients. Our hypothesis is strengthened, then, when we see that shapes that protrude downwards have *lower* heave damping coefficients, as shown in figure 6-44.

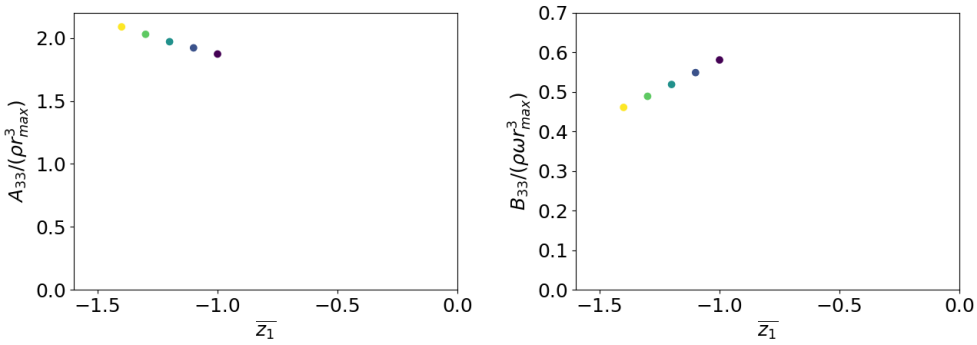

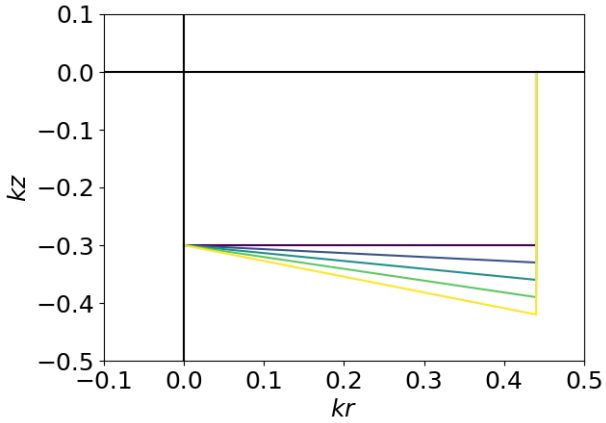

Figure 6-44: Demonstrating protruding downwards shapes, and showing how heave added mass (A_{33}) increases and heave damping (B_{33}) decreases with decreasing $\overline{z_1}$, keeping R, $\overline{r_1}$ and kH constant

Therefore, since almost none of the optimal shapes protrude downwards, and since heave damping decreases as $\overline{z_1}$ decreases, we can again hypothesize that generally shape with larger heave damping are optimal.

It is important to note that many of the conclusions we were able to make in this section was from our study of the cylinder, as well as the conclusions and observations we made in section 4.3, which are true for any given class of shapes. Although we optimize entire groups in this chapter, we used the physical insights we gained from the general shape of the curve of $\mathcal{S}(\mathbb{R}_3)$ for a given class, and how it is affected by constraints, to make some conclusions about why certain shapes are optimal and how the optimal shapes change with the constraints.

Hemisphere and other axisymmetric shapes

Another conical axisymmetric shape is the hemisphere. We will mention here that there is only one hemisphere that is in resonance in heave. This hemisphere has a kR value of 1.055, corresponding to $kl_V = 1.35$ and $kl_S = 2.64$. These numbers are not optimal in any case, so we do not consider the hemisphere further anywhere. Furthermore, we did not consider any toroidal shapes. This could be an interesting shape to look at, but it is very different dynamics to the solid axisymmetric shapes

we consider in this thesis.

6.8 Showing the benefit of optimization

In this section, we will demonstrate the benefit of this thesis by showing how much the optimization can improve the performance of a wave energy converter. Specifically, we will discuss how much less material (i.e. surface area and volume) the optimal shapes have, compared to the *optimal* cylinders found in the previous chapter. That is, to extract the *same power*, how much less material does the optimal shape have, compared to the optimal cylinder?

In tables 6.41 - 6.44, we show the decrease of surface area and volume, in percentage, for the optimal shapes from the overall Pareto Fronts (figures 6-33 to 6-40), compared to the optimal cylinders. So for the percentages for surface area, it is the percent difference of the surface area of the shape on the overall Pareto Front in the corresponding constraint regime with the minimum surface area, compared to the surface area of the cylinder on the Pareto Front in the corresponding constraint regime with the minimum surface area. Similarly, for volume, it shows the percent difference of the volume of the shape on the overall Pareto Front in the corresponding constraint regime with the minimum volume, compared to the volume of the cylinder on the Pareto Front in the corresponding constraint regime with the minimum volume.

	$\epsilon = 0.1$	$\epsilon = 0.2$
$\alpha = 3$	72 %	61 %
$\alpha = 1$	55 %	51 %

Table 6.41: Percentage decrease of surface area for the optimal heave-only shapes, compared to the optimal cylinders

	$\epsilon = 0.1$	$\epsilon = 0.2$
$\alpha = 3$	93 %	87 %
$\alpha = 1$	89 %	91 %

Table 6.42: Percentage decrease of volume for the optimal heave-only shapes, compared to the optimal cylinders

	$\epsilon = 0.1$	$\epsilon = 0.2$
$\alpha = 3$	31 %	15 %
$\alpha = 1$	17 %	17 %

Table 6.43: Percentage decrease of surface area for the optimal heave-surge-pitch shapes, compared to the optimal cylinders

	$\epsilon = 0.1$	$\epsilon = 0.2$
$\alpha = 3$	46 %	56 %
$\alpha = 1$	16 %	10 %

Table 6.44: Percentage decrease of volume for the optimal heave-surge-pitch shapes, compared to the optimal cylinders

Figures 6-45 and 6-46 show visual representations of these decreases of material. The optimal shapes are shown in green and the optimal cylinders are shown in blue. For simplicity, we only plot the shape on the overall Pareto Front for the corresponding constraint regimes with the minimum surface area, and the cylinder on the Pareto Front for the corresponding constraint regime with the minimum surface area. These figures show that the optimal shapes require *significantly* less surface area and volume than the optimal cylinders. We note that the differences for the **heave** problem are greater than the differences for the heave-surge-pitch problem.

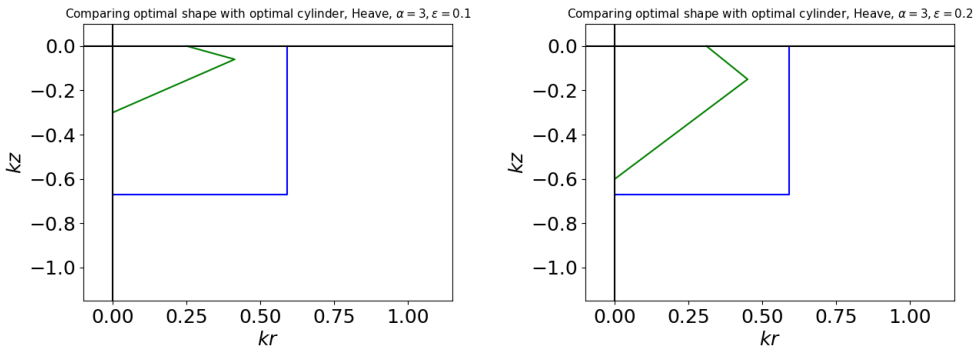

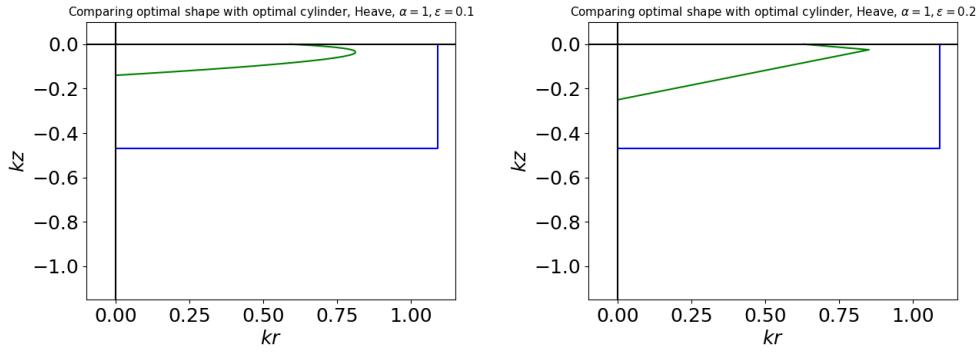

Figure 6-45: Comparing the optimal shapes from the overall Pareto Fronts to the optimal cylinders, for the heave-only problem

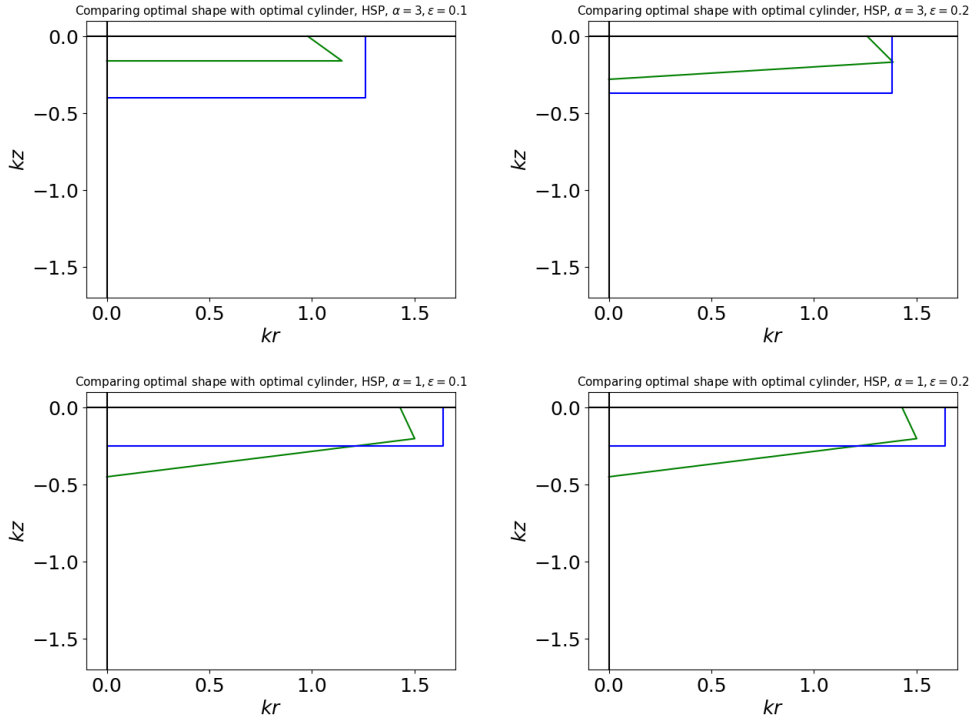

Figure 6-46: Comparing the optimal shapes from the overall Pareto Fronts to the optimal cylinders, for the heave-surge-pitch problem

These plots and tables show that to extract the *same power*, the optimal shapes have up to 72 % less surface area and 93 % less volume than the optimal cylinder.

We can also see the benefit of our optimization framework by considering figure 6-47. This figure shows the optimal shape from the heave-only problem for $\alpha = 3, \epsilon = 0.1$ in green. We compare it to a cylinder with radius equal to the maximum radial

dimension for the green shape and the same draft as the maximum depth dimension for the green shape, which is shown in red. The green shape will produce 9.1 times the amount of power compared to the red shape. This number was calculated by assuming that $\beta_3 = B_{33}$. This shows the benefit of our framework, as well: changing geometry can drastically increase the energy you can get from a WEC.

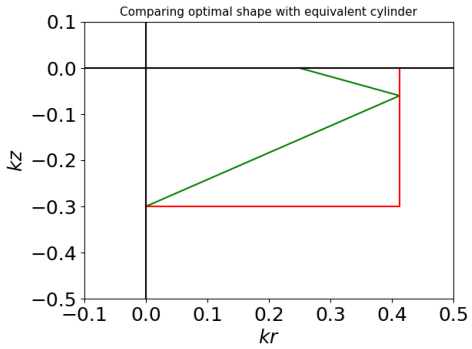

Figure 6-47: Comparing one of the optimal shapes with the cylinder with radius equal to the maximum r dimension and draft equal to the maximum z dimension. The green shape extract more than 9 times the red cylinder.

Physical dimensions and power output for typical wave

We will know calculate actual dimensions and power output for the optimal shapes for a typical sea state. The extractable power is

$$P = \frac{kW}{k}\frac{1}{2}\rho g A^2 V_g \tag{6.8.1}$$

For the heave-only problem, $kW_3 = 1$, so a 10-second wave with amplitude $A = 1$ would produce approximately 1 MW. Let's consider the optimal shapes in the least and most restrictive constraint regimes. For simplicity, let's consider the shapes on the Pareto Fronts with minimum kl_S. For $\alpha = 3, \epsilon = 0.1$, the dimensions of the optimal shape (shown in purple in figure 6-33) would be $R = 6.25$m (with $r_{max} = 10.3$m) and $H = 7.5$m. The optimal cylinder in this constraint regime has $R = 14.8$m and $H = 16.8$m. For $\alpha = 1, \epsilon = 0.2$, the dimensions of the optimal shape (shown in purple in figure 6-36) would be $R = 15.8$m (with $r_{max} = 21.3$m) and $H = 6.25$m. The optimal cylinder in this constraint regime has dimensions $R = 27.3$m and $H = 11.8$m.

For the heave-surge-pitch problem, $kW_{135} = 3$, meaning that the WEC would produce approximately 3 MW. For $\alpha = 3, \epsilon = 0.1$, the optimal shape, shown in purple in figure 6-37, would have dimensions $R = 24.5$m (with $r_{max} = 28.7$m) and $H = 4$m. The optimal cylinder in this constraint regime has dimensions $R = 31.5m$ and $H = 10m$. For $\alpha = 1, \epsilon = 0.2$, the optimal shape, shown in purple in figure 6-40, would have dimensions $R = 35.8$m (with $r_{max} = 37.5$m) and $H = 11$m. The optimal cylinder in this constraint regime has dimensions $R = 41m$ and $H = 6.25m$.

Compare these numbers to a wind turbine. According to their website, GE's 1 MW wind turbine has a rotor diameter of 82.5 to 103 meters. The optimal cylinders even have smaller dimensions than this, but the optimal shapes have *considerably* smaller dimensions.

Figures 6-45, 6-46 and 6-47, along with these analyses of real dimensions and extractable power amount show the advantage that the optimization framework and results give. Through the discovery of WECs that extract maximum power and require less material, whilst ensuring the WEC shapes are practically feasible, this thesis is a step forward in our understanding of WECs and ultimately could pave the way for wave energy becoming a viable source of renewable energy in future.

6.9 Discussing the overall optimal shape

In this section, we will discuss the shape with the minimum kl_S value for the heave-only problem, for $\alpha = 3$ and $\epsilon = 0.1$. This is the green shape in the first plot in figure 6-45 and in figure 6-47. This is a linear piecewise one-kink shape with $kR = 0.25$, $kH = 0.3$, $\overline{r_1} = 1.65$, and $\overline{z_1} = -0.2$. The kl_V value is 0.4 and kl_S is 1.

Response to irregular waves

This thesis is based on a single monochromatic wave with a given wavenumber k. However, in real seas an ocean spectrum is used to describe the spread of incoming

frequencies. A commonly used spectrum to describe real seas is the Bretschneider Spectrum. For figure 6-48, we assume a 7.5 second wave ($k = 0.07\text{m}^{-1}$) in blue, tune the optimal shape to that wave (that is, for example $R = 0.25/0.07 = 3.57\text{m}$), fix that shape, and then consider a range of different frequencies. In figure 6-48 we plot kW_3 at the different frequencies (kR is changing wavenumber k times fixed radius $R = 3.57\text{m}$). Note that we assume here that for each frequency $\beta_3 = B_{33}$. In purple, we plot the Bretschneider spectrum, with a peak at 7.5 seconds ($\omega = 0.84$) and a significant wave height of 3m (just so we can see the response in the same range as kW). We can see that the bandwidth of the response of the optimal shape is wide, suggesting it will do well in real seas.

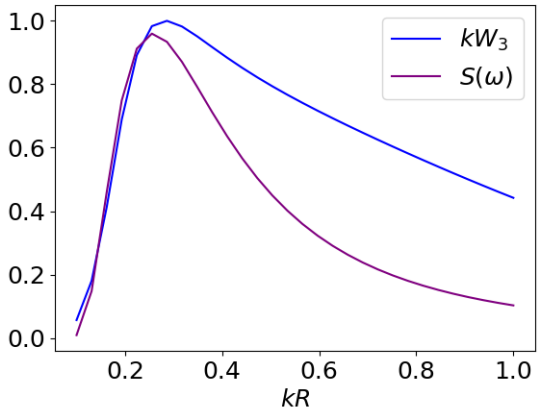

Figure 6-48: The response (in blue) of the optimal shape (shown in figure 6-47 in green), compared to a typical ocean spectrum - the Bretschneider spectrum (in purple)

Sensitivity of the shape

To consider the sensitivity of the shape, we changed each geometric parameter and calculated kW_3. If changing a geometric parameter by 5% resulting in a large change in kW_3, this would suggest that the performance of the shape was very sensitive. We found, however, that this was not true: a small change in each parameter corresponded to a *small* change in kW_3. When the parameters are as described at the beginning of this section, $kW_3 = 1$. When $kR = 0.238$ instead of 0.25, which is a 5% change, and all other parameters are the same, $kW_3 = 0.989$, which is a 1.1% decrease. We

did this sensitivity analysis for each other geometric parameter, changing it by 5% while keeping all the other geometric parameters at their optimal value. For kH, this resulted in a 0.4% decrease in kW_3, for $\overline{r_1}$, this resulted in a 5.5% decrease, and for $\overline{z_1}$, this resulted in a 0.3% decrease. These numbers suggest that the results are not very sensitive. If geometric shape changes slightly, it will not result in a significant loss of performance. This is very important for real-world application. Additionally, this suggests to us that if we were to round the edge of the shape instead of keeping it as a sharp corner, which is important to prevent flow separation, it would be essentially the same performance. This is in contrast to the phenomenon discussed in Tokić and Yue (2019), whereby arrays are very sensitive to configuration, with narrow banded spikes.

6.10 Summary

In the previous chapter, we presented the results of the optimal cylinders. In this chapter, we presented the rest of the results of the optimal shapes, through a systematic investigation of a broad range of shapes. In the introduction, we presented the four groups of shapes that we considered in this thesis: flat-bottomed shapes, one-kink shapes, compound cylinders, and no-kink-2nd-order shapes. In the following four sections, we presented 8 Pareto Fronts for each group. There were 4 Pareto Fronts for the heave-only problem, corresponding to the two values of α and two values of ϵ, and 4 Pareto Fronts for the heave-surge-pitch problem, corresponding to the two values of α and ϵ. After each Pareto Front, we also included a table of the dimensions and characteristics of each shape on that Pareto Front. In section 6, we presented the overall Pareto Fronts from all of the groups together, for each constraint regime.

In section 7 we discussed general trends and physical insights gained through these optimizations. The six main trends/ insights were (1) The optimal shapes generally protrude outwards, (2) In general, the maximum radius occurs closer to the waterline than the maximum draft (when allowed by the shape definition), (3) The trends

that we observe in the optimal shapes are consistent across all the groups of shapes, implying these may be features of a general optimum, (4) As the motion constraint becomes stricter (i.e. α decreases), the optimal shapes for the heave-only problem generally get wider and shallower, and the optimal shapes for the heave-surge-pitch problem generally get wider and deeper, (5) Compared to the heave-only problem, the optimal shapes from the heave-surge-pitch problem are generally wider and less protruding outwards, resulting in a larger volume and surface area, and (6) Shapes that protrude downwards are generally not optimal.

We went over each of these trends to dissect, using hydrodynamics, why each trend is true. For example, we concluded that the best shapes protrude outwards because they have larger heave damping, compared to shapes that do not protrude outwards as much.

In section 8, we showed the benefit of our optimization: to extract the same, maximum power, the optimal shapes have up to 72 % less surface area and up to 93 % less volume than the optimal cylinder for the heave-only problem. For the heave-surge-pitch problem, to extract the same, maximum power, the optimal shapes have up to 31 % less surface area and up to 56 % less volume than the optimal cylinder. This is shown in figures 6-45 and 6-46. We also showed that the optimal shape extracts more than 9 times more power than the cylinder with radius equal to the maximum radial dimension and equal draft (shown in figure 6-47), demonstrated that geometry greatly affects the extractable power from a WEC.

Furthermore, we looked at real, physical dimensions and power numbers. For a 10 second wave with amplitude of 1 meter, the WECs for the heave-only problem extract approximately 1MW, and the WECs for the heave-surge-pitch problem extract approximately 3MW. The dimensions of the WECs that produce that power from our optimization are significantly less than the corresponding dimensions of a wind turbine that extracts the same energy. Therefore, our optimization could pave the way to significantly improve wave energy converter technology to move it towards a

viable source of renewable energy.

And finally, in section 9, we looked more at the overall optimal shape. We define this as the shape with minimum kl_S for the heave-only problem, for $\alpha = 3, \epsilon = 0.1$. We see that the response of the optimal shape has a wide bandwidth, suggesting it will perform well in real, irregular seas. We also showed that the geometry is not overly sensitive: a small change in geometric parameter results in a small change in performance, kW_3.

Chapter 7

Conclusions

In this chapter, we will summarize the main contributions of this thesis. We will also discuss future work that is informed by the research done in this thesis.

7.1 Thesis contributions

Although there have been many ideas for wave energy converter technologies, as yet there is no convergence on the optimal shape of a wave energy converter. Furthermore, there is no agreed-upon definition of what it means for a WEC to be 'optimal' and no established framework to find optimal shapes. The main contributions from this thesis are:

1. A novel, scientifically rigorous framework to find practically realistic optimal shapes of WECs

2. A general, efficient and efficacious procedure to execute the optimization and provide physical insights

3. Comprehensive and unforeseen results for the optimal shapes of axisymmetric WECs, found by performing a systematic investigation of a broad range of shapes

4. Original insights to gain physical intuition about the best WEC shapes

We will now elaborate on these four contributions.

A novel, scientifically rigorous framework to find practically realistic optimal shapes of WECs

When optimizing a wave energy converter, the main goals are to maximize power and minimize cost, while ensuring that the shapes are practically realistic. The novel framework described in this thesis accomplishes these goals. Because for an axisymmetric shape the maximum extractable power does not depend on the geometric shape, we identified that we cannot define optimality by shapes that extract maximum power alone. Rather all shapes that can achieve resonance can extract maximum power, so we impose the requirement of resonance and establish a clean, well-defined method to compare shapes while ensuring maximum power.

When incident frequency is known, the geometric shape becomes the independent parameter in the heave resonance equation for which we must solve. There are design parameters in each of the surge-pitch resonance equations that can be changed once the geometry is known. Therefore, we realized that we must solve for geometric shape using the heave resonance equation and then change the design parameters to ensure resonance in the surge-pitch equations. This formulation, to the best of our knowledge, is novel and has not been covered in previous literature.

With the requirement that bodies be in resonance, we recognized that there was a need for motion constraints. Additionally, there was a need for constraints on the design parameters used to ensure resonance in surge-pitch. All of these constraints ensure that the discovered shapes are practically realistic and feasible. This grounds our theoretically rigorous and novel framework, ensuring that the shapes it yields are achievable options for real devices.

A general, efficient and efficacious procedure to execute the optimization and provide physical insights

Our developed procedure allows us to evaluate a large number of general geometries efficiently. By describing geometries using piecewise parametric polynomial basis sets, we are able to describe and optimize a very wide range of shapes with relatively few parameters.

A novel theorem to find the roots of the heave resonance equation was presented and proved, with the implications discussed. This theorem adds to our understanding of the heave resonance equation and significantly decreases the computation time for the optimization. Using the theorem we essentially reduced the degrees of freedom of the optimization by one, increasing the efficiency 100x compared to brute-force tests. The heave resonance equation is difficult to solve due to the presence of the heave added mass, therefore in this theorem, we use an approximation for heave added mass. The theorem states that for a given class of shape, below a certain volume there are two roots of the heave resonance equation, which using the added mass approximation can be found by solving a simple cubic equation. Above that volume there are no roots of the heave resonance equation. This approximation was used in other areas of this thesis to better understand why certain shapes are optimal. For example, from this theorem we can understand the curve of the heave population and Pareto Front, discussed in chapter 4.

Comprehensive and unforeseen results for the optimal shapes of axisymmetric WECs, found by performing a systematic investigation of a broad range of shapes

We started with a simple, easily describable shape: the cylinder. In chapter 5, we showcased our optimization framework and procedure on the cylinder and presented the best cylinders under different constraint regimes, for the heave-only problem and the heave-surge-pitch problem. Before this thesis, the dimensions (draft and radius) of the optimal cylinders were not known. We also discuss how the optimal cylinders change due to stricter motion and steepness constraints.

In chapter 6 we presented the optimization results for the rest of generalized geometries. We perform a systematic investigation of a vast range of shapes, spanning shapes with a flat bottom to compound cylinders to shapes described by second-order functions. For each group of shapes we performed eight optimization runs: four for the heave-only problem and four for the heave-surge-pitch problem, corresponding to two values of the motion constraint parameter, α, and two values of the steepness constraint, ϵ.

The results show shapes that are able to achieve maximum power with minimum material, while ensuring the shapes are practically feasible. To demonstrate the benefit of the optimization, we showed that to produce the same maximum power, the optimal shapes found in this thesis have up to 72 % less surface area and 93 % less volume than the optimal cylinders. Another way to show the benefit of optimization is that the optimal shape extracts more than 9 times more power than the cylinder with radius equal to the maximum radial dimension and equal draft of the optimal shape. Furthermore, we saw that the optimal shapes have wide bandwidth responses, suggesting that it will do well in real, irregular seas. These numbers show that optimizing the geometry of a WEC could move WEC technology significantly closer to becoming a viable source of renewable energy.

Optimizing the geometry of a WEC could provide the significant improvement needed in WECs to extract more power for less cost. By nondimensionalizing all geometric parameters by wavenumber k, we can tune the optimal shapes to any incoming wave. Currently, WECs are only considered in very energetic locations, which corresponds to sea states with very large wave periods and extreme events. By finding optimal shapes that minimize material while extracting power, it could be possible for WECs to be efficient in sea states that have fewer extreme events and thus increase their survivability.

Original insights to gain physical intuition about the best WEC shapes

In chapter 4, we presented our observations and conclusions for any given class of shapes. We observed that, for any given class, the curve of the set of shapes in resonance in heave in the $kl_V - kl_S$ space has certain characteristics: it is one-to-one, concave down, starting at the origin with a maximum at $(kl_V)^{max}$, where the left 'branch' corresponds to the smaller roots of the heave resonance equation, and the right 'branch' corresponds to the larger roots of the heave resonance equation. The heave motion constraint will eliminate shapes on the lower left branch and the heave steepness constraint will eliminate shapes on the lower left branch and the lower right branch. As the constraints become stricter, more of the corresponding branches are eliminated. Therefore, there are three possible shapes a heave population in the $kl_V - kl_S$ space can take, and three corresponding shapes for the heave Pareto Front. From this, we were able to show a counter-intuitive phenomenon whereby stricter motion constraints can result in fuller Pareto Fronts for a given class. This is demonstrated in chapter 5 for the cylinder. Furthermore, the general description of the shape of the heave population added to our physical intuition and enabled us to draw conclusions about more complex shapes and general optimizations.

In chapter 6, we presented and discussed six main conclusions from the overall results:

1. The optimal shapes generally *protrude outwards* below the waterline.

2. In general, the maximum radius occurs closer to the waterline than the maximum draft (when allowed by the shape definition).

3. The trends that we observe in the optimal shapes are consistent across all the groups of shapes, implying these may be features of a general optimum.

4. As the motion constraint becomes stricter (i.e. α decreases), the optimal shapes for the heave-only problem typically become wider and shallower, and the optimal shapes for the heave-surge-pitch problem typically become wider and deeper.

5. Compared to the heave-only problem, the optimal shapes from the heave-surge-

pitch problem are generally wider and less protruding outwards, resulting in a larger volume and surface area.

6. Shapes that *protrude downwards* are generally not optimal.

The combination of points 1 and 2 above shows that shapes which protrude outwards below the waterline, with their maximum radius occuring closer to the waterline than the maximum draft, are generally optimal. We demonstrate that such shapes have larger heave damping coefficients, and since the heave body motion at resonance is inversely proportional to the heave damping coefficient, we hypothesize that allowing shapes to protrude outwards enables smaller volumes while still adhering to the motion constraints.

From our systematic investigation of a broad range of shapes, we studied four main groups of shapes. When we compare the shapes on Pareto Fronts across different groups, the shapes have many common features and follow similar patterns of how they change with different constraint values. One of these general trends is that as the motion constraint becomes stricter (i.e. α decreases), for the heave-only problem the optimal shapes get wider and shallower and for the heave-surge-pitch problem the optimal shapes get wider. Also, compared to the optimal shapes for the heave-only problem, the optimal shapes for the heave-surge-pitch problem are generally wider and less protruding. These trends are true for the *overall* Pareto Fronts, but they are also true within *each* group. Moreover, the actual dimensions of shapes are similar between different groups. These similarities across the different groups of shapes suggests that these trends are *general* in nature. This suggests that these are features of a general optimum.

Limitations

This thesis has produced a number of novel and innovative contributions, but the work also has some limitations. For example, we stated that one of the goals of the optimization is to minimize cost. We use amount of material (volume and sur-

face area) as a proxy for cost, but there will be other factors that will contribute to cost, such as deployment costs, repair costs, costs associated with mooring, etc. Furthermore, we only minimize surface and volume *below* the waterline. There must be material above the waterline, too, and so it would be important to consider this when estimating cost. We model the PTO as a simple linear damper, which is a good approximation for a linear direct-drive generator, but more sophisticated modeling should be considered as well. We modeled mooring forces as a linear spring in surge, but more sophisticated models for mooring forces should be considered, as well.

7.2 Future work

This thesis provides a significant step in advancing our understanding of WECs, and consequently also helps us realize what the next steps should be in this research field.

Experimental validation

We found exciting new optimal shapes and trends that were previously unknown. These results were found computationally, so experimental validation is needed. The shapes found by our optimization framework and procedure are feasible theoretically and computationally, but the feasibility in real fluid still needs to be assessed. A logical next step would be to test them in a laboratory, in a small scale experiment. Because the results are novel, experimental information is not available, particularly for the more complex optimal shapes which differ from the shapes of current WEC designs.

It would be advisable to start with the simplest shapes to build, such as a cylinder, to assess how accurate the models and approximations in this thesis are at modeling real-fluid effects. And then, the more complex shapes (particularly the protruding outwards shapes) should be tested. For example, we saw that to extract the same power, optimized compound cylinders can have 50 % less surface area and 77 % less volume than optimized cylinders. Compound cylinders are relatively easy to build,

so this would be a good experiment to run.

It would be prudent to test the heave-only shapes first, since this is an easier way to extract energy. It is important to test the heave-surge-pitch shapes as well, to test the viability of our novel formulation of how to ensure resonance in surge-pitch by changing the design parameters k_1, z_G and I_{55}, and also to test the optimal shapes from the heave-surge-pitch optimization.

Spectrum

In this thesis, we only consider a unidirectional monochromatic wave. In section 6.8 we did show the response of the optimal shape in other frequencies, and found that the response has a wide bandwidth, suggesting it will do well in irregular seas. However, to further this research, real narrow-banded frequency and directional ocean spectra need to be introduced to the overall problem. Even for axisymmetric bodies these results are as yet unknown. The optimization framework would need to be updated, since the body would not be in resonance at every frequency. One idea would be to require it be in resonance at the peak frequency, and then change the objective functions to (1) maximize power (integrated over the spectrum), and (2) minimize surface area or volume. The reason we need to maximize power is that shapes with narrow bandwidths would not work as well as those with wider bandwidths. Shapes with narrow bandwidths are usually deep, narrow shapes, and our motion constraint eliminates these shapes, so we hypothesize that the optimal shapes found in this thesis would perform well when evaluated across a spectrum. Since body motion is maximum at resonance, the motion constraints and steepness constraints at resonance would still apply. Everything else in the optimization framework could then stay the same. We could still find the resonating bodies for a given k_p using the theorem developed in this thesis, again reducing the computational time needed considerably. Then, the Pareto Front would be evaluated to maximize extractable power over incident power integrated across the spectrum and to minimize surface area or volume (or, perhaps, a three-objective algorithm could be developed, to mini-

mize both surface area and volume). These objective functions would be well-defined since resonance is still required for the peak frequency. Another important aspect to be considered are the PTO coefficients. Setting the PTO coefficient equal to the radiation damping at resonance is optimal if the body is in resonance, but considering irregular seas this may no longer be true. Therefore, it would be necessary to make a formulation about how to optimize that parameter.

Non-axisymmetric shapes

This thesis only considers axisymmetric WECs, because in real oceans the direction of the incoming wave is not constant. However, it would be a good next step to consider non-axisymmetric shapes. The limits of capture width do not apply to non-axisymmetric shapes, so we would need to change the optimization framework, since the maximum power would now depend on the geometric shape and size.

Arrays

An important aspect of wave energy research is in looking at *arrays* of WECs. The interaction of WECs with one another in an array can significantly increase the extractable power. For example, Garnaud and Mei (2010, 2012) show that using a compact array, instead of one large buoy, can broaden the bandwidth of power extraction. Tokić and Yue (2019) found that WECs in arrays can extract up to 10 times that amount of power as isolated WECs. In their research, the configuration of arrays of WECs are optimized, where they assume cylindrical and constant geometries. However, as we see in this research, the geometry of WECs greatly affects the performance of WECs, and particularly enables the same amount of power to be extracted with less material. It would be a good next step to test one of the optimal geometries found in this research in an array configuration. But further, we could use the framework and parameterization used in this thesis and apply it to the work done on arrays to find if WEC geometry should change based on the location in an array – that is, optimize the geometries of all of the WECs in an array.

Nonlinear effects, viscous effects, and survivability in extreme conditions

In this thesis, we optimized WECs for normal operating conditions, instead of looking at extreme conditions. Therefore, we assumed that wave motions are sufficiently small to linearize. We also assumed that the bodies are large relative to the wave amplitude, so flow separation is unimportant. However, it may be good to verify the conclusions from this thesis with weakly or fully nonlinear theory, for example for non-wall-sided shapes.

To summarize, this thesis sets up a theoretically rigorous foundation for how to best optimize the geometry of a WEC and presents optimal shapes found computationally. We believe these contributions can aid future research and development of wave energy converters, and the framework and results from this thesis could move wave energy significantly towards becoming a viable source of renewable energy.

Appendix A

Stability constraint

In the heave-surge-pitch problem, one of the constraints is that the shape must be in stable equilibrium in pitch. One of the controllable design parameters we change to ensure resonance in surge-pitch is z_G, the vertical location of the center of gravity. However, we know from stability analysis that there is maximum value that z_G can take such that above this value the body would be unstable. In this section, we outline how to find z_G^{max} for a given shape. For more information, see *Principles of Naval Architecture* (Lewis, ed., 1988).

Consider a small angle of pitch displacement $\delta\phi$, shown in figure A-1.

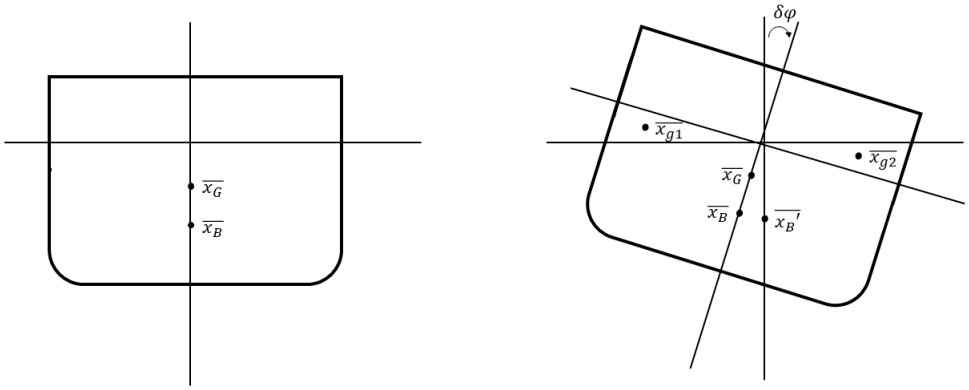

Figure A-1: A small angle $\delta\phi$ of pitch displacement to a body.

The original center of buoyancy is $\overline{x}_B$ and changes to $\overline{x}'_B$ when the body rotates $\delta\phi$. $\overline{x}_M$ is the point of intersection between a vertical line through $\overline{x}'_B$ and a line through the body's center axis, as shown in figure A-1

When the body rotates, the new waterline will intersect the original waterline at the body's vertical centerline axis since the volume of the two wedges are equal, meaning there is no change in displacement, as shown in figure A-1. If the volume of each wedge is v, the total volume of the body is $\forall$ and the centers of gravity of the wedges are $\overline{x}_{g1}$ and $\overline{x}_{g2}$, then the distance between $\overline{x}_B$ and $\overline{x}'_B$ will be

$$\overline{\overline{x}_B\overline{x}'_B} = \frac{v\overline{\overline{x}_{g1}\overline{x}_{g2}}}{\forall} \tag{A.0.1}$$

where $\overline{\overline{x}_B\overline{x}'_B}$ is parallel to $\overline{\overline{x}_{g1}\overline{x}_{g2}}$. As $\delta\phi \to 0$, $\overline{\overline{x}_B\overline{x}'_B}$ becomes perpendicular to the body's vertical centerline axis, and so the distance between $\overline{x}_B$ and $\overline{x}_M$ is

$$\overline{\overline{x}_B\overline{x}_M} = \frac{\overline{\overline{x}_B\overline{x}'_B}}{\tan\delta\phi} \tag{A.0.2}$$

Putting equation A.0.1 in for $\overline{\overline{x}_B\overline{x}'_B}$ we get

$$\overline{\overline{x}_B\overline{x}_M} = \frac{v\overline{\overline{x}_{g1}\overline{x}_{g2}}}{\forall\tan\delta\phi} \tag{A.0.3}$$

Since the body is axisymmetric,

$$v\overline{\overline{x}_{g1}\overline{x}_{g2}} = \int_0^\pi \frac{2}{3}\tan\delta\phi R^3\sin^3\theta R d\theta = \frac{8}{9}R^4 tan\delta\phi \tag{A.0.4}$$

Putting this into equation A.0.3, we get

$$\overline{\overline{x}_B\overline{x}_M} = \frac{8R^4}{9\forall} \tag{A.0.5}$$

Therefore, since z_G must be below z_M, we find z_G^{max} to be

$$z_G^{max} = z_M = \overline{\overline{x}_B\overline{x}_M} + z_B \tag{A.0.6}$$

When putting equation A.0.5 in for $\overline{\overline{x}_B\overline{x}_M}$, we get an expression for z_G^{max} in terms of

z_B, R and $\forall$:

$$z_G^{max} = \frac{8R^4}{9\forall} + z_B \tag{A.0.7}$$

This expression will serve as a maximum value of z_G^r, the value of z_G needed to put the body in resonance.

Appendix B

Verifications for theorem

In chapter 4, we presented a theorem about the heave resonance equation. We also explained a procedure to use this theorem to find roots of the heave resonance equation that is 100x more efficient than brute-force searches. In this appendix we show some examples of the verifications we did to validate this approach.

Theorem

Consider a WEC of volume l_V^3, with an incoming wave of unit-amplitude and wavenumber k. Suppose body class vector $\overline{\mathscr{B}_E}$ is given. If nondimensional added-mass coefficient, $\overline{A_{33}} = \frac{A_{33}}{\rho l_V^3}$, where A_{33} is the dimensional added mass coefficient, can be approximated by the function

$$\overline{A_{33}} = f(\overline{R}, kl_V) = A(kl_V)\overline{R}^3 \tag{B.0.1}$$

with the following restrictions on $A(kl_V)$:

1. $A(kl_V) > 0$ for all $kl_V > 0$
2. $\Delta = kl_V \left[-27\left(A(kl_V)\right)^2 (kl_V)^3 + 4\pi^3\right]$ must have 1 positive real root, $(kl_V)^{max}$, such that $\Delta > 0$ for $kl_V < (kl_V)^{max}$ and $\Delta < 0$ for $kl_V > (kl_V)^{max}$

then for $kl_V < (kl_V)^{max}$ there are two shapes, with R-values $\overline{R}_1$ and $\overline{R}_2$, that achieve resonance, and for $kl_V > (kl_V)^{max}$ there are no shapes that achieve resonance. The

proof to this theorem is given in chapter 4.

How we use this theorem

In our optimization, each organism is given by kl_V and $\overline{\mathscr{B}_E}$. Given these, we can find A_{33} for a few values of $\overline{R}$. Then, we fit this data to the function $A_c\overline{R}^3$ to find A_c. We use this value of A_c in the approximated version of the heave resonance equation:

$$-(kl_V)A_c\overline{R}^3 + \pi\overline{R}^2 - kl_V = 0 \tag{B.0.2}$$

which, given kl_V is simply a cubic equation in $\overline{R}$. We can solve explicitly for the two roots of the equation (if they exist – that is, if $kl_V < (kl_V)^{max}$), $\overline{R}_1^a$ and $\overline{R}_2^a$, which are the approximate roots of the resonance equation. Then, we can use $\overline{R}_1^a$ and $\overline{R}_2^a$ to perform local optimizations (bracket methods using WAMIT values of A_{33}) to find more accurate values of $\overline{R}_1$ and $\overline{R}_2$, the actual values of the resonance equation.

What needs to be validated

In this appendix, we show examples from the two parts of the validation needed to use this theorem. First, we look at the added mass approximation that given kl_V, $\overline{A_{33}}$ can be approximated as $A_c\overline{R}^3$, where A_c is a constant. The validation for that is shown in section B.1. And then in section B.2 we show the validation of finding $\overline{R}_1$ and $\overline{R}_2$ – that is, we use the procedure described above and compare it to brute-force searches to show that our procedure works well.

B.1 Verification of added mass approximation

In this section, we show a a few examples of verifications of the added mass approximation. We performed these verifications for a wide range of classes of shapes, but in this appendix we just show one example class from each group of shapes. In the following figures, we look at a few values of kl_V, with different colors for different kl_V values. The solid line shows the heave added mass from WAMIT, for a range of $\overline{R}$

values. The dashed line is a fit to a function $A_c\overline{R}^3$, where A_c is a constant. Then, we plot $1 - R^2$ vs. kl_V, where R^2 is the coefficient of determination.

Cylinder

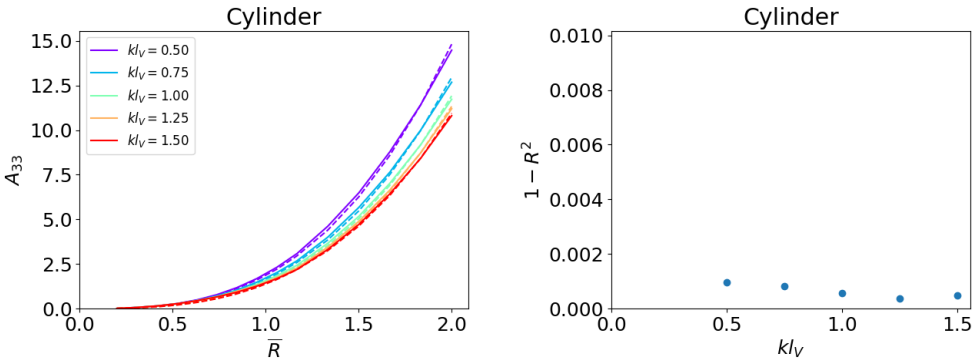

Figure B-1: Cylinder added mass approximation verification

One kink shape

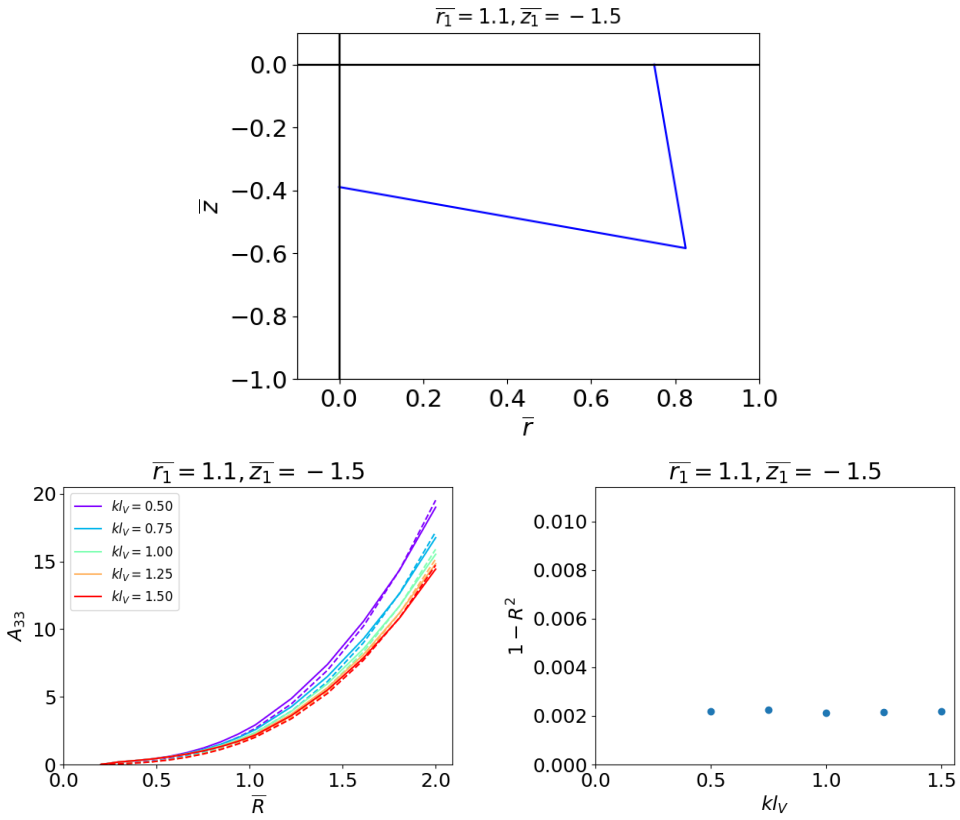

Figure B-2: One-kink shape added mass approximation verification

Compound cylinder

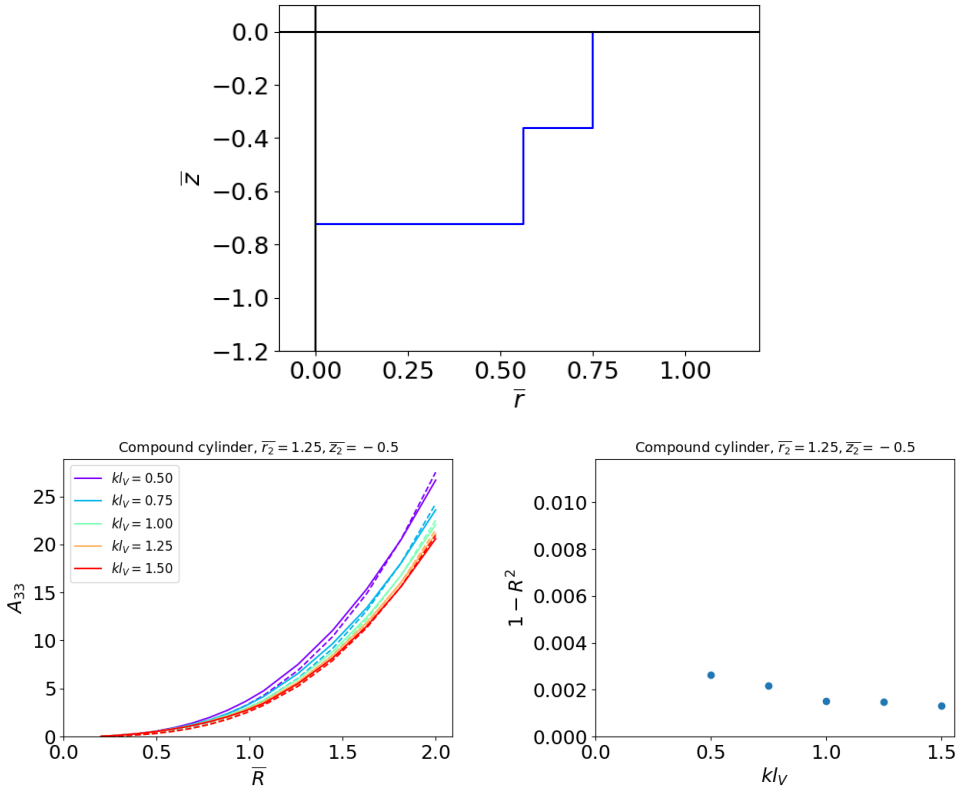

Figure B-3: Compound cylinder added mass approximation verification

No-kinks-2nd-order shape

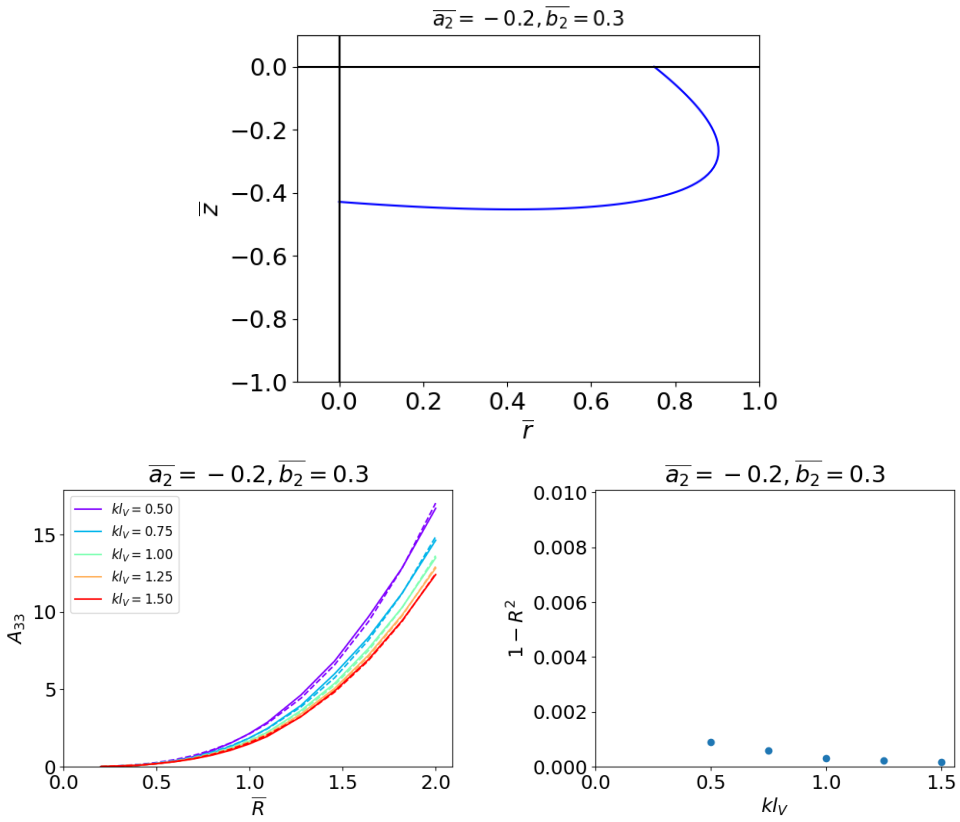

Figure B-4: No-kink 2nd-order shape added mass approximation verification

From all of these plots, we can see that the approximation is valid for each class tested. The minimum R^2 value is 0.996. These plots only show one example from each group of shapes, but in reality we tested a wide range of classes within each group. For example, for the one-kink shapes, we tested $\overline{r_1}$ values less than 1 and greater than 1, and we tested $\overline{z_1}$ values less than -1 and greater than -1. We found similar results in all classes that we tested – that is, R^2 values always greater than 0.995.

B.2 Verification of finding roots

In this section, we show the verification for the rest of the procedure we use to find the roots of the resonance equation. We again show one example class for each group.

We show the percent error of the roots found from our method against brute-force searches for both $\overline{R}_1$ and $\overline{R}_2$. We look at a few values of kl_V for each shape. We look at 10 values of $\overline{R}$ from 0 to 3.5, record added mass, fit it to the cubic equation, find approximate roots by solving the cubic equation, and then do a local optimization to get a more accurate value of the root. We compare this to roots found from brute-force method (looking at all values of $\overline{R}$).

Cylinder

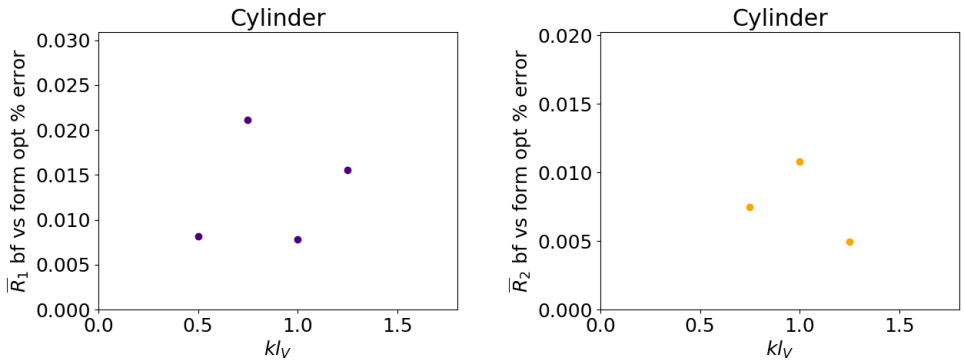

Figure B-5: Cylinder finding roots verification

One kink shape

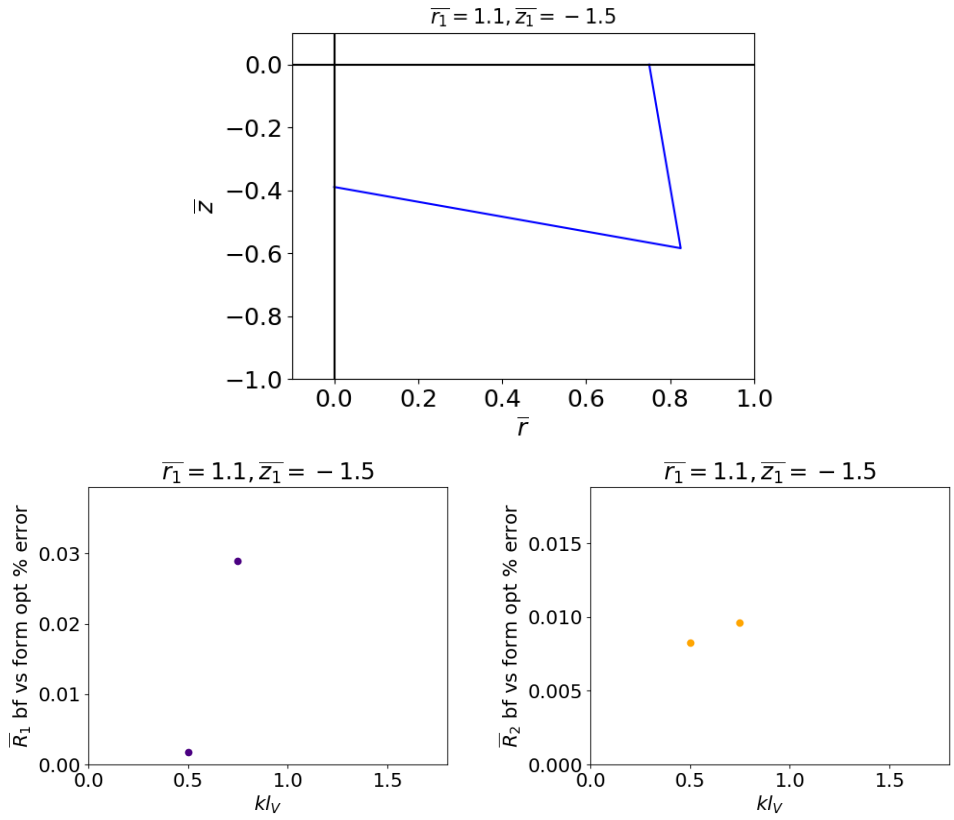

Figure B-6: One-kink shape finding roots verification

Compound cylinder

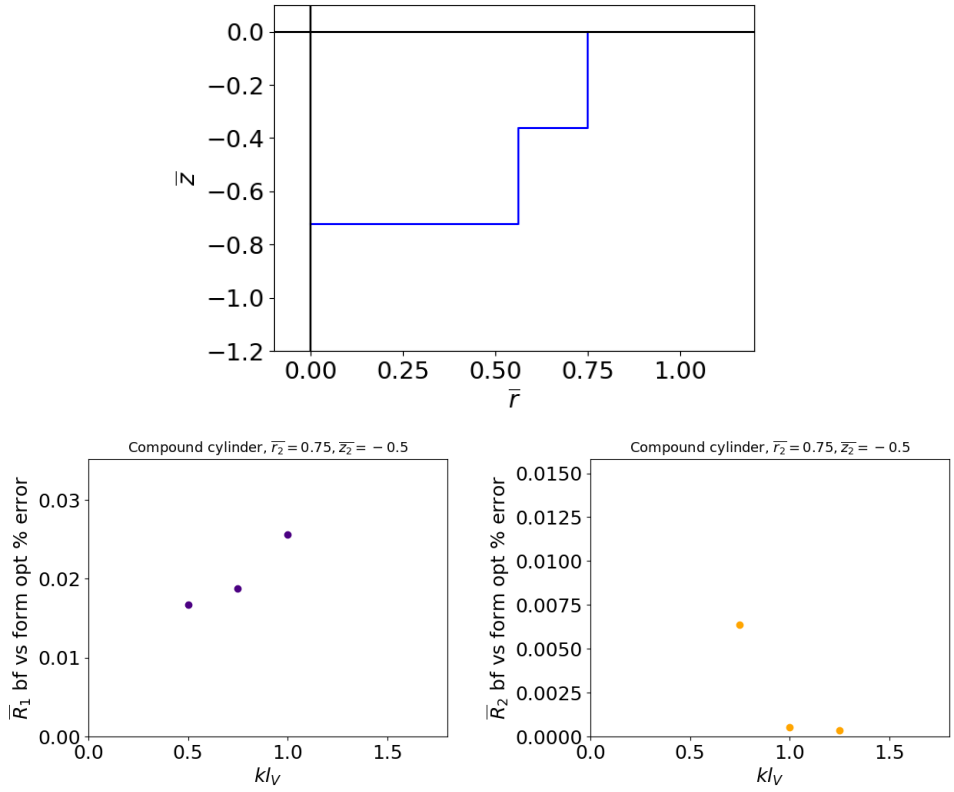

Figure B-7: Compound cylinder finding roots verification

No-kinks-2nd-order shape

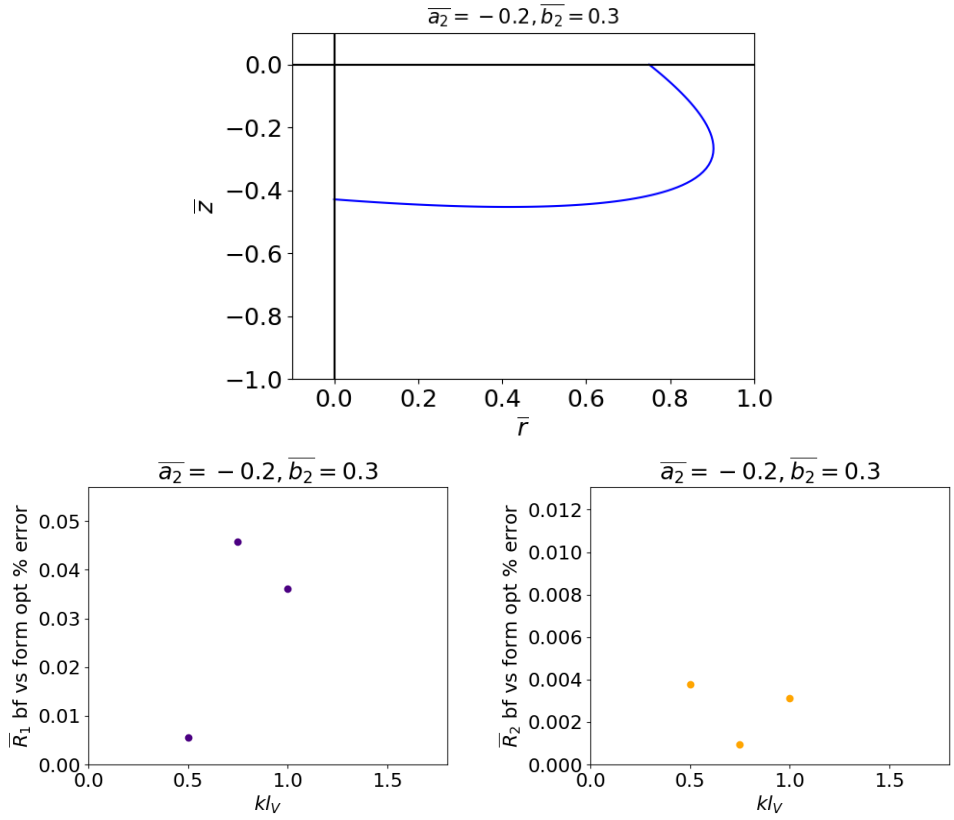

Figure B-8: No-kinks 2nd-order shape finding roots verification

As we can see from all of these plots, the percent error of the roots is never above 5%. Therefore, we can say that our method for finding roots works well. Again, these are just examples of classes we looked at. We looked at many more classes of shapes within each group.

Appendix C

Sensitivity study for multi-objective evolutionary algorithm

In this appendix we show the sensitivity study performed for the multi-objective optimization. From this sensitivity study we determined the mutation probability, initial population size, and the number of generations for each run in the optimization.

We looked at the flat-bottomed group for this sensitivity study, because it only has two geometric parameters (kl_V and $\overline{r_1}$) to optimize. For each of the following sensitivity studies, we looked at kl_V from 0.5 to 1.5, with a step-size of 0.02 – that is, the values kl_V could take were 0.5, 0.52, 0.54, ..., 1.48, 1.5. This corresponds to 51 possible values for kl_V. We looked at $\overline{r_1}$ from 0.25 to 1.39, with a step-size of 0.02 – that is, the values $\overline{r_1}$ could take were 0.25, 0.27, 0.29, ..., 1.37,1.39. This corresponds to 58 possible values for $\overline{r_1}$. Therefore, since every combination of kl_V and $\overline{r_1}$ is possible, there are 2958 possible organisms.

We ran each of these 2958 organisms to determine the (actual) minimum kl_V and kl_S values. Then, we ran the optimizations using different mutation probability values and different initial population ('popsize') values. We ran each optimization until

the minimum kl_V and minimum kl_S in the optimization was within 5% of the actual minimum kl_V and kl_S values. For each value of mutation probability and initial population size, we repeated this process 20 times and recorded the average number and the maximum number of generations needed to get within 5% of the actual minimum kl_S and kl_V values.

C.1 Heave

C.1.1 Initial population size

For these tests, we kept the mutation probability at 0.1. We tested 'popsize' values from 50 to 1000. The following plots show the average number of generations needed for the minimum kl_V and kl_S values in the optimization to get within 5% of the actual minimum kl_V and kl_S values, the maximum number of generations, and then the average total number of runs (popsize + number of generations) and maximum number of runs.

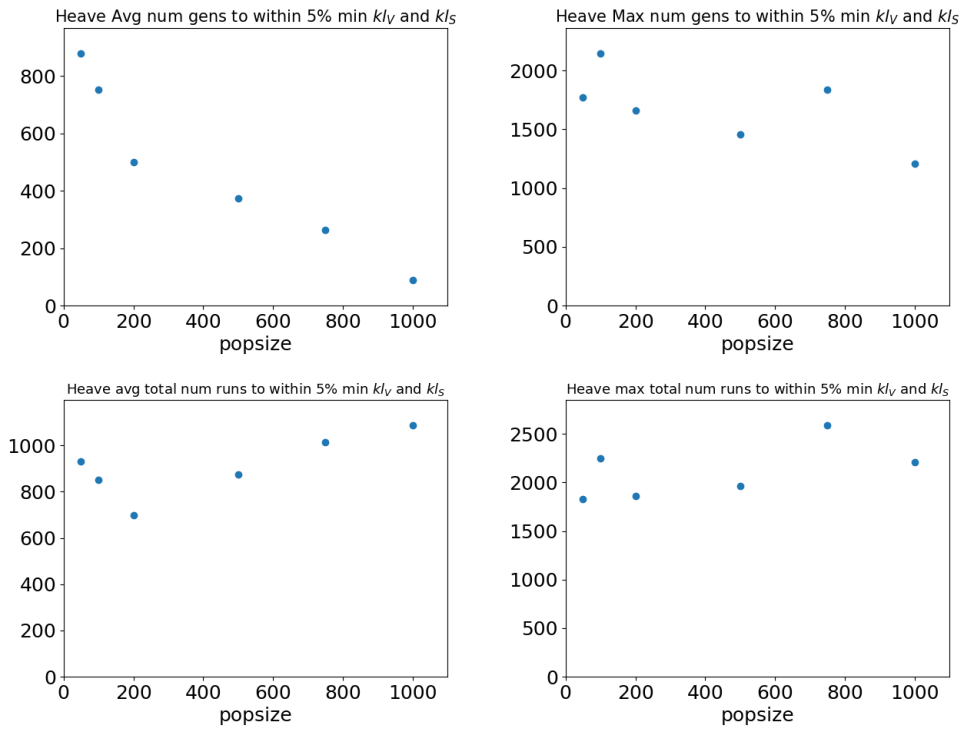

Figure C-1: Sensitivity study for initial population size for the heave problem. The first plot shows the average number of generations needed for the minimum kl_V and kl_S values in the optimization to get within 5% of the actual minimum kl_V and kl_S values, the second plot shows the maximum number of generations, the third plot shows the total number of runs (popsize + number of generations) and the fourth plot shows the maximum total number of runs

From this analysis, we determined that an initial population size of 200 performed best since it had the smallest average total number of runs needed to get kl_V and kl_S values within 5% of the actual minimum kl_V and kl_S values. The maximum number of generations needed for a 'popsize' value of 200 was approximately 2000, and the average number of generations was 750. Comparing these numbers to the number of possible values, 200/2958=0.07, 2000/2958=0.68, and 750/2958=0.25. Therefore, for each optimization in the runs described in chapter 6, we generally chose an initial population size of 0.07 times the total number of possible organisms and ran 0.5 times the total number of possible organisms generations in each optimization run.

C.1.2 Mutation probability

For these tests, the initial population size was 150. The following figures show the average and maximum number of generations needed for the minimum kl_V and kl_S values in the optimization to get within 5% of the actual minimum kl_V and kl_S values. We tested mutation probability from 0.05 to 0.9, and we tested each 20 times.

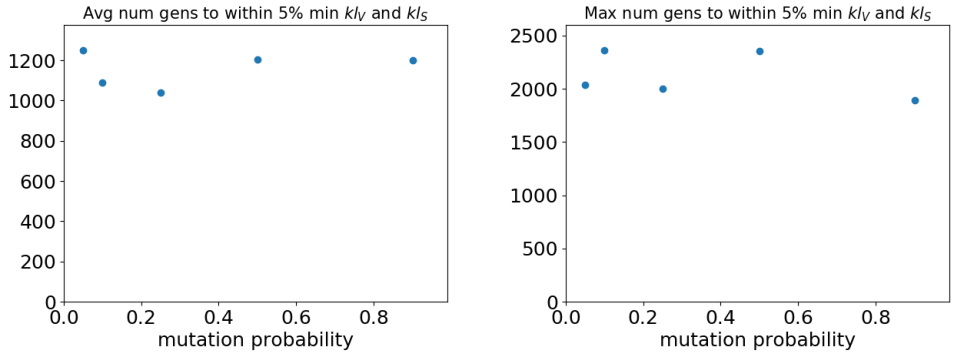

Figure C-2: Sensitivity study for mutation probability for the heave problem. The first plot shows the average number of generations needed for the minimum kl_V and kl_S values in the optimization to get within 5% of the actual minimum kl_V and kl_S values, the second plot shows the maximum number of generations

From these tests, we concluded that a mutation probability of 0.1 is optimal, so we use this in all of our optimization in chapter 6.

C.2 Heave surge pitch

We tested the same values for kl_V and $\overline{r_1}$. Of course, for the heave-surge-pitch problem the minimum values for kl_V and kl_S are going to be different, so we again ran all possible organisms to get the actual values for minimum kl_V and minimum kl_S.

C.2.1 Initial population size

For these tests, we kept the mutation probability at 0.1. We tested 'popsize' values from 50 to 200. The following plots show the average number of generations needed for the minimum kl_V and kl_S values in the optimization to get within 5% of the actual minimum kl_V and kl_S values, the maximum number of generations, and then

the average total number of runs (popsize + number of generations) and maximum number of runs.

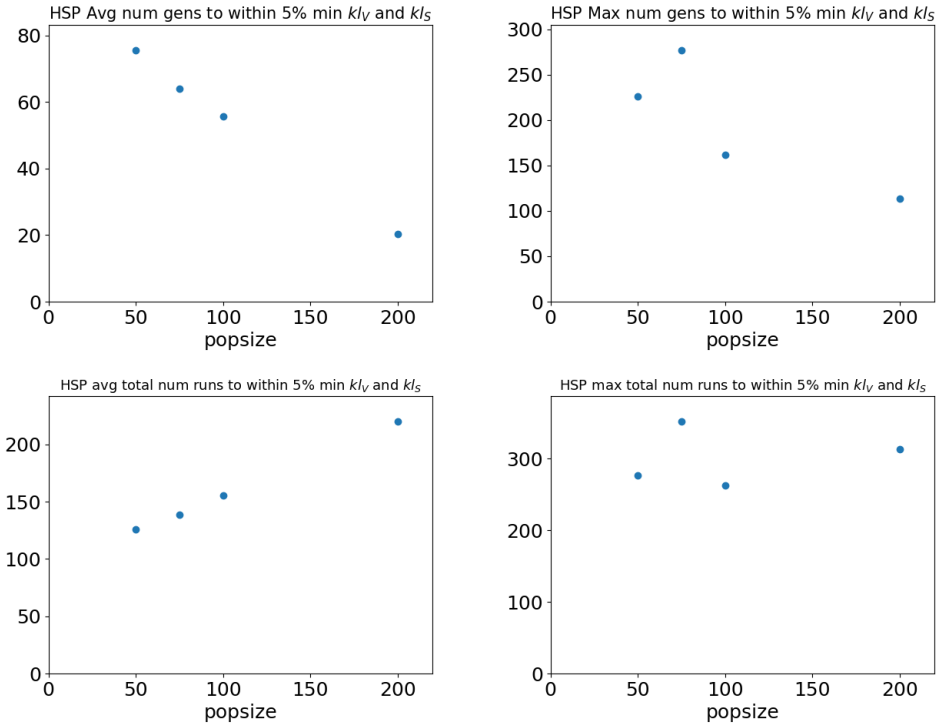

Figure C-3: Sensitivity study for initial population size for the heave-surge-pitch problem. The first plot shows the average number of generations needed for the minimum kl_V and kl_S values in the optimization to get within 5% of the actual minimum kl_V and kl_S values, the second plot shows the maximum number of generations, the third plot shows the total number of runs (popsize + number of generations) and the fourth plot shows the maximum total number of runs

From this analysis, we see that an initial popualtion size of 50 is best. That is 2% of the number of possible organisms. It corresponds to an average of 75 generations needed and a maximum of 220 generations needed. This corresponds to 7% of the total number of possible organisms. So these are the percentages we use in the heave-surge-pitch optimizations in chapter 6.

C.2.2 Mutation probability

For these tests, the initial population size was 150. The following figures show the average and maximum number of generations needed for the minimum kl_V and kl_S

values in the optimization to get within 5% of the actual minimum kl_V and kl_S values. We tested mutation probability from 0.05 to 0.9, and we tested each 20 times.

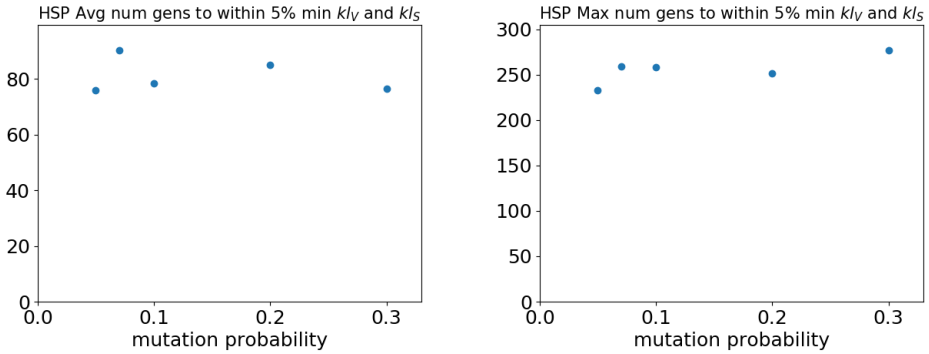

Figure C-4: Sensitivity study for mutation probability for the heave-surge-pitch problem. The first plot shows the average number of generations needed for the minimum kl_V and kl_S values in the optimization to get within 5% of the actual minimum kl_V and kl_S values, the second plot shows the maximum number of generations

From these tests, we concluded that a mutation probability of 0.1 is optimal, so we use this in all of our optimization in chapter 6.

Appendix D

Wall-sided results

In this appendix, we present the optimal shapes of vertical wall-sided shapes. We present them here instead of chapter 6 since they do not perform well compared to the other groups of shapes. These shapes, which we will call 'flat-sided' shapes are piecewise-linear with one slope discontinuity, where the segment from the waterline to the slope discontinuity is vertical. That is, $\overline{r_1} = 1$. Figure 4-11 shows examples of classes of shapes in this group. The parameters to optimize are kl_V and $\overline{z_1}$. $\overline{z_1}$ can be any number less than 0. A value of $\overline{z_1} < -1$ would signify a protruding downwards shape.

D.1 Heave-only

For the heave-only problem, the possible values of kl_V were [0.4,1.4,0.05], the possible values of $\overline{z_1}$ were [-2,0.1,0.05]. The initial population size was 60, and the number of generations was 500.

D.1.1 $\alpha = 3, \epsilon = 0.1$

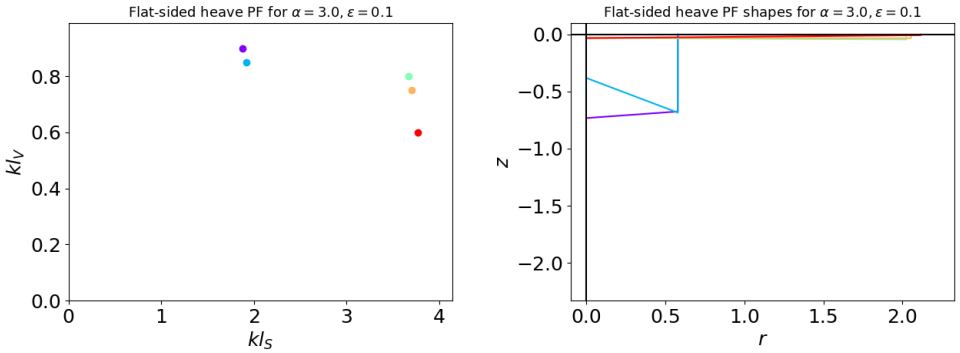

Figure D-1: Pareto Front (left) and corresponding shapes in the $r - z$ plane (right), resulting from the multi-objective evolutionary algorithm for 'flat-sided' shapes for the heave-only problem, with motion constraint $\alpha = 3$ and steepness constraint $\epsilon = 0.1$

kl_S	kl_V	kR	kH	$\overline{z_1}$	$\frac{\lvert\xi_3\rvert}{A}$
1.87	0.9	0.58	0.73	-0.92	2.96
1.92	0.85	0.58	0.38	-1.79	2.98
3.67	0.8	2.02	0.03	-1.44	0.27
3.7	0.75	2.05	0.03	-1.23	0.27
3.74	0.74	2.08	0.03	-1.0	0.27
3.76	0.72	2.09	0.03	-1.0	0.26
3.76	0.6	2.12	0.03	-0.2	0.25

Table D.1: Dimensions and characteristics of the 'flat-sided' shapes on the Pareto Front for the heave-only problem, with motion constraint $\alpha = 3$ and steepness constraint $\epsilon = 0.1$ (shown in figure D-1)

D.1.2 $\alpha = 3, \epsilon = 0.2$

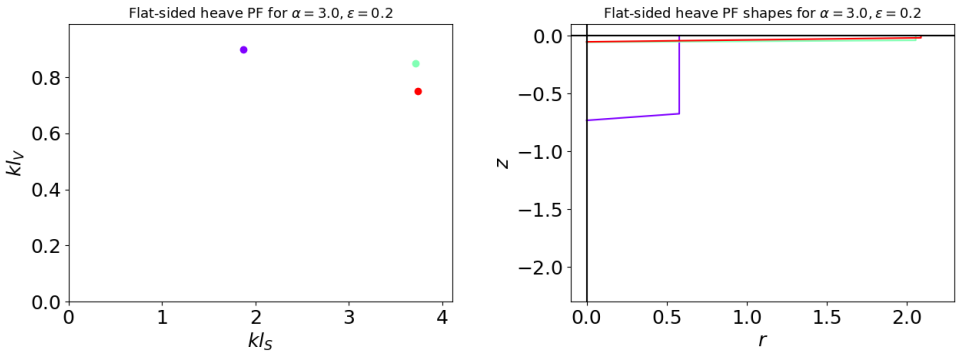

Figure D-2: Pareto Front (left) and corresponding shapes in the $r - z$ plane (right), resulting from the multi-objective evolutionary algorithm for 'flat-sided' shapes for the heave-only problem, with motion constraint $\alpha = 3$ and steepness constraint $\epsilon = 0.2$

kl_S	kl_V	kR	kH	$\overline{z_1}$	$\frac{\lvert\xi_3\rvert}{A}$
1.87	0.9	0.58	0.73	-0.92	2.96
3.71	0.85	2.05	0.06	-0.72	0.27
3.73	0.75	2.09	0.05	-0.36	0.26

Table D.2: Dimensions and characteristics of the 'flat-sided' shapes on the Pareto Front for the heave-only problem, with motion constraint $\alpha = 3$ and steepness constraint $\epsilon = 0.2$ (shown in figure D-2)

D.1.3 $\alpha = 1, \epsilon = 0.1$

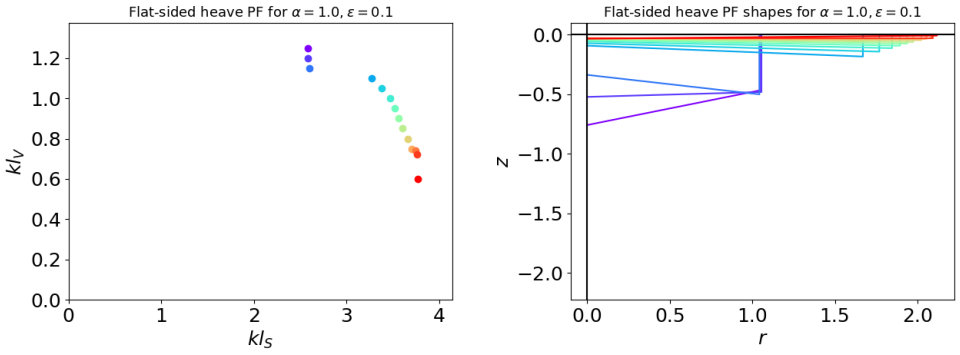

Figure D-3: Pareto Front (left) and corresponding shapes in the $r - z$ plane (right), resulting from the multi-objective evolutionary algorithm for 'flat-sided' shapes for the heave-only problem, with motion constraint $\alpha = 1$ and steepness constraint $\epsilon = 0.1$

kl_S	kl_V	kR	kH	$\overline{z_1}$	$\frac{\lvert\xi_3\rvert}{A}$
2.58	1.25	1.05	0.76	-0.61	0.98
2.59	1.2	1.06	0.52	-0.92	0.97
2.59	1.15	1.04	0.34	-1.49	1.0
3.27	1.1	1.67	0.09	-2.0	0.38
3.38	1.05	1.77	0.07	-2.0	0.35
3.47	1.0	1.85	0.06	-2.0	0.32
3.51	0.95	1.89	0.05	-2.0	0.31
3.56	0.9	1.94	0.04	-1.95	0.29
3.6	0.85	1.97	0.03	-2.0	0.29
3.66	0.8	2.02	0.03	-1.49	0.28
3.7	0.75	2.05	0.03	-1.23	0.27
3.74	0.74	2.08	0.03	-1.0	0.27
3.76	0.72	2.09	0.03	-1.0	0.26
3.76	0.6	2.12	0.03	-0.2	0.25

Table D.3: Dimensions and characteristics of the 'flat-sided' shapes on the Pareto Front for the heave-only problem, with motion constraint $\alpha = 1$ and steepness constraint $\epsilon = 0.1$ (shown in figure D-3)

D.1.4 $\alpha = 1, \epsilon = 0.2$

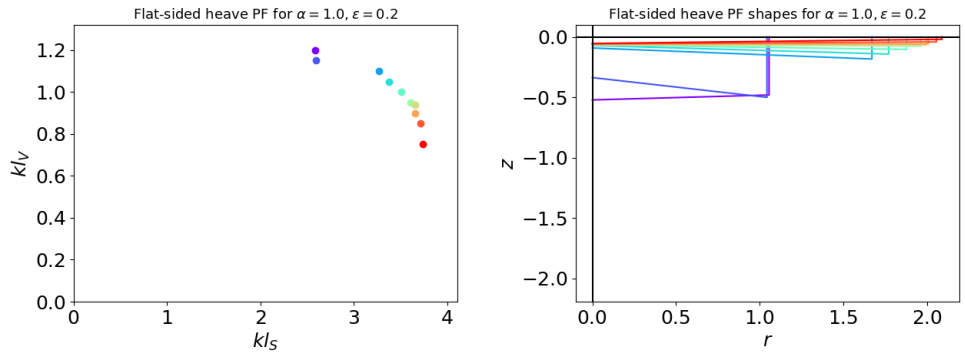

Figure D-4: Pareto Front (left) and corresponding shapes in the $r - z$ plane (right), resulting from the multi-objective evolutionary algorithm for 'flat-sided' shapes for the heave-only problem, with motion constraint $\alpha = 1$ and steepness constraint $\epsilon = 0.2$

kl_S	kl_V	kR	kH	$\overline{z_1}$	$\frac{\lvert\xi_3\rvert}{A}$
2.59	1.2	1.06	0.52	-0.92	0.97
2.59	1.15	1.04	0.34	-1.49	1.0
3.27	1.1	1.67	0.09	-2.0	0.38
3.38	1.05	1.77	0.07	-2.0	0.35
3.5	1.0	1.88	0.06	-1.59	0.31
3.61	0.95	1.96	0.06	-1.23	0.29
3.65	0.94	2.0	0.07	-1.0	0.29
3.66	0.9	2.01	0.06	-1.02	0.28
3.71	0.85	2.05	0.06	-0.72	0.27
3.73	0.75	2.09	0.05	-0.36	0.26

Table D.4: Dimensions and characteristics of the 'flat-sided' shapes on the Pareto Front for the heave-only problem, with motion constraint $\alpha = 1$ and steepness constraint $\epsilon = 0.2$ (shown in figure D-4)

Trends/ observations

- These shapes cannot protrude outwards, which is the trend we saw to be optimal in other groups. We see that the kl_V and kl_S values are significantly higher than the corresponding values for all of the other groups in chapter 6.
- There is generally not really a trend on if $\overline{z_1}$ less than -1 or greater than -1 is better. That is, it's not clear if protruding downwards shapes are better or worse.
- We still see that as α decreases, shapes get wider and shallower.

D.2 Heave-surge-pitch

For the heave-only problem, the possible values of kl_V were [0.4,1.4,0.05], the possible values of $\overline{z_1}$ were [-2,0.1,0.05]. The initial population size was 20, and the number of generations was 400.

D.2.1 $\alpha = 3, \epsilon = 0.1$

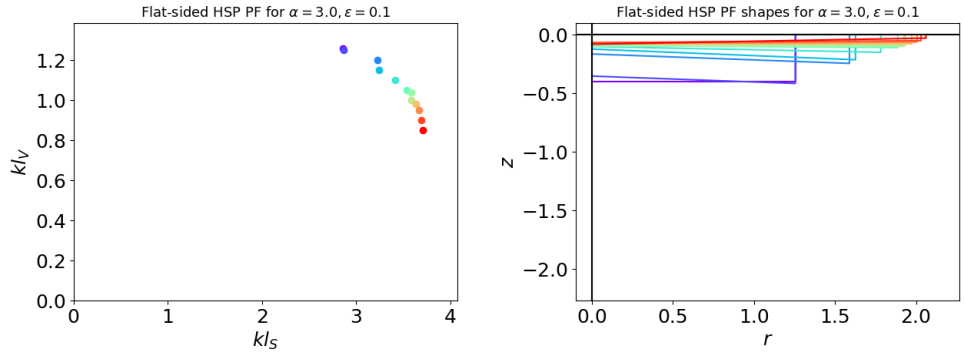

Figure D-5: Pareto Front (left) and corresponding shapes in the $r - z$ plane (right), resulting from the multi-objective evolutionary algorithm for 'flat-sided' shapes for the heave-surge-pitch problem, with motion constraint $\alpha = 3$ and steepness constraint $\epsilon = 0.1$

kl_S	kl_V	kR	kH	$\overline{z_1}$	$\frac{\lvert\xi_3\rvert}{A}$	$\frac{\lvert\xi_1\rvert}{A}$	$\frac{\lvert\xi_5\rvert}{A/R}$	$\overline{k_1}$	$\overline{z_G}$	$\overline{r_g}$
2.86	1.26	1.26	0.4	-1.0	0.7	0.66	2.41	1.39	0.12	0.5
2.87	1.25	1.25	0.35	-1.18	0.71	0.66	2.56	1.41	0.07	0.07
3.22	1.2	1.59	0.16	-1.49	0.43	0.79	1.14	1.33	0.34	0.67
3.24	1.15	1.63	0.12	-1.74	0.41	0.84	1.19	1.35	0.1	0.76
3.41	1.1	1.78	0.1	-1.49	0.35	1.04	0.95	1.31	0.45	0.86
3.53	1.05	1.89	0.09	-1.23	0.31	1.31	0.81	1.27	1.21	0.96
3.58	1.04	1.93	0.1	-1.0	0.3	1.49	0.72	1.23	1.98	0.99
3.58	1.0	1.94	0.08	-1.13	0.3	1.53	0.77	1.25	1.8	1.04
3.63	0.98	1.97	0.08	-1.0	0.29	1.69	0.72	1.23	2.32	1.08
3.67	0.95	2.01	0.08	-0.82	0.28	2.08	0.66	1.19	3.54	1.12
3.69	0.9	2.03	0.07	-0.77	0.28	2.5	0.64	1.18	4.49	1.22
3.7	0.85	2.06	0.08	-0.36	0.27	2.45	0.72	1.19	5.1	1.32

Table D.5: Dimensions and characteristics of the 'flat-sided' shapes on the Pareto Front for the heave-surge-pitch problem, with motion constraint $\alpha = 3$ and steepness constraint $\epsilon = 0.1$ (shown in figure D-5)

D.2.2 $\alpha = 3, \epsilon = 0.2$

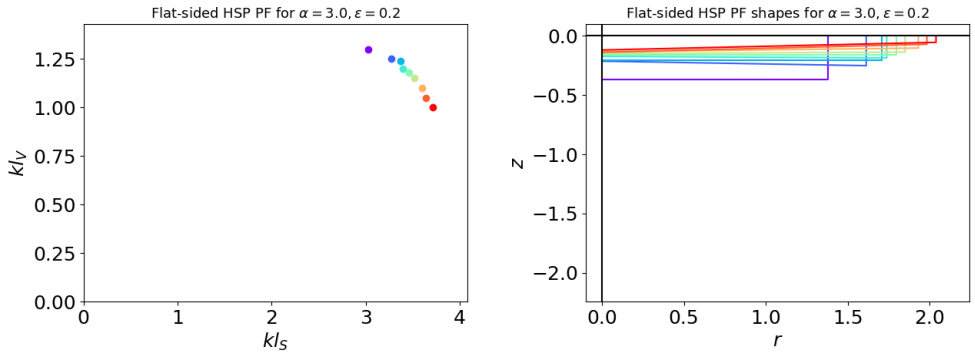

Figure D-6: Pareto Front (left) and corresponding shapes in the $r - z$ plane (right), resulting from the multi-objective evolutionary algorithm for 'flat-sided' shapes for the heave-surge-pitch problem, with motion constraint $\alpha = 3$ and steepness constraint $\epsilon = 0.2$

kl_S	kl_V	kR	kH	$\overline{z_1}$	$\frac{\lvert\xi_3\rvert}{A}$	$\frac{\lvert\xi_1\rvert}{A}$	$\frac{\lvert\xi_5\rvert}{A/R}$	$\overline{k_1}$	$\overline{z_G}$	$\overline{r_g}$
3.03	1.3	1.38	0.37	-1.0	0.6	0.67	1.69	1.34	0.22	0.53
3.27	1.25	1.61	0.21	-1.18	0.43	0.81	1.03	1.28	0.54	0.61
3.37	1.24	1.71	0.21	-1.0	0.39	0.91	0.87	1.24	0.82	0.71
3.39	1.2	1.74	0.17	-1.08	0.37	0.96	0.85	1.26	0.9	0.72
3.46	1.18	1.8	0.16	-1.0	0.35	1.05	0.78	1.24	1.13	0.79
3.51	1.15	1.85	0.15	-0.92	0.33	1.17	0.72	1.22	1.45	0.8
3.6	1.1	1.93	0.13	-0.77	0.31	1.5	0.65	1.18	2.09	0.88
3.64	1.05	1.98	0.14	-0.51	0.29	1.68	0.65	1.18	2.48	0.95
3.71	1.0	2.04	0.12	-0.46	0.28	2.64	0.54	1.11	3.59	1.03

Table D.6: Dimensions and characteristics of the 'flat-sided' shapes on the Pareto Front for the heave-surge-pitch problem, with motion constraint $\alpha = 3$ and steepness constraint $\epsilon = 0.2$ (shown in figure D-6)

D.2.3 $\alpha = 1, \epsilon = 0.1$

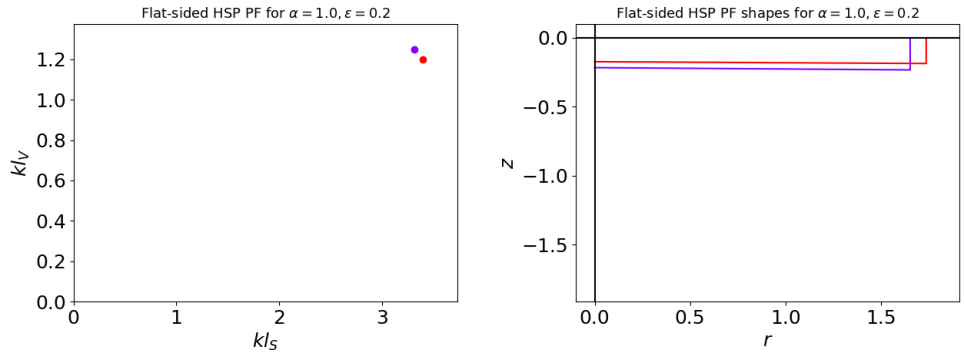

Figure D-7: Pareto Front (left) and corresponding shapes in the $r - z$ plane (right), resulting from the multi-objective evolutionary algorithm for 'flat-sided' shapes for the heave-surge-pitch problem, with motion constraint $\alpha = 1$ and steepness constraint $\epsilon = 0.1$

kl_S	kl_V	kR	kH	$\overline{z_1}$	$\frac{\lvert\xi_3\rvert}{A}$	$\frac{\lvert\xi_1\rvert}{A}$	$\frac{\lvert\xi_5\rvert}{A/R}$	$\overline{k_1}$	$\overline{z_G}$	$\overline{r_g}$
3.3	1.2	1.66	0.17	-1.28	0.4	0.85	0.98	1.3	0.58	0.68
3.34	1.15	1.71	0.13	-1.44	0.38	0.94	0.98	1.31	0.52	0.78

Table D.7: Dimensions and characteristics of the 'flat-sided' shapes on the Pareto Front for the heave-surge-pitch problem, with motion constraint $\alpha = 1$ and steepness constraint $\epsilon = 0.2$ (shown in figure D-8)

D.2.4 $\alpha = 1, \epsilon = 0.2$

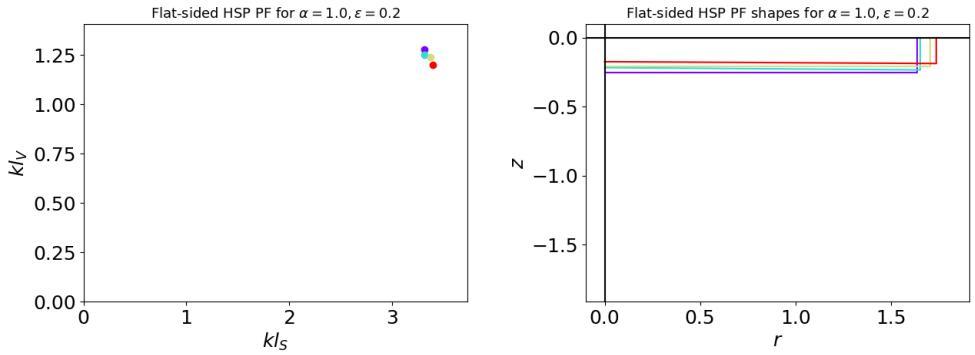

Figure D-8: Pareto Front (left) and corresponding shapes in the $r - z$ plane (right), resulting from the multi-objective evolutionary algorithm for 'flat-sided' shapes for the heave-surge-pitch problem, with motion constraint $\alpha = 1$ and steepness constraint $\epsilon = 0.2$

kl_S	kl_V	kR	kH	$\overline{z_1}$	$\frac{\lvert\xi_3\rvert}{A}$	$\frac{\lvert\xi_1\rvert}{A}$	$\frac{\lvert\xi_5\rvert}{A/R}$	$\overline{k_1}$	$\overline{z_G}$	$\overline{r_g}$
3.31	1.28	1.64	0.25	-1.0	0.43	0.82	0.97	1.25	0.62	0.66
3.32	1.25	1.65	0.22	-1.08	0.41	0.84	0.94	1.27	0.67	0.62
3.37	1.24	1.71	0.21	-1.0	0.39	0.91	0.87	1.24	0.82	0.71
3.39	1.2	1.74	0.17	-1.08	0.37	0.96	0.85	1.26	0.9	0.72

Table D.8: Dimensions and characteristics of the 'flat-sided' shapes on the Pareto Front for the heave-surge-pitch problem, with motion constraint $\alpha = 1$ and steepness constraint $\epsilon = 0.1$ (shown in figure D-5)

Trends/ observations

- All of these shapes are either cylinders or very close to cylinders. There is still not a clear trend on if it is better to protrude down or not.
- Compared to the heave-only shapes, these shapes are wider and shallower

Bibliography

[Al Shami et al., 2019] Al Shami, E., Zhang, R., and Wang, X. (2019). Point absorber wave energy harvesters: A review of recent developments. *Energies*, 12(1):47.

[Alamian et al., 2019] Alamian, R., Shafaghat, R., and Safaei, M. R. (2019). Multi-objective optimization of a pitch point absorber wave energy converter. *Water*, 11(5):969.

[Babarit, 2015] Babarit, A. (2015). A database of capture width ratio of wave energy converters. *Renewable Energy*, 80:610–628.

[Babarit et al., 2012] Babarit, A., Hals, J., Muliawan, M. J., Kurniawan, A., Moan, T., and Krokstad, J. (2012). Numerical benchmarking study of a selection of wave energy converters. *Renewable energy*, 41:44–63.

[Budal et al., 1975] Budal, K., Falnes, J., et al. (1975). Power generation from ocean waves using a resonant oscillating system. *Marine Science Communication*, 1(3, 4):269–288.

[Chang et al., 2018] Chang, G., Jones, C. A., Roberts, J. D., and Neary, V. S. (2018). A comprehensive evaluation of factors affecting the levelized cost of wave energy conversion projects. *Renewable Energy*, 127:344–354.

[Cretel et al., 2011] Cretel, J. A., Lewis, A. W., Thomas, G. P., Lightbody, G., et al. (2011). A critical assessment of latching as control strategy for wave-energy point absorbers. In *The Twenty-first International Offshore and Polar Engineering Conference*. International Society of Offshore and Polar Engineers.

[Dallman et al., 2018] Dallman, A., Jenne, D. S., Neary, V., Driscoll, F., Thresher, R., and Gunawan, B. (2018). Evaluation of performance metrics for the wave energy prize converters tested at 1/20th scale. *Renewable and Sustainable Energy Reviews*, 98:79–91.

[De Andrés et al., 2014] De Andrés, A. D., Guanche, R., Vidal, C., and Losada, Í. J. (2014). Analysis of the geometric tunability of a wec from a worldwide perspective. In *International Conference on Offshore Mechanics and Arctic Engineering*, volume 45530, page V09AT09A039. American Society of Mechanical Engineers.

[Deb, 2011] Deb, K. (2011). Multi-objective optimisation using evolutionary algorithms: an introduction. In *Multi-objective evolutionary optimisation for product design and manufacturing*, pages 3–34. Springer.

[Deb et al., 2005] Deb, K., Mohan, M., and Mishra, S. (2005). Evaluating the ε-domination based multi-objective evolutionary algorithm for a quick computation of pareto-optimal solutions. *Evolutionary computation*, 13(4):501–525.

[Drew et al., 2009] Drew, B., Plummer, A. R., and Sahinkaya, M. N. (2009). A review of wave energy converter technology.

[Durren, 2012] Durren, R. A. (2012). Absorber geometry optimization for a new wave energy converter.

[Esmaeilzadeh and Alam, 2019] Esmaeilzadeh, S. and Alam, M.-R. (2019). Shape optimization of wave energy converters for broadband directional incident waves. *Ocean Engineering*, 174:186–200.

[Evans, 1976] Evans, D. (1976). A theory for wave-power absorption by oscillating bodies. *Journal of Fluid Mechanics*, 77(1):1–25.

[Evans, 1980] Evans, D. (1980). Some analytic results for two and three dimensional wave-energy absorbers.

[Evans, 1981] Evans, D. (1981). Maximum wave-power absorption under motion constraints. *Applied Ocean Research*, 3(4):200–203.

[Evans, 1986] Evans, D. (1986). The hydrodynamic efficiency of wave-energy devices. In *Hydrodynamics of Ocean Wave-Energy Utilization*, pages 1–34. Springer.

[Evans and Porter, 1997] Evans, D. V. and Porter, R. (1997). Efficient calculation of hydrodynamic properties of owc-type devices.

[Falcão, 2010] Falcão, A. F. d. O. (2010). Wave energy utilization: A review of the technologies. *Renewable and sustainable energy reviews*, 14(3):899–918.

[Falnes, 1980] Falnes, J. (1980). Radiation impedance matrix and optimum power absorption for interacting oscillators in surface waves. *Applied ocean research*, 2(2):75–80.

[Falnes, 2007] Falnes, J. (2007). A review of wave-energy extraction. *Marine structures*, 20(4):185–201.

[Falnes and Kurniawan, 2020] Falnes, J. and Kurniawan, A. (2020). *Ocean waves and oscillating systems: linear interactions including wave-energy extraction*, volume 8. Cambridge university press.

[Garnaud and Mei, 2010] Garnaud, X. and Mei, C. (2010). Comparison of wave power extraction by a compact array of small buoys and by a large buoy. *IET renewable power generation*, 4(6):519–530.

[Garrison, 1975] Garrison, C. (1975). Hydrodynamics of large objects in the sea part ii: motion of free-floating bodies. *Journal of Hydronautics*, 9(2):58–63.

[Gilloteaux and Ringwood, 2010] Gilloteaux, J.-C. and Ringwood, J. (2010). Control-informed geometric optimisation of wave energy converters. *IFAC Proceedings Volumes*, 43(20):366–371.

[Gomes et al., 2012] Gomes, R., Henriques, J., Gato, L., and Falcão, A. d. O. (2012). Hydrodynamic optimization of an axisymmetric floating oscillating water column for wave energy conversion. *Renewable Energy*, 44:328–339.

[Gunn and Stock-Williams, 2012] Gunn, K. and Stock-Williams, C. (2012). Quantifying the global wave power resource. *Renewable Energy*, 44:296–304.

[Hager et al., 2012] Hager, R., Fernandez, N., Teng, M. H., et al. (2012). Experimental study seeking optimal geometry of a heaving body for improved power absorption efficiency. In *The Twenty-second International Offshore and Polar Engineering Conference*. International Society of Offshore and Polar Engineers.

[Haskind, 1957] Haskind, M. (1957). The exciting forces and wetting of ships in waves. *Izvestia Akademii Nauk SSSR, Otdeleni Tekhnicheskikh Nauk*, (7):65–79. Originally in Russian. English translation available as David Taylor Model Basin Translation No. 307.

[Kelly and Alam, 2019] Kelly, M. and Alam, M.-R. (2019). Shape optimization of a submerged pressure differential wave energy converter for load reductions. In *International Conference on Offshore Mechanics and Arctic Engineering*, volume 58899, page V010T09A030. American Society of Mechanical Engineers.

[Kim, 1963] Kim, W. (1963). The pitching motion of a circular disk. *Journal of Fluid Mechanics*, 17(4):607–629.

[Kurniawan, 2013] Kurniawan, A. (2013). Modelling and geometry optimisation of wave energy converters.

[Kurniawan and Moan, 2012] Kurniawan, A. and Moan, T. (2012). Optimal geometries for wave absorbers oscillating about a fixed axis. *IEEE Journal of Oceanic Engineering*, 38(1):117–130.

[Lee, 1995] Lee, C. (1995). Theory manual.

[Lee and Newman, 2006] Lee, C.-H. and Newman, J. N. (2006). Wamit user manual. *WAMIT, Inc*, page 42.

[Lehmann et al., 2017] Lehmann, M., Karimpour, F., Goudey, C. A., Jacobson, P. T., and Alam, M.-R. (2017). Ocean wave energy in the united states: Current status and future perspectives. *Renewable and Sustainable Energy Reviews*, 74:1300–1313.

[Lewis, 1988] Lewis, E. V. (1988). Principles of naval architecture second revision. *Jersey: SNAME*, 2.

[MARTINS-RIVAS and MEI, 2009] MARTINS-RIVAS, H. and MEI, C. C. (2009). Wave power extraction from an oscillating water column at the tip of a breakwater. *Journal of Fluid Mechanics*, 626:395–414.

[McCabe, 2013] McCabe, A. (2013). Constrained optimization of the shape of a wave energy collector by genetic algorithm. *Renewable energy*, 51:274–284.

[McCabe et al., 2010] McCabe, A., Aggidis, G., and Widden, M. (2010). Optimizing the shape of a surge-and-pitch wave energy collector using a genetic algorithm. *Renewable Energy*, 35(12):2767–2775.

[McCabe and Aggidis, 2009] McCabe, A. P. and Aggidis, G. A. (2009). A preliminary study into optimising the shape of a wave energy collector using a genetic algorithm. In *2009 International Conference on Sustainable Power Generation and Supply*, pages 1–7. IEEE.

[Mei et al., 2005] Mei, C., Stiassnie, M., and Yue, D. (2005). Theory and applications of ocean surface waves. part 1. linear aspects, adv. ser. *Ocean Eng*, 23:506.

[Mei, 1976] Mei, C. C. (1976). Power extraction from water waves. *JShR*, 20:63–66.

[Mei, 2012] Mei, C. C. (2012). Hydrodynamic principles of wave power extraction. *Philosophical Transactions of the Royal Society A: Mathematical, Physical and Engineering Sciences*, 370(1959):208–234.

[Miles, 1987] Miles, J. W. (1987). On surface-wave forcing by a circular disk. *Journal of Fluid Mechanics*, 175:97–108.

[Newman, 1976] Newman, J. (1976). The interaction of stationary vessels with regular waves. In *Proceedings of the 11th Symposium on Naval Hydrodynamics, London, 1976*.

[Newman, 1979] Newman, J. (1979). Absorption of wave energy by elongated bodies. *Applied Ocean Research*, 1(4):189–196.

[Newman, 2018] Newman, J. N. (2018). *Marine hydrodynamics*. The MIT press.

[Ricci et al., 2006] Ricci, P., Alves, M., Falcão, A., Sarmento, A., et al. (2006). Optimisation of the geometry of wave energy converters. In *Proceedings of the OTTI International Conference on ocean energy*.

[Ringwood et al., 2014] Ringwood, J. V., Bacelli, G., and Fusco, F. (2014). Energy-maximizing control of wave-energy converters: The development of control system technology to optimize their operation. *IEEE control systems magazine*, 34(5):30–55.

[Rosenberg and Mundon, 2016] Rosenberg, B. J. and Mundon, T. R. (2016). Numerical and physical modeling of a flexibly-connected two-body wave energy converter. In *Proceedings of the 4th marine energy technology symposium (METS), Washington, DC*.

[Shadman et al., 2018] Shadman, M., Estefen, S. F., Rodriguez, C. A., and Nogueira, I. C. (2018). A geometrical optimization method applied to a heaving point absorber wave energy converter. *Renewable energy*, 115:533–546.

[Tokić, 2016] Tokić, G. (2016). *Optimal Configuration of Large Arrays of Floating Bodies for Ocean Wave Energy Extraction*. Phd dissertation, Massachusetts Institute of Technology.

[Tokic and Yue, 2015] Tokic, G. and Yue, D. K. (2015). Optimal configuration of large arrays of floating bodies for ocean wave energy extraction. *APS*, pages H31–002.

[Tokić and Yue, 2019] Tokić, G. and Yue, D. K. (2019). Hydrodynamics of periodic wave energy converter arrays. *Journal of Fluid Mechanics*, 862:34–74.

[Uihlein and Magagna, 2016] Uihlein, A. and Magagna, D. (2016). Wave and tidal current energy–a review of the current state of research beyond technology. *Renewable and Sustainable Energy Reviews*, 58:1070–1081.

[Warpindyasmoro and Gunadi, 2018] Warpindyasmoro, H. S. and Gunadi, K. (2018). Geometric development of point absorber wave energy conventer. In *MATEC Web of Conferences*, volume 164, page 01011. EDP Sciences.

[Wen et al., 2018] Wen, Y., Wang, W., Liu, H., Mao, L., Mi, H., Wang, W., and Zhang, G. (2018). A shape optimization method of a specified point absorber wave energy converter for the south china sea. *Energies*, 11(10):2645.

[Xu et al., 2018] Xu, D., Stuhlmeier, R., and Stiassnie, M. (2018). Assessing the size of a twin-cylinder wave energy converter designed for real sea-states. *Ocean Engineering*, 147:243–255.

[Zhang et al., 2016] Zhang, W.-c., Liu, H.-x., Zhang, L., and Zhang, X.-w. (2016). Hydrodynamic analysis and shape optimization for vertical axisymmetric wave energy converters. *China Ocean Engineering*, 30(6):954–966.